POLITECNICO DI MILANO
DEPARTMENT OF MECHANICAL ENGINEERING
DOCTORAL PROGRAMME IN MECHANICAL ENGINEERING

EXPERIMENTAL CHARACTERIZATION AND MODELING OF THE MECHANICAL BEHAVIOUR OF PARTICLEBOARD

Doctoral Thesis of:
Riccardo Galeazzi

Supervisors:
Prof. Andrea Bernasconi
Prof. Roberto Corradi

Tutor:
Prof.ssa Bianca Maria Colosimo

The Chair of the Doctoral Program:
Prof.ssa Bianca Maria Colosimo

2016 – XXIX Cycle

Ringraziamenti - Acknowledgement

27 aprile 2017, pochi giorni prima della consegna, in questo lavoro è racchiuso tutto il sacrificio profuso in questi tre anni. Il raggiungimento di questo traguardo non sarebbe stato possibile se non grazie al fondamentale aiuto delle persone che hanno contribuito per questo risultato.

Voglio ringraziare in maniera sentita il Prof. Andrea Bernasconi, per la sua pazienza e professionalità. Durante questo periodo ho avuto modo di lavorare assieme a lui e conoscerlo in maniera più profonda. Mi sono reso conto di aver trovato una persona su cui poter contare. Grazie Andrea!

Un sincero grazie ai miei studenti Andrea Carini e Tiziano Villa, i quali hanno dato un significativo contributo nello sviluppo di questo documento scientifico e con i quali ho stretto un sincero rapporto di lavoro nella parte finale del mio dottorato.

Ringrazio il Gruppo Mauro Saviola per aver fornito i dati e i campioni di materiali.

Non per ultimi ringrazio la mia famiglia, i miei amici e tutte le persone che mi hanno accompagnato in questo periodo in cui ho potuto vivere professionalmente il Politecnico di Milano.

Index

Index ……V

Figure index ……VIII

Table index ……XVI

Introduction …… - 20 -

Chapter 1- State of the Art.....- 22 -

1.1Types of panels used in furniture industry and their production process. ..... - 22 -

1.1.1 Introduction..... - 22 -

1.1.2 Medium Density Fiberboard (MDF)..... - 24 -

1.1.3 Oriented Standard Board (OSB) ..... - 26 -

1.1.4 Hard-board and Soft-board ..... - 28 -

1.1.5 Plywood ..... - 29 -

1.1.6 Particleboard ..... - 31 -

1.2Mechanical and physical characterization of the particleboard panels, brief literature review ……...- 36 -

1.3Macro-mechanical modeling techniques to study heterogeneous materials..... - 43 -

1.3.1Three point bending tests for the evaluation of the flexural modulus E_1 and the out of plane shear modulus G_{12} in adhesive joint crack length determination..... - 45 -

1.3.2.....Three point bending application: in plane shear properties determination of anti-symmetric laminates ..... - 46 -

1.3.3. Three point bending test with varying span: out-of-plane elastic properties of honeycomb sandwich panels. ..... - 47 -

1.4Micro-mechanical modeling techniques applied to heterogeneous natural materials ..... - 48 -

1.4.1On Mean-field methods. Predicting the damage and modelling grain size effect of heterogeneous composites materials.. ..... - 49 -

1.4.2 On Mean-field methods. Mori-Tanaka model to micromechanical modelling of heterogeneous materials (composites materials)..... - 51 -

1.4.3..... Micromechanical model of heterogeneous composite materials by the finite element method (FEM)..... - 54 -

1.5Experimental techniques involved in Macro and Micro mechanical modeling development of particleboard panels ..... - 58 -

1.5.1Micro Computer Tomography, a briefly overview ..... - 59 -
1.5.1.1Absorption mode: Interaction between material and X-Ray Beam ..... - 62 -
1.5.1.2X-Ray source used: Synchrotron light ..... - 65 -
1.5.1.3Digital Image Correlation method with mono-camera set-up, a preface ..... - 67 -
1.5.1.4DIC Set-up arrangement..... - 68 -
1.5.1.5DIC algorithm implemented in N-Corr software, a brief overview ..... - 70 -

Chapter 2 – Micro CT particleboard analysis .....- 75 -

2.1 Outline..... - 75 -
2.2 Micro CT set – up, parameters and sample's preparation..... - 76 -
2.3 Micro-CT qualitative image analysis: Particleboard microstructure and their constituents... - 86 -
2.4 Micro-CT quantitative image analysis: Particleboard's Vertical Density Profile estimation. - 97 -
2.4.1 Particleboard's moisture content determination..... - 97 -
2.4.2 Particleboard's Vertical Density Profile (VDP)..... - 99 -
2.5 Vertical Density Profile of particleboard by industrial equipment: measurement and comparison with Micro-CT result. ..... - 108 -
2.5.1 Sample's mean density by gravimetric method ..... - 108 -
2.5.2 Vertical density profile measurement by industrial equipment..... - 110 -
2.5.3 Comparison ..... - 114 -

Chapter 3 – Particleboard, Macro mechanical characterization..- 117 -

3.1 Outline..... - 118 -
3.2 Experimental set-up and calibration: Three Point Bending Test, Iosipescu Test and Digital Image Correlation…….-119-
3.2.1 Three Point Bending Test set-up ..... - 119 -
3.2.2 Iosipescu test set-up..... - 122 -
3.2.3 Digital Image Correlation set-up..... - 124 -
3.2.4 DIC Calibration ..... - 128 -
3.2.5 Particleboard's sample preparation ..... - 130 -
3.3 Elastic constants determination by Three Point Bending Test ..... - 135 -
3.4 Analysis of the relationship between panel density and Elastic longitudinal modulus profiles …… - 145 -
3.5 Elastics constants validation: Iosipescu and TPBT coupled with DIC field method..... - 147 -
3.5.1 Iosipescu and DIC validation ..... - 147 -
3.5.2 TPBT with fixed span validation coupled with DIC field method..... - 166 -
3.6 Conclusions……- 176 -

Chapter 4 – Micro-mechanical model of particleboard wood based material.....- 178 -

4.1 Outline..... - 178 -

4.2 Digimat software..... - 180 -

4.3 Backlit wood-particles geometrical measurement set-up ..... - 183 -

4.4 Particleboard Micro mechanical model building input data collecting ..... - 186 -

4.4.1 Manual detection of the geometrical properties of the wood particles…….....-186-

4.4.2 Particles wood automatically detection using particles before glued spreading and hot-pressing phase……- 192-

4.4.3 Wood fibres geometry comparison ..... - 195 -

4.4.4 Particleboard volume fraction determination..... - 197 -

4.4.5 Mechanical characteristics of particleboard constituents: Wood..... - 203 -

4.4.6 Mechanical characteristics of particleboard constituents: Urea-Formaldehyde Adhesive..... - 207 -

4.4.7 Evaluation of Digimat-FE algorithms to build RVE's particleboard: Classical FE algorithm ..... - 207 -

4.4.8 Evaluation of Digimat-FE algorithms to build RVE's particleboard: Stacking algorithm ..... - 210 -

4.4.9 RVE generation strategies..... - 211 -

4.4.10 RVE Convergence analysis..... - 212 -

4.5 Results and discussion ..... - 214 -

4.6 Conclusion and Further developments..... - 219 -

References .....- 221 -

Figure index

Figure 1: MDF Panel (10) (11) ..... - 24 -
Figure 2: a) Layers orientation OSB (13); b) final product (14). ..... - 26 -
Figure 3: a) Hardboard aspect (17); b) Soft-board aspect (18) ..... - 28 -
Figure 4: Plywood aspect (23) ..... - 30 -
Figure 5: Raw particleboard production workflow ..... - 32 -
Figure 6: Finishing Process Workflow ..... - 33 -
Figure 7: Wood-Mattress formations ..... - 35 -
Figure 8: Particleboard of different thicknesses. ..... - 35 -
Figure 9: Ennobled particleboard panel (26) ..... - 36 -
Figure 10:Mechanical properties evaluation of particleboard (ASTM D1037): a) Typical Stress-Strain curve in bending condition. b) Internal bond test set-up. ..... - 38 -
Figure 11: a) Vertical density profile of PB of 38mm of thickness; b) Elastic modulus profile .. - 43 -
Figure 12: Particleboard projection ..... - 44 -
Figure 13: Extraction of the slice XY ..... - 44 -
Figure 14: Multiscale Homogenization Method (45) ..... - 50 -
Figure 15: Composite unit cells. a) Periodic; b) Random (45) ..... - 50 -
Figure 16: Comparison between results. a) Von-Mises Stress in the 15wt.% E-Glass; b) Stress distribution in the composite at different weight percentage of reinforcement; c) Elastic Modulus comparison (53). ..... - 55 -
Figure 17: a) RVE containing 100 perfectly aligned fibers with different fiber lengths,; b) Prediction of the Young's Modulus in function of number of fibers contained in RVE (57). ..... - 56 -
Figure 18: Results comparisons between different macro and micro models. a) Level of damage; b) Reaction force obtained in global damage case; c) Reaction force obtained in local damage case (57) ..... - 57 -
Figure 19: Specimen geometry tested in this PhD thesis. a) Three Points Bending Test specimen; b) Iosipescu Test Specimen; c) Micro-CT specimen. ..... - 59 -
Figure 20: Micro-CT principle ..... - 60 -
Figure 21: From 2D image (slices) to 3D Image (reconstructed volume) of the object. ..... - 60 -
Figure 22: a) Ovine mitral valve; b) Micro-CT 3D reconstruction; c) 3D FE model of mitral valve using 3D model b) (60) ..... - 60 -
Figure 23: a) 3D image reconstructed of textile composites using experimental set-up proposed in b) (61) ..... - 61 -
Figure 24: a) Particleboard sample 10x10x18mm; b) Particleboard reconstructed 3D volume by Micro-CT imaging in absorption mode and using Synchrotron light source ..... - 61 -
Figure 25: Mass attenuation coefficients as a function of photon energy for five pure materials. - 62 -
Figure 26: Adsorption mode using Fan set-up (59) ..... - 65 -
Figure 27: 2D-Image production workflow ..... - 65 -
Figure 28: Electrons Source LINAC of Elettra Synchrotron (66) ..... - 66 -
Figure 29: a) Bending magnets at Synchrotron facility; b) Beam Lines (66) ..... - 67 -

Figure 30: Different speckle-pattern on tensile test specimens. From left to right the speckle pattern reproduce “white noise”, random distribution that simulates the white spray paint on black surface and the three cyrcle diameters repetitive subset (70) ..... - 68 -
Figure 31: Two different DIC set-up: a) Macroscopic field displacement measurement of Four Point Bending Test (71); b) Microscopic field displacement measurement in tensile test of high temperature conditions (72). ..... - 69 -
Figure 32: Subset and node definition (77) ..... - 70 -
Figure 33: Vertical displacement comparison along ab line. a) N-Corr results; b) Vic-2D results; c) Comparison between N-Corr and Vic-2D (71) ..... - 72 -
Figure 34: ε_{xx} field deformations comparison along ab line. a) N-Corr results; b) Vic-2D results; c) Comparison between N-Corr and Vic-2D (71) ..... - 72 -
Figure 35: SYRMEP Control Room ..... - 76 -
Figure 36: Tomograph Room at SYRMEP Lab ..... - 77 -
Figure 37: Micro-CT set-up. a) from X-Ray beam source; b) from detector ..... - 77 -
Figure 38: Particleboard sample mounted on rotating table of the tomograph ..... - 79 -
Figure 39: different sections of the same particleboard’s sample (iii). a); b); c); d) sample’s sections acquired applying vertical displacement (Z direction) equal to 5.5mm to reach entire volume reconstructed ..... - 79 -
Figure 40: Particleboard’s samples extraction. a) Sample’s extraction from the main board; b) Band saw; c) from the center of particleboard 1860 wide and 3860mm long, small squared pieces of 50mm of side are cut and then reduced in to specimens of 10 x 10 x 18 mm ..... - 81 -
Figure 41: a) Thermo-sealer and hermetic bags; b) Parafilm tape (80); c) Particleboard’s sample sealed by Parafilm tape. ..... - 82 -
Figure 42: Reference materials. a) Aceton; b) Distilled water; c) Glycerol ..... - 82 -
Figure 43: a) Absorption coefficients of the reference materials; b) Mass absorption coefficient of the reference materials ..... - 83 -
Figure 44: de-noising images. a) Dark image; b) Flat image ..... - 83 -
Figure 45: Test image to control the sample position ..... - 84 -
Figure 46: Particleboard’s projections acquired during Micro-CT scan ($\Delta\theta = 0.1°$) from a sample with reference adhesive quantity and composition (Table 14). a) Projection number 1 ($\theta = 0°$); b) Projection number 300 ($\theta = 30°$); c) Projection number 450 ($\theta = 45°$); d) Projection number 750 ($\theta = 75°$); e) Projection number 900 ($\theta = 90°$); f) Projection number 1800 ($\theta = 180°$). ..... - 85 -
Figure 47: Reference materials projections. a) Aceton; b) Water; c) Glycerol ..... - 85 -
Figure 48: Sinograms principle (59). ..... - 86 -
Figure 49: Density zones of the particleboard. a) 18mm particleboard thickness; b) Visualization of the high and low density zone to define the skins and core; c) 18mm particleboard density profile obtained by industrial measurements. ..... - 87 -
Figure 50: Particleboard’s volume reconstructed. a) Particleboard’s sample (“Reference”); b) 3D Volume of particleboard from Micro-CT ..... - 88 -
Figure 51: 8-bit gray-level Particleboard’s slices with adhesive content equal to 75 kg/m^3 and no tracker, it is defined as a “Reference Sample”. a) Slice extracted from high-density zone at thickness level (Z-axis) of 0.87mm (Lower-Skin); b) Slice extracted from low-density zone at thickness level (Z-axis) equal to 8.9mm (Core) (5.5% Moisture Content). ..... - 89 -
Figure 52: Micro-CT of Solid wood, in (i) the images refers to reconstruction of beech wood, in (ii) the image refers to the Scots pine’s reconstructions. A) Longitudinal image, B) Transverse view, C) 3D view (83). ..... - 90 -
Figure 53: Particle wood characterization. a) beech wood in longitudinal view taken from literature (83); b) particle wood extracted from slice 990 of Reference sample (Figure 50b) from particleboard

studied in this Thesis; c) beech wood in transverse view from literature(72); d) particle wood extracted from slice 990 of Reference sample from particleboard characterized in this Thesis (Figure 50b)..... - 90 -
Figure 54: Particle wood characterization. a) Scots pine sapwood in transverse view (83); b) two particles wood extracted from slice 97 of Reference sample (Figure 50a)..... - 91 -
Figure 55: Histogram plots of the particle extracted from Figure 50. i); ii) Histogram of core's particle of Figure 52b and Figure 52d; iii) Histogram of skins particle wood of Figure 53b..... - 91 -
Figure 56: 8-bit gray-level Particleboard's slices with adhesive content equal to 80 kg/m^3 and 1% of TiO_2 as contrast agent, it is defined as a "Full Sample". a) Slice extracted from high-density zone at thickness level (Z-axis) of 17.6mm (Upper-Skin); b) Slice extracted from low-density zone at thickness level (Z-axis) equal to 10.7mm (Core)..... - 93 -
Figure 57: Adhesive gray-level quantification..... - 94 -
Figure 58: Thresholding procedure to isolate the adhesive coating. a) 2D image with pixels with gray-value between 47 and 49; b) binary image after thresholding..... - 95 -
Figure 59: Adhesive distribution from particleboard's Micro-CT made of radiata pine (84). a) Accumulation of adhesive around small wood's particle; b) Radiata pine particleboard's slice with tracked adhesive; c) Binary image that highlight the adhesive distribution around the particles and in capillary channels between the particles (black arrows) (84)..... - 95 -
Figure 60: Set-up used to determine the moisture content of the particleboard. a) Scale; b) Oven; c) Dryer ..... - 97 -
Figure 61: Three reference's materials reconstruction results. Staking 200 slices in the middle of the container's tube to obtain the 3D images. a) Aceton's 3D volume; b) 3D volume of aceton cut; c) 2D aceton's slice; d) distilled water's 3D volume; e) 3D volume of water cut; f) 2D water's slice; g) glycerol's 3D volume; h) 3D volume of glycerol cut; i) 2D Glycerol's slice. ..... - 100 -
Figure 62: reference's materials histograms. a) Aceton; b) Distilled Water; c) Glycerol; d) Air .- 101 -
Figure 63: Reference materials 32-bit Gray-Level ..... - 101 -
Figure 64: Relation between the absorption coefficient of the reference's materials and their Gray-Level from Micro-CT images at 15keV of beam energy..... - 102 -
Figure 65: From particleboard's gray levels to particleboard's absorption coefficients. a) 3D particleboard's volume. The specimen reconstructed is Reference 1 (no tracker used and adhesive quantity equal to 75kg/m^3; b) Gray-Level of each slices; c) Particleboard's absorption coefficients..- 103 -
Figure 66: Relation between the density of the reference's materials and their absorption coefficients at 15keV of beam energy..... - 103 -
Figure 67: Vertical Density profile estimated for specimen Reference 1 with adhesive quantity equal to 75kg/m^3, no tracker used and 5.4% of moisture content..... - 104 -
Figure 68: Density evaluation procedure ..... - 105 -
Figure 69: Particleboard's Vertical Density Profiles from quantitative image analysis of Micro-CT acquired with beam's energy equal to 15keV and exposure time equal to 1.001s. a) Full1; b) Full2; c) Full3; d) Full4; e) Reference1; f)Normal2..... - 105 -
Figure 70: Characterization of the anomaly peaks found in VDP of the specimens. a) VDP of the specimen "Full1"; b) 32-Bit Gray-Level profile of the specimen "Full1"; c) Full 1's Slice at thickness level equal to 9.2mm; a) VDP of the specimen "Full3"; b) 32-Bit Gray-Level profile of the specimen "Full3"; c) Full 3's Slice at thickness level equal to 8.9mm..... - 106 -
Figure 71: SEM Micro-graphy of the surface at the inclusion's thickness level of the Full1 sample..- 107 -
Figure 72: Sample's dimension determination ..... - 108 -

Figure 73: IMAL DPX 300 Vertical Density Profile detector (81). a) Real machine; b) 3D model....- 110 -
Figure 74: Particleboard's sample dimensions to load it in the VDP detector. ..... - 111 -
Figure 75: Samples loader of VDP detector. a) Before the acquisition; b) at the end of the acquisition ..... - 111 -
Figure 76: Sample "Reference 1" extraction from specimen used to evaluate VDP by IMAL's detector..... - 112 -
Figure 77: Vertical Density Profiles measured along the particleboard's thickness by VDP detector DPX300 provided by IMAL facility located in Modena. a) Six VDP of particleboard's samples with thickness equal to 8mm; b) mean density profile of six samples of 8mm of thickness; c) Six VDP of particleboard's samples with thickness equal to 18mm; d) mean density profile of six samples of 18mm of thickness; e) Six VDP of particleboard's samples with thickness equal to 38mm; f) mean density profile of six samples of 38mm of thickness. ..... - 113 -
Figure 78: Mean density comparison between profile estimated by Micro-Ct Image analysis and DPX300 measurement: a) two profiles without the rescale; b) Density profile from Micro-CT analysis scaled by 10% compared to industrial one. ..... - 114 -
Figure 79: TPBT Load configuration (32) ..... - 119 -
Figure 80: MTS Bend Fixture 642.10B. a) 642.01A roller block assembly; b) 642.10B roller block assembly; c) MTS three points bending fixture 86 ..... - 120 -
Figure 81: Multipurpose electro mechanic machine MTS Alliance RT/100 and Force Transducer 4501055..... - 120 -
Figure 82: Three points bending set-up. a) Set-Up overview; b) load configuration ..... - 121 -
Figure 83: Three points bending test shear load (T) and bending moment load (M). ..... - 122 -
Figure 84: Iosipescu fixture device. a) Device's description (97); b) Iosipescu equipment..... - 122 -
Figure 85: Iosipescu internal actions: Shear load (T) and Bending moment load (M)..... - 123 -
Figure 86: a) The active elements of two orthogonal strain gauges are centered between the notch roots at the angle shown (97); b) particleboard's surface ..... - 124 -
Figure 87: Iosipescu and Digital Image Correlation set-up ..... - 124 -
Figure 88: DIC set-up prepared to TPBT..... - 125 -
Figure 89: Designed procedure to govern properly the electro mechanic machine to allow the image acquisition. a) Iosipescu test procedure; b) three points bending test procedure..... - 126 -
Figure 90: N-Corr Graphic User Interface ..... - 127 -
Figure 91: DIC calibration samples. 1) Black spray paint speckle; 2) black airbrush paint speckle....- 128 -
Figure 92: Calibration test performed on samples of polyamide 66 with 30% glass fiber as a reinforce parallel to their longitudinal direction. a)=i); b)=ii); c)=iii; d)=iv..... - 129 -
Figure 93: Deformation-Load curves of the PA66GF30 samples tested in their longitudinal direction considering DIC-Radius equal to 50pixels and Subset spacing equal to 5 pixels. a) Black on white speckle, produced by spray paint and tested with led lamp positioned to reach raking light on the sample; b) black on white speckle produced, by airbrush and tested with led lamp positioned to reach raking light on the sample; c) black on white speckle produced by spray paint and tested without led lighting; d) black on white speckle produced by airbrush paint and tested without led lighting. ..... - 130 -
Figure 94: Three points bending test sample extraction ..... - 130 -
Figure 95: Iosipescu's sample. a) Standard geometry (97); b) Sample without notch ..... - 131 -
Figure 96: Iosipescu's samples extraction from the main board ..... - 132 -
Figure 97: Iosipescu samples. a) Original raw geometry of 38mm; b) After the skin's discharge; c) Iosipescu core sample starting from panel with thickness equal to 38mm. ..... - 132 -

Figure 98: TPBT and Iosipescu tests ROIs ..... - 133 -
Figure 99: Workflow to produce the suitable ROI of the specimen for DIC measurement ..... - 133 -
Figure 100: DIC Samples. a) Iosipescu test; b) TPBT test ..... - 133 -
Figure 101: Reference images to DIC acquired to perform particleboard core's shear modulus validation. a) Iosipescu Test; b) Three Points Bending Test. ..... - 134 -
Figure 102: Bending stresses theoretical distribution. a) Vertical Density Profile; b) Sandwich model of the particleboard; c) Normal stress in the skins; d) Shear stress in the core ..... - 135 -
Figure 103: Density clouds from industrial measurements. a) 8mm; b) 18mm; c) 38mm ..... - 136 -
Figure 104: R^2 to select the suitable linear equation to interpolate the density of the skins (black arrows). a) Upper skin; b) lower skin. ..... - 137 -
Figure 105: a) first tentative interpolation of the skins and core; b) magnification..... - 137 -
Figure 106: Density profile interpolation. a) Comparison between the approximations; b) final results. ..... - 138 -
Figure 107: Elastic constants evaluation algorithm. ..... - 139 -
Figure 108: TPBTVS load-strain curves. a) 38mm; b) 18mm; c) 8mm ..... - 139 -
Figure 109: geometrical quantities of particleboard's model b) real shear stress distribution in a sandwich beam; c) Modelled shear stress in a sandwich beam; d Modelled normal stress in a sandwich beam ..... - 141 -
Figure 110: three sandwich models to express the flexural stiffness. a) Pure sandwich model (PSM); b) Bi-Linear sandwich model (BSM); c) Quadratic-Bi-Linear sandwich model (QSM) ..... - 143 -
Figure 111: Density – E modulus relationship starting from elastic constants determined by TPBTVS and Bi-Linear Sandwich Modulus (BSM). a) 38mm; b)18mm; c) 8mm. ..... - 145 -
Figure 112: Density – E modulus relationship starting from elastic constants determined by TPBTVS and Quadratic-Bi-Linear Sandwich Modulus (QSM). a) 38mm; b)18mm; c) 8mm... - 146 -
Figure 113: Iosipescu DIC results about Horizontal Displacement (U) reported in [mm] of 18mm sample. a) 10N; b) 100N; c) 210N; d) 360N. ..... - 148 -
Figure 114: Iosipescu DIC results about Vertical Displacement (V) reported in [mm] of 18mm sample. a) 10N; b) 100N; c) 210N; d) 360N. ..... - 149 -
Figure 115: Iosipescu DIC results about ε_{xx} reported in [mm/mm] of 18mm sample. a) 10N; b) 100N; c) 210N; d) 360N. ..... - 149 -
Figure 116: Iosipescu DIC results about ε_{yy} reported in [mm/mm] of 18mm sample. a) 10N; b) 100N; c) 210N; d) 360N. ..... - 150 -
Figure 117: Iosipescu DIC results about ε_{xy} reported in [mm/mm] of 18mm sample. a) 10N; b) 100N; c) 210N; d) 360N. ..... - 150 -
Figure 118: Iosipescu DIC results about Horizontal Displacement (U) reported in [mm] of 38mm sample without skins. a) 10N; b) 100N; c) 210N; d) 288N. ..... - 151 -
Figure 119: Iosipescu DIC results about Vertical Displacement (V) reported in [mm] of 38mm sample without skins. a) 10N; b) 100N; c) 210N; d) 288N. ..... - 152 -
Figure 120: Iosipescu DIC results about ε_{xx} reported in [mm/mm] of 38mm sample without skins. a) 10N; b) 100N; c) 210N; d) 288N. ..... - 152 -
Figure 121: Iosipescu DIC results about ε_{yy} reported in [mm/mm] of 38mm sample without skins. a) 10N; b) 100N; c) 210N; d) 288N. ..... - 153 -
Figure 122: Iosipescu DIC results about ε_{xy} reported in [mm/mm] of 38mm sample without skins. a) 10N; b) 100N; c) 210N; d) 288N. ..... - 153 -
Figure 123: Comparison between vertical displacements measured from DIC (red-line) and Crosshead of the machine (blue-line). a) 18mm particleboard's sample; b) 38mm particleboard's sample without the outer skins. ..... - 154 -
Figure 124: Iosipescu notches geometry. ..... - 155 -

Figure 125: Iosipescu Load-Stain curves obtained by DIC method. a) 18mm sample; b) 18mm proportionality zone to calculate the G_{13}; c) 38mm sample without the skins; d) 38mm proportionality zone to calculate the G_{13}. ..... - 156 -
Figure 126: Iosipescu DIC results about Horizontal Displacement (U) reported in [mm] of 38mm sample without skins and notches. a) 10N; b) 100N; c) 210N; d) 385N. ..... - 158 -
Figure 127: Iosipescu DIC results about Vertical Displacement (V) reported in [mm] of 38mm sample without skins and notches. a) 10N; b) 100N; c) 210N; d) 385N. ..... - 158 -
Figure 128: Iosipescu DIC results about ε_{xx} strain reported in [mm/mm] of 38mm sample without skins and notches. a) 10N; b) 100N; c) 210N; d) 385N. ..... - 159 -
Figure 129: Iosipescu DIC results about ε_{yy} strain reported in [mm/mm] of 38mm sample without skins and notches. a) 10N; b) 100N; c) 210N; d) 385N. ..... - 159 -
Figure 130: Iosipescu DIC results about ε_{xy} strain reported in [mm/mm] of 38mm sample without skins and notches. a) 10N; b) 100N; c) 210N; d) 385N. ..... - 160 -
Figure 131: Iosipescu DIC results about Horizontal Displacement (U) reported in [mm] of 18mm sample without notches. a) 10N; b) 100N; c) 210N; d) 360N; e) 510N; f) 540N. ..... - 161 -
Figure 132: Iosipescu DIC results about Vertical Displacement (V) reported in [mm] of 18mm sample without notches. a) 10N; b) 100N; c) 210N; d) 360N; e) 510N; f) 540N. ..... - 161 -
Figure 133: Iosipescu DIC results about ε_{xx} strain reported in [mm/mm] of 18mm sample without notches. a) 10N; b) 100N; c) 210N; d) 360N; e) 510N; f) 540N. ..... - 162 -
Figure 134: Iosipescu DIC results about ε_{yy} strain reported in [mm/mm] of 18mm sample without notches. a) 10N; b) 100N; c) 210N; d) 360N; e) 510N; f) 540N. ..... - 163 -
Figure 135: Iosipescu DIC results about ε_{xy} strain reported in [mm/mm] of 18mm sample without notches. a) 10N; b) 100N; c) 210N; d) 360N; e) 510N; f) 540N. ..... - 164 -
Figure 136: Shear Modulus profile (G_{13}) calculated on the Iosipescu particleboard sample over the core. a) 18mm core sample; b) 38mm core sample (without the skins). ..... - 165 -
Figure 137: TPBT with fixed span coupled with DIC results about Horizontal Displacement (U) reported in [mm] of 18mm sample. a) 5N; b) 50N; c) 100N; d) 150N. ..... - 167 -
Figure 138: TPBT with fixed span coupled with DIC results about Vertical Displacement (V) reported in [mm] of 18mm sample. a) 5N; b) 50N; c) 100N; d) 150N. ..... - 167 -
Figure 139: TPBT with fixed span coupled with DIC results about ε_{xx} strain reported in [mm/mm] of 18mm sample. a) 5N; b) 50N; c) 100N; d) 150N. ..... - 168 -
Figure 140: TPBT with fixed span coupled with DIC results about ε_{yy} strain reported in [mm/mm] of 18mm sample. a) 5N; b) 50N; c) 100N; d) 150N. ..... - 168 -
Figure 141: TPBT with fixed span coupled with DIC results about ε_{xy} strain reported in [mm/mm] of 18mm sample. a) 5N; b) 50N; c) 100N; d) 150N. ..... - 169 -
Figure 142: TPBT with fixed span coupled with DIC results about Horizontal Displacement (U) reported in [mm] of 38mm sample. a) 25N; b) 75N; c) 125N; d) 280N. ..... - 169 -
Figure 143: TPBT with fixed span coupled with DIC results about Vertical Displacement (V) reported in [mm] of 38mm sample. a) 25N; b) 75N; c) 125N; d) 280N. ..... - 170 -
Figure 144: TPBT with fixed span coupled with DIC results about ε_{xx} strain reported in [mm/mm] of 18mm sample a) 25N; b) 75N; c) 125N; d) 280N. ..... - 170 -
Figure 145: TPBT with fixed span coupled with DIC results about ε_{yy} strain reported in [mm/mm] of 18mm sample a) 25N; b) 75N; c) 125N; d) 280N. ..... - 171 -
Figure 146: TPBT with fixed span coupled with DIC results about ε_{xy} strain reported in [mm/mm] of 18mm sample a) 25N; b) 75N; c) 125N; d) 280N. ..... - 171 -
Figure 147: Deflectometer and DIC vertical displacement comparison. a) 18mm particleboard's sample; b) 38mm particleboard's sample. ..... - 172 -

Figure 148: Shear stress distribution by horizontal equilibrium. a) Sandwich panel scheme; b) calculation scheme. ..... - 173 -
Figure 149: Shear stress distribution in the skin and in the core (only one side is shown, the other is symmetrical). a) Particleboard specimen of 18mm; b) particleboard specimen of 38mm. ..... - 174 -
Figure 150: G_{13} profiles determined knowing the shear stress distribution and shear strain from DIC analysis. a) Shear modulus profile of 18mm core panel; b) shear modulus profile of 38mm core panel. ..... - 174 -
Figure 151: Digimat interface. a) Digimat's control panel; b) Digimat FE model tree. ..... - 181 -
Figure 152: Typical unit cells resulted from the FE simulations. a) 166 aligned fibers in the longitudinal direction 1. The volume fraction of fibers (v) and their aspect ratio (FAR) are respectively v=15.7% and FAR = 15; b) 245 randomly oriented fibres in the 1-2 plane. v=15.7% and FAR = 15 (107). ..... - 182 -
Figure 153: RVE of Nano-composite containing 24 nanoparticles. Is possible to see the surrounding interphase of the particles generated by Digimat-FE. ..... - 182 -
Figure 154: backlit table to visualize the slides, transparencies or X-Ray plate. ..... - 183 -
Figure 155: a) Backlit table set-up; b) wood-particles ready to be framed ..... - 184 -
Figure 156: a) fine wood-particles; b) coarse wood-particles. ..... - 184 -
Figure 157: backlit images. a) Fine particles; b) coarse particles. ..... - 185 -
Figure 158: Equalization procedure and rigid rotation performed on 8-bit Micro-CT slices. a) Original Image after conversion from 32bit to 8bit; b) slice processed by equalization; c) slice after rigid rotation with the material reference system. ..... - 187 -
Figure 159: Fibre detection procedure. The red-dashed lines represent the principal axis while the light blue lines individuates the secondary axis. ..... - 188 -
Figure 160: Principal axis length distribution of the core's fibres for each class length. ..... - 189 -
Figure 161: Principal axis length distribution of the skin's fibres for each class length. ..... - 189 -
Figure 162: Polar diagrams and tensor display. a) core particles orientation distribution; b) skins particles orientation distribution; c) orientation tensor display. ..... - 190 -
Figure 163: Particleboard 3D reconstructed volume observed from different views. a) 3D; b) X-Y plane; c) X-Z plane; d) Y-Z plane. ..... - 191 -
Figure 164: two snapshots. a) X-Z plane view of the core zone; b) X-Z plane view skin zone. - 192 -
Figure 165: a) Original image of core fibres; b) binary image after IS analysis; c) inverted image. ...- 193 -
Figure 166: Example of superposition of the fibres (see the yellow arrows) ..... - 193 -
Figure 167: Principal axis length distribution of the core's fibres from backlit image analysis. - 194 -
Figure 168: Principal axis length distribution of the skin's fibres from backlit image analysis. - 195 -
Figure 169: Principal axis length comparison between Micro-CT and backlit image analysis. a) core's fibres; b) skin's fibres ..... - 196 -
Figure 170: 3D Image saw from XY plane before (a) and after (b) cropping procedure to prepare it to the Quant3D analysis. ..... - 197 -
Figure 171: Particleboard core 3D reconstructed volume as input of Quant3D software. ..... - 198 -
Figure 172: Fibre's wood volume fraction in function of the grey level changing ..... - 198 -
Figure 173: Measured void ratio in relation with OSB mean density and threshold level (119). .- 199 -
Figure 174: a) 8-bit slice; b) grey-level histogram ..... - 199 -
Figure 175: Grey level histogram of the 3D reconstructed volume of particleboard's portions. a) core's portion; b) skin's portion. ..... - 201 -
Figure 176: a) Probabilities for the C_0 class (ω_0) and for C_1 class (ω_1) for the panel's core; b) Mean levels for C_0 class (μ_0) and for C_1 class (μ_1) for the panel's core; c) C_0 class (ω_0) and for C_1 class

(ω_1) for the panel's skin; d) Mean levels for C_0 class (μ_0) and for C_1 class (μ_1) for the panel's skin. ..- 202 -
Figure 177: σb2 trend. a) particleboard's core; b) particleboard's skin. ..... - 202 -
Figure 178: wood orientation of two different extracted samples. ..... - 204 -
Figure 179: Digimat panel to input the wood transversely isotropic properties. ..... - 205 -
Figure 180: Fibre directions definition compared to the principal axis length. ..... - 206 -
Figure 181: Classical FE Algorithm results. a) RVE of particleboard; b) Principal axis length comparison between Micro-CT and Digimat RVE; c) Principal axis length comparison between backlit table and Digimat RVE. ..... - 209 -
Figure 182: Particleboard fiber's comparison. a) Real wood's particles; b) Model of the single fiber. ..... - 210 -
Figure 183: RVE convergence analysis of the 18mm particleboard's core using stacking algorithm and input data from Section 4.4. ..... - 213 -
Figure 184: Micromodelling core strategies flowchart. ..... - 215 -
Figure 185: Core RVE built by Stacking algorithm using fiber geometrical data from backlit table source and without UF-adhesive. a) Visible air (red voxel); b) without air visualization. ..... - 215 -
Figure 186: Core RVE built by Stacking algorithm using fiber geometrical data from backlit table source and considering UF-adhesive. a) Visible air (green voxel); b) without air visualization.- 216 -
Figure 187: RVE – 3D reconstructed volume particleboard comparison. a) Micro-CT volume; b) Core's RVE with UF-Adhesive; c) Core's RVE without UF-Adhesive. ..... - 217 -

Table index

Table 1:Physical and Mechanical Properties of wood species (5-24) ..... - 23 -
Table 2: Required bending strength prescribed to Orented Strand Board (EN300) ..... - 27 -
Table 3: Type of panel tested in (27) ..... - 37 -
Table 4: MOE, MOR and IB calculations (ASTM D1037) ..... - 37 -
Table 5: Experimental design and composition of the core of three layers particleboards (28)... - 39 -
Table 6: Mechanical properties of Particleboard made of kiwi prunings (28). ..... - 40 -
Table 7: Experimental design and results (29) ..... - 40 -
Table 8: Experimental design followed in (30). ..... - 41 -
Table 9: Mechanical Properties of Particleboards made of pinecone and pure wood particles (30). ...- 42 -
Table 10: Case considered in (52). a11 and a22 are the orientation distribution ..... - 53 -
Table 11: Properties of composite's constituents (53) ..... - 54 -
Table 12: Mechanical Properties of Laminas (57) ..... - 57 -
Table 13: Types of particleboard samples scanned with Micro-CT technique ..... - 80 -
Table 14: Reference material characteristics. μ coefficient are obtain from XMuDat database (65) at beam-energy equal to 15 keV. ..... - 83 -
Table 15: Successive weightings ..... - 98 -
Table 16: Particleboard's moisture content in percentage ..... - 98 -
Table 17: 32-bit Mean Gray-Level of four reference's substances. ..... - 101 -
Table 18: Mean results of density, absorption coefficient, 32-bit Gray Level and moisture content. ..- 106 -
Table 19: Mass percentage of the chemical components find in the anomaly region of the sample "Full1" ..... - 107 -
Table 20: Sample's sides measurements ..... - 108 -
Table 21: Mean values of the sample's sides and their volume. ..... - 109 -
Table 22: Comparison between density results from Micro-CT image analysis and gravimetric method ..... - 109 -
Table 23: Technical Data IMAL DPX 300 (81) ..... - 110 -
Table 24: Mean values of every six VDP for each particleboard's thicknesses ..... - 113 -
Table 25: Final mean density comparison between three quantitative methods ..... - 114 -
Table 26: Force transducer and Deflectometer characteristics (96) ..... - 121 -
Table 27: Picture and Camera features ..... - 126 -
Table 28: Three points bending tests sample's dimensions ..... - 131 -
Table 29: Geometrical dimensions of skins and cores for each panel. In the brackets there is the thickness evaluated by statistical analysis ..... - 138 -
Table 30: maximum load and related strain for the TPBTVS ..... - 140 -
Table 31: Particleboard's elastic constants results by Pure Sandwich Model (PSM) (Temperature equal to 26°C and humidity equal to 35%). ..... - 143 -
Table 32: Particleboard's elastic constants results by Bi-Linear Sandwich Model (BSM) (Temperature equal to 26°C and humidity equal to 35%). ..... - 144 -

Table 33: Particleboard's elastic constants results by Quadratic and Bi-Linear Sandwich Model (QSM) (Temperature equal to 26°C and humidity equal to 35%). - 144 -
Table 34: Deviation between BSM and QSM - 144 -
Table 35: Iosipescu coupled with DIC results from five particleboard samples with notches. - 156 -
Table 36: Iosipescu and DIC results compared with three points bending test with varying span results about shear modulus. - 156 -
Table 37: Difference between the methods about the shear modulus determination - 157 -
Table 38: Iosipescu coupled with DIC results from one particleboard sample for each thickness, without notches. - 165 -
Table 39: Iosipescu + DIC results and three points bending test with varying span results final comparison about G_{13} - 165 -
Table 40: TPBT load conditions coupled with DIC field method - 166 -
Table 41: G_{13} results by Three Points Bending Test coupled with DIC field method determined at environment condition of temperature and humidity equal to 26°C and 35%. - 175 -
Table 42: Final comparison between macroscopic methods - 175 -
Table 43: Geometrical characteristics of the core fibres. - 189 -
Table 44: Geometrical characteristics of the skin fibres. - 189 -
Table 45: Orientation tensor components for the core and skins of the panel. - 190 -
Table 46: Fibre's thicknesses. - 191 -
Table 47: Geometrical characteristics of core particles by backlit image analysis. - 194 -
Table 48: Geometrical characteristics of skin particles by backlit image analysis. - 194 -
Table 49: Comparison between fibres geometrical quantities acquired from Micro-CT and backlit images. - 196 -
Table 50: fiber/voids class definition. - 203 -
Table 51: fibers volume fractions. - 203 -
Table 52: Conifer wood properties assigned to fibre's wood. - 206 -
Table 53: Urea-Formaldehyde thermoset adhesive properties. - 207 -
Table 54: Particleboard's constituents volume fractions. - 211 -
Table 55: Convergence analysis results - 213 -
Table 56: Comparison between different RVE dimensions - 214 -
Table 57: Micromechanical model elastic constants results for core portion and comparisons - 216 -
Table 58: New micromechanical model elastic constants results for core portion and comparisons - 217 -

Introduction

In this PhD thesis, different modelling techniques and experimental methods were employed to study the mechanical behavior of particleboard. Particleboard is a wood-based material made of particles of recycled wood bonded together with urea-formaldehyde adhesive. Although the mechanical properties of this material are lower in comparison with well-known composites as carbon fibers reinforced polymers (CFRP) or glass fibers reinforced polymers (GFRP), particlewood is particularly suitable for and designed for the furniture industry. This market is interested in reducing production cost by reducing raw materials consumption and adding value by improving transportation and the assembly operation by reducing the weight of particlewood panels.

Taking in to account these considerations, this thesis is focused on the estimation of elastic constants of actual particleboard and modelling, aiming at understanding the relationship between the properties of the constituents and those of the final product, particularly under bending loads. This knowledge is believed to be fundamental for exploring new solutions, not developed in this PhD work, to manufacture lighter panels, while keeping the same performances or even improve them.

Considering the product range of the major industries involved in the production of particleboard, the panels are classified by their thicknesses from a minimum of 4mm to a maximum of 40mm, but the most diffused thickness 18mm. For this, my work will be focused on the characterization of particleboard having thickness equal to 18mm and in a second time I will exploring the applicability of the same techniques to the panels having thickness equal to 8mm and 38mm. The characterization of the elastic constants of the board will follow a multi-scale approach, considering macro-level and micro-level of the material, by applying un-conventional techniques like micro-CT and micro-scale modelling.

This thesis first reviews the literature to introduce the different types of wood based panels and its production process, focusing in particular on the production of particleboard. Then, the similarities between particleboard and composite materials and structures, in particular sandwich panel, are presented in the perspective of exploiting them to determine experimentally the elastic constants of recycled particlewood panels. Therefore, literature was explored to identify the principal modelling methods used in composites, to understand which could be applied to particleboard panels. In a similar way, the literature about micro modelling methods for heterogeneous material was analyzed to select the best techniques to generate a suitable Representative Volume Element (RVE) of particleboard, allowing for obtaining the homogenized elastic constants and comparing them with macro-level ones. The experimental techniques applied to particleboard to generate the data used in macro and micro approaches are presented: Three points bending test (TPBT) and Iosipescu test (IT).

To collect the data to perform the particleboard's micro-modelling, measurements and imaging methods are exploited, namely Micro Computer Tomography (Micro-CT) and Digital Image Correlation (DIC).

Chapter 2 deals with the analysis of the microstructure of particleboard by standard vertical density profile measurements and by Micro-CT. Elastic properties and bending performances of particleboard panels are mainly related to density. Therefore this chapter is dedicated to measuring particleboard density and obtaining data useful for the evaluation of orientation and dimensions of the wood particles, that will be used for micro-modelling presented in Chapter 4.

Once studied the morphological aspect and the vertical density profile of the particleboard, Chapter 3 presents the results of different experimental approaches to the determination of the elastic constants of particleboard panels, using TPBT, IT and DIC.

Finally, in Chapter 4, the micro-modelling techniques used to generate an RVE of the particleboard samples, extracted from the panel analyzed by micro CT, to estimate its homogenized elastic constants are presented. Results obtained by macro-approaches and micro-approaches are compared and discussed.

Chapter 1- State of the Art

1.1 Types of panels used in furniture industry and their production process.

1.1.1 Introduction

In the furniture industry and in building construction field there are many wood-based materials used to build different components. Their mechanical characteristics, final applications, morphological aspect and cost, are very important factors to decide which material should be used, e.g. to make pieces of furniture for different indoor/outdoor applications: home, office, industries or, more in general, building construction. Based on these final applications and observing the design requirements, the macro-classes of the wood-based materials used are principally (1) (2) (3) (4):

- Solid wood
- Particleboard
- MDF (Medium Density fiberboard)
- OSB (Oriented Strand Board)
- Hardboard
- Softboard
- Plywood

Table 1 reports some physical and mechanical characteristics of this species.

Particleboard, the object of this PhD Thesis, is one of the materials most used in furniture industries. It is a cheap material, versatile, and nowadays it is also environmentally friendly because it is mainly made of recycled wood.

In the past, this type of panel made of particles of wood (size between 0.25 and 10 mm) pressed together and bonded with an adhesive was principally produced using different virgin woods dried after mechanical grinding, to reach the maximum particleboard quality. Nowadays it is possible to obtain high-quality particleboard using 100% of recycled wood, preserving in this manner the environment. This recycled wood comes from “end-of-life” pieces of furniture collected in many

proper collection centers. For this, it is reasonable to suppose that the variety of wood species involved is very wide, from soft wood to hard wood, including already used particleboard.

In particular, the evolution of particleboard production using recycled wood as a raw material from 0% to 100%, starts in 1995, when only 10% of the total wood used was composed of wood waste. In 2003, in agreement with the European Panel Federation report (5), in Germany, the panel's production was made using 19% of recycled wood. In the same year, the Belgium particleboard producers used up to 25% of wood waste. However, in these years, using a maximum of 35% of the recycled wood in particleboard productions means optimum quality level reachable, with mechanical characteristics comparable with those of particleboard made of virgin wood. Using more than 35% of wood scraps as raw material meant lower mechanical properties of the final product and higher amounts of adhesive required, due to lower wettability of recycled chips. The reduction of adhesive use, while increasing the scraps percentage as material raw, was possible only by coating the wood chips with tannin component, but this procedure was very costly compared to the final economic value of the product.

Table 1:Physical and Mechanical Properties of wood species (5-24)

Species	**Density [kg/m^3]**	**Particle size [mm]**	**E [MPa]**	**$\sigma_{rupture}$ [MPa]**
Solid Wood	400 - 1200	-	4400 – 13700	27 – 140
Particleboard	600 – 700	0.25 - 10	2400 – 2800	14 – 18
MDF	550 - 800	~0.1	3200 – 3800	30 – 44
OSB	600 - 680	5 - 100	2400 – 5800	17 – 31
Hardboard	> 900	0.25 - 1	4500 – 5400	> 30
Softboard	140 - 300	0.2 - 2	3000 – 4000	> 15
Plywood	500 - 900	-	2000 – 9300	27 - 80

It was necessary to wait until 2006 for the particleboard panels to be produced using 100% of recycled wood for the Italian market. This important goal was possible thanks to a new process, thermo-hydrolytic disintegration. In this manner, good wettability of the wood particles to the urea formaldehyde adhesive was reached and the adhesive's consumption was decreased obtaining final characteristics comparable to the virgin wood particleboard (sometimes higher) (6). From this moment on, the particleboard production using the wood waste as a raw material became more and more widespread, reaching the optimal compromise between mechanical and physical characteristics, low adhesive consumption and low urea-formaldehyde release compared to the panels produced with virgin chips (6).

Today particleboard and more in general wood-based panels are products that are strong, clean, efficient with low production cost and, as a presented before, minimal effect on the environment. It is possible to use for functional, structural or decorative applications providing a practical combination of economic and ecological (5).

Before explaining in detail the production process of the particleboard panel studied in this PhD work, it is interesting to understand briefly the others types of wood-based products listed in Table 1 and their production process (due to the vast literature, only solid wood properties and technology are not presented).

1.1.2 Medium Density Fiberboard (MDF)

Medium Density Fiberboard (MDF) panel is produced using a dry process. The final product is a wood-based foil as a result of the fiber bonded by a synthetic adhesive matrix. As reported in (7) the fiber observed by electron microscopy, has a diameter in order of magnitude of 100μm. They are obtained starting from wood scraps that are washed and softened in an stem-pressurized and then transported into a pressurized refiner chamber where revolving disks generates the fibers from wood pulp (8). Lastly, to form the board, the following step is named "Hot Pressing Process" (9) where high temperature and pressure acts to reach the final product. MDF panels are classified based on their mean density: high-density MDF (HDF), whose mean density is higher than 800kg/m^3; low-density MDF (LDF) whose mean density is lower than 650kg/m^3; and extra low density MDF (ULDF),whose mean density is lower than 550kg/m^3.

The panel has smoothed surfaces and its aspect is characterized by light coloured straw as shown in Figure 1

Figure 1: MDF Panel (10) (11)

The technical process usually followed to produce the MDF panel consists of several steps. The first step is grinding of wood pieces, to obtain the chips. In the following step, the chips are softened by heating and then, using mechanical process, are reduced in fibres that are glued, dried and compacted to form a "mattress" before the final pressing step. The range of panel's thicknesses varies between 1.8mm to 60mm, the width from 1220mm to 1850mm and the length is usually 3660mm. Types of woods uses as a raw material to produce MDF are equally distributed between soft woods or hard woods, depending on the availability in the geographic zone. However, an MDF panel is normally composed of:

- 82% virgin wood fibers (usually from soft-wood)
- 10% of synthetic matrix of adhesive (urea-formaldehyde based)
- 7% of water
- <1% of paraffin
- <0.05% of silicon

The MDF panel's surface is smooth and it is very good as a substrate for gluing the decorative paper to obtain coated panels used to produce furniture or separation walls for interior applications. The thickness tolerances are ±0.2mm for panels with a maximum thickness of 30mm and ±0.3mm for greater thickness (refers to EM13 Standard). To avoid surface defects, after the finishing process the board surfaces are sanded with 100 – 120 grit (12). To apply the decorative papers on the MDF, the pressing phase varies from 30s and 4min at a temperature equal to 70°C – 130°C. These ranges of time and temperature depend on the press type: mono-vain or multi-vain. The finished panels are stack up for 8 hours before any others process (12).

Final applications of MDF board (raw or ennobled), are principally oriented to produce entire furniture systems or parts of them. Using MDF, it is possible to produce furniture for interiors, offices, reception areas, hotels, restaurants, bars, shops, exhibition areas, laboratories, workshops, classrooms, play areas and museums (12).

Moreover, MDF ennobled panels are largely used in building applications such as separation wall panels, floors, doors, fireplace frames, tiles for ceiling, radiator covers and ladders. This is possible because the MDF is dimensionally stable, has a very low sensibility to changing environment conditions. MDF has very high resistances to shocks and impacts, as well as good resistance to fire and moisture (if the proper additives are used). Though the production is lower, it is possible to use the MDF to external non-structural applications, as signboards, garden furniture and shacks (12).

1.1.3 Oriented Standard Board (OSB)

The wood-based panel named Oriented Standard Board (OSB) is constituted of oriented long and thin lamellar particles, that give very good mechanical characteristics to the final products. The lamellar particles are properly glued and deposed on three different layers, conserving the orientations equally 0/90/0 degrees. In particular, in outer layers the strands are longitudinally oriented along the panel length; whereas in the middle, the strands are generally lie in a crosswise direction. These oriented layers and the following hot-pressing phase give the panel a good mechanical resistance and dimensional stability. Figure 2 show the oriented layers and the final product.

a b

Figure 2: a) Layers orientation OSB (13)*; b) final product* (14).

The very good performances of this panel are high mechanical resistance, similar to the plywood of equivalent class, high stiffness, high interlaminar strength, very good weight/resistance ratio and minimum ecological impact. To produce the OSB panels, raw materials are obtained from virgin wood of trees with small diameter stems, usually grown in ecological sustainable forests (15).

OSB typical density is in the range 600 – 680kg/m^3, the thickness varies between 6mm and 40mm and geometrical dimensions commonly available on the market are 2440mm x 1250mm.

The technical production process requires as a raw material virgin wood from both softwoods and some hardwoods species. The strands are cut using a mechanical process where rotating knives that cut the strand longitudinally from debarked stems. The ribbon of strands is about 75mm wide; it is cut at 100mm along the grain and from 5mm to 50mm across the grain. The strands of this geometry are dried and glued using different types of resins: phenol-formaldehyde resin (PF), melamine fortified urea-formaldehyde adhesive (MUF) or isocyanate (PMDI), all these resins are moisture-resistant adhesives. It is important to underline that OSB core is typically bonded with PMDI while in the outer layers MUF is used to reduce the press cycles and give the bright appearance (15). It is simple to recognize an OSB panel because the strands are visible on the surface. The OSB colours vary from light straw colour to medium brown depending on wood species used, resin and pressing condition.

The strand orientation is not always visible, especially for small pieces extracted from the main panels. The surface roughness, already good, can be improved by sanding process without compromising the unique exterior aspect of OSB (15). However, this panel is not adapt to be covered with decorative papers like MDF panels, because the roughness of the surfaces is too high for this process and the surfaces aspect is mostly in agreement with the final uses of these OSB panels.

In the market, OSB are classified based on different level of load-bearing applications and moisture resistance (ENV 12872, EN 13986; EN300). This classification is:

- General purpose and interior fitments boards (including furniture) for use in dry conditions (OSB/1)
- Load-bearing boards for use in dry conditions (OSB/2)
- Load-bearing boards for use in humid conditions (OSB/3)
- Heavy-duty load-bearing boards for use in humid conditions (OSB/4)

Table 2 lists the required bending strength of OSB for each class.

Table 2: Required bending strength prescribed to Orented Strand Board (EN300)

Types	**Required bending strength on major axis [MPa]**				
	Board Thickness range [mm]				
	6 to 10	**> 10 to 18**	**> 18 to 25**	**> 25 to 32**	**> 32 to 40**
OSB/1	20	18	16	-	-
OSB/2	22	20	18	16	14
OSB/3	22	20	18	16	14
OSB/4	30	28	26	24	22

Good mechanical properties of OSB are directly correlated with the orientation of the strand in the core and in the skins. This material is particularly suitable for structural applications, not only in building construction field as floors, roof decking and wall sheathing but also in exhibition stand construction, shop fitting, packaging, interior partitioning, decorative and laminated furniture, concrete formwork and non-slip coatings.

1.1.4 Hard-board and Soft-board

Natural fiberboard (NFB) is a category of panel produced without any binding agent; Hard-board is one of the panel types of this class. Natural fiberboard complies with all the European health and environmental standards: CE-Marking, FSC PEFC and F-JIS. This panel is considered formaldehyde free; this make this product completely clean, safe, recyclable and biodegradable. The fiberboard NFB has low CO_2 emission and waste can be composted (16).

a b

Figure 3: a) Hardboard aspect (17)*; b) Soft-board aspect* (18)

As shown in Figure 3a, the Hard-board colour appearance is medium brown and its thickness is ≤3.5mm (Standard EN622-2). It is possible to produce painted Hardboard using plain colours or by printing wood-grain or other surface patterns. This production process for Hardboard product, determine the different appearance of two sides of the panel: principal side is smooth and on the reverse side there is a mesh pattern.

Mean density of the Hardboard is > 900kg/m^3, in agreement with Standard EN-323 (19). The Soft-board instead, has a mean density equal to 140 – 300kg/m^3 (EN 1602) and a range of thickness equal to 4 – 200mm (EN 823) (20).

Both Hard-board and Soft-board panels are formed using pure wood fibres from virgin softwood logs of length and diameter equal to 1 – 3m and 100 – 300mm, respectively. These logs are cleaned with sprinkled water and then ground into small fibres. In the following thermo-mechanical treatment, the lignin re-polymerizes to bind the wood fibers without any addition of synthetic glue or resin. Hardboard is formed by high-pressure and temperature during a pressing process, to obtain high-density boards that satisfy the requirements for demanding applications as a result of tempering and other technical processes that allow for achieving great physical and mechanical characteristics and excellent dimensional stability. For example, the bending strength, evaluated according to EN 310, is >30N/mm^2 and the internal bond strength is equal to or > 0.5N/mm^2 (evaluated according to standard EN319) (16) (19). Hardboard panels, raw or painted, have a lot of applications in packaging, furniture,

door-skins, toys, automobile and caravan interiors. Being a fully natural material, hardboard is a very good solution for making food packaging for vegetables, fruits and water bottles. Painted or patterned hardboard is used to create building interior walls, decorations, acoustic insulation walls, exhibitions display walls, or furniture accessories like drawer bottoms, cupboards inners and kitchen fittings.

The soft-board panels are the reference product for good thermal insulation against the cold but also against the summer heat thanks to the high heat storage capacity of this material and its low thermal conductivity equal to 0.037 – 0.070 W/m^2K. Soft-board reduces the noise transmission between adjacent rooms (room to room, neighbor to neighbor and above to below). It is very interesting that this low-density material allows for moisture balance, ensuring full permeability without any use of membranes or cavities (20).

1.1.5 Plywood

Engineered panels composed of an uneven number of thin plies of wood veneers bonded together with rigid adhesive and with the grain direction of adjacent layers perpendicular to each other are called Plywood. Bonding adjacent timber veneers using a rigid adhesive, it is possible to exploit the superior strength and stiffness along the grain (21) (22). The most important properties of Plywood are reported below:

- Stability of dimensions; the change in length along the grain after moisture exposition is 1/100 of that perpendicular to the grain
- Strength and stiffness weight ratio
- Resistance to concentrated loads
- Resilience, impact and fatigue resistance
- Thermal insulation
- Acoustic reflection
- Workability
- Aesthetics

To fabricate Plywood panels like those shown in Figure 4, the production process is divided into two phases: veneer production and Plywood fabrication. Concerning veneer production, the first step is log preparation to debark its surface and increase the moisture content by water sprayed to soften it.

Figure 4: Plywood aspect (23)

The second step is the peeling phase, where the log is properly mounted on a lathe and by its rotation against a lathe knife, the veneer (their thickness are around 3.4mm for the core plies and 0.5mm for the outer plies (24)) is obtained as a continuous ribbon of consistent thickness subsequently cut to the desired dimensions. Then, the veneer are dried with hot air to reach a moisture content of 8% for optimal gluing result. If necessary, it is possible to joint or repair small strips of veneer into full-size sheets to reduce the scraps. The veneers are now ready for Plywood fabrication. The dried veneers are assembled in two bundles: in the first, the graded faces are assembled in longitudinal bands; in the second bundle, in transverse bands; if the final Plywood is composed of three plies, a third layer is constituted by the core. The two bundles are driven to the glue spreader where rollers depose a synthetic resin on both sides of the veneers, by passing through them. The adhesives are thermo-setting resins with different characteristics: partially and fully weather resistant (external applications), high or low humidity resistance (interior applications). At the end of this production phase, all the plies are assembled in Plywood, ready for hot-pressing phase. The hot press requires from 6 to 50 days at 140°C and under a pressure of 1MPa, until the resin curing is achieved (22).

The Plywood normally available on the market are 2400 x 1200mm or 2700 x 1200mm and the thickness varies from 1.5mm to 32mm. The density of the Plywood is approximately equivalent to the density of the timber species used: the pine Plywood density range is 500 – 650kg/m^3, eucalypt hardwood Plywood can exceed the 900kg/m^3 (25).

There are numerous applications: interior design of sport and cultural buildings like theatres, furniture for classrooms, home, office and, more in general, residential or commercial applications.

To summarize, Table 1 reports the mechanical and physical properties ranges of the wood based materials presented in this brief review.

1.1.6 Particleboard

The particleboard panel (PB) is the type of panel studied in this PhD Thesis, therefore more details are given about how this chipboard is produced. The manufacturing process below presented was followed to obtain the panels tested in this work, and more in general, to produce PB for the market obtained from recycled wood.

The process is composed of the following steps:

a) Recycled wood washing
b) First grinding
c) Refining
d) Second grinding
e) Drying
f) Sieving
g) Adhesive spreading
h) Forming
i) Pressing
j) Final Smoothing

These steps are followed to produce raw particleboard. Figure 5 show the related flow diagram. For the production of embossed PB production, five more steps are applied to the raw panels, as shown in the flow diagram reported in Figure 6:

a) Positioning of a resin impregnated paper
b) Hot pressing
c) Edge trimming
d) Quality control and classification
e) Packaging

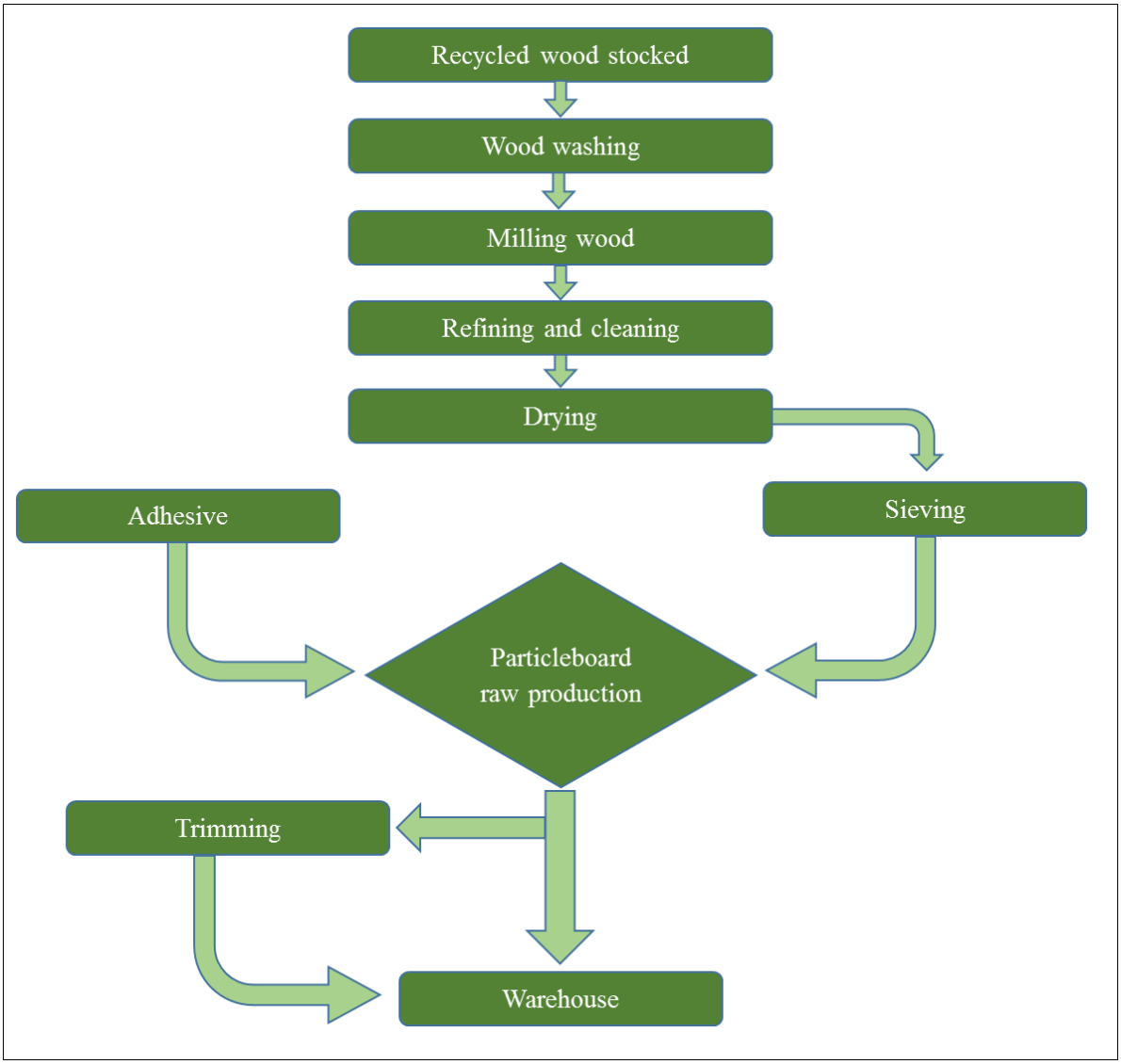

Figure 5: Raw particleboard production workflow

The raw particleboard manufacturing process is now described more in detail. In the first step (a) - recycled wood's washing - the wood, which is the 80% of the total mass of raw particleboard and is collected from different collection points, is disposed on a large square of the plant using wheel loaders and hydraulic forks. These heaps are positioned following logistics, technologic and safety criteria to allow the usage of these woodpiles before they start decaying. These criteria tend to prevent fire risk mainly due to auto-combustion. From the heaps, the wood is taken and washed in a pool of water. Here, by sedimentation, inert and unsuitable materials are separated from the wood. These materials are the "washing scraps" not suitable for PB production, which are disposed of, e.g. by incineration, to produce energy for the plant.

The wood, once properly cleaned, is ready to enter the production cycle of the panels as a raw material. Using wheel loaders, the wood is transported to the second phase of the manufacturing process: grinding.

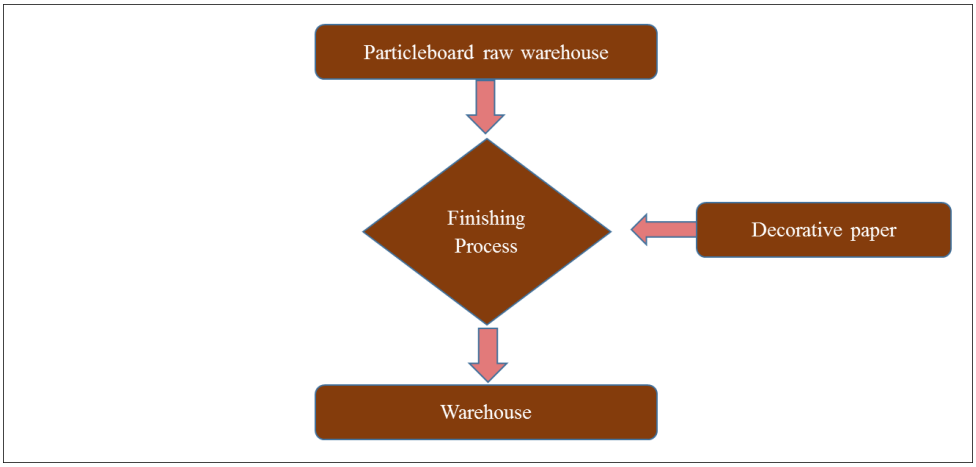

Figure 6: Finishing Process Workflow

Grinding (b and d) is performed using two different shredding systems: first with a knife rotor and then with an eccentric rotor. The choice of the screen basket defines the size of the final product. The automatic metal separation is continuously adjustable and it is done by a metal detector and discharge chute. The metal detector is installed over the conveyor belt and controls a discharge flap, which is installed at the end of the belt.

This step (b) is characterized by two intertwining shredding shafts, that can be operated at the maximum speed of 46 rpm. The material placed into the hopper is drawn in by the shafts, in this manner, the wood-based material is torn and broken down to be routed directly on the horizontal belt. The larger dimension at the first stage of the grinder is 80mm. The material coarsely ground is stocked in a shed from which it is withdraw using tape conveyor. At this point, the wood goes through in another cleaning station (c) to remove any foreign object like stones, sand, paper residues, screws, nails and any other material not suitable for PB production. The cleaning stations use a vibrating screen and pulsated high-speed air, to dry wash the coarse wood pieces. The wood is then sent to the hammer mill powered with a 630 kW engine (d), where hammers mounted on rotating shafts reduce the wood to small splinters similar to ellipsoids. The average size of minor and major axes of these equivalent ellipsoids are equal respectively to 4mm and 55mm.

The fine wood is stocked in suitable silos. It has a moisture content equal to 25% - 50% not suitable for the consequent production steps. It is then necessary to reduce this humidity content to 2.5% - 5%, by drying (e) using a horizontal drum drier with a diameter equal to 7m, heated by exhaust gas from heating generation while rotating. The hot gases are produced in a burning chamber powered by methane gas (120 m^3/h) and wood powder. The wood powder, not used in particleboard production, is obtained from the sieving phase and the final smoothing phase. The dried material is then stocked in a silo, ready for the next production phase, i.e. sieving. Drum dryer processes a wood flow equal to 78 ton/h.

The particles of wood are then divided (f) into different fractions: from coarse to fine, using five screeners with an oscillating sieve with different calibrated openings. The first fraction is represented by the material that remains on the first grid with openings of 5 x 5mm: this material is conveyed to the refining mill. The second fraction is the medium material that has crossed the first grid but remained on the second with openings of 1.5 x 1.5mm. This material fraction is treated in the pneumatic cleaner to separate the wood particles from foreign materials, and then is conveyed to a first silo, ready for the final uses. The third fraction is the wood that has crossed the grid with opening equal to 1.5 x 1.5mm but remained on the grid with openings equal to 0.25 x 0.25mm; this material is cleaned and stocked in a second silo. The last fraction is the material that passed through the last grid; it is considered as wood powder. This powder is eliminated from the panel production because its contains a high percentage of sand that, if present during the bonding phase, would require a too high quantity of adhesive. This powder is used as a combustible to produce thermal energy for the plant. At this time, the material in the two silos is ready to be bonded with resin (g).

The fine and coarse materials are picked from the silos and put in two bunkers where weighing station records the quantities of the wood fraction to assign the right percentage of adhesive and then, the chips-wood are introduced in the resin stations (g). It is important to remember that the adhesive is a mixture of different components: the binder (thermoset resin), water, hardener and paraffin. All the single products are liquid, and then the dosage is set by varying the speed of electric pumps. All the quantities components are possible to be varied in agreement with the quality requirements through the on-line production quality control panel.

The wood particles with proper adhesive quantities are sent to the forming machines (h), two for the coarse material and two for the fine material. The deposition process is shown in Figure 7.

The first forming stage deposes the first fine layer; the second and third deposes the core layer of coarse wood-based material and the last one covers the coarse layer with another fine ply. From the point of view of the nomenclature used in this thesis, the outer fine layers are defined as skins where the typical particles dimensions are in the range from 0.1mm to 6mm and the central one as core, where the typical dimensions are in between 0.3mm and 50mm.

The last step is the hot-pressing. The formed panel (“mattress”) is put in the press where high pressure combined with high temperature produce the final hardened panel (i). The material enters continuously in the press, pressed between two metal conveyor belts pressed by rollers in order to reach the desired panel thickness and mechanical properties.

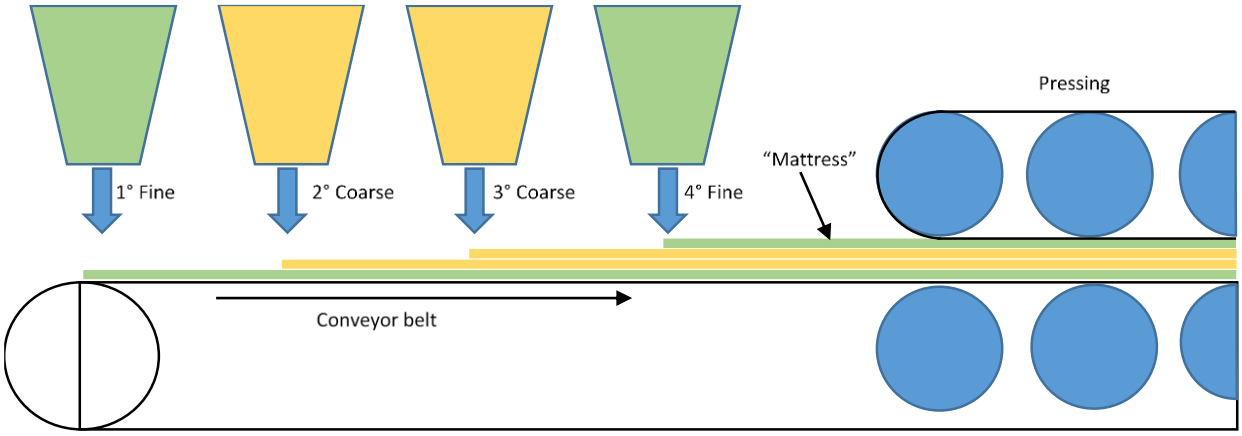

Figure 7: Wood-Mattress formations

The press is 50m long and produces PB with 2120 mm and variable length from 2000 mm to 5600 mm. The board, after cooling in environment air, is calibrated removing from the outer skins 6 – 8 tenths of millimeters, this last phase (j) is performed by abrasive tapes to final polish. Figure 8 show the final particleboard produced following this manufacturing process.

The panels are finally stocked in a warehouse, ready for the ennobling process, trimming or directly sale.

Figure 8: Particleboard of different thicknesses.

The manufacturing process of the ennobled panels starts from raw particleboard stocked in a warehouse to give to the surface of particleboard a decorative aspect. The common geometry for the panels ready for ennobling are:

- Thickness: 3 – 40 mm
- Width: 1860mm – 2120mm
- Length: 3860mm – 5600mm

The paper used to produce these semi-finished panels can be of two types: decorative papers or wallpapers.

The first type of paper (decorative paper) can be single-color, timber look or fantasy. They have density equal to 60-140 g/m^2 before the impregnation; final density is equal to 180 – 270 g/m^2.

The wallpapers are used to improve the surface quality of the PB before applying the decorative paper.

The resins normally used to ennoble panels are melamine, urea-based or acrylic. The process consists of the deposition of the one or two wallpaper sheets on the board surface (in agreement with requirements) and the decorative paper on the top. After this, the paper sheets are stretched using an electric field to prevent any types of folds. Then the board enters a the pressing station where pressure (26 – 32 kg/cm^2) is applied at 158 – 200°C. It is also possible to give the surface bas-relief effect to reproduce the wood texture. To do this, the press is equipped with plates with the drawing of the timber structure in relief, that will be put in contact with the paper surface. Figure 9 show an ennobled particleboard panel.

Figure 9: Ennobled particleboard panel (26)

1.2 Mechanical and physical characterization of the particleboard panels, brief literature review.

Before studying the macro and micro modelling techniques involved in the characterization of the heterogeneous materials, it is important to analyze the scientific literature focused on particleboard taking into account the works about the mechanical characterization of this material that is the topic of this thesis. Particleboard is environment oriented because it is suitable to be made using green waste or by products of the wood industries especially meeting the possibilities offer in the specific geographic area. Monteiro et al (27) studied the possibility of using sugarcane bagasse to produce particleboard, considering that it is the most important waste product of the Brazilian agricultural industry. Here, the authors developed, characterized and compared chipboard panels made with a

mixture of sugarcane bagasse and particles of wood like pine or eucalyptus and bonded with urea formaldehyde (UF) and melamine formaldehyde (MF) adhesives. In (27) the mechanical tests were performed on 9 types of panel produced with different sugarcane bagasse from two supplier of Brazil, with different percentage of mixed wood and types of adhesive. Montero et al defined the two raw material as Industrial Sugarcane Bagasse (ISB) and Still Sugarcane Bagasse (SSB), see Table 3 for the characteristics of 9 types of board tested.

Table 3: Type of panel tested in (27)

Experimental chart.

Panel			Particules		Resin	Waterproffing
Treatment	Density	Quantity	Type		Type	Type
			Bagasse (%)	Wood (%)		
T1	0.7	3	ISB (100)	–	UF	–
T2	0.7	3	ISB (100)	–	MF	–
T3	0.7	3	ISB (100)	–	UF	Paraffin
T4	0.7	3	ISB (100)	–	MF	Paraffin
T5	0.7	3	ISB (50)	Pinnus (50)	UF	–
T6	0.7	3	ISB (50)	Eucalyp. (50)	UF	–
T7	0.7	3	SSB (100)	–	UF	–
T8	0.7	3	SSB (100)	–	MF	–

All the panels of 48cm x 48cm x 1,5cm were produced with 9% of mass of adhesives and hot pressing process under a temperature of 160°C and 4 MPa of pressure for 8 min. The tests performed in this article were Internal Bond test (ASTM D1037), swelling thickness test, Elastic and Rupture modules determination in the static bending test (see Figure 10). Respectively, the mechanical quantities are obtained using the formulae reported in Table 4

Table 4: MOE, MOR and IB calculations (ASTM D1037)

$MOE\ [MPa] = \frac{L^3 \Delta P}{4bd^3 \Delta y}$ $MOR\ [MPa] = \frac{3P_{max}L}{2bd^2}$	L = Length of span [mm] or [in] $\Delta P / \Delta y$ = slope of the straight-line portion of the load-deflection curve (Figure 10a) [N/mm] or [lbf/in]. b = width of the specimen [mm] or [in] d = thickness of the specimen [mm] or [in] P_{max}= maximum load [N] or [mm]
$IB\ [MPa] = \frac{P_{max}}{ab}$	P_{max}= maximum load [N] or [mm] a = width of the specimen [mm] or [in] (Figure 10b) b = length of the specimen [mm] or [in] (Figure 10b)

The main results presented in (27), have shown that the strengths values in the internal bond tests for the panels produced with ISB mixed to other particles are higher than the strength in the board produced with SSB; moreover, the mixture of ISB with pine particles show higher strength when compared to ISB with eucalyptus. The modules of elasticity of the panels produced with ISB are higher than those of the board produced with ISB mixed with other particles. Lastly, the values of swelling in thickness for the panels produced with SSB are superior to the ones produced with ISB (27).

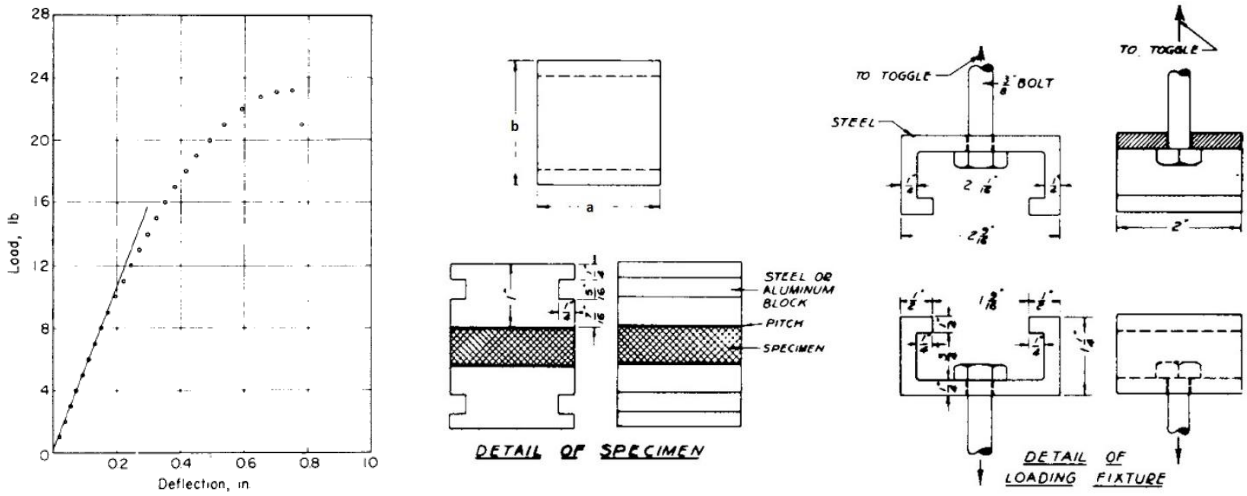

a b

Figure 10: Mechanical properties evaluation of particleboard (ASTM D1037): a) Typical Stress-Strain curve in bending condition. b) Internal bond test set-up.

Nemli et al (28) studied the suitability of kiwi prunings that is a new cultivation in the East Black Sea Region of Turkey, for particleboard production. To prove if this raw material is suitable or not to produce particleboard, the authors in (28) performed physical and mechanical tests to characterize the product. Twelve types of particleboard were produced observing different percentages of kiwi prunings and industrial wood and UF adhesive, obtaining dimensions equal to 56.5 x 56.5 x 2 cm by hot pressing at 150°C and 25kg/cm^2 pressure for 6 min. The morphological aspect of the board was similar to a sandwich panels with three layers superposed onto each other. Table 5 lists the particleboard types and composition.

Table 5: Experimental design and composition of the core of three layers particleboards (28).

Board Type	**Adhesive usage core-outer layers [%]**	**Raw material usage Kiwi:Industrial wood [%]**
1*	8 – 10	0 : 100
2*	8 – 10	12.5 : 87.5
3*	9 – 11	12.5 : 87.5
4*	8 – 10	25 : 75
5*	9 – 11	25 : 75
6*	8 – 10	50 : 50
7*	9 – 11	50 : 50
8[a]	9 – 11	50 : 50
9*	8 – 10	75 : 25
10[b]	8 – 10	100 : 0
11[c]	8 – 10	100 : 0
12[b]	9 – 11	100 : 0
**, Surface layers were consisted of 100% industrial wood particles.*		
[a], The shelling ratio was 45 : 55%.		
[b], About 100% kiwi particles were used in the core and surface layers.		
[c], The density of the board made from 100% fiwi particles was 0.55g/cm^3.		

The tests were performed in accordance with EN 310; EN 319 and EN 317 for determination of the modulus of elasticity, the modulus of rupture, the internal bond, the thickness swelling and water absorption. The modulus of rupture ranged from 7.33 to 13.27 MPa, being the requirement for general purpose applications 11.5 MPa (Standard EN312-2). Particleboard made of 100% of kiwi particles had the modulus of rupture lower than the requirement and the same result is noted increasing the adhesive usage till 11%. The range of data for the internal bond was from 0.483 to 0.648 MPa, the requirement was in the range from 0.24 to 0.50 MPa depending on the field of application. Table 6 shows the mechanical properties determined in (28).

In general is possible to see that increasing the kiwi pruning particles usage, the properties of the board are negatively affected. With a content up to 50% of kiwi pruning particles, the modulus of rupture exceeds the minimum requirement. All the particleboard samples produced from kiwi prunings had internal bond higher than the requirement (required value ranges from 0.24 to 0.50 MPa), however the water absorption and thickness swelling values were very poor (28).

Table 6: Mechanical properties of Particleboard made of kiwi prunings (28).

Board type	MOE [MPa]		MOR [MPa]		IB [MPa]	
	Mean	St. dev	Mean	St. dev	Mean	St. dev
1	13.27	0.27	2661.24	19.36	0.648	0.013
2	11.84	0.12	2354.21	25.36	0.619	0.011
3	12.34	0.18	2558.92	20.08	0.631	0.007
4	11.09	0.14	2012.45	23.14	0.570	0.006
5	11.76	0.15	2324.48	12.12	0.604	0.021
6	10.47	0.36	1892.47	21.48	0.555	0.010
7	11.22	0.22	2092.67	10.36	0.582	0.009
8	11.58	0.36	2113.03	14.28	0.585	0.016
9	10.03	0.19	1784.36	17.41	0.541	0.016
10	8.42	0.16	1587.28	16.45	0.527	0.008
11	9.51	0.21	1646.14	12.13	0.536	0.005
12	7.33	0.11	1335.14	34.62	0.483	0.022

In a similar way in (29) the suitability of date palm wood was studied for the production of particleboard varying the hot pressing temperature, the UF content and the pressing time (see Table 7 were IB stands for the internal bond, BS for bending strength and ST for swelling in thickness).

Table 7: Experimental design and results (29)

Types	Press temperature °C	Press time min.	Adhesive use ratio %		Types	IB N/mm^2	BS N/mm^2	ST %	
			middle layer	outer layers				2-hour soak	24-hour soak
1	150	5	7	9	1	0.43	15.90	11.97	14.40
2	150	6	7	9	2	0.47	16.29	10.25	13.66
3	150	7	7	9	3	0.53	16.40	9.39	12.53
4	135	5	7	9	4	0.35	14.16	14.50	18.67
5	135	6	7	9	5	0.39	15.30	14.29	16.63
6	135	7	7	9	6	0.41	15.85	13.13	15.22
7	150	5	9	11	7	0.67	18.14	5.92	8.75
8	150	6	9	11	8	0.78	18.41	4.02	8.24
9	150	7	9	11	9	0.83	18.94	3.30	7.09
10	135	5	9	11	10	0.56	16.45	8.96	12.26
11	135	6	9	11	11	0.61	16.85	8.14	11.38
12	135	7	9	11	12	0.64	17.23	7.52	10.71

Referring to the same requirements set in (28) for the internal bond, all boards made of date palm had higher internal bond than standard values (29). The minimum bending strength required by the standard is in the range from 11.5N/mm^2 to 18N/mm^2. Observing Table 7, board 7, 8 and 9, had bending strength higher than the upper limits, while the other boards are in the range prescribed by

the standard. Lastly, for the swelling in thickness, the requirements is equal to 15% after 24h of immersion in the water. Board 2, 3, 7, 8, 9, 10, 11, and 12 had lower ST than the standard values (29).

Buyuksari et al (30), investigated the physical and mechanical properties of particleboard manufactured from waste pinecones. This work is interesting because the authors evaluated the properties of the product considering 100% of virgin wood (50:50 blend of pine and beech) and 0% of pinecones to 50% of virgin wood and 50% of pinecones. This article can be considered as one of the many possible references about the mechanical properties of the particleboard. The panels reported in Table 8 are obtained by hot pressing process at 2.6N/mm^2 and 150°C for 7min. The final board dimension are 500 x 500 x 10 with urea-formaldehyde mass content equal to 10%.

Table 8: Experimental design followed in (30).

Board type	Raw material	
	Pine cone (%)	Wood (%)
A	0	100
B	10	90
C	20	80
D	30	70
E	40	60
F	50	50

Focusing on the mechanical properties of the boards, in (30) the authors tested the panels following the EN312 (31) standard where are reported the mechanical requirements of particleboard for different applications and how to determine the modulus of elasticity (MOE), modulus of rupture (MOR) and the internal bond (IB). The MOE and MOR were determined for every board reported in Table 8 in bending condition following the EN310 standard (32). In this thesis, the same standard was adopted to conduct the bending tests to determine the mechanical properties of the material, then I postponed the setup description in the next chapters. The IB was determined following the EN319 (33). All the mechanical results reported in (30) were obtained as mean values over 10 tests for every board (Table 9). The highest MOR and MOE values were observed for particleboard made of pure wood particles without any percentage of pinecone wood. The lowest MOR and MOE values were determined for the panels with 50% of pinecone particles. Comparing the requirements prescribed in the EN312 standard to the values found in (30), it is possible to see that the panels A; B; C and D satisfied the minimum MOR for general-purpose use like furniture manufacturing. The MOE values of the panel A and B met the minimum required. The same observation can be made for the IB characteristic. Panel A shows the highest value of IB, lowest IB is observed for panel F.

The results indicated that increasing the pinecone percentage in the mixture determines a significantly decrease of the mechanical properties of the particleboard (refers to Table 9) (30).

Table 9: Mechanical Properties of Particleboards made of pinecone and pure wood particles (30).

Properties	Board Type	Mean[a]	St.Dev
MOR [MPa]	A	16.07[p]	0.78
	B	14.66[s]	0.81
	C	13.58[u]	0.62
	D	12.57[v]	0.46
	E	11.21[y]	0.85
	F	9.34[z]	0.65
MOE [MPa]	A	2068.6[p]	83.32
	B	1879.3[s]	62.83
	C	1644.2[u]	53.43
	D	1474.4[v]	66.92
	E	1337.9[v]	91.72
	F	1064.6[z]	83.35
IB [MPa]	A	0.568[p]	0.015
	B	0.528[ps]	0.029
	C	0.455[u]	0.023
	D	0.392[v]	0.020
	E	0.320[y]	0.023
	F	0.292[z]	0.020

[a]Mean values are the average of 10 specimens.

[p, s, u, v, y, z] Values having the same letter are not significantly different (Duncan Test) (30)

In conclusion, the modulus of elasticity E of the panel with 0% of pinecone particles and 100% of virgin wood is equal 2068.6 N/mm^2. Considering that the material studied in this thesis is produced by recycled wood, this modulus is not directly comparable, but can be considered as reference only for the order of magnitude.

1.3 Macro-mechanical modeling techniques to study heterogeneous materials

In this PhD thesis, I focused on the research of the appropriate macro-mechanical modelling techniques for the mechanical performance of PB panels, mainly in flexural conditions and limited to the elastic behaviour. The knowledge of the relationship between microstructure and particleboard's mechanical performances is very useful in the perspective of modifying the composition and the microstructure in order to obtain a lighter material, while preserving the mechanical properties. Bending stiffness is one of the most important properties for the furniture market, e.g. in the case of bookcase shelves or drawer's bottoms.

To select the most appropriate macro-modeling techniques for this material and its input and output features, it is fundamental fix the class membership of the particleboard in agreement with all types of material.

Observing the PB's manufacturing process presented in Section 1.1.6 and the raw material involved to produce it, the final product is composed of heterogeneous chips made of different types of recycled wood, with casual orientation and immersed in Urea-Formaldehyde (UF) adhesive. Analyzing the components and the microstructure, it is possible to consider particleboard like a composite material and particleboard panels like composite structures, i.e. sandwich panels. This assumption is reasonable because the material is made of two solid constituents that mixed, produces a final composite material with improved characteristics (34); they are:

- *Polymeric matrix* → UF Adhesive
- *Reinforcement* → Fibres → Not homogeneous chips-wood

Particleboard panels usually have a characteristic vertical density profile, which is the result of the forming process presented in Section 1.1.6. In Figure 11a it is possible to see that the outer skins are denser than the central core.

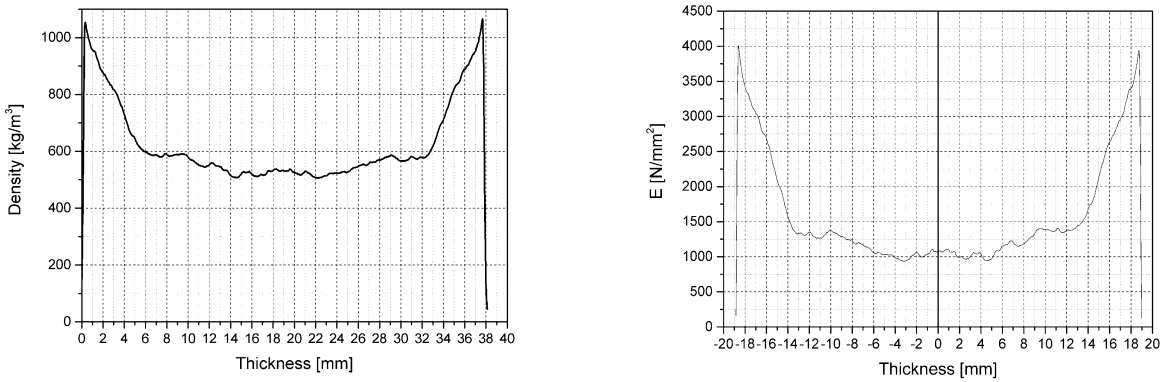

a b

Figure 11: a) Vertical density profile of PB of 38mm of thickness; b) Elastic modulus profile

Considering that the PB's stiffness is strongly related to its density as reported in (35) and (36) (Figure 11b), the outer skins are therefore stiffer than the core. This morphological aspect is similar to the structure of a sandwich panel where the skin usually have a stiffness which is larger than that of the core (34).

This further hypothesis is supported by the disposition of the wood particles through the thickness (see forming step in Section 1.1.6). To understand and visualize the particles' disposition in the particleboard after the production process, I used the Micro-CT technique, as it will be reported in the next Chapter 2.

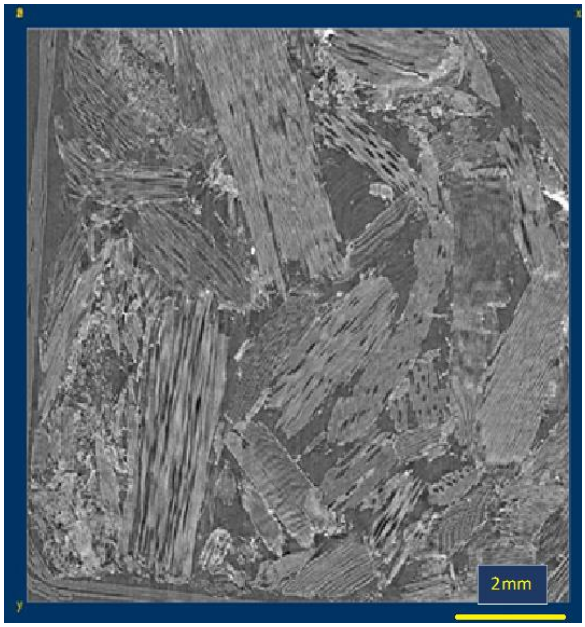

Figure 12: Particleboard projection

Using Micro-CT, it is possible to see the inner structure of a reconstructed volume of a sample prepared for the experimental test. Figure 12 shows one slice parallel to the XY plane of normal Z which is the thickness direction of the particleboard specimen (Figure 13).

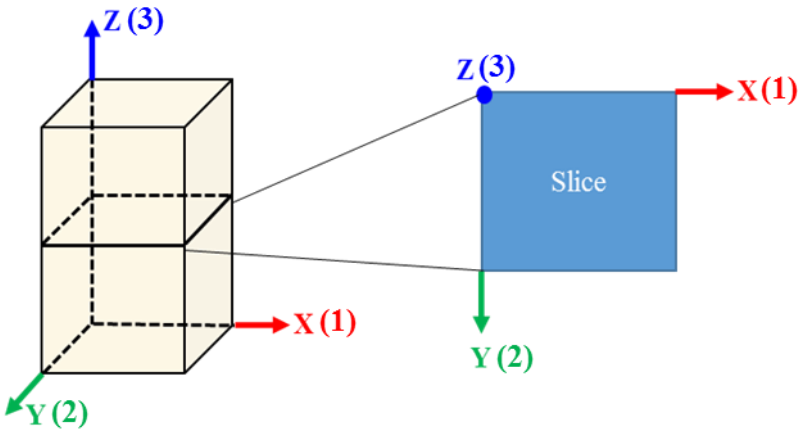

Figure 13: Extraction of the slice XY

In Figure 12, most of the wood particles appears as having a planar distribution. This observation makes it possible to treat the layers of a particleboard panels as laminae made of a discontinuous fibre reinforced material, which is not isotropic both on the plane and in the thickness direction. All these considerations, combined with the layered structure, are likely to make out of plane elastic constants differ from in-plane ones, calling for appropriate macro-mechanical models and related experimental techniques. These experimental techniques are normally adopted in studying composite material and in particular sandwich laminate.

In the perspective of modifying the panels' composition and/or microstructure to achieve lightweight solutions, the understanding of the relationships between the microstructure and the elastic constants of this equivalent composite material is of great importance. The mechanical behavior of the core is of particular interest, since it is the region of the panel which is more likely to be modified to obtain lighter panels, being it required that the properties of the skins remain unaltered to preserve the quality of the surface finishing and the resistance to various forms of surface loading. To study the properties of the core by relatively simple tests and infer the principal elastic constants, three point bending test is often chosen and different versions of this test are discussed hereafter.

1.3.1 Three point bending tests for the evaluation of the flexural modulus E_1 and the out of plane shear modulus G_{12} in adhesive joint crack length determination

In (37) three-point bending tests are performed on adhesively joint laminate composites, where the authors compare various analytical methods to evaluate the strain energy release rate (SERR) and to determine the crack length from the opening face. It was founding that the Krenk theory (38) applied to determine the SERR, which relates the opening face to crack length in the adhesive substrate, was not in agreement with the results obtained from finite element analysis (FEA). The orthotropic behaviour of the material and the role of shear on the deformation were considered as the main causes. To determine the entity of the shear deformation effect, three-point bending test with varying span were performed on specimens having the same stacking sequence as the adherends of the double cantilever beam (DCB) specimens used for SERR evaluation. The elastic constants (E_1 and G_{12}) were evaluated by linear interpolation of load vs strain data to simulate numerically the bending of the CFRP adherends. Deflections at different spans were evaluated analytically separating the shear contribution from the bending contribution. The slopes from FEA results defined by load over the displacement were compared to experimental ones. As expected, it was observed that for shorter span lengths, the shear effect was not negligible.

The authors then modified the Krenk's formulations taking into account the shear effect, to reduce the deviation between composite DCB from double cantilever beam theory.

1.3.2 Three point bending application: in plane shear properties determination of anti-symmetric laminates

Another experimental technique based on three-point bending test was applied to ±45° antisymmetric laminates made of carbon/epoxy material (AS4/8552) to determine their in-plane shear modulus and their in-plane shear strength (39). In this article, the authors present this experimental technique applied to anti-symmetric angle ply laminates in order to decreasing the bending/twisting coupling effect that causes the lift-off of the specimen from the supports. The anti-symmetric sample was modelled by Classical Laminated Plate Theory (40). In that theory, the relation between in-plane forces, moments, reference plane strains and curvature, can be expressed as a function of the extensional stiffness, coupling stiffness and flexural stiffness for a generic laminate and including hygrothermal effect (39). Considering first the configuration of the sample (stacking sequence equal to $[\pm 45]_{n\text{-}as}$) and second, the loading mode (bending), the resultant of internal force are null, then the internal moment can be evaluated separately. In particular, to calculate the shear properties, it is of interest the bending moment component due to the load applied during the test. This quantity, named M_x in the article (39), is used to determine the strain and bending curvature γ_x of the anti-symmetric laminate. From (41) the curvature referred to load axes is expressed using Eq.1:

$$\gamma_x = \frac{48b}{mL^3} M_x \qquad \text{eq.1}$$

where b is the specimen width, m is the slope (load/displacement) and L is specimen length. Equating Eq.1 with the curvature expressed using Classical Laminated Theory (Eq.2) the authors express the G_{12} modulus (Eq.3).

$$\gamma_x = \frac{3}{n^3 t^3}\left(\frac{1}{G_{12}} + \frac{4(1-\upsilon_{12}^2\mu)k_2}{E_1}\right) \qquad \text{eq.2}$$

where n is number of layers, t is the layer thickness, G_{12} is shear modulus referred into principal material axes, υ_{12} is the Poisson coefficient, μ is the modulus ratio ($\mu = E_2/E_1$), E_1, E_2 are respectively

longitudinal and transversal modulus and k_2, k_1 are two constants values proportional to the number of layers n and related engineering constants (39).

$$G_{12} = \frac{1}{4}\left(\frac{4bn^3t^3}{mL^3} - \frac{(1-v_{12}^2\mu)k_2}{E_1}\right)^{-1} \quad \text{eq.3}$$

The shear stress components referred to the principal material axes, can be derived from Classical Laminate Plate Theory, as a function of the number of laminae n, the thickness of each lamina t and moment M_x. See Eq. 4 (39).

$$\tau_{12k}^{M\pm45,Max} = \mp\frac{3M_x}{n^3t^2} \quad \text{eq.4}$$

For this laminate configuration under bending test, the failure is supposed to be due to in-plane shear stresses. When the number of layer increases, a more shear dominated stress state promotes a shear dominated inter-fibre failure in the external plies. It is possible to say that in-plane shear strength is equal to the maximum in-plane shear stress at the failure. Knowing the bending moment per unit of length at the failure load F_{max}, the Eq. 4 become Eq. 5:

$$\tau_{failure} = \frac{3F_{max}L}{4ntb} \quad \text{eq.5}$$

In this work, the authors exploited the three-point bending test on the composite laminate to derive its shear properties.

1.3.3 Three point bending test with varying span: out-of-plane elastic properties of honeycomb sandwich panels.

In (42) the authors studied a honeycomb sandwich panel to derive Young's modulus in the thickness direction and shear modulus of the core. In a very similar way as a performed in (37), the authors expressed total deflection measured in the middle point of the specimen as the sum of pure bending contribution and pure shear contribution. The main difference in this work (42), compared to (37), was that they took into account the deformation of the testing machine to compensate it for the total deflection of the honeycomb sample (Eq.6)

$$\delta = \frac{PL^3}{48EI} + \frac{PL}{4GA} + \frac{P}{k} \quad \text{eq.6}$$

where P is the load, L is the distance between two supports, E is the longitudinal modulus, I is the moment of inertia, A is the core area and the term P/k takes into account the stiffness of the testing machine.

In (37) the deformation of the testing machine was not considered because the displacement was measured using a deflectometer device set in the middle of the specimen. Mujika et al. (42), expressed the flexural modulus in a general form as a reported in Eq.7:

$$E_{3p} = A + Bx^2 + Cx^3 \quad \text{eq.7}$$

where the E_{3p} is the flexural modulus normally derived from three-point bending test, A, B and C are the unknown constants and $x = d/L_0$, (d = sandwich thickness; L_0 = is the initial span).

After obtaining for each span the E_{3p} value, using the least square method, the constants A, B and C are evaluated. They correspond to $1/E_{eq}$, $1/G_{eq}$ and $4w/k$, respectively, where w is the sandwich width and k is the stiffness test machine parameter.

In a very similar way, the same experimental method proposed in (42), was applied to five carbon fibre epoxy matrix specimens for mechanical characterization (43).

1.4 Micro-mechanical modeling techniques applied to heterogeneous natural materials

In this PhD work, after investigating on the mechanical properties of particleboard using macro-mechanical models to estimate the elastic constants, the material was studied at the micro level, using suitable modelling techniques to derive relationships between the particles, voids and adhesive and the macroscopic mechanical properties. The mechanical constants estimated using micro-modelling techniques were compared with the same elastic quantities derived with macro-approach to verify the agreement.

The detailed account of how particleboard was modelled using this micro-scale approach is reported in Chapter 4. Here, micro-modelling and homogenization techniques for the determination of the elastic constants of composite material like fibre reinforced polymer, bones, short fibre composites, porous material, textile and concrete composites are briefly reviewed. It is important to underline that the literature about micro-modelling of particleboard is very poor, so one of the goals

of this thesis is to increase the level of knowledge about this topic, in the perspective of developing predictive tools, allowing to design lightweight panels with modified composition and/or particle arrangement.

Micro-modelling approaches for heterogeneous composite materials can be divided into two classes: analytical and numerical methods. In order to estimate the elastic constants, the software Digimat was used, which implements both analytical and numerical methods, defined as, respectively:

- Mean-Field methods
- Finite Element discretization methods.

In the next paragraphs, I'm presenting some works on composite materials found in the literature that uses these major techniques.

1.4.1 On Mean-field methods. Predicting the damage and modelling grain size effect of heterogeneous composites materials.

A very comprehensive collection of Multiscale Homogenization Methods for composite materials was reviewed in (44) where it is possible to understand that at the current state-of-the-art, the Mean Field Homogenization Methods is one among the best methods that can predict accurately the macroscopic behaviour of heterogeneous materials as composites. In (45) the authors developed a multiscale model for 2-phase composites where the matrix has isotropic elastoplastic behaviour, modelled using Lemaitre-Chaboche ductile damage model (46). The fibres were considered as ellipsoidal, homogeneous and transversely isotropic elastic material inclusions. The material studied in this article (45) is a unidirectional carbon fibre reinforced epoxy.

In a multiscale approach, at each macro-point X, the macro-strain is supposed to be known and the stress is evaluated solving a micro-scale boundary value problem (or vice-versa). It is important to remember that the macro-point X is assumed in the centre of a Representative Volume Element (RVE) (see Figure 14). Considering suitable boundary conditions on the RVE, macro-strains and macro-stresses are equals to average strains and stresses over the RVE (45).

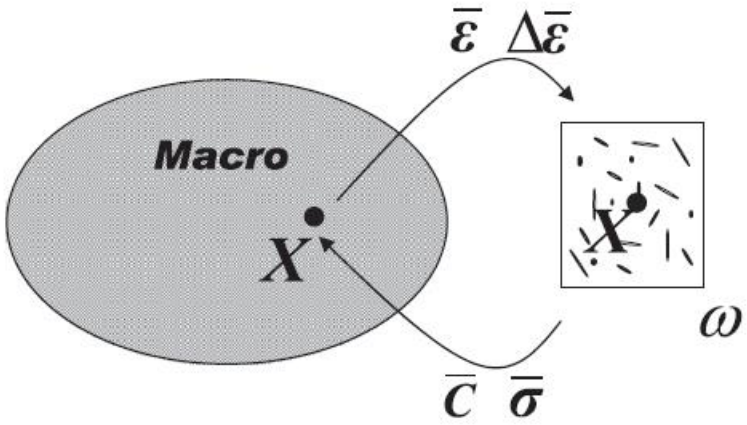

Figure 14: Multiscale Homogenization Method (45)

Considering all the passages reported in (45), the main equations of the Mean Field Homogenization (MFH) method for the two-phase elastoplastic composite material are derived considering the material laws and a non-local damage model in the matrix. The MFH method is based on the introduction of a so called linear comparison composite, which allows for the linear schemes being applied to nonlinear behaviors. This procedure is used to determine the macro-stress, with the knowledge of the macroscopic deformation tensor, internal variables and their gradients, which are applied to the RVE. The authors determine the micro-macro transition level of the material taking into account the implicit formulation of the gradient-enhanced damage model and solving the Helmholtz equations (45) (47). A finite-element implementation is derived to simulate the damage process occurring in unidirectional carbon-fiber reinforced epoxy composites with the periodic unit cell (Figure 15a) and random unit cell (Figure 15b) submitted to different loading conditions.

a b

Figure 15: Composite unit cells. a) Periodic; b) Random (45)

The damage of the matrix was formulated using an implicit approach considering it as accumulated plastic strain obtained by solving the Helmholtz equations. To take into account the damage at the macro-level homogenization, the authors, in (45), write the finite element model considering four degrees of freedom at each node: three are the classical displacement components and the fourth represents the equivalent plastic strain. The results obtained in (45) from this Mean Fields Homogenization Method are used to model the damage in carbon-fiber reinforced epoxy at different loading conditions. The results are compared with the response obtained from numerical

simulation of periodical cells and RVE. For low fibre volume fraction (<30%) the results are in very good agreement, for the volume fraction of the fibre up to 50%, the method is less accurate, being the error up to 20%.

Mean field method is also used to study grain size effects on the mechanical properties of heterogeneous materials. These size effects are known to mainly influence experimental results. However, the literature is not very abundant on modelling materials taking into account the inclusions size effect. In (48) Pipard J. M. et al gave their contribution on this topic, exploring the possibility of modelling material's plasticity at micromechanical level taking into account the grain size effect of the metallic materials.

1.4.2 On Mean-field methods. Mori-Tanaka model to micromechanical modelling of heterogeneous materials (composites materials).

Considering the microscale mechanical modeling of particleboard, the mean field methods like Mori-Tanaka will be studied in Chapter 4 to try to homogenize this heterogeneous material, treating it like a composite with fibre (particles) and matrix (UF-Adhesive). For this, the next brief literature review focuses on modelling short fibres composites or particulate composites, based on Mori-Tanaka methods, which deliver explicit formulae for stiffness tensor and local stress and strain at the micro level (49). This method is used to predict the elastic properties of composite materials, to study thermal stresses in metal composites and to model damage development in polymer matrix composites. Mori-Tanaka method requires that the inclusion shape is ellipsoidal to maintain constant stress and strain in each inclusion (49).

Considering an infinite composite material under uniform stress σ_0 can be determined by Eq.8 (50):

$$\sigma_0 = L^e \varepsilon^0 \qquad \text{eq.8}$$

where σ_0, L^e and ε^0 are respectively: stress tensor, stiffness matrix (equivalent to a stiffness matrix of composite material) and strain tensor. For a composite that contains inclusions, the total stress is given by Eshelby's inhomogeneous inclusion problem in (50) and (51) that takes into account the stiffness matrix of the inclusions or pores (L^p), the stress disturbance in the matrix due to the pores ($\tilde{\sigma}$) and the

strain disturbance due to pores ($\tilde{\varepsilon}$) produced by $\tilde{\sigma}$. Finally σ' and ε' are respectively the stress and the strain disturbance produced by the presence of the pores and Eshelby's factor ε^* accounts for the stress-free of the pores. Eq. 9 considers all the factors listed before, (51) expressing the total field of stress:

$$\sigma^0 + \tilde{\sigma} + \sigma' = L^p(\varepsilon^0 + \tilde{\varepsilon} + \varepsilon') = L^m(\varepsilon^0 + \tilde{\varepsilon} + \varepsilon' - \varepsilon^*) \quad \text{eq.9}$$

Following Eshelby, the strain disturbance ε' is related to the ε^* factor and the tensor of the pores *S*, which depends on the pores' shape and matrix stiffness L^m (Eq.10) (50):

$$\varepsilon' = S\varepsilon^* \quad \text{eq. 10}$$

As usual, the equilibrium of the entire body must be respected, so the stress disturbance over the entire body must vanishes, leading to this relation (Eq.11) (39):

$$\tilde{\varepsilon} = -C(\varepsilon' - \varepsilon^*) \quad \text{eq. 11}$$

where *C* is volume fraction of the pore. Considering $L^p = 0$ due to the pores, the solution of ε^* is given by Eq. 12 (50):

$$\varepsilon^* = (\{L^m - L^m[CI + (1-C)S]\}^{-1}L^m)\varepsilon^0 \quad \text{eq.12}$$

Where *I* is the fourth rank identity tensor. Finally, the equivalent stiff matrix for porous solid L^e that can be solved, is reported in Eq.13: (50):

$$L^e = L^m(I + C(\{L^m - L^m[CI + (1-C)S]\}^{-1}L^m))^{-1} \quad \text{eq.13}$$

Starting from this, the authors of (49) modified the model to take into account the orientation of a textile composite material to identify its elastic constants. In particular, Mori-Tanaka methods (51) was adopted to predict in-plane elastic constants of various types of woven, braided and knitted fabrics composites, comparing the results with classical Voigt method and experimental results.

Table 10: Relative error between the model prediction and the experimental results for in-plane elastic constants of woven, braided and knitted fabric composites (49). *MT(∞,ell): Mori-Tanaka model with infinite elliptical long inclusions; MT($\beta = 2$): Mori-Tanaka model with finite length and $\beta = 2$; VRH: Voigt-Reuss-Hill method with homogenized matrix material*

	Woven fabric composites		Braided fabric composites		Knitted fabric composites			
	Voigt	MT(∞, ell)	Voigt	MT(∞, ell)	Voigt	MT(∞, ell)	MT($\beta = 2$)	VRH(h)
Young's modulus E	$5 \pm 8\%$	$-1 \pm 9\%$	$10 \pm 9\%$	$8 \pm 10\%$	$15 \pm 12\%$	$12 \pm 12\%$	$2 \pm 9\%$	$-11 \pm 8\%$
Shear modulus G	$1 \pm 8\%$	$-4 \pm 11\%$	$6 \pm 12\%$	$4 \pm 13\%$	$14 \pm 12\%$	$10 \pm 12\%$	$0 \pm 8\%$	$-13 \pm 9\%$
S_{12}	$8 \pm 18\%$	$12 \pm 22\%$	$-9 \pm 17\%$	$-7 \pm 19\%$	$-5 \pm 29\%$	$-3 \pm 29\%$	$9 \pm 31\%$	$36 \pm 44\%$

Moreover, for knitted fabric composites, in (49) the authors proposed to introduce an empirical parameter β in $L_i = \beta R_b$, where the L_i is inclusions length, and R_b the radius of curvature of the yarn. The parameter β was chosen so that the Mori-Tanaka predictions are in agreement with the experimental results. $\beta = 2$ is the best compromise to match the Mori-Tanaka results and the experimental ones (49). Table 10 lists the error observed between the Mori-Tanaka model modified to take into account the different orientations of textile composites, Voigt method and experimental results, in terms of identified mechanical constants (49). Is possible to see that Mori-Tanaka model applied to knitted fabrics composites predicts elastic constants in better agreement with experiments than the classical Voigt theory. For others composites materials listed in Table 10, Mori-Tanaka offers some interesting perspective.

Mori-Tanaka model is used in a similar way in (52) to predict the stress distribution in the inclusion phase and in the matrix phase of composite materials. The authors compare the predictive results for stresses in one inclusion and in the matrix for Mori-Tanaka formulation and pseudo-grain discretized Mori-Tanaka formulation (PGMT), confronting all the results with FE simulations. The short fibre composite materials studied in (52), have different configurations of fibre orientation. In particular, fully aligned fibres (inclusions), not-aligned inclusions and random 2D statistical distributions for lengths and orientations are considered. Table 11 lists all the cases. The reinforcement and matrix phases considered, are made of glass fibre with Young's modulus and Poisson's ratio equal to 72 GPa and 0.22 and polyamide with Young's modulus and Poisson's ratio equal to 3GPa and 0.37, respectively.

Table 11: Case considered in (52). *a11 and a22 are the orientation distribution*

Cases	Description	Volume fraction of inclusion
Case 1a	Fully aligned inclusions with an aspect ratio 3, orientation angle, $\varphi = 0$	0.161
Case 1b	Fully aligned inclusions with an aspect ratio 3, orientation angle, $\varphi = 90$	0.161
Case 2a	Inclusions with aspect ratio 3 having orientation distribution close to uniform random; $a_{11} = 0.54$, $a_{22} = 0.46$	0.01
Case 2b	Inclusions with aspect ratio 3 having orientation distribution close to uniform random; $a_{11} = 0.51$, $a_{22} = 0.49$	0.1
Case 2c	Inclusions with aspect ratio 3 having orientation distribution close to uniform random; $a_{11} = 0.52$, $a_{22} = 0.48$	0.25
Case 3a	Inclusion having an aspect ratio of 3, having orientation distribution tensor; $a_{11} = 0.65$, $a_{22} = 0.35$	0.161
Case 3b	Inclusions having aspect ratios 3 and 15; the orientation of the inclusion with lower aspect ratio is uniformly random, while longer inclusions are aligned in one direction	0.05 of each phase

The authors of (52) found that for planar distribution of inclusions, Mori-Tanaka model gives a good correlation with the FE calculations. PGMT, however, failed to give good estimates for stress level in the individual inclusions while predicting correctly the phase average stresses. For the matrix phase, Mori-Tanaka method and PGMT are in good agreement with the prediction of stress levels. The deviation between the FE results and Mori-Tanaka formulation increases with increase in volume fraction and when there is a length distribution of the inclusions. The authors conclude that the Mori-Tanaka model is a better approximation of reality and should be used as the first choice mean-field homogenization method.

1.4.3 Micromechanical model of heterogeneous composite materials by the finite element method (FEM)

In the literature, there is a huge number of works about micromechanical modelling of composite materials using the finite element methods. In (53) Patniak et al characterised mechanically the binary composite material reinforced with glass fibres randomly oriented and impregnated with epoxy resin to validate the finite element simulation (FE) using ANSYS and verify the possibility of predicting the mechanical properties using FE. Various experimental test are reported in (53), but in order to determine the elastic modulus and tensile strength, the tensile tests in agreement with ASTM D3039-79 were performed.

Table 12: Properties of composite's constituents (53)

Properties	Glass fiber	Epoxy resin
Density	ρ_f = 2.4 gcc	ρ_m = 1.5 g/cc
Young's modulus	E_f = 73,000 MPa	E_m = 3416 MPa
Poisson's ratio	ν_f = 0.20	ν_m = 0.4
Tensile strength	2300 MPa	75 MPa
Thermal conductivity	K_f = 1.3 W/m K	K_m = 0.363 W/m K
Thermal expansion coefficient	54×10^{-6}/°C	80×10^{-6}/°C
Fiber volume fractions (V_f)	9, 15, 21, 27%	–
Fiber diameter	d = 21 μm	–

A finite element model is built to produce the representative volume element (RVE) of the composite structure and modelling their aspect to calculate the stress and the strain acting inside the

components of the RVE. In this regard, representative area elements (2D analysis) are generated using different volume/weight fractions and considering the properties of single composite's constituents listed in Table 12 and assigning linear elastic isotropic properties to each component. This procedure is accomplished to determine the micro-mechanical behaviour of composite structures (53). To perform the micro-mechanical analysis the authors in (53) generated a RVE of the material by placing long randomly oriented glass fibres inside the RVE and applying a unit strain on one face, while the opposite faces were constrained along all directions.

The stress and strain calculation were performed using micromechanics equations obtained from equilibrium and compatibility relationships, assuming that stresses, strains and RVE dimensions do not change along the length, obtaining the averaged stress and strain of the composite. See equation 14 and 15 (54).

$$\tilde{\sigma} = \frac{1}{V}\int \sigma dV \qquad \text{eq. 14}$$

$$\tilde{\varepsilon} = \frac{1}{V}\int \varepsilon dV \qquad \text{eq. 15}$$

In (53) the tensile strength was theoretically determined using micro-mechanical models, in particular, the Cox model, the rule of mixture using classical shear lag theory (55) and the Halpin-Tsai model (56).

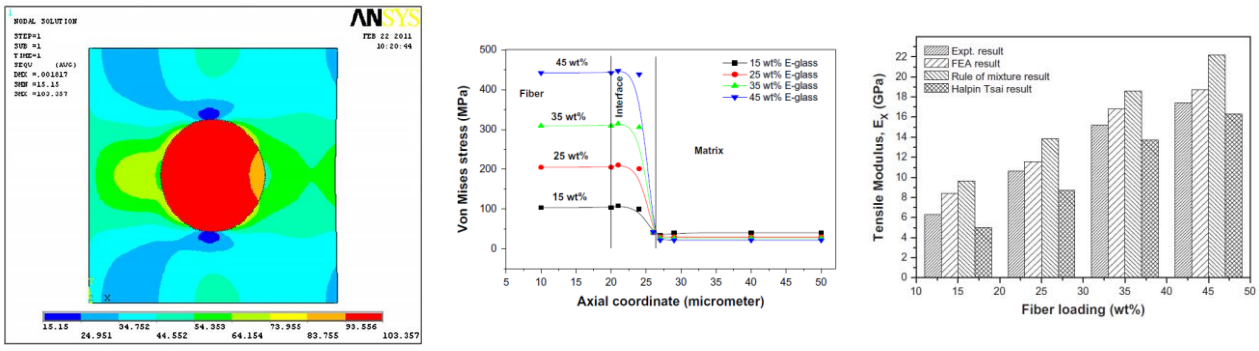

a b c

Figure 16: Comparison between results. a) Von-Mises Stress in the 15wt.% E-Glass; b) Stress distribution in the composite at different weight percentage of reinforcement; c) Elastic Modulus comparison (53).

Observing Figure 16a and Figure 16b, a very complex stress distribution is visible in the RVE of the composite. In particular, it is possible to see a concentration of the stresses around the interface between the fibre and the matrix, which can play an important role in damage of the composite. In Figure 16c the elastic modulus is determined using different theoretical models (55) (56). It is possible to see that the Halpin-Tsai results and FEM results are closer to the experimental, and more in general

that the elastic modulus increases for increasing percentage of glass fibres (53). Similar results are obtained in (57) where Hine et al. show how the elastic modulus can be predicted with a good confidence by FEM analysis considering at least 100 fibers (Figure 17).

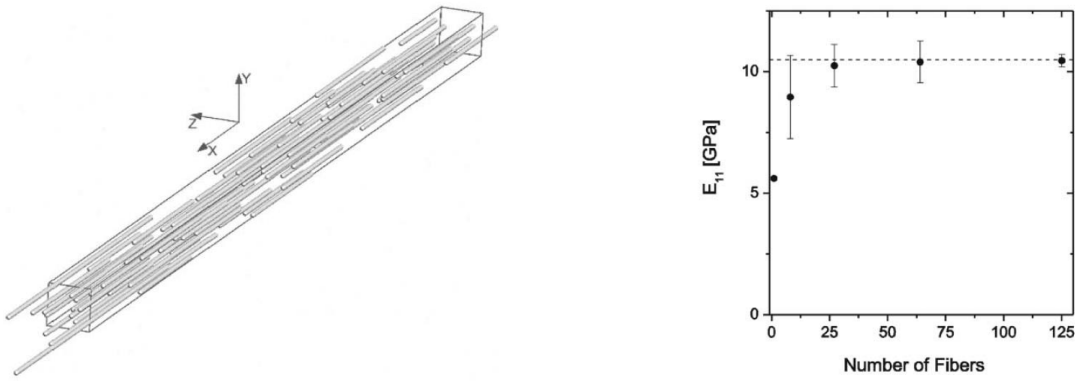

a b

Figure 17: a) RVE containing 100 perfectly aligned fibers with different fiber lengths,; b) Prediction of the Young's Modulus in function of number of fibers contained in RVE (57).

Another example found in the literature presents a two-scale homogenization procedure to analyses composite structures using a FEM approach (58). Here the authors compare this homogenization method with other micro-structural formulations like Serial-Parallel mixing theory and micro modelling.

By Serial-Parallel mixing theory (SP-Theory), the behaviour of the composite is obtained combining the constitutive response of their constituents under the following assumptions. The composite's constituents are supposed to be interested by equal strains in fibre direction (parallel) and to be subjected to equal stresses in the transversal direction (serial). The composite material response is strongly related to the volume fraction of its constituent materials, which are considered homogeneously distributed and perfectly bonded (58). The authors derives the stress and strain equations along parallel or transversal directions. These equations satisfy both the equilibrium and compatibility between the composite's components and can predict the behaviour of the constituents in different loading directions (58) (59).

By Micro-Modelling, the constituents of composites are modelled explicitly, considering for each material its own constitutive law, without taking into account any simplifying hypothesis and for this, these model are very powerful even if the computational cost is very high (58).

The multiscale homogenization method proposed in (58) is based on the use of an RVE corresponding to a microstructural sub-region representative of entire subscale to determine the effective properties at the homogenised macro scale. It is fundamental that the composite material

contains a sufficient number of inclusions to make the module independent of homogeneous force or displacement applied onto the RVE's boundaries. In general, the first-order homogenization can be defined as a driven deformation; in this manner, the elastic modulus, strain tensor and stress tensor can be determined at RVE level by imposing a deformation at macro-scale. Considering these bases, the authors in (58), defined the homogenised variables, strain and stress tensors, elastic constitutive tensor and linear-elastic homogenization to perform numerical implementation.

Table 13: Mechanical Properties of Laminas (58)

Simple mat.	Color Ref.	*E* (GPa)	*G* (GPa)	*v*
Lamina 1	Black	210	80.76	0.3
Lamina 2	Gray	3.5	1.46	0.2
Lamina 3	White	3.5	0.146	0.2

To prove the soundness of this multi-scale approach, a clamped beam with vertical load at mid-span was modelled using the macro-FEM and micro-mechanical model presented briefly, to simulate the behaviour of the material modelled with these different theories. The material is a generic laminate composed of laminae with different mechanical characteristics, as reported in Table 13, to simulate the undamaged material or different grade damaged composite (Figure 18a). The generic composite material was created overlapping different number of layers named Lamina 1, Lamina 2 and Lamina 3 to simulate higher level of damage. For example Lamina 3 in Table 13 simulates the damage with shear modulus G reduced by ten compared to Lamina 2. In the article (58), the authors tested two situations varying the stacking sequences and percentage of layers Lamina 1, Lamina 2 and Lamina 3: globally damaged material and locally damaged material. The comparison between model responses is done by measuring the reaction force in the middle span of the beam.

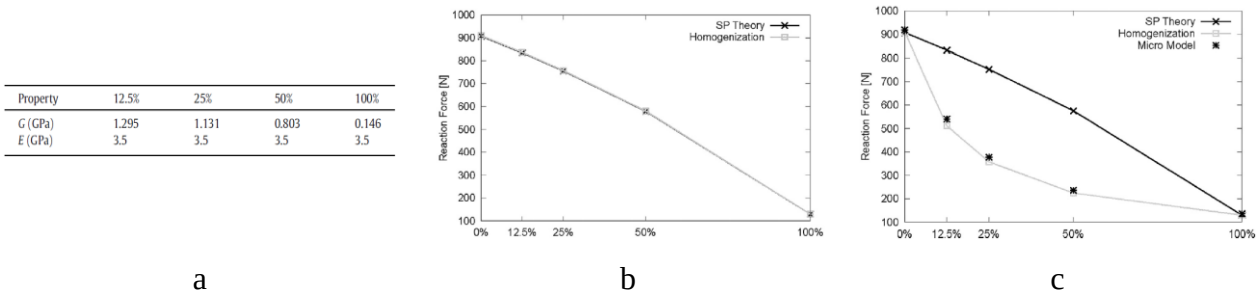

Figure 18: Results comparisons between different macro and micro models. a) Level of damage; b) Reaction force obtained in global damage case; c) Reaction force obtained in local damage case (58)

Observing Figure 18b, if the material is globally damaged, the two theories (SP theory and Homogenization) respond in an equal manner. Moreover, it is possible to see, as expected, that if the stiffness of a single layer decreases, the global stiffness of the composites decrease too. This is

interpreted as delamination failure (58). In Figure 18c there is a difference between the reaction force determined using SP-Theory, that is equal to the one obtained in a global damage case, compared to the reaction force obtained using homogenization or micro-model techniques. This difference due to the assumption of constant stresses and strains at the boundary condition that induce a regularization of the response of the material within the numerous laminae. On other hand, with the homogenization and the micro-model, the damaged layer is discretized specifically and it is possible capture the drop of stiffness that take place responsible of the decrease of the reaction force (58). The authors conclude that the homogenization method can accurately capture the effect of local damage because the microstructure is physically modelled in the RVE. Moreover, for linear analysis, homogenization is an excellent alternative to other formulations. Its computational cost is substantially lower than the one required by micro-models and it is able to capture several microstructural phenomena that are not automatically recorded by the serial-parallel methods. Even if the computational cost is the major limitation, homogenization is extended to nonlinear cases, concluding that it is a very promising method to simulate materials with complex microstructures (58).

1.5 Experimental techniques involved in Macro and Micro mechanical modeling development of particleboard panels

As said before in Section 1.1, for both modelling techniques, applied on particleboard at Macro and Micro level, experimental data are required.

To evaluate the bending performance at the macro level and to determine the particleboard's elastic constants, I have performed Three Point Bending Test (TPBT) and Iosipescu Test (IT). To collect the deformation data in TPBT, I used both deflectometer placed in mid-span of the samples (geometry reported in Figure 19a) and Digital Image Correlation to get field deformations in the region of interest. For Iosipescu, for the nature of the test, the deformation maps was collected using DIC on the region of interest on the Iosipescu specimen (Figure 19b).

For micro modelling and to analyze the interior of the particleboard and to characterize the particles' distribution, Micro-CT quantitative analysis was performed to visualize the reconstructed volume of the material to identify the single constituents and estimate its density (the geometry shown in Figure 19c). It is important to remember that the type of particleboard principally studied in this PhD work has a thickness equal to 18mm, although this thesis will explore others two thicknesses: 8mm and 38mm.

Leaving the description of TPBT and IT to a more detailed treatment in Chapter 3, in this last Section 1.5 of Chapter 1, I focus in particular on Micro-CT and DIC techniques.

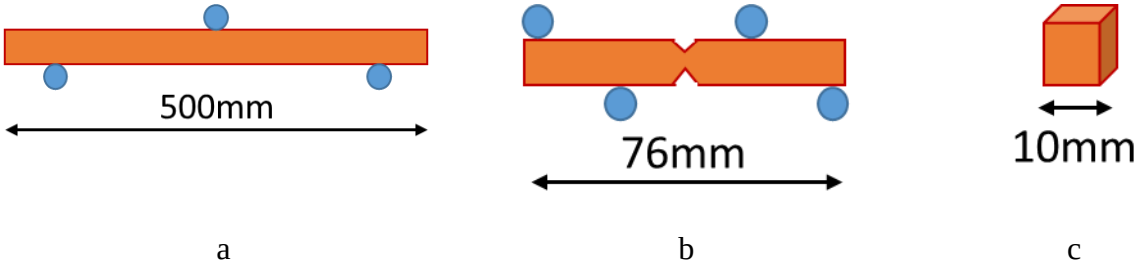

Figure 19: Specimen geometry tested in this PhD thesis. a) Three Points Bending Test specimen; b) Iosipescu Test Specimen; c) Micro-CT specimen.

1.5.1 Micro Computer Tomography, a briefly overview

The tomographic technique is an imaging method that is noninvasive and nondestructive with respect to the object observed and studied. It is possible to divide this method into two categories, considering the grade of resolution that is achieved. If the set-up uses high-resolution sensors that provide suitable contrast and spatial resolutions (50-100µm at least) (60), the technique is called Micro-Computed Tomography (Micro-CT), otherwise, the same technique is named X-Ray Computed Tomography (CT). In both cases, this unconventional advanced experimental test is based on an imaging method where individual projections, normally called radiographs, recorded from different viewing directions, are used to reconstruct the internal structure of the sample of interest, see Figure 20.

Single projections produced by CT or Micro-CT are in gray-level scale and provides an accurate map of variation of X-Ray absorption from interaction between the X-Ray and material's object crossed. Combining these X-Ray 2D maps (projections) using projective geometry algorithms, it is possible to obtain a series of 2D images that represent the internal structure of the sample, called slices. Finally, to reconstruct the 3D volume of the object observed including internal structure, another algorithm superimposes all the slices obtained, see Figure 21.

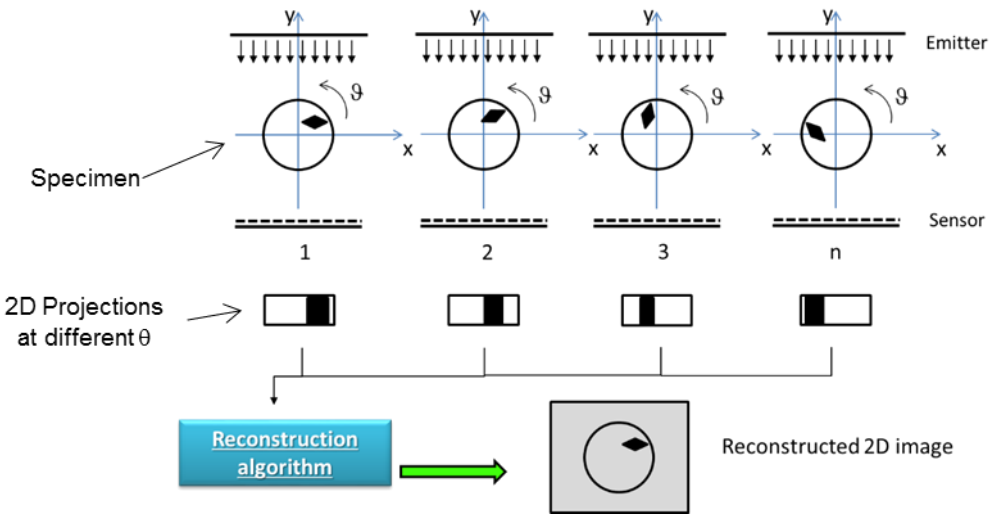

Figure 20: Micro-CT principle

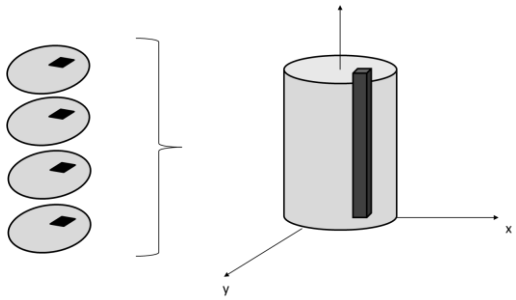

Figure 21: From 2D image (slices) to 3D Image (reconstructed volume) of the object.

X-Ray CT or Micro-CT are often used in medical or biology applications, see an example in (61) where the authors use Micro-CT imaging to produce an FE model of mitral valve (Figure 22). These imaging methods are likewise applied in the study of mechanical components or materials.

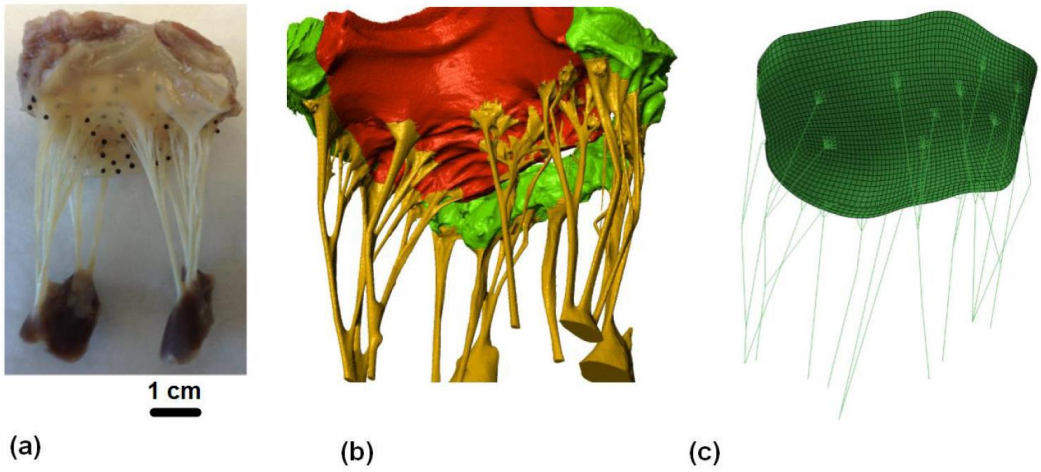

Figure 22: a) Ovine mitral valve; b) Micro-CT 3D reconstruction; c) 3D FE model of mitral valve using 3D model b) (61)

It is important to underline the advantages of these techniques. The information provided from Micro-CT or CT can drastically reduce the required time in iterative cycles of prototype

manufacturing and testing. Moreover integrating tomography data of manufactured components into FEM analysis or more in general into structural analysis, seems very promising in particular for anisotropic materials such as composites. For example in (62) the authors characterized textile ceramic composites in 3D space, using Micro-CT imaging technique, see Figure 23. Other applications of Micro-CT and CT are the damage propagation analysis based on extremely sensitive measurements of density variation of the material or final assembly verification as reported in (63).

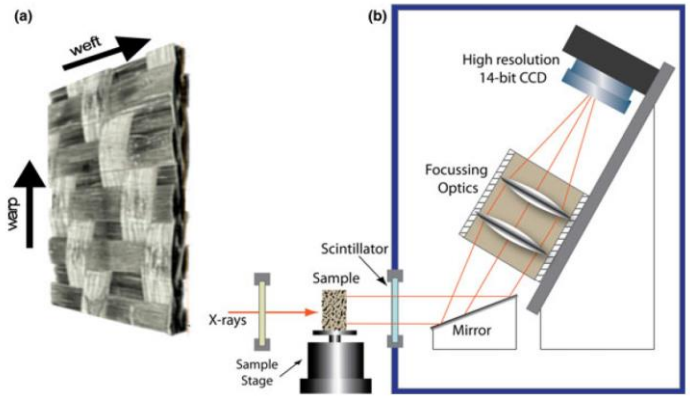

Figure 23: a) 3D image reconstructed of textile composites using experimental set-up proposed in b) (62)

In this thesis, I used the Micro-CT technique (spatial resolution equal 9µm) to observe the internal structure of particleboard and to characterize it, by the estimation of the density and recognition of single wood particles and adhesive. To reach this first goal, I acquired all projections in absorption mode using synchrotron light as an X-Ray source. The detector's Field of View limited the dimensions of the sample sides. These side dimensions, equal to 10 mm, can be smaller than the wood particles size (see next Chapters). In Figure 24a it is possible to see a sample of particleboard and the corresponding reconstructed volume in Figure 24b.

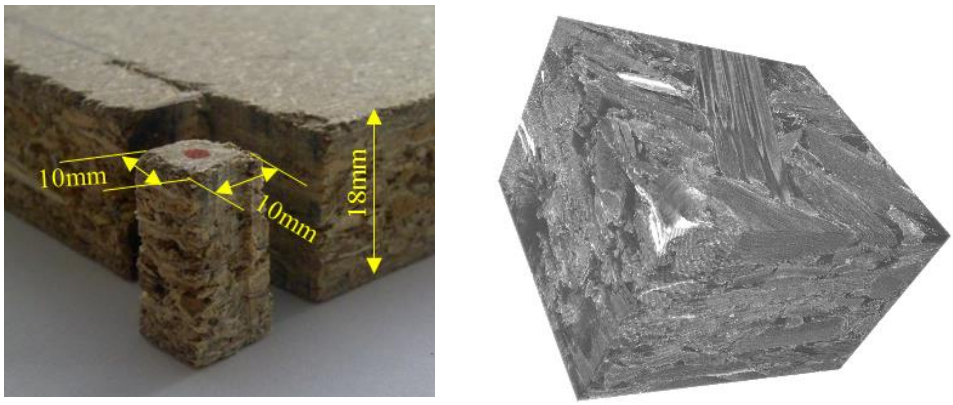

a b

Figure 24: a) Particleboard sample 10x10x18mm; b) Particleboard reconstructed 3D volume by Micro-CT imaging in absorption mode and using Synchrotron light source

1.5.1.1 Absorption mode: Interaction between material and X-Ray Beam

When an X-Ray source produces a beam with a certain intensity I_0, and this goes through the material, the beam's intensity I after passing through the object is expressed by Eq.16 (60) (64):

$$I = I_0 e^{-\mu x} \qquad \text{eq.16}$$

where μ is the linear attenuation coefficient typically given in [cm^{-1}] and x is the thickness of the material crossed [cm]. Rewriting Eq.16 multiplying and dividing the exponent by the material density ρ [g/cm^3], it is possible to obtain the expression of the intensity of the transmitted radiation using the mass attenuation coefficient μ/ρ [cm^2/g] (see Eq. 17) (60) (64):

$$I = I_0 e^{-\left(\frac{\mu}{\rho}\right)x\rho} \qquad \text{eq.17}$$

μ/ρ is a material property strongly related to the atomic number Z of the absorbing material and X-Ray wavelength λ. For most energy levels of the X-Ray beam and materials, μ/ρ can be expressed by Eq. 18 (60):

$$\left(\frac{\mu}{\rho}\right) \cong Z^m \lambda^n \qquad \text{eq.18}$$

where m is comprised between 3 and 4 and n is equal to 3 (60).

Using XMuDat database (65) (66), it is possible to plot μ/ρ values for many types of materials and mixtures, as a function of the photon energy of the X-Ray beam.

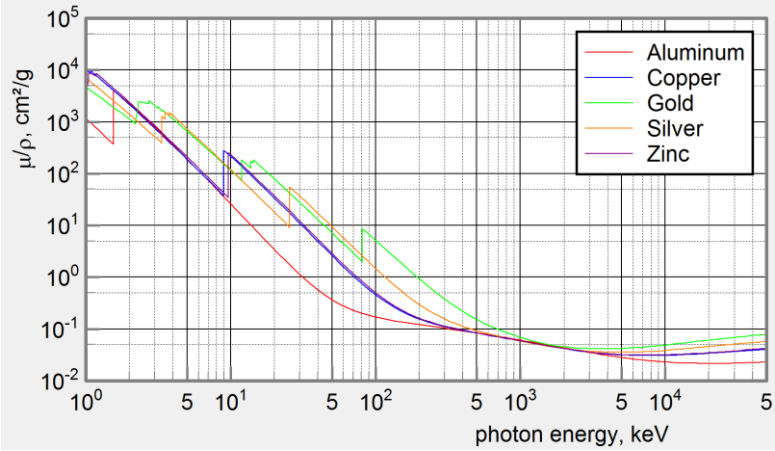

Figure 25: Mass attenuation coefficients as a function of photon energy for five pure materials.

For example in Figure 25 the mass attenuation coefficients μ/ρ as a function of the wide range of photon energy for five metal pure materials are reported. It is clearly shown that for high beam energy, the mass attenuation coefficient is lower and that for low photon energy μ/ρ increases by different orders of magnitude, depending on the material. Figure 25 shows that some materials (Zinc, Silver, Gold and Copper) have a different absorption profile at lower energy.

In presence of a mixture or a compound of materials, the mass attenuation coefficient can be calculated using Eq. 19 (64):

$$\left(\frac{\mu}{\rho}\right)_{mixture} = \sum_{i=1}^{n} w_i \left(\frac{\mu}{\rho}\right)_i \qquad \text{eq.19}$$

where n is a number of components of the mixture and w_i is the fraction by weight of the i^{th} constituent. It is important to underline that these equations (Eq. 17 and Eq. 18) are incomplete because do not consider that X-Rays are affected by refraction and wave fronts distortion when the beam passes through solids and mixtures with components with different densities. However, these expressions are often sufficient, particularly when the beam possesses significant spatial coherence (Synchrotron Light conditions) (60).

In general, it is possible to underline that the projections (mass absorption coefficient maps), obtained during Micro-CT, are generated from the X-Ray beam that goes through the object and hits the sensor called detector. This converts the photon energy I of the beam into electrical signals and finally, after proper conversions, into images. The intensity I of the energy captured by the sensor is proportional to the μ/ρ coefficient of the material crossed.

To get good quality projections to be used in reconstructions of the slices and 3D volume, the following factors are very important: the spatial resolution of the detectors in relation to the structural features of the material to be observed and the contrast. Spatial resolution is defined as the accuracy by which small details can be located with respect to some reference points (60).

Contrast, instead, is a measure of how well a feature can be distinguished from the neighboring background (60). For better understanding, considering Figure 20, let's suppose that the cylindrical specimen is composed of two different materials: a cylinder of low-density material with a low atomic number and the rhomboid feature made of high-density material. In general, if you use Eq. 18, the μ/ρ coefficient for the cylinder will be lower than that of the rhomboid. In this manner, the intensity of the X-Ray beam hitting the detector that goes through the material with higher μ/ρ will be lower than that of the section of the material with the material with lower μ/ρ. The resulting projection will be a 2D-image with white zones related to the material with high density, high μ/ρ and lower beam intensity, and black zones with low density, lower μ/ρ coefficient and higher beam intensity on the

detector. This physical process is responsible for the contrast formation between features in the image of the observed object.

Considering the physical process of X-Ray Imaging, it is possible to determine which is the best thickness of the sample that can be scanned using Micro-CT or CT techniques. If the specimen is too thick, no X-Rays pass through it and no contrast is produced. On the contrary, if the specimen is too thin, the variation of the intensity transmitted through the specimen cannot be distinguished. The optimum imaging in micro-CT is achieved when μx (see Eq. 16) is less than 2 for the longest path length through the sample, which corresponds to a transmission through the specimen greater than 13-14 percent. It is fundamental to remember that the relationships proposed in Eq. 16 and Eq. 17 are valid for monochromatic X-Ray, which means that the photons have a single energy level. Normally Synchrotron Light and X-Ray from tubes are polychromatic, then it is necessary a filtering operation between the X-Ray source and target to remove the undesired wavelengths. The filtering operation made by a monochromator device (60), although it reduces the overall level of energy of the beam, prevents undesired effect called beam hardening on the projections This effect is the results of the increasing of the average photon energy of the polychromatic beam when it penetrates the target. The average photon energy increases with increasing sample thickness because the lower-energy photons are absorbed at much higher velocity than the higher-energy photons (60). Observing a slice affected by beam-hardening, it will appear with abnormally low gray level in the interior (near to black) and high values at the periphery (near to white).

Two major Micro-CT techniques largely adopted in scientific field are absorption mode and phase contrast. The Micro-CT performed in this thesis are in absorption mode, but it is also interesting to understand how the phase contrast method works. It is important to underline that X-Rays are ever so slightly refracted when passing through objects so that X-Ray wavefronts distort when passing through region of different electron density. By suitable X-Ray source as a Synchrotron radiation and proper method named Propagation, it is possible to detect change in contrast resulting from X-Rays beam traversing samples with different electron densities. The Propagation Method requires a detector placed at a distance equal to 1m from the specimen, in this manner the refracted X-Rays diverge and interfere with other X-Rays at the detector plane, producing a detectable fringes at the external and internal boundaries between materials with different electron density. The contrast that permit to recognize the object borders, will be provided by differences in the second derivative of the X-Ray phase (60).

Come back to absorption mode adopted in this thesis, there are many configurations of the experimental set-up to perform it. The one was used in this PhD work was similar to the "Fan Set-Up" described in (60).

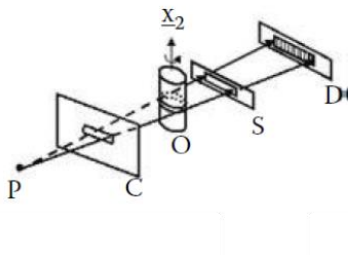

Figure 26: Adsorption mode using Fan set-up (60)

Observing Figure 26, Fan beam set-up uses a rotating table where the specimen is placed. A flat beam of X-Rays originates from the source *P*, it is shaped by the collimator *C*, passes through the sample and the scatter shield *S* and it is finally collected by the X-Ray detector *D*. A very important factor is the distance between the sample and the detector that, for the absorption technique, must be in the range of few centimeters (60).

The workflow that it is followed to collect the projections (2D-Images) is shown in Figure 27.

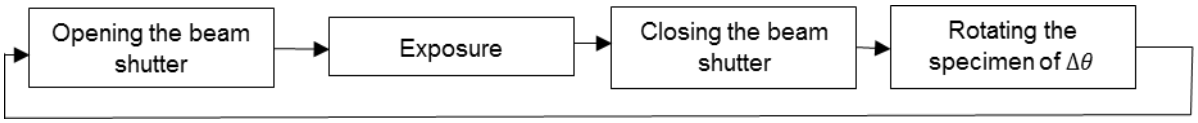

Figure 27: 2D-Image production workflow

1.5.1.2 X-Ray source used: Synchrotron light

The Synchrotron radiation sources are defined as super X-Ray tubes, where an accelerated electron beam generates X-Rays by hitting a target (60). My experiments with Micro-CT were performed at the Elettra Synchrotron radiation facility located near Trieste. Here the radiation is produced by LINAC source where the electrons start off from a ceramic disc that is heated to a very high temperature. An electric field up to 100kV draws out the electrons that are then accelerated through two radio-frequency structures that make up the LINAC. The source has a overall length of 12m (Figure 28) and it is composed of a ceramic disc container, a low-energy section and two high-energy sections both of 5m long.

Figure 28: Electrons Source LINAC of Elettra Synchrotron (67)

The LINAC operates at 3GHz and generates a pulse of electrons accelerated to the final energy equal to 100MeV. In order not to lose electrons after the acceleration, LINAC operates under vacuum. The electrons at 100MeV of photon energy are sent to the booster, a synchrotron of 118m of circumference that can accelerate a maximum of 6mA current from 100MeV to 2.5GeV with a repetition rate equal to 3Hz. Once the electrons reach the requested energy, they are extracted and sent to a storage ring. Here the electrons travel at the speed of light and to maintain a good quality of the beam and increase its lifetime, it is necessary that the electrons do not collide with gas molecules. To prevent this phenomenon, very powerful bending magnets (Figure 29a) are used to maintain the right direction of the electrons along the ring.

The radiation is extracted tangentially and sent at every laboratory, named BeamLines, for different types of tests: in general medical or industrial applications (Figure 29b).

The Micro-CT experiments presented in this thesis were performed at the SYRMEP BeamLine (Synchrotron Radiation for MEdical Physics). This Lab was designed in collaboration with the University of Trieste for medical research, material science and life science applications. Here, the beam extracted from the ring goes through a Monochromator, having an optic based on a double-crystal of Si 111 which works in the energy range between 8 keV and 35keV. SYRMEP BeamLine provides from a distance equal to 20m from the extraction (source), a monochromatic laminar-section X-Ray beam with a maximum area equal to 120 x 4mm^2. The maximum beam's divergence from the source to the target is 7mrad. In this configuration, I have performed the Micro-CT imaging of the particleboard in absorption mode.

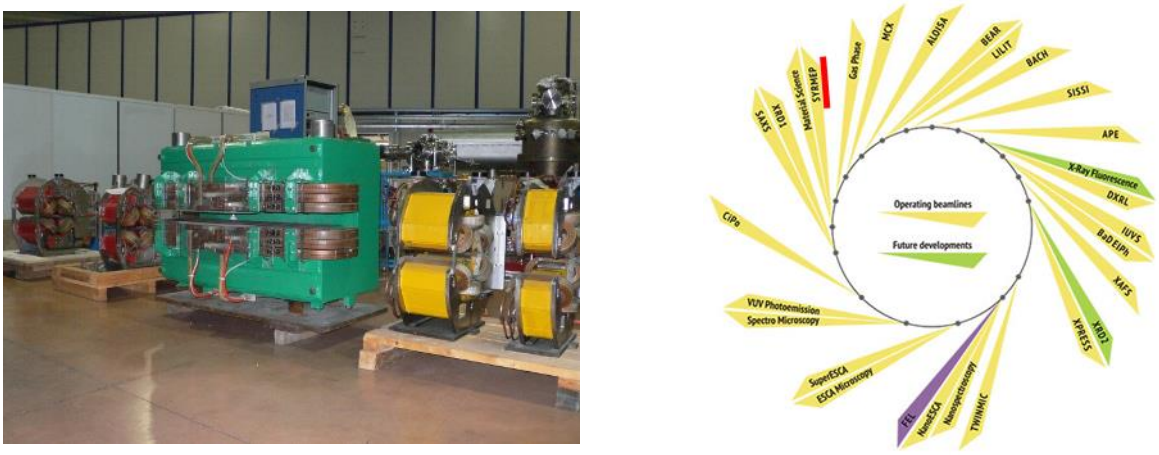

a) b)

Figure 29: a) Bending magnets at Synchrotron facility; b) Beam Lines (67)

At the SYRMEP Lab, it is possible perform Micro-CT, CT or radiography in absorption or phase contrast modes in dedicated end-station.

On this BeamLine hundreds of works are performed focusing on very different scientific fields. Concerning my work about wood-based material, there are different studies developed by experiment performed on wood at SYRMEP lab. For example in (68) Derossi et al uses the Synchrotron radiation to characterize the archaeological wood structure in non-destructive manner. Zanini et al in (69) analyzed the 3D wood structure by Micro-CT performed at SYRMEP BeamLine.

Details on the reconstruction algorithms and the procedures to generate the slices from projections are not provided herein, see ref. (60) and Chapter 3.

1.5.1.3 Digital Image Correlation method with mono-camera set-up, a preface

As presented before and as it will be treated in details in the next Chapter 3, I performed experimental tests (TPBT and IT) in order to determine the elastic constants of particleboard samples. To validate the results and to understand the failure mechanism of the material in each type of tests, field measurements of the displacements and strains was necessary. Digital Image Correlation (DIC) field methods were selected to perform these measurements. Accuracy of displacement measurement was checked against rigid motions, as measured using a deflectometer (TPBT only) or by the crosshead's displacement of the machine for IT. Strains, particularly shear strains, were compared with values obtained applying analytical formulae to the macro-mechanical test results.

In this Chapter I'm presenting a brief introduction to this field method, while details and results are presented in Chapter 3.

1.5.1.4 DIC Set-up arrangement

As mentioned before, the results of the DIC method are the measurement of the displacement components and the evaluation of the strain fields inside a certain region of interest (ROI), i.e. a portion of the outer surface of the material samples being examined. Several images of the sample's ROI are captured, starting from an un-deformed situation to create a reference picture, until the maximum desired deformation is reached. Using all images recorded at increasing deformations, the displacement field is estimated by tracking each sample point position from start to the end. In order to obtain a one-to-one correspondence between the material point in the reference state and in the current picture of the deformed structure, the surface of the sample being framed must be treated by applying a monochrome speckle to provides proper contrast between different points. In particular, the ROI must be planar to prevent out-of-plane displacement and a speckle-pattern must be produced on it using, for instance, spray painting or toner powder deposition (70). For macroscopic length scale (2cm ROI and above), the samples are usually painted using non-reflective spray paint applied by hand, even if other techniques are available, like airbrush or transfer paper deposition directly on the ROI (not so frequent) (71). One example of different speckle patterns numerically generated by laser surface treatment on the tensile specimens is shown in Figure 30.

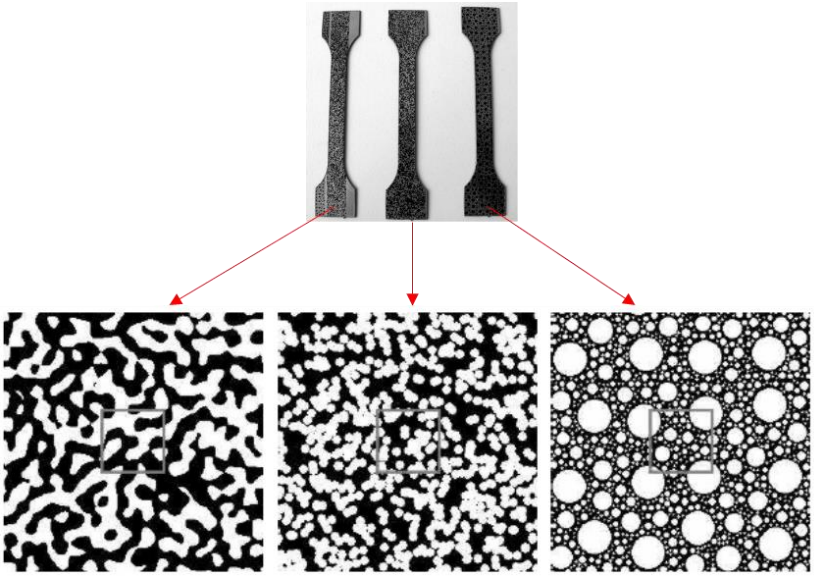

Figure 30: Different speckle-pattern on tensile test specimens. From left to right the speckle pattern reproduce "white noise", random distribution that simulates the white spray paint on black surface and the three cyrcle diameters repetitive subset (71)

As well as the speckle-pattern, also image acquisition and lighting are very important for producing accurate DIC measurements. More in general, the spatial resolution of the camera must be enough to provide an adequate number of pixels to locate every point of the speckle pattern with respect to the dimensions of the ROI and the magnitude of the displacement that can be observed. There are many works where DIC was used at different levels of magnification. For example in (72) the authors worked at macroscopic level on specimens cut from epoxy plate of 6mm of thickness casted in house by mixing C-51 epoxy resin and K-6 hardener (commercially available) in proportion equal to 10:1 by weight. The material obtained has E modulus equal to 3300 MPa, yield strength equal to 35 MPa and Poisson's ratio of 0.37. The experimental set-up used to frame a ROI of 220mm x 40mm used a CCD Camera with spatial resolution equal to 2448 x 2048 pixels. Babler et al in (73) framed a ROI of 5mm x 5mm using a CCD Camera with spatial resolution equal to 3326 x 2504 pixels. The material studied in this work was a PWA1484 single crystal nickel-based superalloy.

The lenses are very important because they should provide a suitable magnification to capture the displacement phenomena of interest. A wide choice is available, which spans from macro lenses, e.g. in (72), the CCD Camera was connected to a Tamron lens with focal length of 180mm, to microscope tubes, as in (73) where a Questar QM100 long distance microscope was used to provide high magnification at long distances.

Another very important aspect is the light set-up. For this experimental technique, the ideal light source is a diffuse light, in order to mitigate surface's reflections. In (73), the authors used a semi-rigid light guide, while in (72) a LED diffused illuminator was used.

Figure 31 shows two different DIC set-ups: in Figure 31a the authors measured the displacement and the strain fields of a Four-Point Bending Test of a solid beam; in Figure 31b the field of displacement and strain are measured performing Microscopic DIC method a heated tensile specimen.

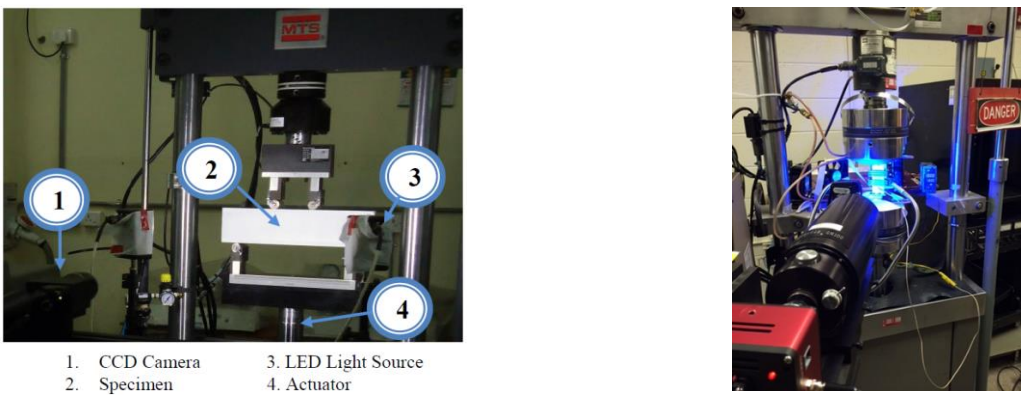

a b

Figure 31: Two different DIC set-up: a) Macroscopic field displacement measurement of Four Point Bending Test (72)*; b) Microscopic field displacement measurement in tensile test of high temperature conditions* (73)*.*

From the images captured during the deformation of the sample, in order to reconstruct the displacement field and then the deformation field, it is necessary to track the position of a certain number of points distributed within the ROI. This operation is performed by an algorithm that correlates the "deformed" image with a reference image (undeformed state). There are numerous software packages available; ViC2D (74) is one of the most widely used, another possibility is Q-400 DIC (75); in this work, I used N-Corr software (76). This is a sub-routine of Matlab (77), it is an open-source software and has an intuitive GUI. More importantly the fields of displacements and strains are immediately available in matrix form, usable in Matlab environment for further manipulation without any conversion or preliminary data treatment. In general, the images processed using any DIC software, need being converted to gray-scale image with third party software, in order to make possible to apply the correlation algorithm.

1.5.1.5 DIC algorithm implemented in N-Corr software, a brief overview

The N-Corr software used in this PhD work first divides the ROI into small subsections from the reference image to process them using correlation algorithm. These small parts of the image named subsets, contain a group of coordinate points and a central reference node (Figure 32).

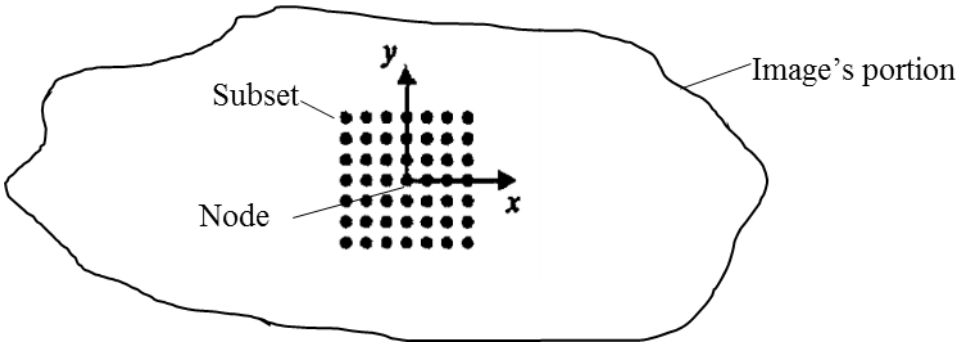

Figure 32: Subset and node definition (78)

It is possible to determine the subset's location observing the position of each node with respect to the reference configuration, (normally in this condition, no displacements or deformations are applied to the specimen's ROI) and compare it with the current one. If the specimen's ROI is deformed by two-dimensional deformation, each of these nodes can be mapped using Eq. 20 (78):

$$\tilde{x} = x + U(x,y); \quad \tilde{y} = y + V(x,y) \qquad \text{eq. 20}$$

where *U* and *V* are the horizontal and vertical displacements components of each subset point, *x* and *y* are the position of each coordinates-point in the reference image and $\tilde{x}$ and $\tilde{y}$ are the new location of the points in the "deformed" image. In (78) the assumption is made that *U* and *V* can be approximated by a second-order Taylor series expansion in the neighborhood of the nodes (centre of the subset) introducing twelve mapping parameters. This approximation permits to represent more accurately large deformation from a combination of these twelve parameters. In order to locate each subset's centre (node), a bi-cubic spline interpolation was proposed in (78) between the reference image and deformed images, determining the set of coefficients for each subset. Further refinement was applied in (66) following (79) where more parameters were added in the interpolation to take into account that approximately, the gray-levels in the reference image are equal those in the "deformed" images, to compensate for possible variations of the lighting on the field measurements from the first image to the last one.

In order to determine the optimum values for the mapping parameters (vector P in (78)), in N-Corr software, least square correlation coefficient was used (Eq. 21):

$$C = \frac{\sum_{Sp\,\epsilon\,S}\{g(Sp) - h(Sp,P\}^2}{\sum_{Sp\,\epsilon\,S} g^2(Sp)} \qquad \text{eq. 21}$$

where *S* represents all the points in the subset, S_p represents every single point in the subset. *g* and *h* are respectively the grey levels in the reference image and in the deformed image. *P* is the vector with all 13 mapping parameters of the bi-cubic interpolation. When the value of *C [0;∞)* reaches the minimum, the difference between *g* and *h* are minimized, in this manner, the set of thirteen parameters of vector *P* are found and the position of the every node of the deformed image subset are likely to have been located. To find the minimum value of *C*, the gradient of *C* must converge to zero. Newton-Raphson method is used to find the roots of the gradient of the least square correlation coefficient, see Eq. 22 (78), (80) where P_0 is the initial guess solution and *P* is the next iterative approximate solution.

$$[\nabla\nabla C(P_0(P - P_0)] = -[\nabla C(P_0)] \qquad \text{eq. 22}$$

Using this optimization technique to reach the optimal values of the bi-cubic interpolation parameters between the reference and deformed images, it is possible to determine the position of all the points of the deformed images and then calculate all field displacement and strains. The vector

reported in Eq. 23 contains all the displacement components and their first order derivatives evaluated.

$$\left\{U, V, \frac{\partial U}{\partial x}, \frac{\partial U}{\partial y}, \frac{\partial V}{\partial x}, \frac{\partial V}{\partial y}\right\} \qquad \text{eq. 23}$$

The authors in (72) reported the displacement field (Figure 33) and the strain field (Figure 34) measured using N-Corr and they compared these results with the results obtained using the Vic-2D commercial software. Observing Figure 33a and Figure 33b that refers to Four-Point Bending Test of an epoxy beam under 1kN load applied from the bottom, the vertical displacement contours measured using N-corr software are in good agreement with values obtained using Vic-2D. Finally, the vertical displacement extracted along the a-b line is compared between the two software packages in Figure 33c, showing a good agreement.

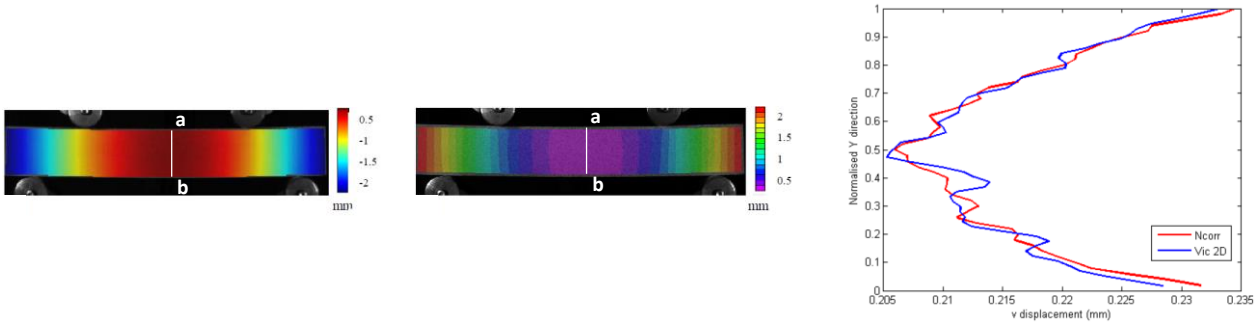

a) b) c)

Figure 33: Vertical displacement comparison along ab line. a) N-Corr results; b) Vic-2D results; c) Comparison between N-Corr and Vic-2D (72)

Likewise, in (72) a comparison was made between the ε_{xx} strain (Figure 34 shows the strain field parallel to the beam axis) measured using both N-Corr and Vic-2D along the *ab* line.

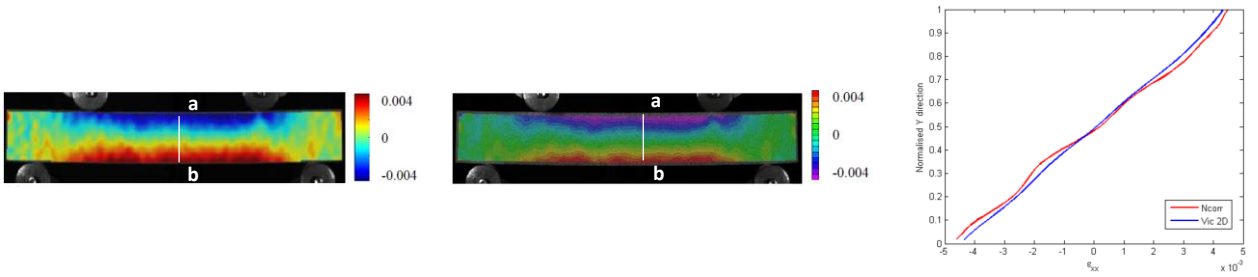

a) b) c)

Figure 34: ε_{xx} field deformations comparison along ab line. a) N-Corr results; b) Vic-2D results; c) Comparison between N-Corr and Vic-2D (72)

Even for the ε_{xx} field, N-Corr and Vic-2D are quantitatively in good agreement; see Figure 34.

In Chapter 3 of this PhD thesis, the validation of the measurements obtained using N-Corr open-source software was performed using tensile samples tested under tensile loading, comparing field deformation with the extensometer measurements.

Chapter 2 – Micro CT particleboard analysis

2.1 Outline

Before any mechanical characterization of particleboard to determine its elastic constants and define its bending performances, it is very important to observe the internal structure of this material. This preliminary phase of the work is useful to understand how the material is made, identifying its constituents and their size and orientation distribution inside the particleboard volume. After this qualitative image analysis to characterize particleboard's microstructure, a quantitative density analysis is required to estimate the vertical density profile (VDP) of the material. In fact, the density is the most important characteristic of which the mechanical characteristics of the particleboard are strongly related as reported in (35) and in (25).

This second Chapter focuses on the description of the Micro-CT's set-up used to obtain the projection of the particleboard of 18mm of thickness and related reconstructed slices. Then, the particleboard's microstructure is analyzed to recognize the constituents and their geometric properties. Finally, by quantitative image analysis, the VDP of the material is estimated. The last part of this Chapter is dedicated to comparing the VDP obtained from Micro-CT analysis with the VDP obtained using a commercial device named profilometer. This machine is usually used to evaluate the quality of the particleboard during the production process, by controlling its VDP.

2.2 Micro CT set – up, parameters and sample's preparation

As presented before in Chapter 1 (Section 1.5.1), the tomographic scans were performed at the Elettra Synchrotron facility located near Trieste, using the SYRMEP BeamLine. Spatial resolution of the detector installed in this lab is 9µm. With this resolution, it is possible to obtain an experimental set-up on SYRMEP Lab suitable for Micro-CT, in agreement with the limit of 50 – 100 µm (60) of the spatial resolution beyond which the slices obtained are defined as a CT.

The SYRMEP beamline is organised on two level, on the first floor there is the control room (Figure 35) where it is possible to govern the projections acquisition and perform the reconstruction to obtain the slices of the material. In Figure 35 is possible to see the SYRMEP console where all beam's parameters can be controlled, in particular: setting beam's energy, managing monochromator filters, controlling the stability of the beam between each Micro-CT acquisition, calibrating the sample's vertical position at different vertical position for vertical combination of multiple scans. For the Micro-CT acquisition, it is possible to set the exposure time for each projection, the angular sector to scan, the position of the sample from the detector and, finally launch the acquisition. From the monitor it is possible to control the status of the acquisition, e.g. by controlling the rotation of the small shaft that connect the motor to the rotating table that supports the sample.

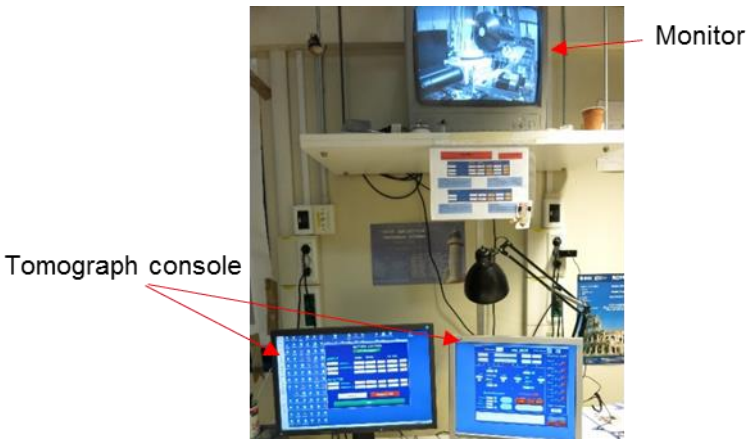

Figure 35: SYRMEP Control Room

At the ground floor, there is the Micro-Tomography set-up, where the devices are closed in a security room that is accessible only if the Beam-Shutter is closed to prevent any X-Ray absorption by the operator. For this, SYRMEP Lab is equipped with a security system that allows for entering in the room to position the sample, following a security procedure that prevent that the operator remains in the room or he opens the door before the X-Ray beam is turned off.

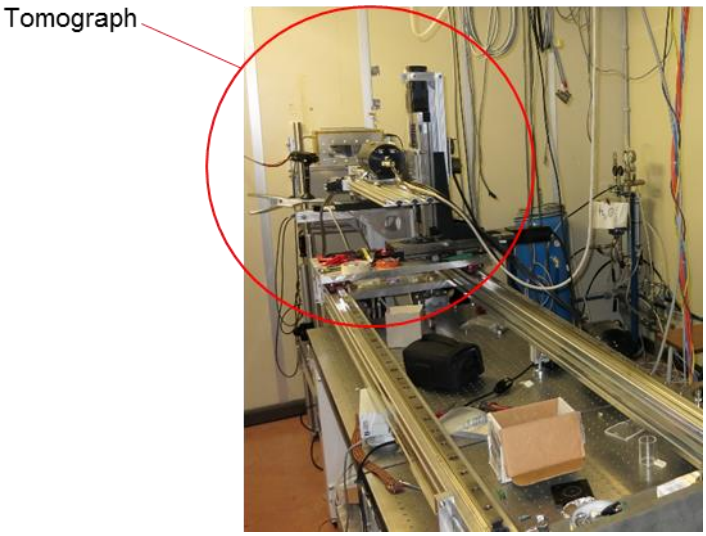

Figure 36: Tomograph Room at SYRMEP Lab

In Figure 36 shown is the room where all the X-Ray projections are acquired. Is possible to see the detector, two linear guide ways that allow to set the distance of the sample from the detector and from the X-Ray source and all the accessory devices to provide water, gases, electrical power, or signal acquisition.

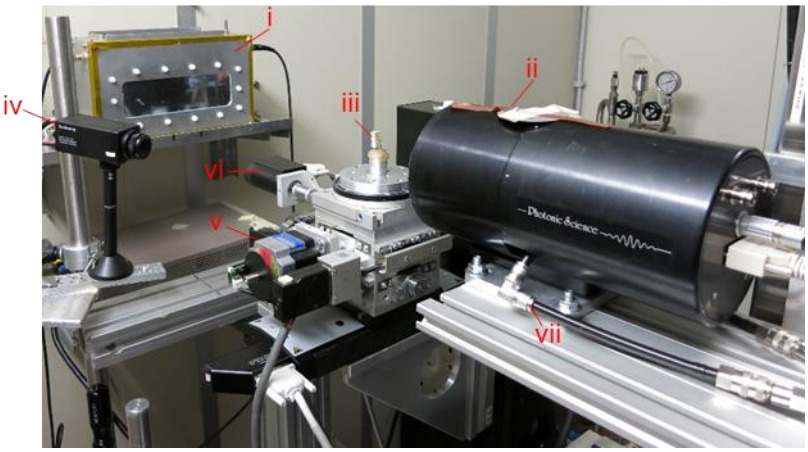

a

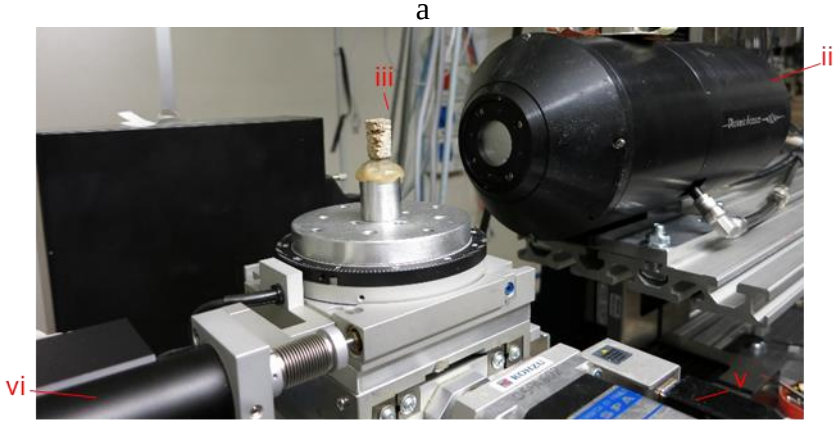

b

Figure 37: Micro-CT set-up. a) from X-Ray beam source; b) from detector

The X-Rays extracted from the Synchrotron Ring (Section 1.5.1) hits on a double-crystal SI111 Monochromator and reaches the sample placed on the rotating table inside the Tomograph room. Figure 37 shows in detail the Micro-CT experimental set-up of SYRMEP BeamLine used in this PhD thesis to acquire the projections of the specimen and combining them by reconstruction to obtain the slices of the material's volume. Observing Figure 37a and Figure 37b and comparing them with Figure 26 that describe a general set-up for Micro-CT in absorption mode, it is possible to find the same components. In Figure 37 is possible to recognize:

- *i* the collimator that produces a flat beam of 120 x 4mm^2. It is considered as the X-Ray Source.
- *ii* the CCD Photonic Science XDI-VHR 1:2 detector based on a cooled charge-coupled device camera of 4008 x 2672 pixels and a Gadolinium Oxysulphide scintillator placed on a straight fibre optic coupler. As cited before, the maximum spatial resolution achievable using this detector is equal to 9µm.
- *iii* the particleboard sample 10 x 10 x 18mm positioned on a rotating table using malleable wax.
- *iv* the observation camera connected to the monitor shown in Figure 35.
- *v* postioning system: horizontal axis motor (Y coordinate, see Figure 38). The movement of the rotating table is orthogonal compared to the X-Ray beam direction (X dir., see Figure 38).
- *vi* positioning system: rotating motor. This motor rotates the worktable around Z coordinate, see Figure 38
- *vii* cooling system of the detector.

Particleboard samples were mounted on the rotating table of the tomograph in the center of the baseplate, on a small aluminum stand, bonded using malleable wax. The rotation axis Z of the sample is parallel to the through thickness direction of the particleboard (in this case of 18mm thickness (see Figure 38).

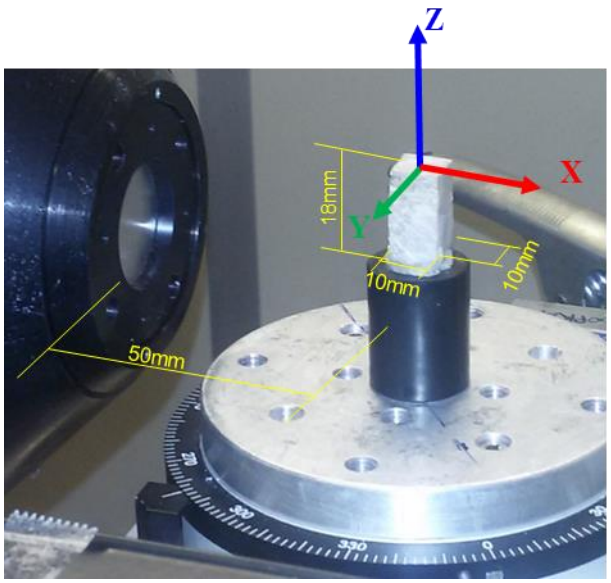

Figure 38: Particleboard sample mounted on rotating table of the tomograph

The particleboard's thickness that the X-Ray beam must be cross, is equal to 10mm when the sample is parallel to the sensor, exactly the position represented in Figure 38. When the rotating table reaches an angle equal to 45°, the thickness crossed from the beam, is the diagonal length equal to $10\sqrt{2}$ mm. To select the proper beam energy, many attempts was made reaching a good compromise on the contrast on the particleboard's projection when it is parallel to the sensor or orthogonal. The beam energy is set equal to 15 keV. To perform Micro-CT imaging, the absorption mode was selected imposing the distance between the centre of the sample and the surface's detector equal to 5cm, see Figure 38.

The detector's field of view is 6mm high and 16mm wide. Therefore, having the particleboard's sample thickness equal to 18mm, it is not possible to frame it in one shot. To observe completely the specimen, I made four Micro-CT of the same sample, displacing it along the Z direction (see, Figure 38) with $\Delta Z = 5.5$mm and imposing a proper overlap between each sector (Figure 39). Finally, the angular sector to complete one Micro-CT, on which every sample's projection is acquired at 0.1°, was set equal to 180°, for a total number of particleboard's projections equal to 1800. The exposure time was set to 1.001 seconds.

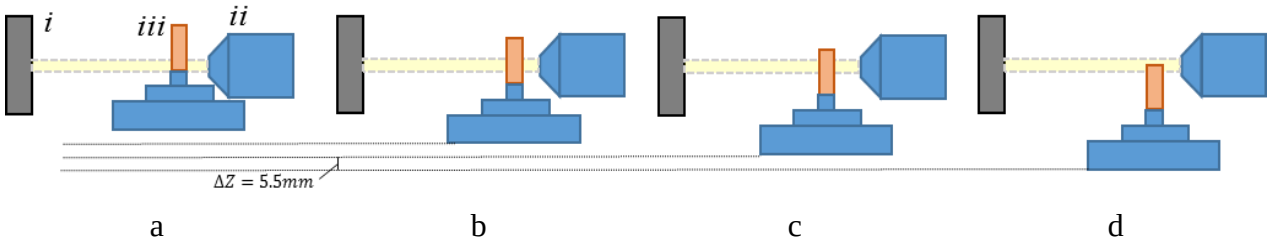

Figure 39: different sections of the same particleboard's sample (iii). a); b); c); d) sample's sections acquired applying vertical displacement (Z direction) equal to 5.5mm to reach entire volume reconstructed

The preparation of the specimens before the acquisition is very important. The samples were prepared in agreement with the need of performing qualitative image analysis to recognise the constituents (wood particle, adhesive and impurities) and to perform quantitative analysis of the Micro-CT, to determine the VDP of the particleboard. To perform qualitative characterization of the microstructure of the particleboard and try to visualise the adhesive dispersion inside of sample's volume, I scanned 10 x 10 x 18 mm samples extracted from three types of particleboard listed in Table 14, each with different quantities of urea-formaldehyde adhesive based mixed with 1% of titanium dioxide. TiO_2 was added as contrast agent, increasing the mass absorption coefficient (μ/ρ) of the adhesive. The sample named "Reference" correspond to the material with adhesive quantity and formulation equal to the commercial one; it was considered to perform the quantitative VDP estimation.

Table 14: Types of particleboard samples scanned with Micro-CT technique.

Type	***Adhesive quantities***	***% TiO_2 Tracker***
Normal	75 kg/m^3	1%
Full	80 kg/m^3	1%
Reference	75 kg/m^3	--

The particleboard's samples were extracted from the main boards (Figure 40a), using mechanical separation by band saw as shown in Figure 40b. The specimens produced in this manner were ready to be scanned and were extracted from the centre of the main board of 18mm of thickness and 1860mm width and 3860mm length to ensure that possible edge effects, like deviations form nominal density, were negligible (Figure 40a). This sample's extraction, performed to estimate the VDP, was accomplished knowing that the density is reasonably invariant along the board width. The observation comes from the production process of the particleboard presented in Chapter 1, where the forming step is carried out deposing in an equal manner the particles across the board width. Then, it is reasonable to suppose that the vertical density profile of the sample extracted from the center of the main board, is very similar to that estimated from a sample extracted from another point across the board width, of course far from the external edge.

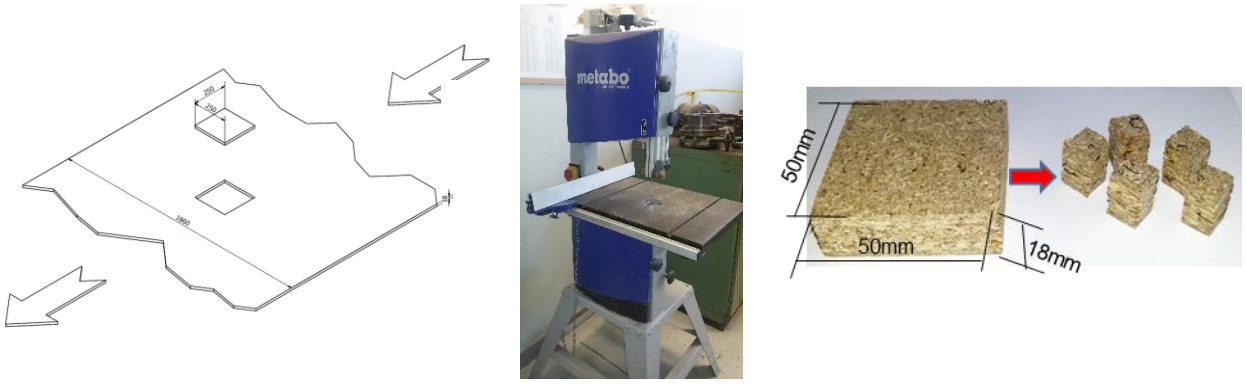

a b c

Figure 40: Particleboard's samples extraction. a) Sample's extraction from the main board; b) Band saw; c) from the center of particleboard 1860 wide and 3860mm long, small squared pieces of 50mm of side are cut and then reduced in to specimens of 10 x 10 x 18 mm

The samples of different types (see Table 14), were prepared in the laboratory at environment temperature equal to 23°C but relative humidity unknown, and therefore the moisture content of the samples was unknown. This information was obtained after the Micro-CT experiment, therefore it was important that the humidity content did not change during the scan, transportation and handling. To prevent any humidity change, after the mechanical separation the samples were closed in a hermetic bag sealed by thermosealer (Figure 41a). Before starting the Micro-CT acquisitions, the particleboard's samples were wrapped in parafilm tape (Figure 41b), a paraffin-based material "transparent" to the X-Ray beam, to seal the samples and to protect them from the environment humidity and prevent moisture variation of the specimens (Figure 41c).

Knowledge of the moisture content of the samples scanned with Micro-CT technique is crucial for further comparison and development. However, since all the particleboard samples tested in this thesis were stocked and tested in the same laboratory, it is reasonable to suppose that the humidity content was the same for the all the samples, particularly those prepared for Three Point Bending Test and Iosipescu Test (see the next Chapters). It is therefore possible to affirm that the elastic constants thus determined, are referred to the moisture content determined here.

As it will be described later, to perform quantitative image analysis using Micro-CT to determine the VDP of the particleboard it is necessary to analyze different reference materials of known density and composition. This allows for associating the grey levels of the reconstructed slices of the reference materials with their density and derive a relationship between gray levels and density. Thus, using this relationship, it will be possible to determine the particleboard's density measuring its grey levels.

a b c

Figure 41: a) Thermo-sealer and hermetic bags; b) Parafilm tape (81)*; c) Particleboard's sample sealed by Parafilm tape.*

The density of the reference materials to be selected must fall in the range of the expected values of the density of the constituents of the material to be analysed. Knowing that the particleboard's mean density is equal to 700 kg/m^3 (26), the reference materials used in this thesis available in the Synchrotron Laboratory are distilled water (H_2O density of 1000 kg/m^3, glycerol ($C_3H_8O_3$ density of 1261 kg/m^3 and acetone (C_3H_6O density of 789.9 kg/m^3) (66) . They were put into three small plastic tubes of 0.5ml of volume and scanned in the same condition of the particleboard's samples Figure 42

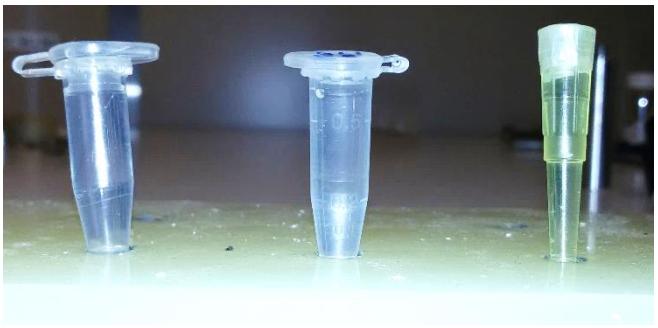

a b c

Figure 42: Reference materials. a) Aceton; b) Distilled water; c) Glycerol

Table 15 lists the reference materials characteristics and report the absorption coefficients for a beam energy of 15 keV. The variation of the absorption coefficients as a function of the beam energy in the neighborhood 15 keV is shown in Figure 43. It is possible to observe that there isn't any discontinuity compared to the metals reported in Figure 25, in particular for values of the beam energy close to that used in Micro-CT acquisitions of particlewood. This fact is desirable to prevent indetermination of the absorption coefficient at a certain beam energy.

Table 15: Reference material characteristics. μ coefficient are obtain from XMuDat database (66) *at beam-energy equal to 15 keV.*

Name	***Density [g/cm³]***	***μ [1/cm]***	***μ/ρ [cm²/g]***
Distilled Water	1	1.67	1.67
Glycerol	1.26	1.65	1.31
Aceton	0.79	0.83	1.05

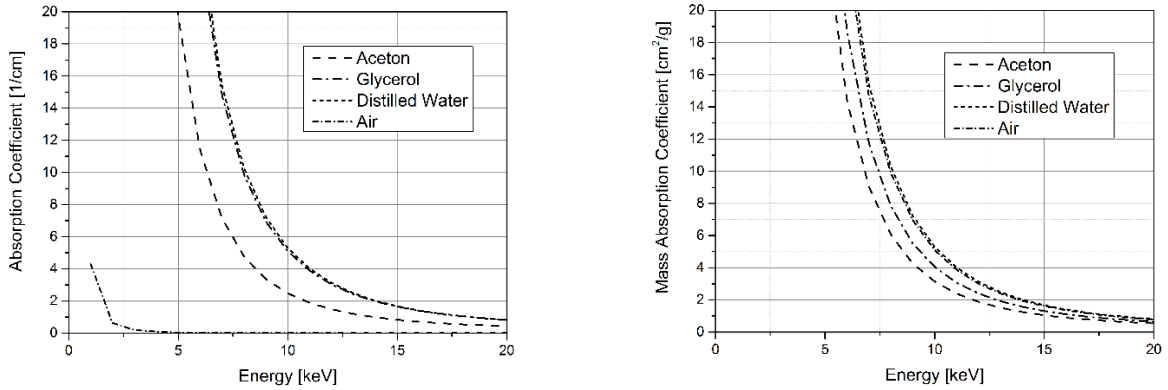

a b

Figure 43: a) Absorption coefficients of the reference materials; b) Mass absorption coefficient of the reference materials

After describing the preparation of the all particleboard's samples and reference materials tubes, I report here the procedure followed to launch the Micro-CT acquisition to get the X-Ray projection of different materials. The procedure is divided into the following steps:

1) Positioning the sample of particleboard on the rotating table of the tomograph, modelling the wax to ensure a vertical position (see Figure 38).
2) Close the tomograph room and give the consent to open the beam shutter.
3) Acquire ten dark images before starting the Micro-CT to reduce the noise on reconstructed slices. The reconstruction algorithm automatically performs this de-noising procedure (Figure 44a).
4) Open the beam shutter.
5) Acquire ten flat images, as reported in Figure 44b before starting the Micro-CT to reduce the noise (similar to the step 3)

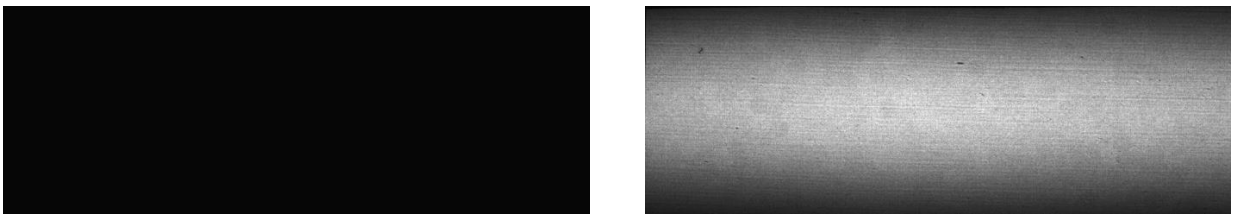

a b

Figure 44: de-noising images. a) Dark image; b) Flat image

6) Displace upward (Z direction, see Figure 38) the rotating table to the first height, to scan the first sector of the particleboard's sample.
7) Acquiring a test image to control that the specimen is correctly framed inside the detector's field of view (Figure 45).

Figure 45: Test image to control the sample position

8) Provide a connection between the rotating table's motor and detector's exposure time to assure the synchronism between them.
9) Launch the Micro-CT acquisition.
10) Move down (Z direction, see Figure 38) the rotating table until the sample is out of the field of view.
11) Acquire ten post-flat images to reduce the noise on the reconstructed slice (similar to step 3 and 4).
12) Close the beam shutter.
13) Acquire ten post dark images (similar to step 3, 4 and 11).
14) At this time it is possible to change the sample or repeat the procedure except Step 1 and 2 to scan another sample's sector, positioning at the suitable height the sample ($\Delta Z = 5.5mm$).

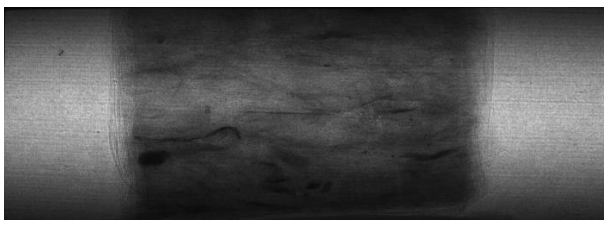

a

b

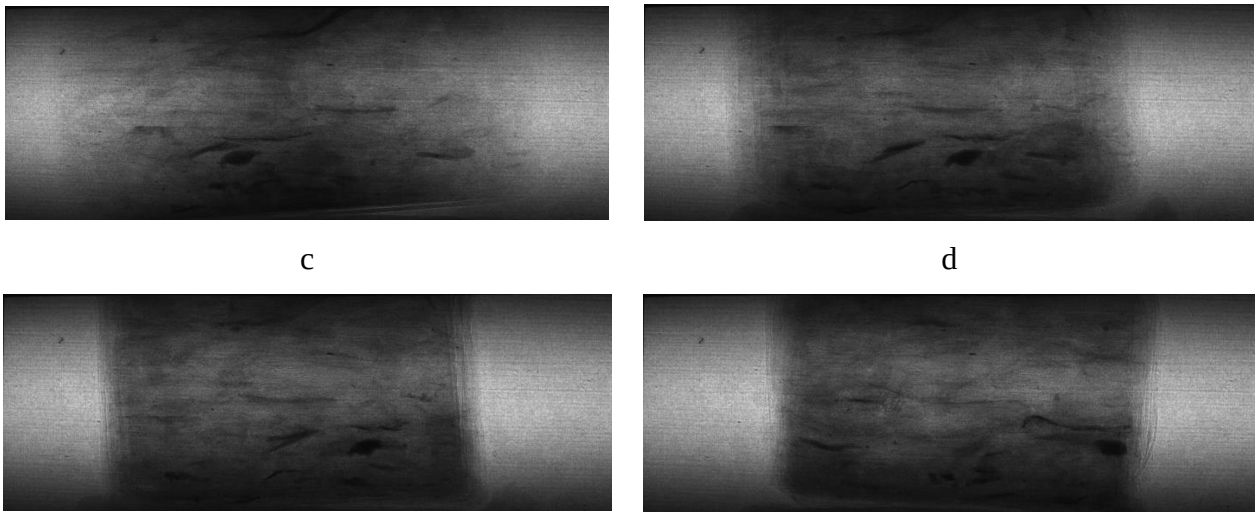

Figure 46: Particleboard's projections acquired during Micro-CT scan ($\Delta\theta = 0.1°$) from a sample with reference adhesive quantity and composition (Table 14). a) Projection number 1 ($\theta = 0°$); b) Projection number 300 ($\theta = 30°$); c) Projection number 450 ($\theta = 45°$); d) Projection number 750 ($\theta = 75°$); e) Projection number 900 ($\theta = 90°$); f) Projection number 1800 ($\theta = 180°$).

Figure 46 shows different projections of particleboard's sample with adhesive quantity equal to 75kg/m^3 and without any contrast agent. Figure 47 shows the projections of the reference materials selected to perform quantitative analysis of Micro-CT to determine the particleboard vertical density. Observing Table 15, distilled water, glycerol and acetone have μ/ρ coefficient equal to 1.67cm^2/g; 1.65cm^2/g and 0.83 cm^2/g, respectively. As expected, the material with higher mass absorption coefficients (distilled water and glycerol) produces darker zone than the one with lower coefficient (aceton).

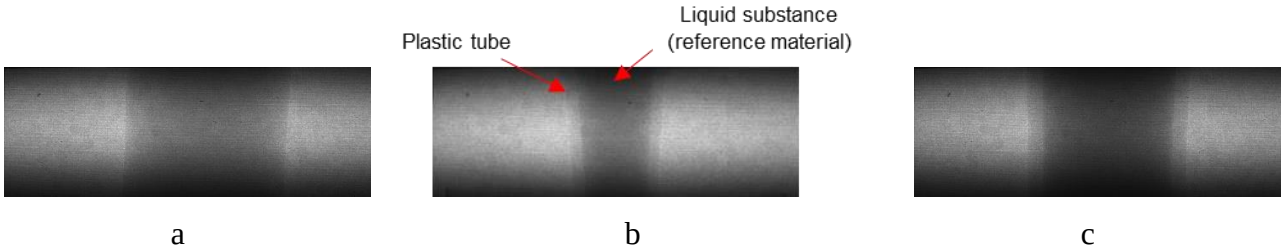

Figure 47: Reference materials projections. a) Aceton; b) Water; c) Glycerol

The total number of samples scanned by Micro-CT techniques was eight for particleboard and three reference materials (Figure 47). In particular, four particleboard's specimens with adhesive quantity equal to 80kg/m^3 ("Full" sample) tracked with 1% of TiO_2 and two particleboard's specimen with 75kg/m^3 of urea-formaldehyde adhesive based and 1% of TiO_2 as a contrast agent ("Normal" specimen). Moreover, two particleboard's specimens, named "Reference", with 75 kg/m^3 without any contrast agent.

In order to perform the reconstructions, 54000 projections of all samples had to be processed, to obtain the slices of the particleboard's samples and the reference materials. In this thesis, I do describe the reconstruction algorithm used, but I'm showing the results of Micro-CT and I will use that results to characterise the particleboard microstructure and by quantitative analysis, determining the VDP of the particleboard. For any details of reconstruction algorithm, the interested reader may refer to (60).

2.3 Micro-CT qualitative image analysis: Particleboard microstructure and their constituents

The projections collected for all eight particleboard's samples and the three reference materials were processed using a software developed at Beam Line of Synchrotron that allows for reconstructing the Micro-CT slices. The software's name is *SYRMEP Tomo Project (STP)* and it has different advantages compared to other commercial software packages. In particular the STP software can be installed on common PCs equipped with SSD storage and GPU to perform reconstructions in a reasonable time, it is developed in IDL language, and the STP's GUI is written for Windows by Python scripts. The STP software performs the numerous image processing operations, pre- and post-reconstruction, like removal of imperfection and Micro-CT artifacts. STP is available at the SYRMEP Beam Line to all the users (82).

In general, the STP software works producing a single "volume" data file, (extension *tdf), containing both X-Ray projections and sinograms. The sinogram, shown in Figure 48, is one of the methods to represent all the projections of a Micro-CT for reconstructing a slice. Very briefly, it is a plot of the absorption data in each projections as a function of rotation angle (60).

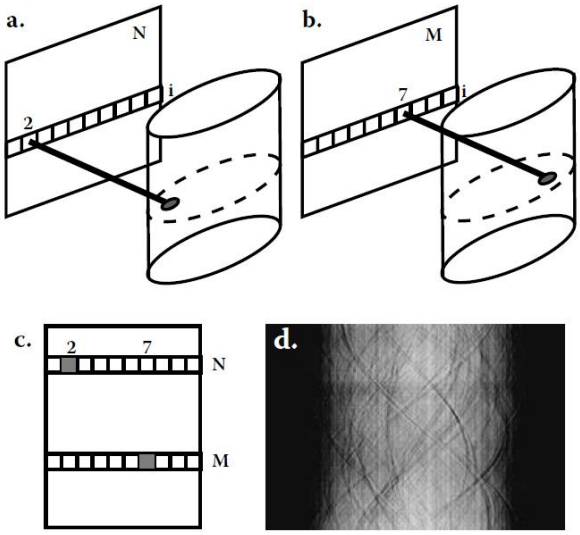

Figure 48: Sinograms principle (60).

Observing Figure 48a, the X-Ray projection *n* is a pixel matrix with a certain spatial resolution *b* x *h* produced by the detector during the exposure time. *b* and *h* are respectively the numbers of columns and rows forming the pixel matrix, which is the 2D image. On the n^{th} -projection, the position of the black feature in the cylindrical object is impressed on the i^{th} row at second column. After the rotation about the vertical axis (Figure 48b), a new projection *m* of the cylindrical object will be recorded. The black feature on *m*-projection will be still at i^{th} row but in the seventh column. The sinogram (Figure 48c and Figure 48d) is a 2D image with a number of rows equal to the number of the projection acquired (related to the angular steps), the columns are the successive absorption profile derived from projection *n, ……, m.* The slice will be reconstructed from each i^{th} row. The name "sinogram" is derived from the resulting sinusoidal path, as shown in Figure 48d.

The STP software, after creating the sinograms from the projections, can correct beam and detector imperfections, applying operations like flat fielding, hot/dead pixel correction, ring artifact removal and Field of View correction, and finally produce the single slice reconstructions (82). The resultant slices produced by STP software are 32-bit grey level scale files, suitable for quantitative image analysis, which can be converted into 8-bit grayscale files for qualitative analyses or for easier processing. All the Micro-CT images reconstructed using STP software at Synchrotron facility in Trieste were subsequently analyzed using FIJI Software, an open source platform normally dedicated to image analysis (83).

As proposed in Section 1.3 (Figure 11), and as reported in Figure 49, the particleboard with the thickness equal to 18mm has three density zones along the thickness direction, respectively two of high density (external particleboard's part defined as skins) and one of low density (central particleboard's part defined as core).

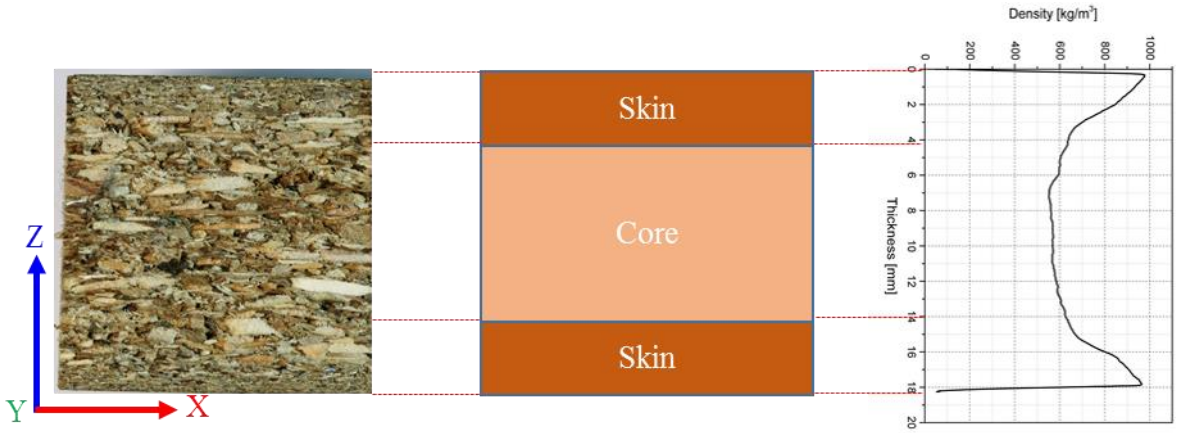

a b c

Figure 49: Density zones of the particleboard. a) 18mm particleboard thickness; b) Visualization of the high and low density zone to define the skins and core; c) 18mm particleboard density profile obtained by industrial measurements.

To understand the differences in the microstructure of the particleboard, in the next figures are shown for every particleboard's sample type, skins and core slices at different thickness levels (Z direction) with different quantities of adhesive and TiO_2 contrast agent. All samples have a nominal thickness equal to 18mm. To know the position through the thickness of the slice being visualised, it is necessary to calibrate the images knowing the dimension of the sample and number of pixel of the images, thus obtaining the calibration ratio *px/mm* . The sample's dimensions are reported in the next Section 2.5.1, where I measured the sample's density by gravimetric method. Figure 50 shows the 3D volume of the particleboard sample, obtained by staking the reconstructed slices. The sample is "Reference sample" with 75% of adhesive and no contrast agent. It is fundamental to underline that the following images, that are presented in this section, are adjusted varying the brightness/contrast only to better visualise the included features, while gray-level measurements, histograms and analysis were performed on the original images converted from 32-bit to 8bit.

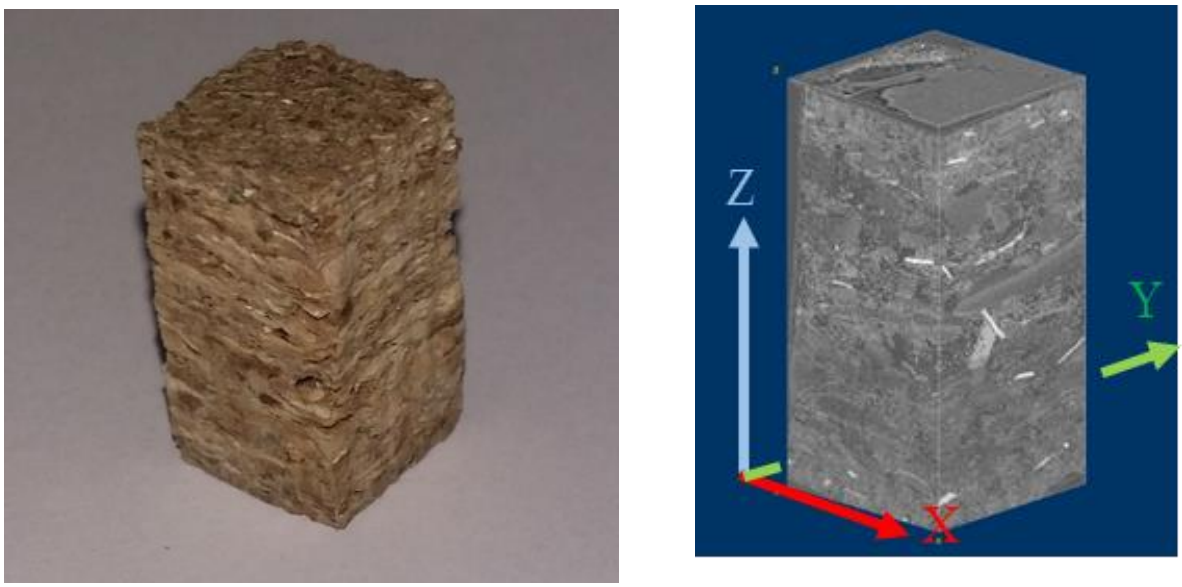

a b

Figure 50: Particleboard's volume reconstructed. a) Particleboard's sample ("Reference"); b) 3D Volume of particleboard from Micro-CT

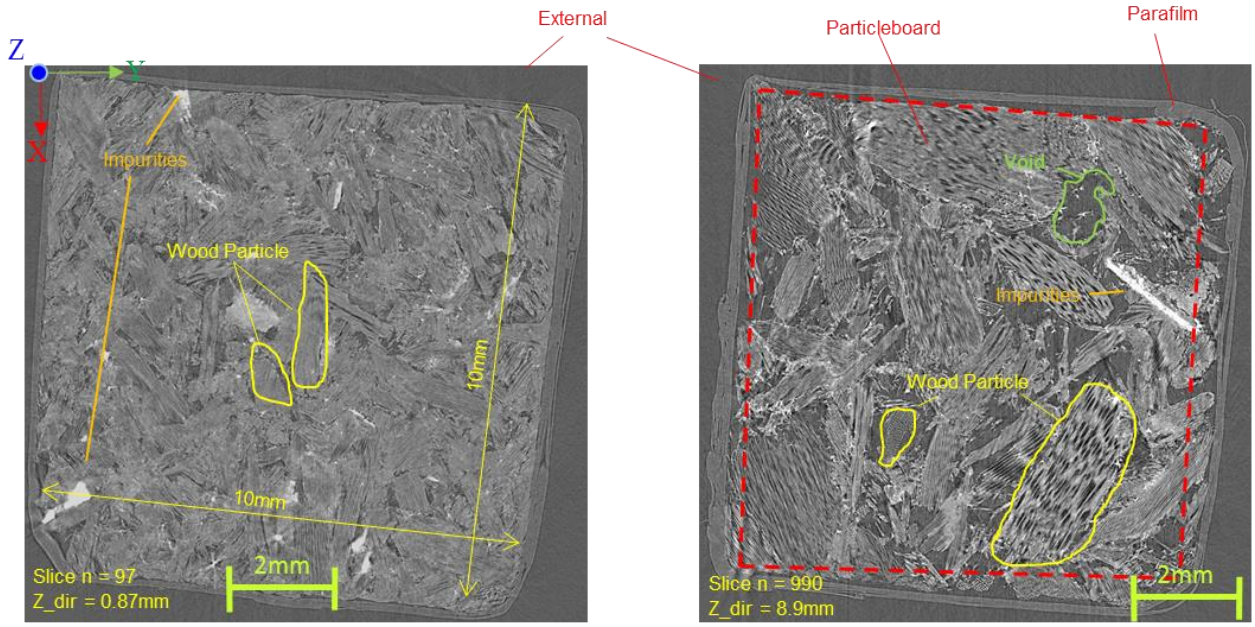

a b

Figure 51: 8-bit gray-level Particleboard's slices with adhesive content equal to 75 kg/m^3 and no tracker, it is defined as a "Reference Sample". a) Slice extracted from high-density zone at thickness level (Z-axis) of 0.87mm (Lower-Skin); b) Slice extracted from low-density zone at thickness level (Z-axis) equal to 8.9mm (Core) (5.5% Moisture Content).

Figure 51 shows two slices extracted from a 3D volume of the particleboard's sample defined as the "Reference sample" containing 75 kg/m^3 of adhesive and no TiO_2 as contrast agent. Observing both pictures in Figure 51, every particle that forms the sample is clearly visible, but the composition is unknown. In order to identify wood particles and distinguish them from impurities and the adhesive, it is necessary to compare the image of wood's microstructure within the particles observed in Figure 51 with the images of wood taken from the literature about this topic (having not scanned the specimens of solid wood during the beam time at Synchrotron). For example, in (84) the authors examined both hardwood (Scots pine sapwood) and softwood (beech) species to characterise the differences in their anatomical structures. The sample prepared in (84) has dimensions equal to 30mm x 5mm x 5mm and it was scanned by Micro-CT technique at 130keV of beam's energy for an exposure time of 2.3ms to reach a spatial resolution in the reconstructed slices equal to 10µm (Figure 52). Comparing the particle's structure extracted from Figure 51b with the image of beech wood of Figure 52i-A, the similarity with the cellular structure of the solid wood is clearly apparent, see Figure 53 where it is also possible to see the voids inside the wood's microstructure.

In a similar way, extracting a particle from a skin slice of Figure 51a, its microstructure appears to be similar to scots pine sapwood microstructure band studied in (84), as shown in Figure 54. These observations justify the fact that most the particles individuated on the slices are made of wood, although it is not possible define which kind of wood. Clearly, this comparison is qualitative, just to identify the wood structure of the particles dispersed in the particleboard. In fact, it is not possible to

match two gray-level images and compare the levels from acquisitions at different conditions as beam's parameters and energies.

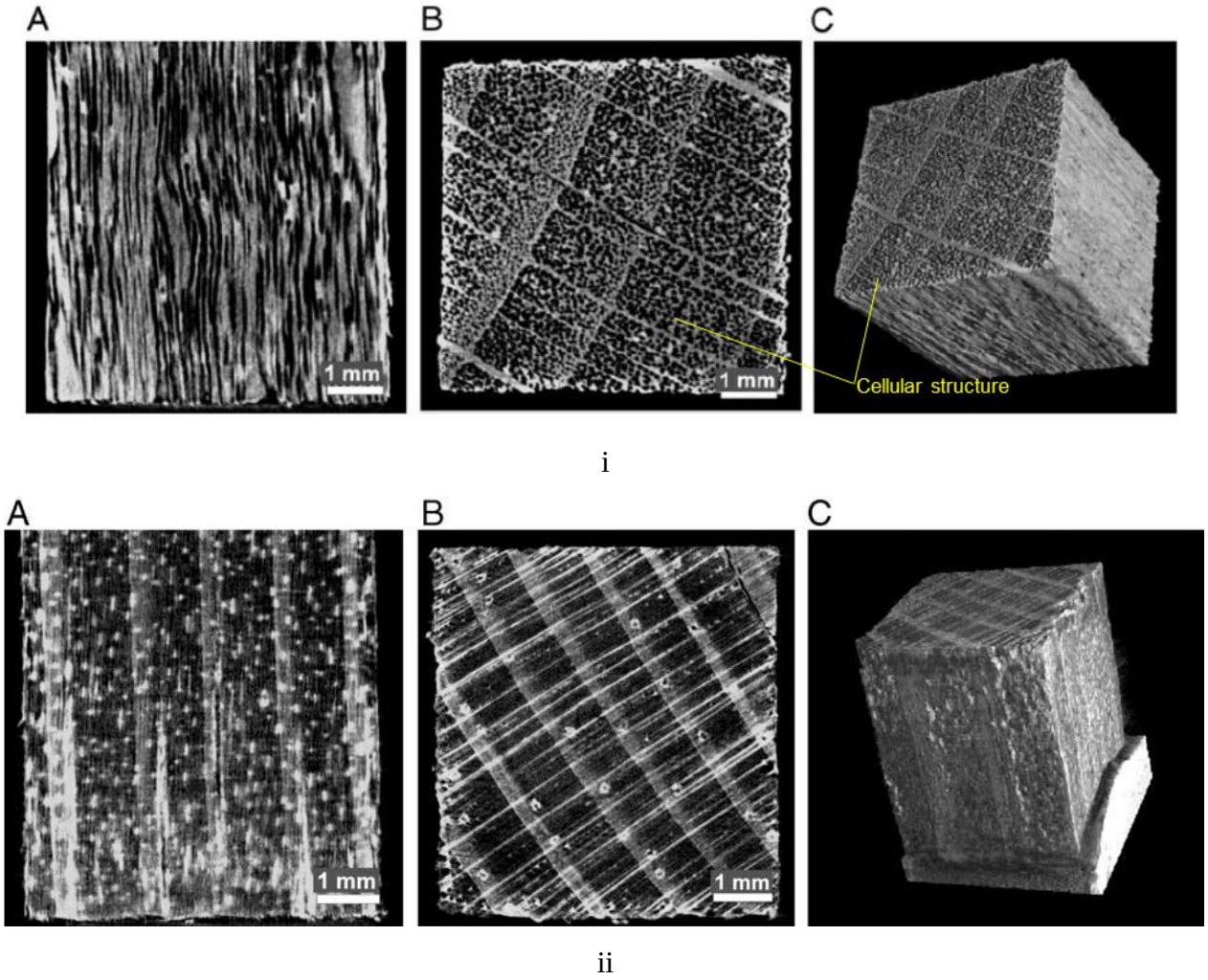

Figure 52: Micro-CT of Solid wood, in (i) the images refers to reconstruction of beech wood, in (ii) the image refers to the Scots pine's reconstructions. A) Longitudinal image, B) Transverse view, C) 3D view (84).

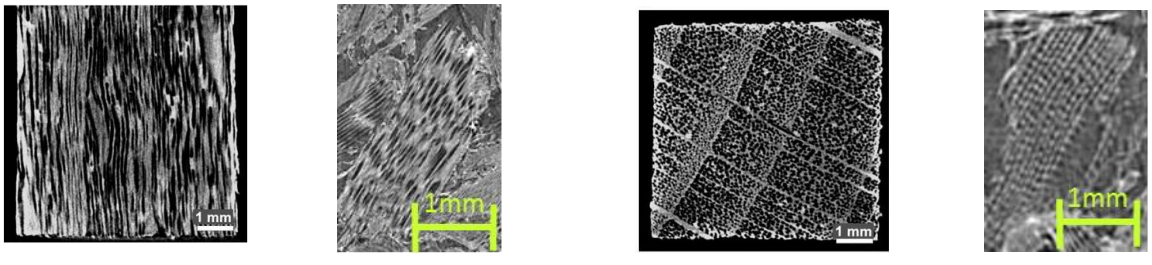

Figure 53: Particle wood characterization. a) beech wood in longitudinal view taken from literature (84)*; b) particle wood extracted from slice 990 of Reference sample (Figure 51b) from particleboard studied in this Thesis; c) beech wood in transverse view from literature(72); d) particle wood extracted from slice 990 of Reference sample from particleboard characterized in this Thesis (Figure 51b).*

a b

Figure 54: Particle wood characterization. a) Scots pine sapwood in transverse view (84)*; b) two particles wood extracted from slice 97 of Reference sample (Figure 51a).*

Moreover, using FIJI software it is possible to observe the gray-level histograms of the 8-bit image of a portion of it. Histogram plot counts the number of pixels with the same gray-level included in the range 0-256 for 8-bit images. In particular in the reconstructed slice, gray-level equal to 0 correspond to black colour (low density), otherwise gray-level equal to 256 is white colour (high density). By this, I studied the histograms of ten particles extracted from core's particleboard (two are reported in Figure 53b and Figure 53d, respectively) and I compared it with the particles extracted from skins reported in Figure 54b.

It is visible that the mean grey value is equal to 45.5 for the core's particle reported in Figure 53b, equal to 42.7 for the particle in Figure 53d and 42.1 in Figure 54b (see the histograms in Figure 55).

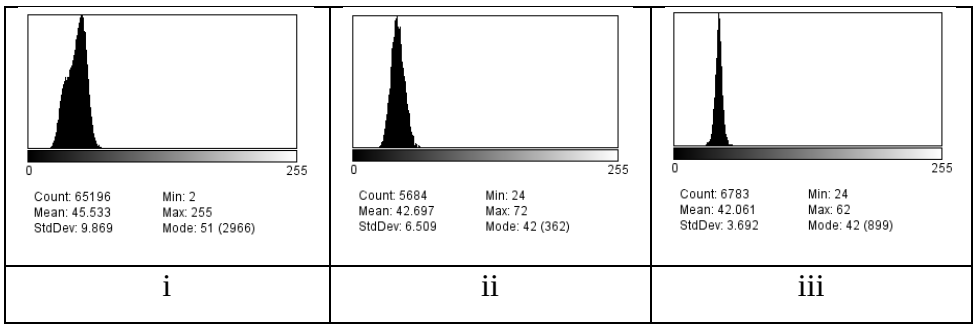

i ii iii

Figure 55: Histogram plots of the particle extracted from Figure 51. i); ii) Histogram of core's particle of Figure 53b and Figure 53d; iii) Histogram of skins particle wood of Figure 54b.

Observing the histogram plots in Figure 55, as an example of 20 histograms of the 10 particles extracted respectively from skin and core, the mean grey value is 41.3 for the skin's particles and 46.0 for the core's particles, with standard deviation respectively equal to 1.1 and 1.9. As expected, the mean gray value of the particles extracted from skin and core are similar, being the material of the same species (wood). However is possible to see an increment of the standard deviation from skin to core. It is reasonable to suppose that this increment of histogram's dispersions (standard deviation) for the core's particles compared to the skin's particles is due to the more accentuated wood cellular structure. About this, it is possible to assume that particle wood gray-level is in the range of 41 – 46

in the particleboard' slices obtained at beam energy of 15keV. All the particles with grey level outside this range, are likely not to be wood, but other materials. Considering the manufacturing process of particleboard explained in Chapter 1, features visible in the slices with higher grey level can be urea-formaldehyde adhesive, sand, paper or metals. This assumption can be made only in a qualitative manner (as reported in the next of this Chapter) because evaluating gray-scale images obtained by the energy of the beam not calibrated to observe this particular material, can be useless. The particles with lower absorption coefficient will appear as a saturated white and particles with higher absorption coefficient will be black, hiding the real characteristics gray-levels.

Considering now the particles dimensions in the slices of Figure 51, it is possible to see that the higher density of the skins, visible in the vertical density profile of Figure 49, is related to the high number of small particles closer to each other with a very low number of empty spaces between them (Figure 51a). Conversely, lower density in the core corresponds to the low number of big particles distant to each other that generates empty spaces between them (Figure 51b).

It is interesting for the developments presented in the next Chapters to consider the particle's distribution observed in these slices from core or skins, with respect to the forming process of the panel. As presented in Chapter 1, in the section dedicated to the particleboard production process, before the pressing phase, the particles are dropped on the transportation tape from the forming machine (Figure 7). By gravity, the single particles fall down in their natural position parallel to their longitudinal direction equal to the major particle's length. Thus, it is expected that the principal disposition of the particles inside of the particleboard is planar in the X-Y plane (X and Y are respectively panel lamination and transverse directions) and orthogonal to the thickness direction (Z-axis). Observing Figure 51 it is reasonable to conclude that this assumption is correct, as it appears that the majority of the particles are disposed parallel to the X-Y plane and orthogonal to Z direction, the thickness direction. In Chapter 4 this assumption will be verified further by analysing the particles orientation in the perspective of modelling the particleboard's microstructure.

To locate the adhesive and analyze its distribution, Micro-CT of the "Full Sample" are displayed in Figure 56, where the urea-formaldehyde adhesive quantities are equal to 80 kg/m^3 with 1% of TiO_2 as contrast agent.

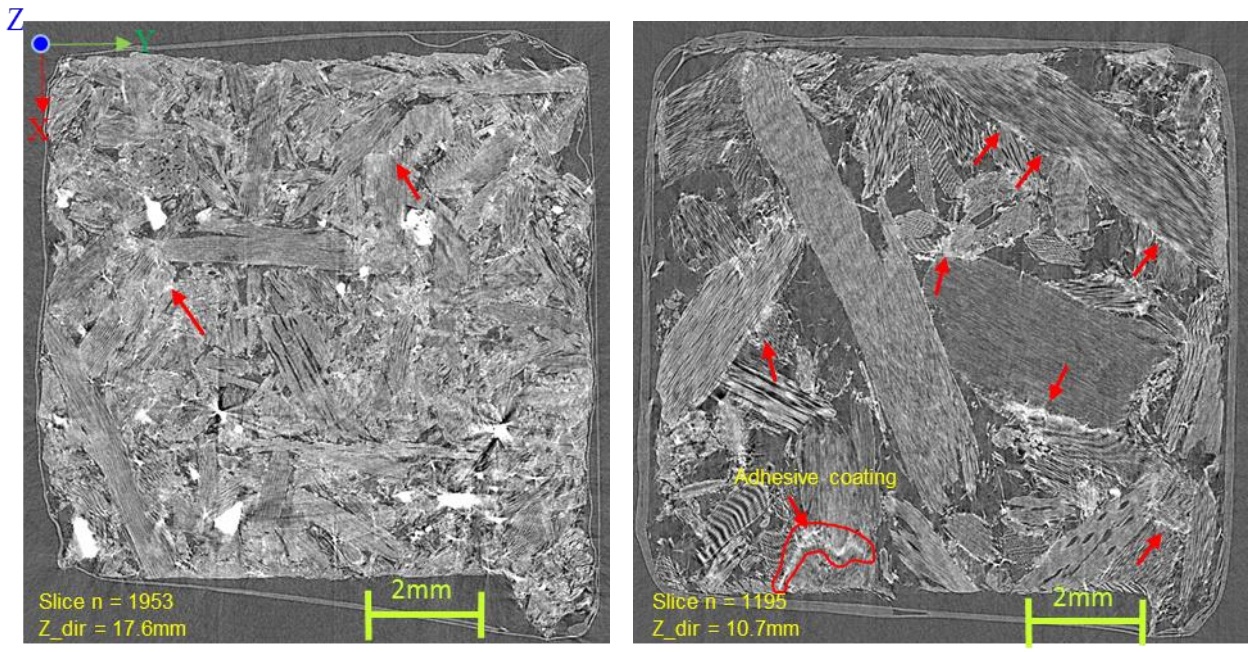

a b

Figure 56: 8-bit gray-level Particleboard's slices with adhesive content equal to 80 kg/m^3 and 1% of TiO_2 as contrast agent, it is defined as a "Full Sample". a) Slice extracted from high-density zone at thickness level (Z-axis) of 17.6mm (Upper-Skin); b) Slice extracted from low-density zone at thickness level (Z-axis) equal to 10.7mm (Core)

Although the exact composition of urea-formaldehyde adhesive and the species of woods in the sample are unknown, mixing the adhesive with a chemical compound as a contrast agent derived from titanium (TiO_2), produce an absorption of X-Ray beam of the mixture greater than that of the same adhesive without any contrast agent. In the reconstructed slices, it is expected that the mixture between adhesive and contrast agent will be visualised with higher gray-level, near to white . To try to characterise the adhesive distribution, it is useful observing the particleboard's production process, in particular during the adhesive spreading phase (Section 1.2.6), where the urea-formaldehyde in liquid solution is nebulized over the particles. Then, it is reasonable to suppose that part of adhesive remains on the particle's surface and only few is absorbed. By this observation, in Figure 56a, but better in Figure 56b, it is possible to see the particle's contour with higher gray-level, as an outer shell. Most likely, these high grey-level shells around the particles can be considered as adhesive (red arrows in Figure 56).

I measured the gray-level around the particles, considering the small portion highlighted in Figure 56b. As expected, Figure 57 reports a mean grey value of the selected zone equal to 48, measured over 3035 pixels. Using this grey value, I separated the adhesive from the particles imposing a threshold. Threshold algorithm produces a binary image from the slice selected, where all the pixels within the gray-level limits are converted into black pixels, as all the others pixels with gray values outside the limits are converted in white pixels. I selected the lower threshold limit equal

to 47 and the upper threshold limit equal to 49. In this manner the identified gray-level equal to 48, supposed to be the gray-level of the adhesive, falls in the middle of the range of interest.

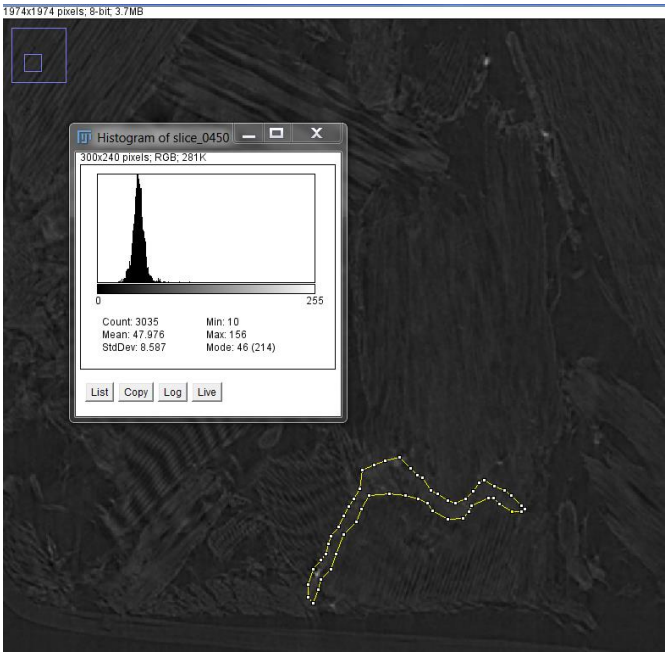

Figure 57: Adhesive gray-level quantification

Figure 58a reports the image with pixels with a grey level falling within the threshold limits and Figure 58b is the same image in binary mode, where the small black points are supposed to represent the urea-formaldehyde adhesive. Considering in particular Figure 58b, it is possible infer that part of adhesive is around the particles and part of it is absorbed in capillary channels of the particles, especially in the case of softwood, which is more permeable than the hardwood, because of o its cellular microstructure (indicated by the red contour and the arrows in Figure 58). These observations are in agreement with the literature (85), where the authors performed Micro-CT image analysis on particleboard's sample of 12mm x 12mm x 19mm made of Radiata pine bonded by melamine-urea-formaldehyde (MUF), whose contrast was enhanced by copper sulphate at 1.7% of weight. In that case, the Micro-CT was performed using a commercial scanner equipped with a X-Ray source of 40kV beam energy and a filament current equal to 200mA, reaching a spatial resolution equal to 2μm. Figure 59 reports the adhesive distribution mainly around the particles.

It is important to underline that it would have been better to scan by Micro-CT a small quantity of Urea Formaldehyde. However, the supply time of the substance and safety requirements were not compatible with the scheduled program at Synchrotron Facility.

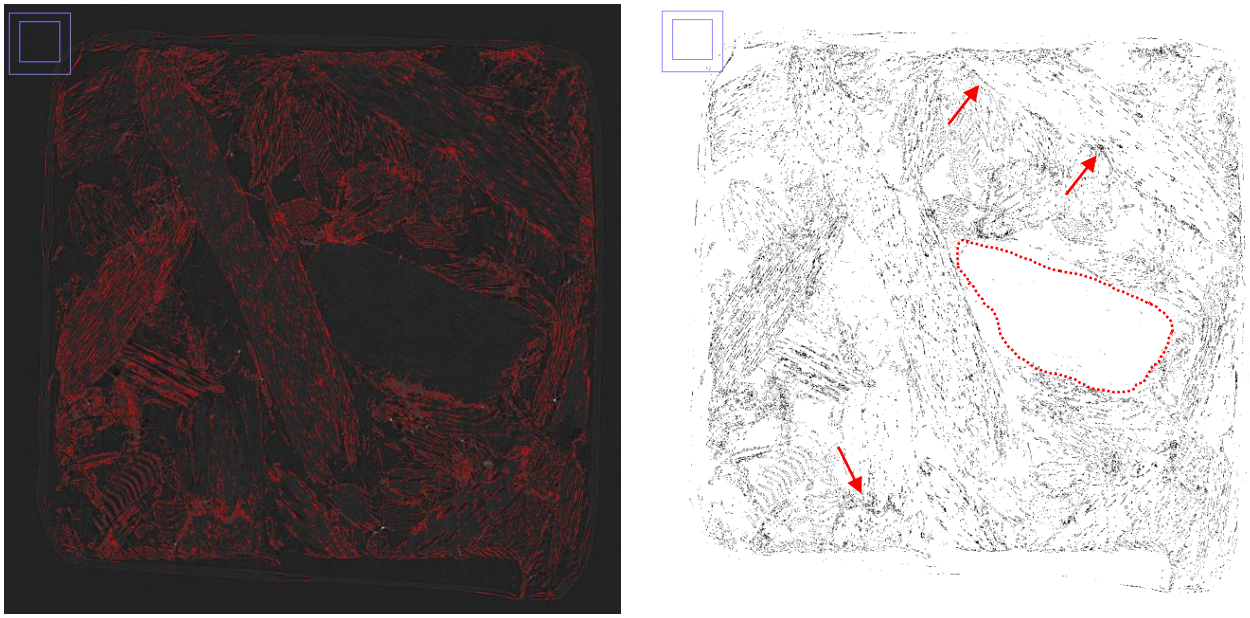

a b

Figure 58: Thresholding procedure to isolate the adhesive coating. a) 2D image with pixels with gray-value between 47 and 49; b) binary image after thresholding

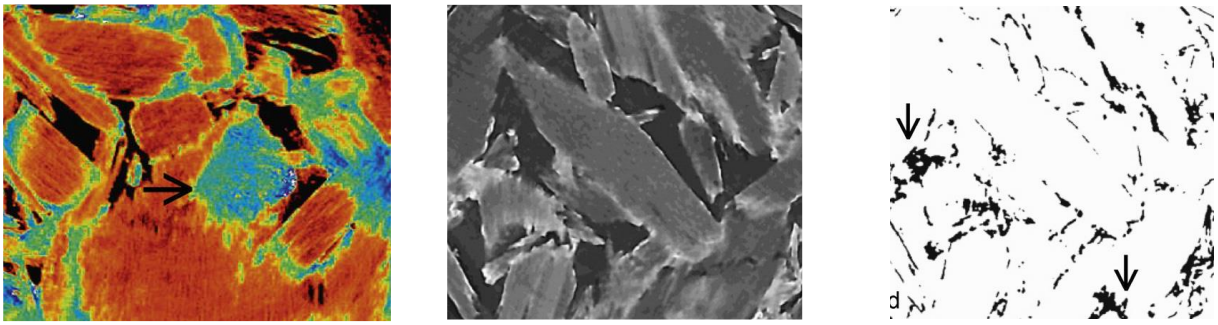

a b c

Figure 59: Adhesive distribution from particleboard's Micro-CT made of radiata pine (85)*. a) Accumulation of adhesive around small wood's particle; b) Radiata pine particleboard's slice with tracked adhesive; c) Binary image that highlight the adhesive distribution around the particles and in capillary channels between the particles (black arrows)* (85)*.*

Concluding this section, the qualitative image analysis performed using Micro-CT images allowed for the identification of the particleboard components, assuming that the most of the features visualized in the slices are effectively originated from wood. This assumption is supported by the comparison of the particles' microstructure with that of solid wood. Partial conclusions are listed below:

- The gray-level of particlewood is around 41 – 46. Others particles outside this range, are likely not to be wood and are considered as impurities or adhesive. These impurities can be metals, paper, sand, or small stones, deriving from the wood recycling process.
- The standard deviation of the gray level measured for the particles extracted from the core is higher than the skin's particles probably due to the more accentuated cellular structure. The

standard deviation values are respectively 1.1 for the skin's particles and 1.9 for the core's particles.

- Orientation distribution of the particles is principally planar, parallel to the X-Y plane (see Figure 38). This assumption will be verified in Chapter 4 during the micro-modelling procedures.

Next step will focus on the quantitative image analysis, to measure the particleboard vertical density profile by Micro-CT images, being the density the most important physical quantity, from which depend the elastic modulus and the bending performances. Density will be used to macro and micro model the panel of 18mm of thickness.

2.4 Micro-CT quantitative image analysis: Particleboard's Vertical Density Profile estimation

2.4.1 Particleboard's moisture content determination

Due to the hygroscopic behaviour of wooden materials, in order to obtain reliable results from quantitative Micro-CT imaging, it is necessary to determine the moisture content of the sample scanned. This was done after micro-CT. To keep the moisture of the samples unchanged before and during micro-CT, samples were sealed using hermetic bags and using Parafilm during the scan (see Figure 41). To determine the moisture content, I followed the standard (86). The dimensions of the sample prescribed in the standard are not in agreement with 10 x 10 x 18mm observed by Micro-CT, but these dimensions are fixed by the field of view of the detector. The procedure requires that the sample is put into an oven at the temperature of 103±2°C and its weight is monitored until a constant weight is reached. The set-up is composed of a precision scale with resolution equal to 0.01g shown in Figure 60a, an oven controlled by a thermostat with resolution equal to 1°C represented in Figure 60b and a Silica Gel Dryer to transport the samples from the oven to balance station shown in Figure 60c.

a b c

Figure 60: Set-up used to determine the moisture content of the particleboard. a) Scale; b) Oven; c) Dryer

The procedure followed consists of the following steps:

1) Turn on the oven, set the temperature to 103°C and wait for the thermal equilibrium
2) Prepare the dryer using regenerated silica gel
3) Weight the sample before drying
4) Put the sample in the oven
5) Wait at least 6 hours between two weights.
6) Remove rapidly the samples from the oven and put them in the dryer to wait for the sample's cooling

7) Weight the sample for the second time
8) Repeat the procedure until the sample's weight reach a constant value.

It took two days to complete the procedure. Results are reported in Table 16.

Table 16: Successive weightings

Time [h] **Sample's name**	**0** **P1 [g]**	**8.5** **P2 [g]**	**23.5** **P3 [g]**	**33** **P4[g]**
Full 1	1.15	1.10	1.10	1.07
Full 2	1.11	1.06	1.05	1.05
Full 3	1.16	1.10	1.09	1.09
Full 4	1.12	1.07	1.07	1.07
Normal 1	0.95	0.90	0.90	0.90
Normal 2	0.95	0.90	0.90	0.90
Reference 1	1.17	1.11	1.11	1.11
Reference 2	1.10	1.05	1.05	1.05

The standard (86) prescribes that the constant weight between two successive weighting is reached when the variation is minor or equal to 0.1% compared to the sample's weight. The moisture content *H* expressed by percentage is determined using Eq. 24:

$$H = \frac{P1 - P_{last}}{P_{last}} * 100 \qquad \text{eq.24}$$

Where *P1* is the initial sample's weight and P_{last} is the last weight after the overall period in the oven. Table 17 reports the total percentage of sample's weight variation referred to *P1* corresponding to the moisture content for each sample. The mean value of moisture content at the moment of Micro-CT scan was equal to 5.5% of the sample's weights with a standard deviation equal to 0.2%.

Table 17: Particleboard's moisture content in percentage

Sample's name	**Total H[%]**
Full 1	5.4
Full 2	5.7
Full 3	5.6
Full 4	5.4
Normal 1	5.5
Normal 2	5.5
Reference 1	5.4
Reference 2	5
Mean	5.5
Std. Err.	0.071

2.4.2 Particleboard's Vertical Density Profile (VDP)

Before performing VDP measurements, a brief literature search was performed. The number of studies focusing on Micro-CT image analysis of particleboard it is very limited. In (85) Micro – CT was used to determine the adhesive distributions inside the volume and similary in (87) the authors visualised the adhesive distribution on the wood's microstructure by Micro-CT and optical microscopy. However, in both works the density of the materials are not measured using image analysis. The only works addressing this topic are focused on solid wood. In (88) the author calculated the absorption coefficient and the CT-Number (absorption coefficient normalization to the corresponding water's absorption) for both dry and wet wood. These two coefficients were used to find the relationship to the wood's density by linear regression. Ref. (89) reports the solid wood density determination by Micro-CT image analysis. The authors performed an image's calibration to associate the grey levels to the density of the wood. This calibration was performed knowing the absorption coefficient of known materials like cellulose, hemicellulose and lignin. The authors of (89) measured the absorption coefficient of the dry wood, considering the effect of the water content, finding a very good agreement between densities determined by Micro-CT analysis and by gravimetric method for eight wood species at three beam's energy levels. Similarly, in (90) the author evaluated the effect on the wood's density determination using a different scanner to acquire Micro-CT images. Another example is reported in (91), where the authors determined the wood density by quantitative image analysis after image calibration by specimens of known density.

In general, in Refs. (88) to (91), in order to calculate the density by image analysis, the authors performed image calibrations using specimens of known density covering the range of the density to be measured. In this manner, it is possible to associate the gray-level of the Micro-CT images directly to the material's density, which must be determined using absorption coefficient.

It is important to recall that the raw materials composing particleboard are various. There are many types of wood, urea-formaldehyde adhesive and a small parts, mainly to be considered impurities, like metals, sand, paper and tiny stones. To determine the particleboard's VDP, a similar calibration procedure like that presented before was performed. I used three materials of known density and I considered air as a fourth material. These materials, available at the Synchrotron Laboratory are Acetone, Glycerol and Distilled Water. This calibration procedure is normally adopted in the medical field as reported in (92), where the authors associate the grey level of reference materials to the absorption coefficient by a linear relationship. I performed the same procedure to calibrate the gray-levels of the particleboard's Micro-CT images.

The calibration starts reconstructing the projections of the three reference materials reported in Figure 42 to obtain the slices and the 3D volume. The atmosphere around the plastic tubes is also reconstructed and then it is possible to consider it as air (the fourth material). Reconstruction results are reported in Figure 61.

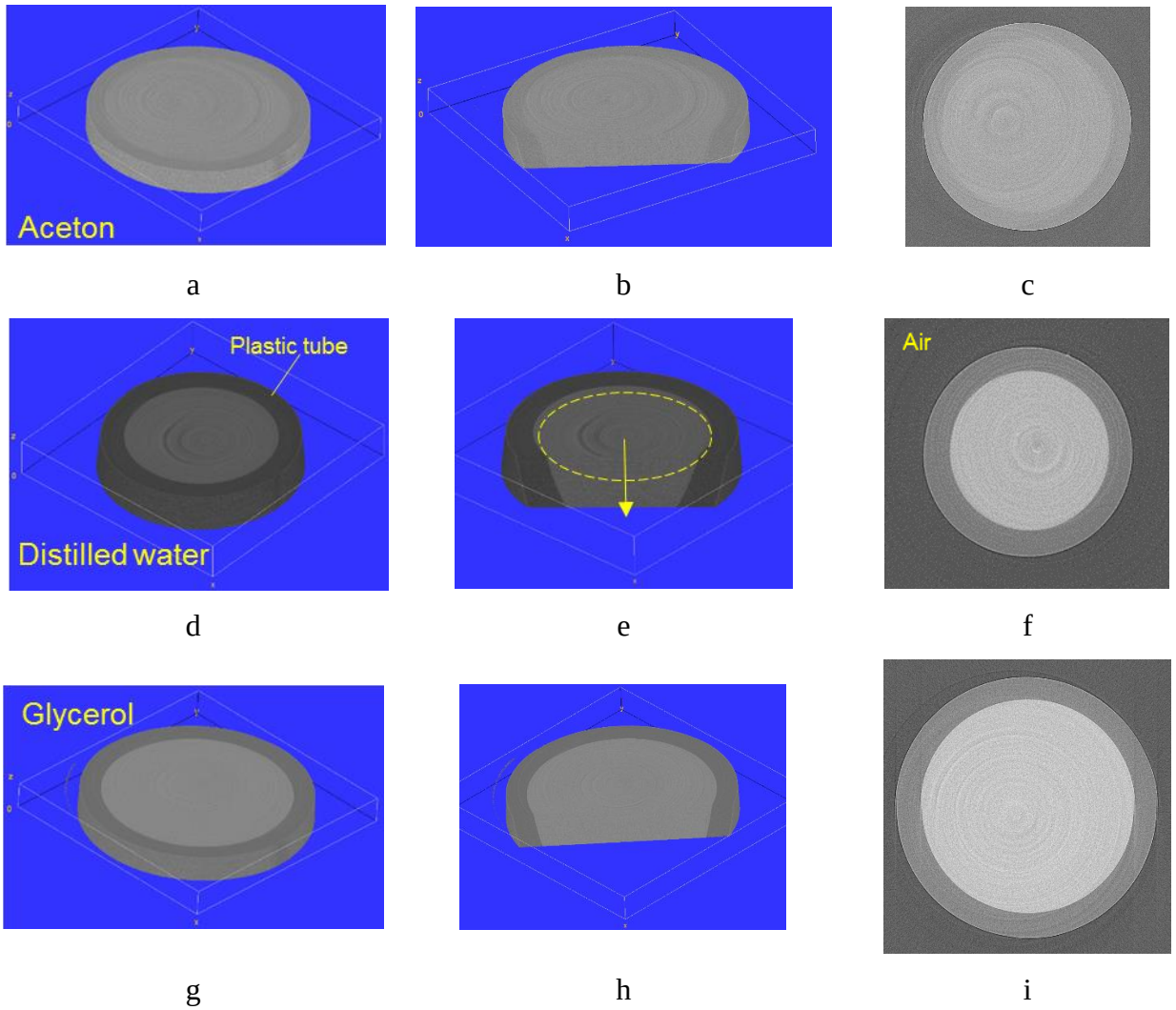

Figure 61: Three reference's materials reconstruction results. Staking 200 slices in the middle of the container's tube to obtain the 3D images. a) Aceton's 3D volume; b) 3D volume of aceton cut; c) 2D aceton's slice; d) distilled water's 3D volume; e) 3D volume of water cut; f) 2D water's slice; g) glycerol's 3D volume; h) 3D volume of glycerol cut; i) 2D Glycerol's slice.

To associate the gray-level of each reference material to its absorption coefficient, it is necessary to analyze the histogram and evaluate the mean grey value. This procedure was accomplished using FIJI in way similar to that presented before for qualitative particle's analysis. I isolated each reference material from the plastic tube by circular cropping (see Figure 61e) and evaluated the average grey values over the cropped area for every slice through the Z direction (see the yellow arrow in Figure 61e). The histograms for acetone, distilled water, glycerol and air, are shown in Figure 62 and the mean gray values are evaluated over 200 slices. It is interesting to check

if the grey value is constant across all slices. To do this, FIJI allows to plot a diagram named *Z-axis profile*, which represents the average gray value for every slice (see Figure 63).

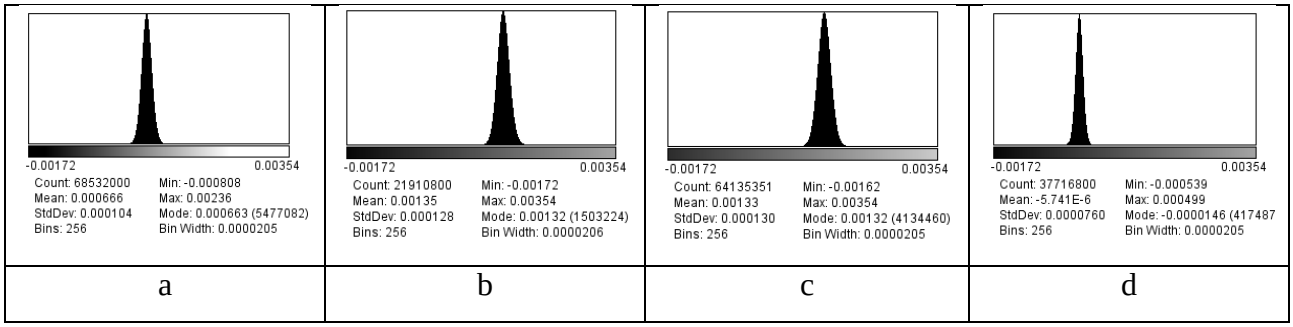

Figure 62: reference's materials histograms. a) Aceton; b) Distilled Water; c) Glycerol; d) Air

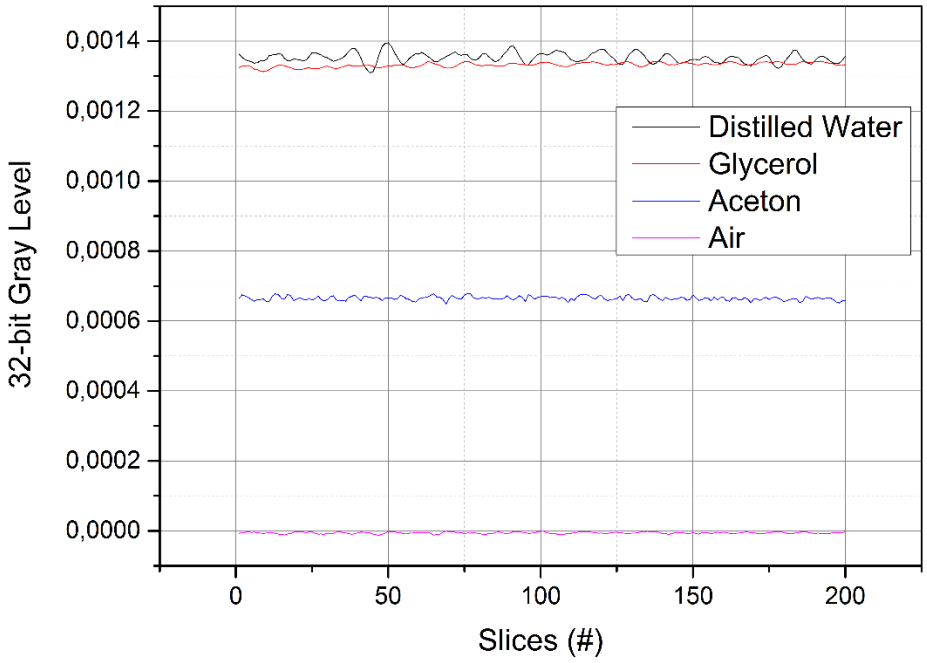

Figure 63: Reference materials 32-bit Gray-Level

Table 18 reports the mean 32-bit Gray-Level of the four reference materials scanned by energy beam equal to 15keV.

Table 18: 32-bit Mean Gray-Level of four reference's substances.

Distilled Water 32-bit GL	***Glycerol 32-bit GL***	***Aceton 32-bit GL***	***Air 32-bit GL***
0.00135	0.00133	0.000666	-5.741E-6

Next step is to relate these reference gray-levels to the absorption coefficients obtained for these materials at beam's energy equal to 15keV reported in Table 15. The relationship is obtained by linear regression between absorption coefficients and Gray-Levels.

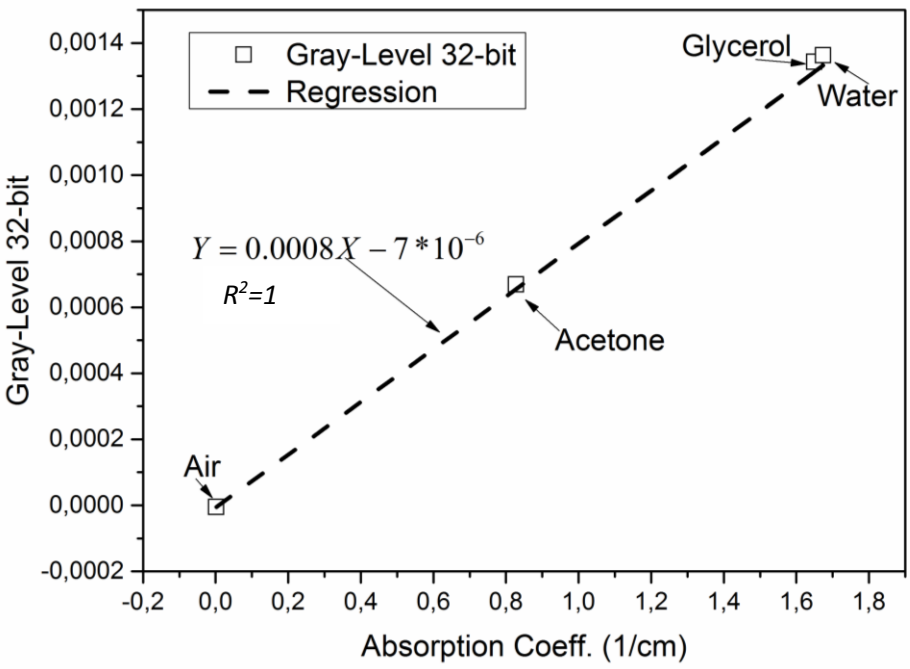

Figure 64: Relation between the absorption coefficient of the reference's materials and their Gray-Level from Micro-CT images at 15keV of beam energy.

From regression, I obtained the linear equation (Eq.25) that will be used to express the absorption coefficient of the particleboard material of unknown density.

$$Y = 0.0008 * X - 7 * 10^{-6} \qquad \text{eq.25}$$

where *Y* is the Gray-Level and *X* are the absorption coefficient measured in *[1/cm]*. Manipulating Eq. 25 it is possible to obtain directly the value of the absorption coefficient as a function of the gray level. Eq 26 reports the relationship that calibrates the Micro-CT images.

$$X = \frac{Y+7*10^{-6}}{0.0008} \qquad \text{eq.26}$$

Practically, using the FIJI's function named *Plot Z-axis profile* I obtained mean grey values for each slice, disregarding the external part covered by parafilm tape. This value was used to calculate the mean absorption coefficient. The absorption coefficient thus estimated will represent the mean absorption of every slice of the scanned sample (see Figure 65).

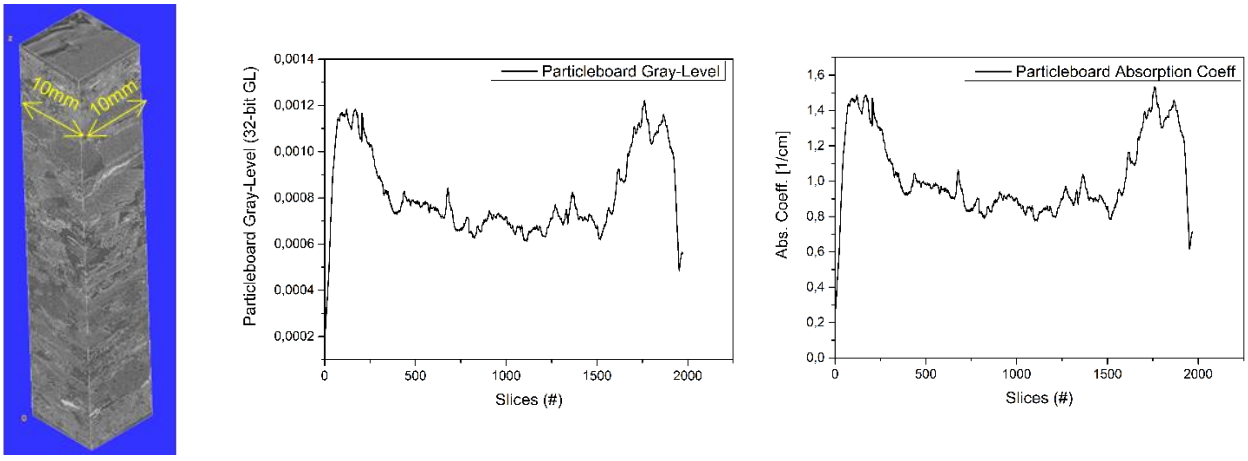

a b c

Figure 65: From particleboard's gray levels to particleboard's absorption coefficients. a) 3D particleboard's volume. The specimen reconstructed is Reference 1 (no tracker used and adhesive quantity equal to 75kg/m^3; b) Gray-Level of each slices; c) Particleboard's absorption coefficients.

The second step required to determine the particleboard's VDP consists of the estimation of the linear relationship between the absorption coefficient and the density of the material. Remembering the proportionality of the absorption coefficient with the material's density (Eq. 18 of Chapter 1 (60)), the densities of the reference's materials and their absorption coefficients (Table 15) were used to perform a regression and find the linear relationship between them. Then it was possible to obtain the density of unknown materials knowing its absorption coefficient.

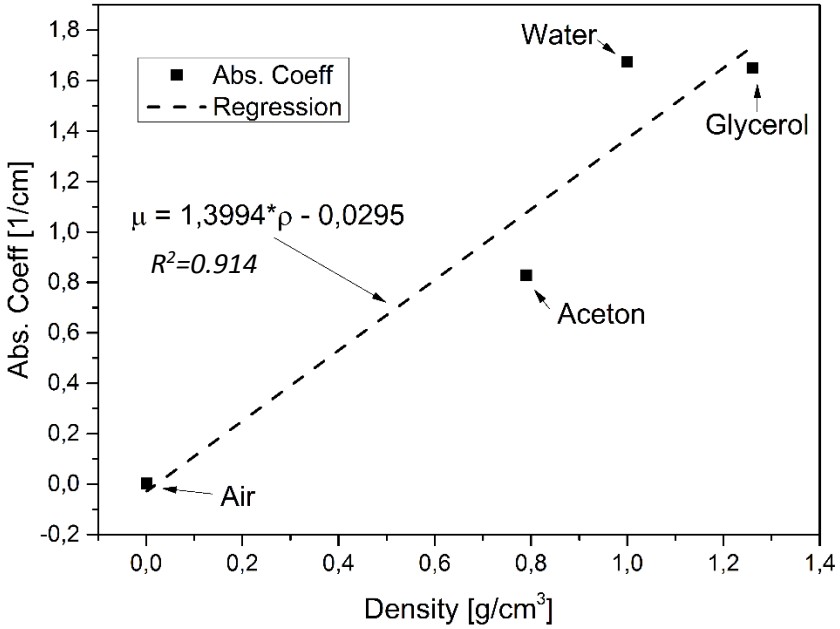

Figure 66: Relation between the density of the reference's materials and their absorption coefficients at 15keV of beam energy

The result of the linear regression between density and absorption coefficient is reported in Eq. 27:

$$\mu = 1.3994 * \rho - 0.0295 \quad \text{eq.27}$$

where μ is the linear absorption coefficient and ρ is the material density measured in *[g/cm^3]*. Manipulating Eq. 27, it is possible to obtain directly the value of the density knowing the absorption coefficient from the grey level conversions. Eq. 28 reports the relationship that allows for the density calculation.

$$\rho = \frac{\mu + 0.0295}{1.3994} \quad \text{eq. 28}$$

Finally, using the data reported in Figure 65c, it was possible to obtain the Vertical Density Profile of the particleboard. Figure 67 shows the Particleboard VDP for the specimen named *Reference 1* in which the adhesive quantity was equal to 75kg/m^3, no contrast agent was used and the moisture content was equal to 5.4% of the sample's weight. No others mathematical corrections on the resulted density profile was performed.

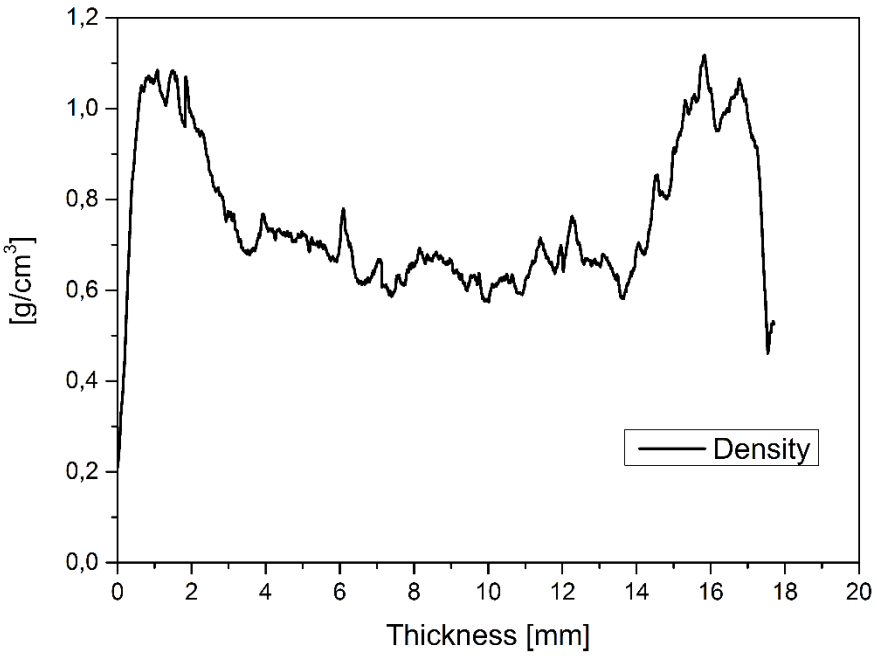

Figure 67: Vertical Density profile estimated for specimen Reference 1 with adhesive quantity equal to 75kg/m^3, no tracker used and 5.4% of moisture content.

It is possible to combine Eq. 28 with Eq. 26, in order to determine the density of the material directly from Gray-Level measured from the slices, following the workflow diagram shown in Figure 68, thus obtaining Eq. 29

$$\rho = \frac{Y + 3.06 * 10^{-5}}{1.12 * 10^{-3}} \qquad \text{eq.29}$$

where Y is the 32-bit Gray-Level measured from the slices of the sample scanned by Micro-CT technique with energy beam equal to 15keV and exposure time equal to 1.001s and ρ is the density in $[g/cm^3]$.

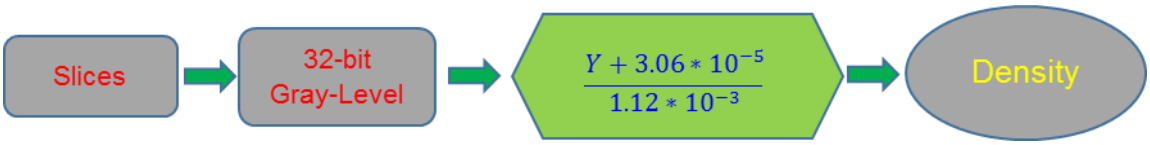

Figure 68: Density evaluation procedure

Using the procedure presented in Figure 68, I measured the VDP of samples scanned by Micro-CT. The VDP's results are reported in Figure 69, where is possible to see the typical density profiles of particleboard panels for every sample. It is worth observing that the core density is almost constant compared to the skin's density.

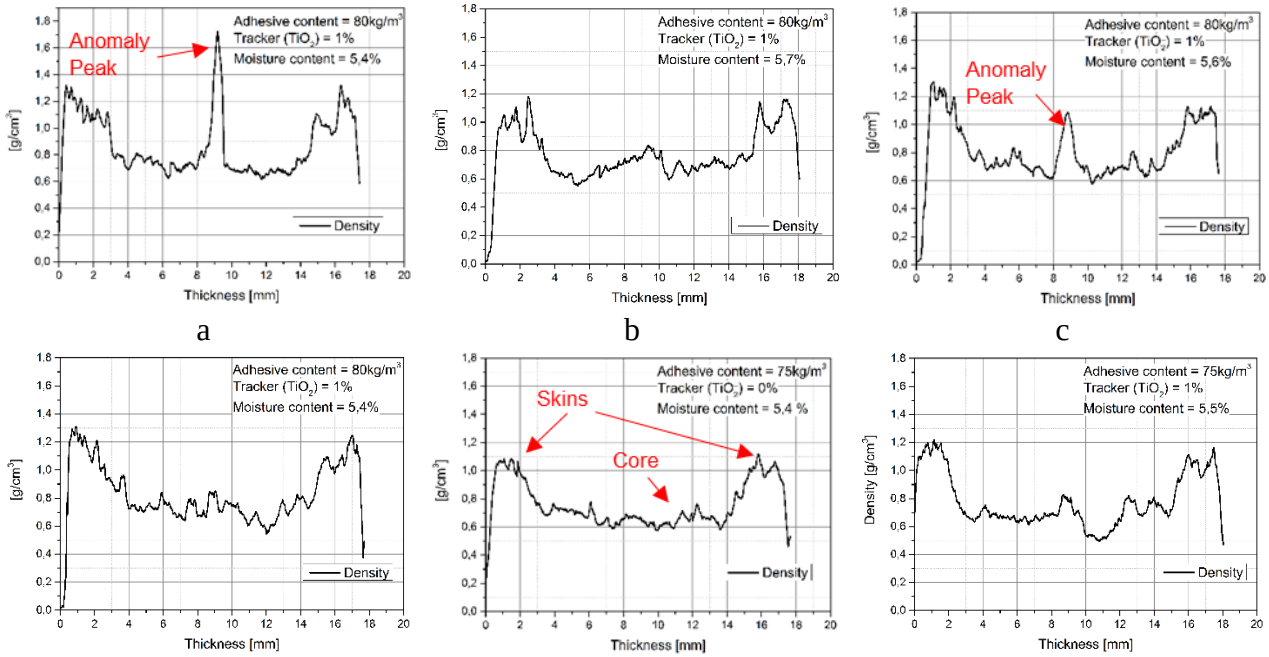

Figure 69: Particleboard Vertical Density Profiles from quantitative image analysis of Micro-CT acquired with beam's energy equal to 15keV and exposure time equal to 1.001s. a) Full1; b) Full2; c) Full3; d) Full4; e) Reference1; f)Normal2

Table 19 reports the results of this quantitative analysis in terms of mean values of density, absorption coefficient, Gray value and moisture content. Sample *Reference 1* was later used to validate the mean value of density by the gravimetric method and for comparison with the VDP measured by an industrial equipment.

Table 19: Mean results of density, absorption coefficient, 32-bit Gray Level and moisture content.

Sample's name	ρ m[g/cm^3]	μ [1/cm]	GL m 32-bit	H[%]
Full 1	0.87	1.19	0.000943	5.4
Full 2	0.76	1.04	0.000839	5.7
Full 3	0.80	1.09	0.000881	5.6
Full 4	0.82	1.12	0.000905	5.4
Normal 2	0.78	1.06	0.000841	5.5
Reference 1	0.75	1.02	0.000813	5.4
Mean	*0.80*	*1.09*	*0.000870*	*5.5*
Std. Err.	*0.02*	*0.02*	*0.000019*	*0.04*

Observing the vertical density profiles reported in Figure 69a and in Figure 69c it is possible to see an anomaly compared to the others profiles. In both profiles, a very high-density peak appears, with density value equal to 1.7 g/cm^3 for the peak visualized in Figure 69a and 1.1 g/cm3 for the peak in Figure 69c. These two values exceed the mean core density of 0.75g/cm^3 by 56% and 32%, respectively. I investigated this fact observing the corresponding slice at the corresponding thickness level for these two anomalies, which effectively were associated to relatively large particles, with a Gray-Level near to white. Figure 70 reports these observations and the corresponding Gray-Level profile for both samples.

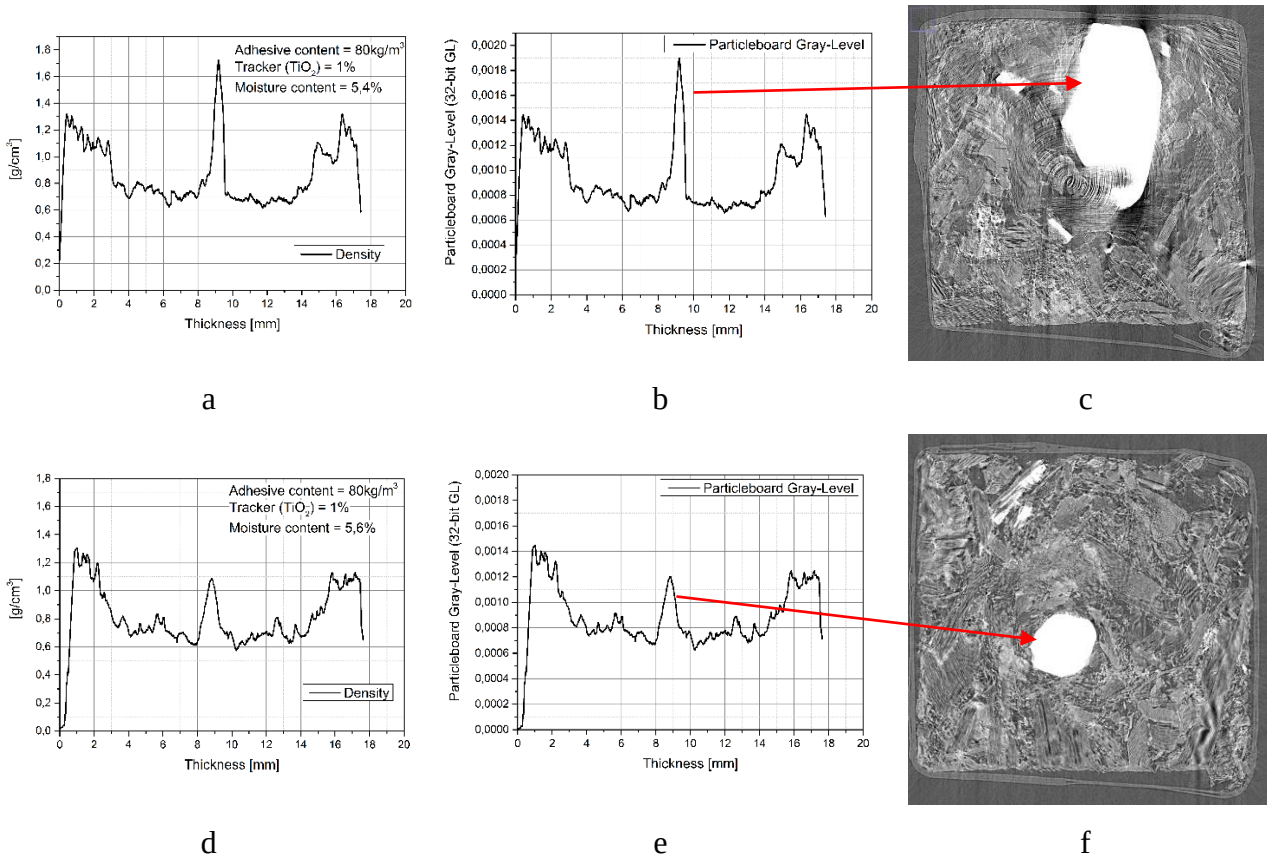

Figure 70: Characterization of the anomaly peaks found in VDP of the specimens. a) VDP of the specimen "Full1"; b) 32-Bit Gray-Level profile of the specimen "Full1"; c) Full 1's Slice at thickness level equal to 9.2mm; a) VDP of the specimen "Full3"; b) 32-Bit Gray-Level profile of the specimen "Full3"; c) Full 3's Slice at thickness level equal to 8.9mm

The nature of the particles was investigated by SEM (Scanning Electron Microscope): it resulted that these particles had a large quantity of calcium equal to 6.7% weight fraction. The percentage of oxygen and carbon are due to the wood's cellulose chains $(C_6H_{12}O_5)_n$. The magnification adopted is equal to 70x and the scale is equal to 200μm. By considering the particleboard production process through recycling of post-consumer wood, the probability of finding sand particles or stones inside the material's volume is high, even if the raw materials are usually cleaned before hot pressing. Figure 71 and Table 20 represents SEM Analysis results.

Table 20: Mass percentage of the chemical components find in the anomaly region of the sample "Full1"

Sample position	Chemical components			
	%C	%O	%Ca	%Total
Wood	65.7	34.3	-	100
Anomaly	53.8	39.5	6.7	100

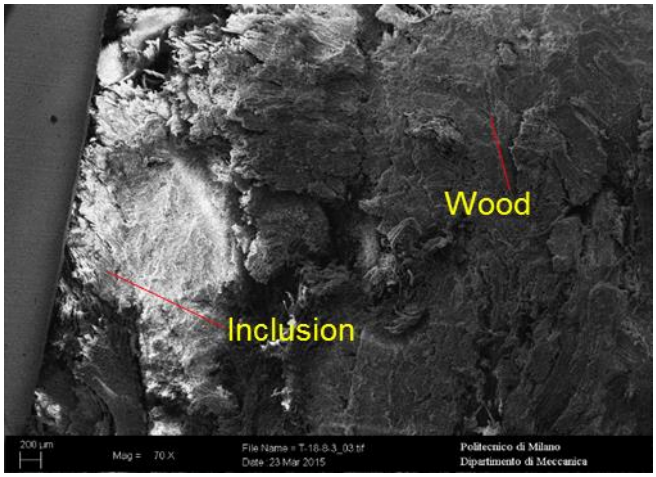

Figure 71: SEM Micro-graphy of the surface at the inclusion's thickness level of the Full1 sample.

In the next section, the results of the quantitative micro-CT image analysis are compared in terms of mean density from the Vertical Density Profile of the sample "*Reference 1"* with the mean density obtained using the gravimetric method and the VDP is compared with the VDP measured by an industrial equipment. The measurements of VDP by industrial equipment were performed before the Micro-CT acquisition on the standard particleboard. The samples prepared with the higher content of the adhesive, TiO_2 as a tracker, and the Micro-CT acquisition were performed after the experimental campaign at the industrial facility of IMAL (next paragraph), then the only possible comparison was between the VDP measurements from standard specimen *Reference 1.*

2.5 Vertical Density Profile of particleboard by industrial equipment: measurement and comparison with Micro-CT result.

2.5.1 Sample's mean density by gravimetric method

The first comparison of the micro-CT based density measurement was made with the gravimetric method. The set-up adopted is very simple and includes the scale used during moisture content determination with resolution equal to 0.01g, reported in Figure 60a and a caliper with spatial resolution of 0.1mm. The volume measurement of these samples is crucial for the accurate evaluation of their density. To accomplish this procedure, the width, the length and the height at several locations of the sample were measured, following the scheme reported in Figure 72.

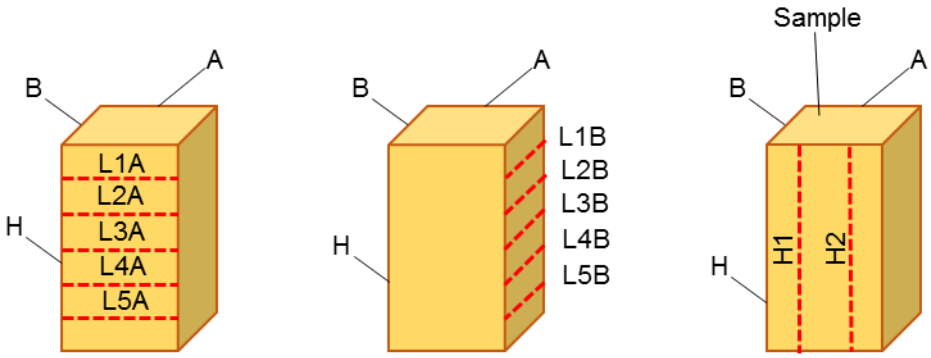

Figure 72: Sample's dimension determination

Table 21 lists all the sample's dimensions recorded following the scheme shown in Figure 72.

Table 21: Sample's sides measurements

Sample's Name	***L1A [mm]***	***L2A [mm]***	***L3A [mm]***	***L4A [mm]***	***L5A [mm]***	***L1B [mm]***	***L2B [mm]***	***L3B [mm]***	***L4B [mm]***	***L5B [mm]***	***H1 [mm]***	***H2 [mm]***
Full 1	9,6	9,7	9,6	9,6	9,7	9,8	9,8	9,9	9,97	10	17	17
Full 2	9,6	9,7	9,6	9,5	9,6	9,5	9,6	9,6	9,66	9,8	17	17
Full 3	9,4	9,5	9,5	9,5	9,7	10	10	10	10,1	10	18	18
Full 4	9,7	9,7	9,5	9,4	9,5	9,9	9,9	9,8	9,78	9,5	18	17
Normal 2	9,5	9,4	9,4	9,4	9,5	9,1	9	9	8,94	9,1	17	17
Reference 1	10	10	9,9	10	10	9,9	10	9,9	9,83	10	18	18

Table 22 reports the mean values of the dimensions of every sample and the volumes calculated by multiplying the average values of *A*, *B* and the height *H*.

Table 22: Mean values of the sample's sides and their volume.

Sample's Name	***A [mm]***	***B [mm]***	***H [mm]***	***Vol [mm^3]***
Full 1	9,6	9,9	17,4	1662,2
Full 2	9,6	9,6	17,5	1607,5
Full 3	9,5	10,0	17,5	1680,4
Full 4	9,6	9,8	17,5	1634,8
Normal 1	9,4	8,9	17,5	1453,4
Reference 1	10,0	9,9	17,7	1752,4

To calculate every sample's density by the gravimetric method, it is necessary to know their weight. This quantity was already measured for the moisture content determination; in particular, the first weight recorded before placing the samples in the oven (refers to the second column of Table 16). Knowing samples' volumes and weights, the densities were obtained by evaluating the weight to volume ratio. Table 23 reports the densities obtained by the gravimetric method (fourth column) compared with the mean density estimated by Micro-CT image analysis (fifth column).

Table 23: Comparison between density results from Micro-CT image analysis and gravimetric method

Sample's Name	***Vol [cm^3]***	***P0 [g]***	***ρ [g/cm^3]***	***ρ Micro-CT [g/cm^3]***	***%***
Full 1	1.662	1.15	0.70	0.87	19.5
Full 2	1.607	1.11	0.65	0.76	15.5
Full 3	1.680	1.15	0.69	0.80	13.7
Full 4	1.634	1.12	0.69	0.82	15.8
Normal 1	1.453	0.95	0.65	0.78	16.7
Reference 1	1.752	1.17	0.67	0.75	10.7
Mean	*1.63*	*1.11*	*0.68*	*0.80*	*15.3*
Std. Err.	*0.004*	*0.03*	*0.008*	*0.016*	*1.2*

As it clearly appears, there is a mean difference of 15.3% between the densities evaluated by two methods. In particular, the density obtained by Micro-CT image analysis is greater than the density evaluated by the gravimetric method. In order to explain this difference, comparison with the VDP of the particleboard by an industrial equipment was also performed.

2.5.2 Vertical density profile measurement by industrial equipment.

The equipment used for the VDP measurement is the IMAL DPX 300 (93) reported in Figure 73, and it was designed to analyse the VDP of samples extracted from particleboard, MDF or OSB for quality control of their production (refers to Chapter 1 to more explanations about the acronyms). The VDP's measurement is performed following the theory of radio control systems by using an X-Ray source and a scintillator as a receiver. Source and receiver are fixed to the machine's chassis and the samples, positioned in a loader and put on a micrometric slider under the X-Ray source, where it can be moved at a maximum speed of 0.5mm/s . Linear translation of the sample is controlled by high precision handling system with a spatial resolution equal to 0.01mm between two successive positions during the measure.

a b

Figure 73: IMAL DPX 300 Vertical Density Profile detector (81). a) Real machine; b) 3D model

Technical data of the X-Ray emitter are reported in Table 24

Table 24: Technical Data IMAL DPX 300 (81)

Nominal electric voltage	*25kV*
Filament current	*0.25mA*
Filtering	*0.8mm*
Tilt anode	*19°*

The main principle that is used to perform this VDP measurement is X-Ray absorption. The emitter produces an X-Ray beam that has a blade shape. This goes through the particleboard sample and hits the scintillator. Here, the X-Rays that go through the sample are converted into visible light (94) and finally converted into the corresponding electric signals, proportional to the beam's intensity,

as presented before for acquisition of Micro-CT projection during absorption tomography. More details about the detector and the calibration adopted to convert the beam intensity to the board density are not available.

Regarding the geometry of the particleboard sample prepared to perform these measurements, Figure 74 shows a schematic representation and dimensions of the samples, that must comply with the machine's loader dimensions.

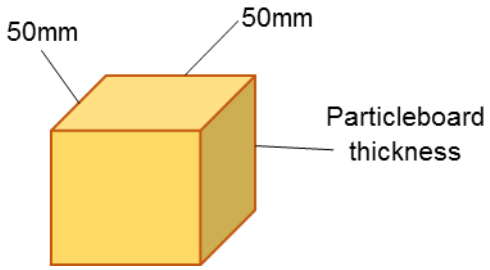

Figure 74: Particleboard's sample dimensions to load it in the VDP detector.

In the loader, it is possible to charge a maximum number of six samples separated by aluminum plates. The machine will recognise different absorption of the X-Ray beam passing through the particleboard or the aluminum dividers, stops the VDP acquisition and start again with the new sample. Figure 75 reports two steps of the VDP acquisition.

a b

Figure 75: Samples loader of VDP detector. a) Before the acquisition; b) at the end of the acquisition

The measurements were performed at the IMAL facility in Modena (IT) before the experimental campaign at the Synchrotron. Of the six samples with a thickness equal to 18mm scanned at IMAL, one was cut and observed by Micro-CT technique and image analysis. This sample was named "Reference 1". It is important to underline that the sample (Reference 1) after VDP

measurement at IMAL facility, was cut in the centre to obtain the right dimensions suitable for the tomography as shown in Figure 76.

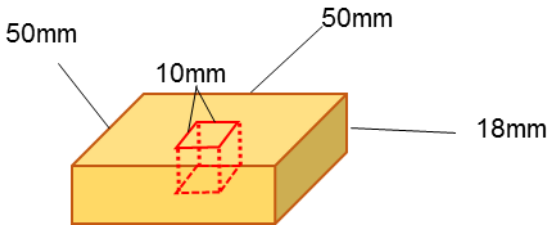

Figure 76: Sample "Reference 1" extraction from specimen used to evaluate VDP by IMAL's detector

The VDP measurements performed at IMAL included also 8mm and 38mm particleboard samples that were subjected to mechanical characterization tests, as presented in the following chapter. The VDPs thus obtained are shown in Figure 77. On the left side, all six VDPs are shown, while on the right average VDPs are shown, obtained by averaging density values at each position through the thickness.

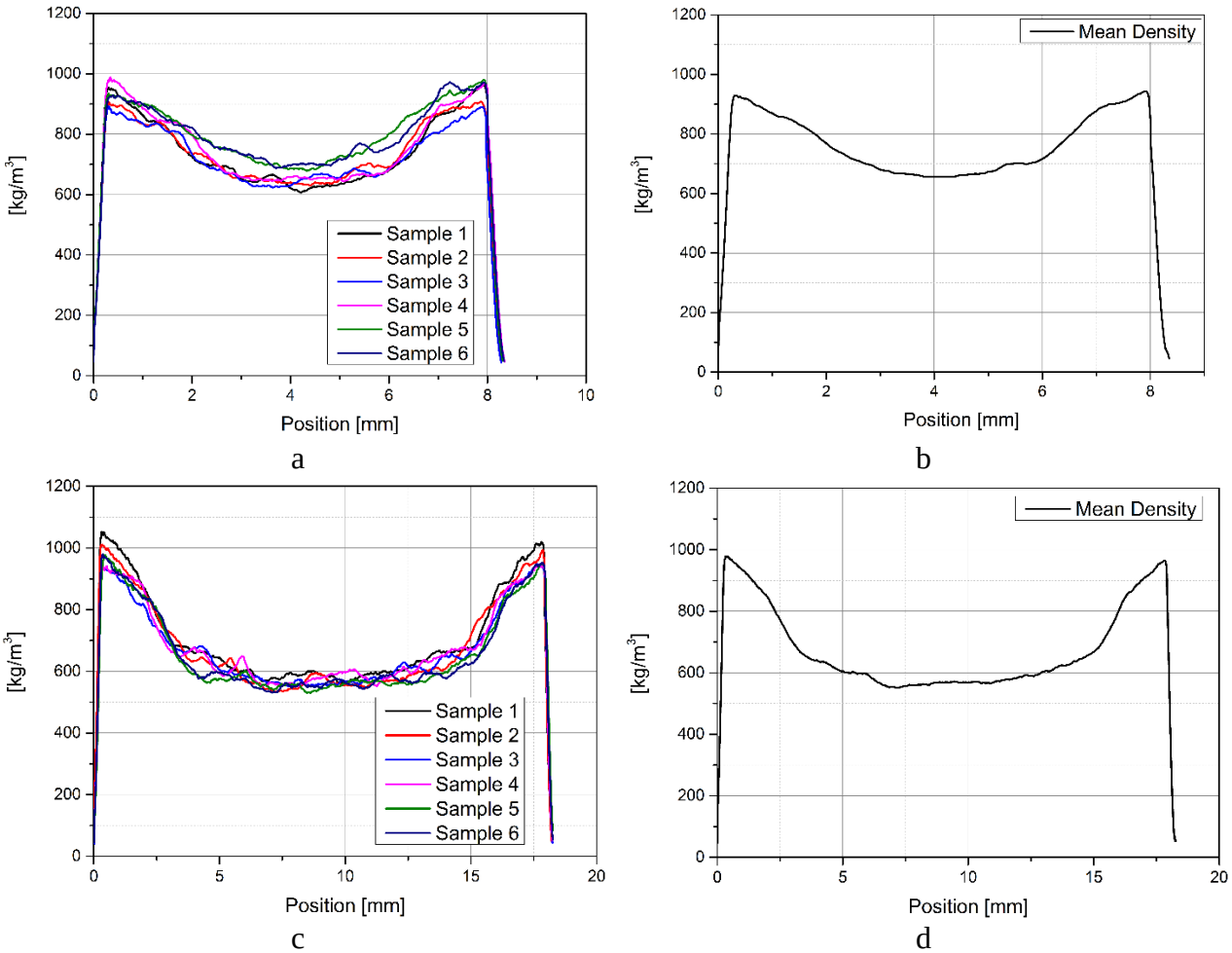

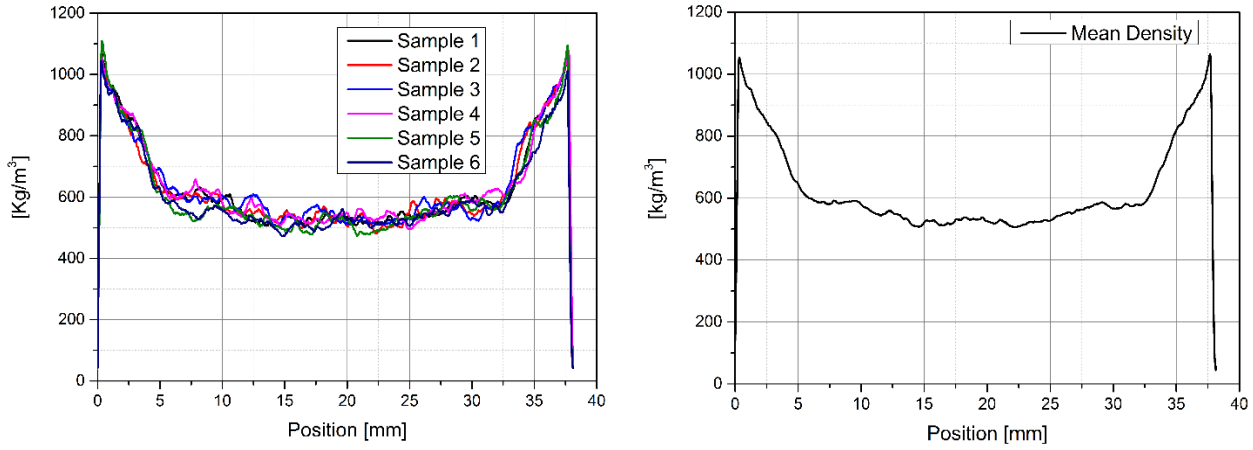

e f

Figure 77: Vertical Density Profiles measured along the particleboard thickness by VDP detector DPX300 provided by IMAL facility located in Modena. a) Six VDP of particleboard samples with thickness equal to 8mm; b) mean density profile of six samples of 8mm of thickness; c) Six VDP of particleboard samples with thickness equal to 18mm; d) mean density profile of six samples of 18mm of thickness; e) Six VDP of particleboard samples with thickness equal to 38mm; f) mean density profile of six samples of 38mm of thickness.

The Table 25 reports the density for all board thicknesses. The particleboard samples with thicknesses equal to 8mm, 18mm and 38mm have density mean values equal to 743.8kg/m^3, 669.9 kg/m^3 and 620.8 kg/m^3, respectively.

Table 25: Mean values of every six VDP for each particleboard's thicknesses

Sample's name	**Thick. 8mm Density [kg/m^3]**	**Thick. 18mm Density [kg/m^3]**	**Thick. 38mm Density [kg/m^3]**
Sample 1	724.5	697.1	627.0
Sample 2	726.4	676.8	624.1
Sample 3	711.4	666.9	631.5
Sample 4	740.5	674.7	630.8
Sample 5	782.2	651.2	609.1
Sample 6	777.8	652.9	602.2
Mean	*743.8*	*669.9*	*620.8*
Std. Err.	*12.1*	*7.0*	*6.1*

To validate the Vertical Density Profile obtained by Micro-CT image analysis, it was compared with that obtained by VDP industrial detector. From the density profile's measurements of the 18 mm thick particleboard, the profile of specimen named "*Sample 4"* coincident with *Reference 1* in image analysis was extracted. Figure 78a reports the Vertical Density Profile comparison after density conversion from g/cm^3 to kg/m^3 and Table 26 reports the final comparison between the mean density values obtained with the three quantitative methods for particleboard samples of 18 mm thickness.

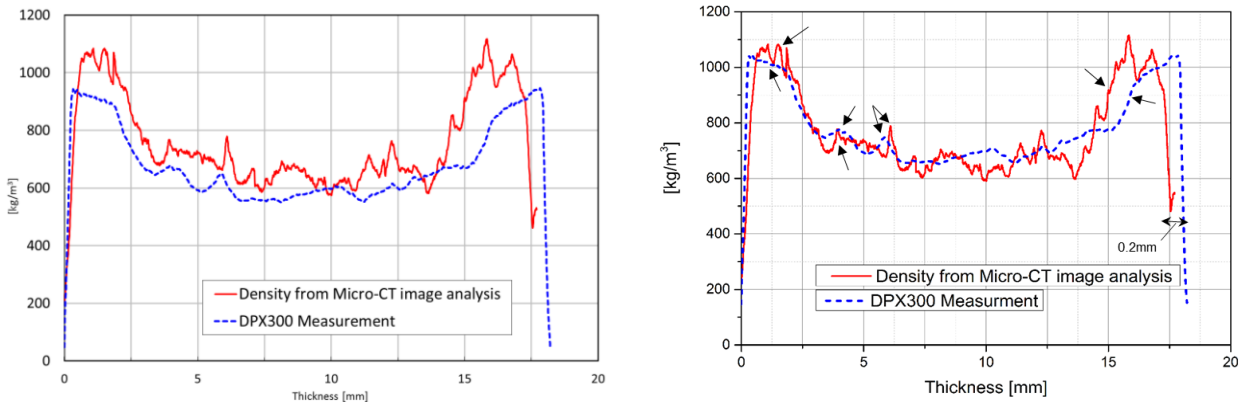

a b

Figure 78: Mean density comparison between profile estimated by Micro-Ct Image analysis and DPX300 measurement: a) two profiles without the rescale; b) Density profile from Micro-CT analysis scaled by 10% compared to industrial one.

Table 26: Final mean density comparison between three quantitative methods

Sample's Name	***ρ [kg/m³]***	***ρ Micro-CT [kg/m³]***	***ρ DPX300 [kg/m³]***
Reference 1 = Sample 4	670	750	675
% (Gravimetric and Micro-CT)		10.7	
% (Micro-CT and DPX300)		10	

It appears that the mean density value obtained by micro CT differs from the values obtained by the other two methods by approximately 10%. Applying a correction of 10% to the density profile obtained by Micro-CT image analysis, it becomes very comparable with the industrial one (Figure 78b). Possible explanations of this shift between two profiles are presented in the next sections.

2.5.3 Comparison

Observing Figure 78 it is possible to compare the two Vertical Density Profiles obtained by the two techniques, the red line referring to the particleboard's VDP determined by Micro-CT image analysis and the blue dashed one to the VDP obtained using the IMAL detector DPX300. Assuming the blue-dashed profile as a reference, the red profile appears to be in qualitative agreement but increased of 10% higher (Figure 78a). The position of the characteristics peaks in the shell region is slightly off set, particularly on the right side. However, considering the mean density values reported in Table 26, comparing the Micro-CT value with the density obtained by the gravimetric method and

the mean value of the VDP obtained by DPX-300 detector, a difference of 15% and 10%, respectively, is clearly apparent.

Considering the shape of the two profiles of Figure 78, that micro CT VDP appears more noisy than the DPX-300 detector one, which is smoother. This fact can be related to the higher spatial resolution of the VDP obtained by micro CT, being each grayscale value associated to each slice, but also to the smaller size of the volume considered by micro CT and, therefore, to the possible larger impact of the differences in particle number and distribution from slice to slice.

At this time, the shift between two profiles equal to 10% is not acceptable for analysis of the mechanical behavior presented in the next chapter. For this reason, I decided to rescale the original profile obtained from image analysis of 10% respect of the mean value obtained from the gravimetric method and industrial one. In this manner, the two profiles (Figure 78b) become very similar and then equivalent for use in the next particleboard modelling. Lastly, the difference in the extension through the sample's thickness visualized in Figure 78b between the blue and red profiles is due to the necessity of putting the sample on the rotating table of the tomograph and the reconstruction procedure followed. As explained in the previous section, it is required to fix the sample using malleable wax that can leave a small section of the particleboard's specimen out of the field of view of the detector, causing the 0.2mm of difference compared to the blue VDP.

To prevent loss of density information due to the difference in extension through the sample thickness, I decide to refer to the DPX-300 results, for the macroscopic modelling (Chapter 3), while the micro CT observations were used for the definition of the particle size and orientation distribution, to be used in the micro modelling presented in Chapter 4. Nevertheless, it is necessary to try to explain the observed differences between the density profiles determined using Micro-CT image analysis and industrial device (Figure 77a).

One possibile source of error regards the image calibration. The acquisition of the Micro-CT projections of reference materials (see Section 2.4.2) was performed during different scans, one for each material and in any case not simultaneously as the analysis of the particleboard sample, opening and closing the tomograph's chamber. This fact could have changed the environment near the specimen, e.g. causing an increase of the absorption near the sample, shifting the gray-level upward. The result is an increment in the overall density profile. It is worth remarking that the better choice would have been to perform Micro-CT of the reference materials and sample at the same time. Unfortunately, the field of view of the detector did not allow for framing the reference materials and the sample together.

A second possible explanation for the observed differences consist of the effect of the distance between the detector and the sample. As reported in (60) the X-Rays are more or less refracted when

passing through solids, in particular when the X-Rays pass through materials with different density and electron density. With a synchrotron source, producing X-Rays with high spatial coherence, it is possible to observe different levels of contrast when the X-Rays pass through volumes of different electron density. The X-Rays that are refracted, diverge and interfere with the other X-Rays. This physical phenomenon produces detectable fringes near the boundaries of the objects with different densities contained in the scanned volume. The fringes increase the contrast that can be observed as an increase of the gray level on the image. In particular, the contrast increase is related to the second derivative of the X-Ray phase. Typically, images acquired with a specimen-detector separation ranging from 5mm to 1m, contain right phase information (60). In the case of particleboard, the sample was placed at 50mm from the detector (see Figure 38), and could have produce a phase contrast effect on the images. As explained before, the phase contrast effect can increase the boundary's contrast of the wood's particles with different densities, thus allowing for easier identification. However, this can result into an increment of the mean density of the sample, thus explaining the 10% increase. In the case of further developments of this PhD work, it would be necessary to apply phase retrieval algorithms to reduce this effect and repeat the calibration to verify the shift reduction between the samples.

The last points regards the extraction of the sample *Reference 1* from the specimen scanned with the DPX-300 detector. The sample scanned by the industrial device has dimensions equal to 50 x 50 x 18mm, while the Micro-CT's sample has dimensions equal to 10 x 10 x 18mm. As presented before and further discussed in Chapter 4, considering the average dimensions of the constituents, particularly in the core, these dimensions are not large enough to allow for capturing the average properties of the particleboard panel under examination. Thus, it is likely that the vertical density profile of the sample *Reference 1* is effectively corresponding to the actual properties of the smaller sample which measured, but it is not representative either of the larger sample it was extracted from or of the entire panel, particularly considering the dimension of samples prescribed by the standard (95). To improve this analysis in the case of future developments, it would be necessary to conduct Micro-CT scans using larger particleboard samples, possibly 50 x 50 x 18mm, and to use a more suitable Micro-CT detector with a field of view compliant with these sample's dimensions.

Chapter 3 – Particleboard, Macro mechanical characterization

3.1 Outline

Up to now, I performed qualitative and quantitative image analysis to understand the inner structure of the particleboard material, how the adhesive is distributed in the volume of the samples and, mostly, measure the density profile along the thickness (VDP). As mentioned before, the density is the most important physical characteristic as well as the particles properties, shape and orientations for the particleboard characterization. However, the density is the physical property more controlled in the industry of this material because it is related with the elastic modulus, as a reported in (35) and (36). The objective of the task reported in this Chapter is the determination of the proper statistical relationship between the density and the elastic modulus of the particleboard parallel to its main (longitudinal) direction because this mechanical quantity is the most important parameter controlled in the particleboard industries (it is clear that the particleboard is not isotropic).

The interest into this relationship stems from two industrial needs: the first is related to the quality control of the fabrication of the panel made of recycled wood, i.e. by measuring the VDP also the mechanical properties can be inferred, the second deals with possible future developments aiming at manufacturing lighter panels. In the latter case, it is important to evaluate the expected particleboard's stiffness before varying the production process parameters or the composition of the raw material. In particular, this last topic is related to exploring the possibility of reduction of the panel's weight principally for 18mm and 38mm thickness panels, leaving the mechanical performance unchanged or improved.

In the perspective of weight reduction, the zone of the particleboard where one has to act to reduce the weight is essentially the core. For this, I will focus on the identification of the elastic constants, particularly in the central core region. In this analysis, the analogy between sandwich panels and particleboard is exploited. In this manner, even if there is not a sharp variation of properties through the thickness and the particleboard should be treated as a graded material, it was possible define approximately a core and external skins in agreement with the density profile and an elastic modulus profile, as shown in Figure 11 in Section 1.3. At the end of this Chapter, the elastic constants of the core and the skins will be known.

Experimental techniques used for this mechanical characterization will be Three-Points Bending Test with Varying Span (TPBTVS). Then, to validate the values of the elastic modulus of

the core, Iosipescu Test (IT) and Three Point Bending Test (TPBT) with fixed span were performed coupled to Digital Image Correlation (DIC) field method to measure displacements and strains of the samples. At this point, knowing the particleboard elastic constants and its density, it will be possible to derive a relationship between them.

3.2 Experimental set-up and calibration: Three Point Bending Test, Iosipescu Test and Digital Image Correlation.

3.2.1 Three Point Bending Test set-up

As explained before, considering the particleboard as a sandwich panel, it is possible to follow the standard normally used for sandwich's mechanical characterization (96). For the experimental equipment, I followed the standard (32) that prescribes the loading scheme reported in Figure 79, where the loading nose has a diameter equal to 30mm and the support's diameters equal to 15mm.

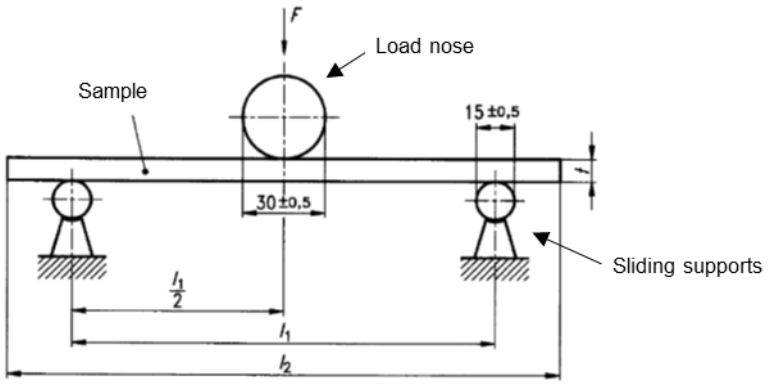

Figure 79: TPBT Load configuration (32)

To perform the TPBTVS, the three points bending device provided by MTS company (97), type 642.10B, that permits a maximum distance between the supports equal to 325mm, was used. The supports can be moved along the longitudinal direction in order to modify the length l_1 (see, Figure 79). The available accessories are reported in Figure 80.

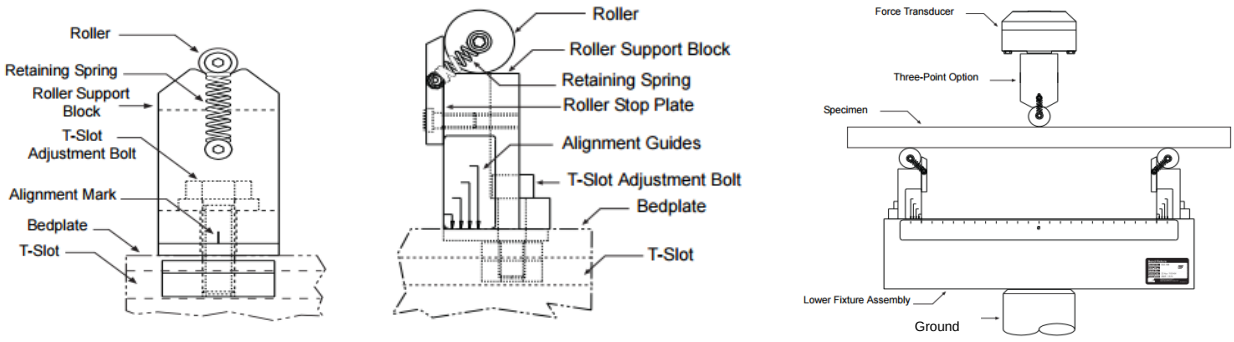

a b c

Figure 80: MTS Bend Fixture 642.10B. a) 642.01A roller block assembly; b) 642.10B roller block assembly; c) MTS three points bending fixture 86

All the experimental tests reported in this Chapter were performed using MTS multipurpose electro mechanic tensile machines (Figure 81), with maximum load capacity equal to 100kN. An additional load cell of 10 kN capacity was used, considering that the maximum load reached will be around 1500N.

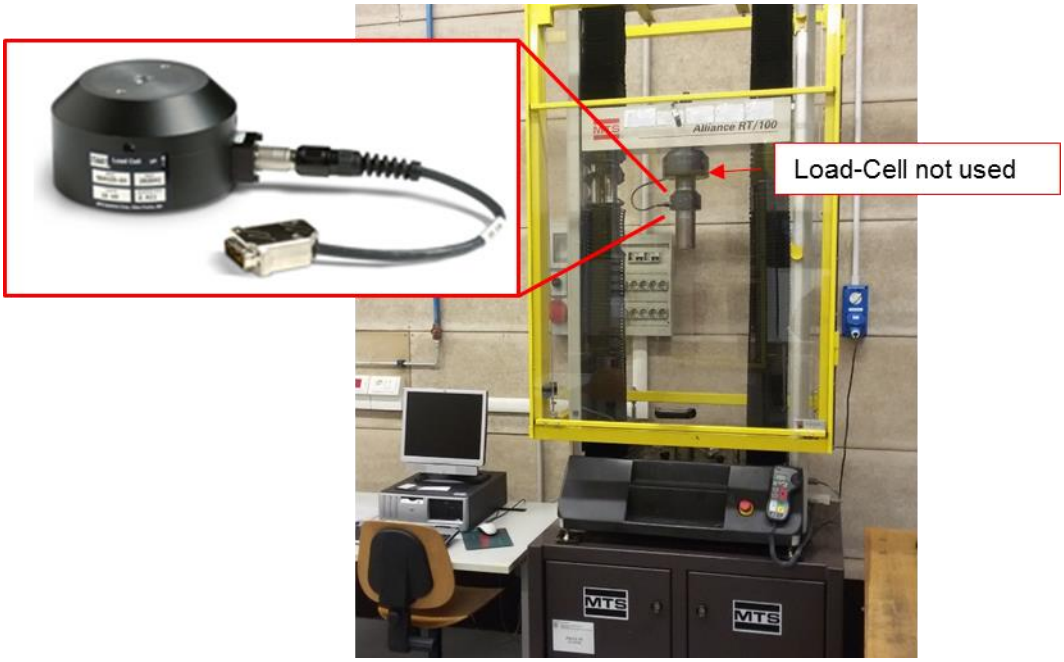

Figure 81: Multipurpose electro mechanic machine MTS Alliance RT/100 and Force Transducer 4501055

To acquire the sample's deflection during TPBTVS and TPBT, to guarantee the best resolution and compensate for the machine's compliance, the deflectometer MTS 632.06H-30 opt 003 was placed in the middle side of the samples (Figure 82). The characteristics of the load cell and the deflectometer are reported in Table 27.

Table 27: Force transducer and Deflectometer characteristics (97)

MTS Force transducer 4501055				
Units	**Force capacity**		**Thread size**	
Metric	10kN		M12 x 1.25	
MTS Deflectometer 632.06H30 opt. 003				
Travel	**Zero adv**	**Force at zero**	**Height**	**Length**
±12.5mm	8mm	80g	101mm	190mm

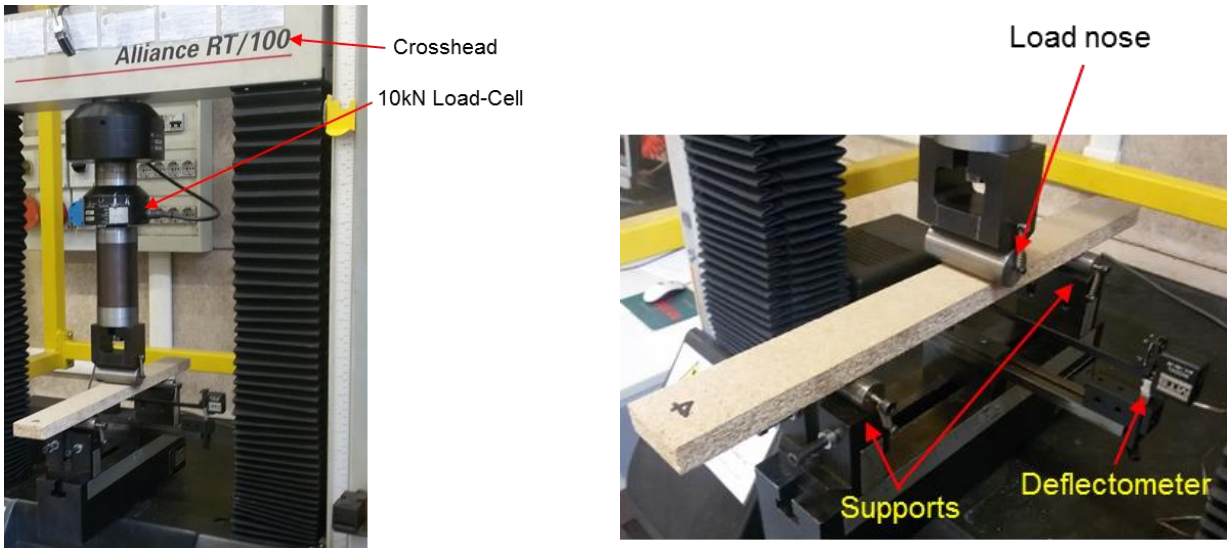

a b

Figure 82: Three points bending set-up. a) Set-Up overview; b) load configuration

Considering the TPBT loading scheme, the diagrams of the shear (T) and the bending moment (M) are reported in Figure 83. The maximum value of the bending moment equal to $\frac{PL}{4}$ is reached at midspan. To evaluate the panel's elastic constants, the deflection due to both shear and bending moment is taken into consideration. For the validation of the properties of the core of the panel, I will focus on the shear deformation and related stresses, in particular considering the shear diagram (T) reported in Figure 83.

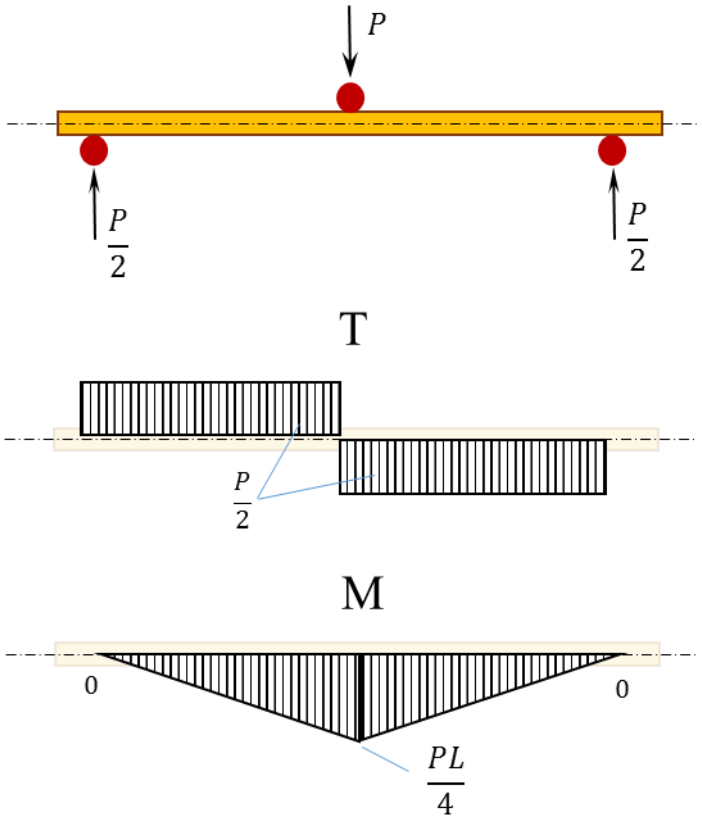

Figure 83: Three points bending test shear load (T) and bending moment load (M).

3.2.2 Iosipescu test set-up

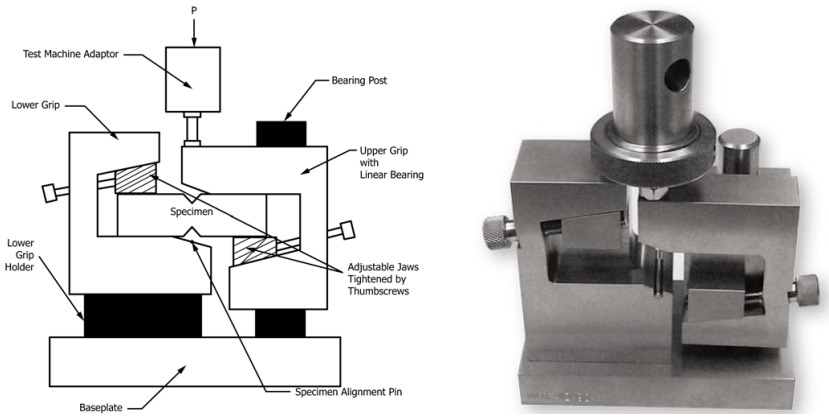

a b

Figure 84: Iosipescu fixture device. a) Device's description (98)*; b) Iosipescu equipment*

The Iosipescu test will be performed to validate the elastic constants of the particleboard previously determined by TPBTVS, in particular for the core's shear modulus G. This test is normally applied to the evaluation of the shear properties of laminate composites. The set-up, test's conditions

and procedure are explained in (98). To perform this test, a specific test rig shown in Figure 84 is required. The Iosipescu's device generates in the sample an ideal antisymmetric bending. This load condition reported on the internal action diagrams (taken from (97), based on the theory of slender beams, even if the specimen should be treated as a thick beam) produces in the middle of the sample a negligible bending action in favour of shear action. In the middle of the sample, the deformation can be considered as pure shear deformation.

The sample, must be prepared in agreement with the geometrical dimensions and V-notches, as prescribed by the standard (98). The notches influence the shear strain along the loading direction, making the distribution more uniform than it would be without the notches.

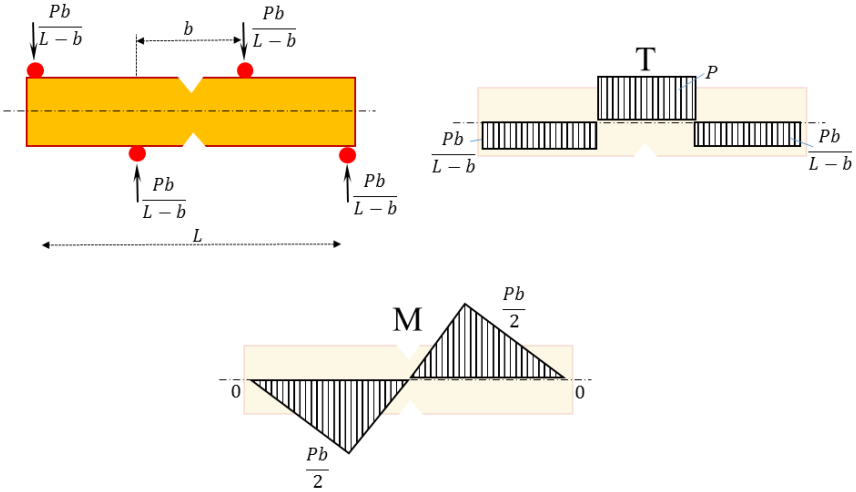

Figure 85: Iosipescu internal actions: Shear load (T) and Bending moment load (M)

To capture the shear deformation, the standard (98) prescribes to glue two strain gauges close to the V-Notches inclined by ±45° with respect to the longitudinal direction as reported in Figure 86a. The strain measured from these two active elements will be composed in agreement with the relationship $\gamma = |\varepsilon_{+45}| + |\varepsilon_{-45}|$ to obtain the engineering shear strain.

Observing the particleboard's surface (Figure 86b), it appears irregular, with wood particles and voids clearly visible. Glueing strain gauges on this surface can result very difficult and the measurement can be affected by the size effect of the wood particles. In facts, the prescribed strain gauge active length is 1.5mm, considering the millimetre scale superimposed on the particleboard (Figure 86b), it clearly appears that some wood particles are longer than the strain gauge. Therefore, the strain measurement by the prescribed strain gauges would not be useful to characterise the panel's elastic constants.

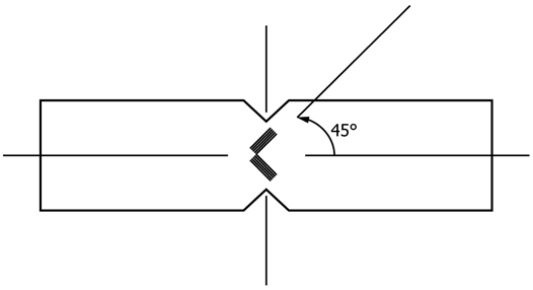

a

b

Figure 86: a) The active elements of two orthogonal strain gauges are centered between the notch roots at the angle shown (98)*; b) particleboard's surface*

Based on these observations, I opted for non-contact measurement as a Digital Image Correlation (DIC) field method. Figure 87 reports the Iosipescu set-up coupled to the (DIC) equipment.

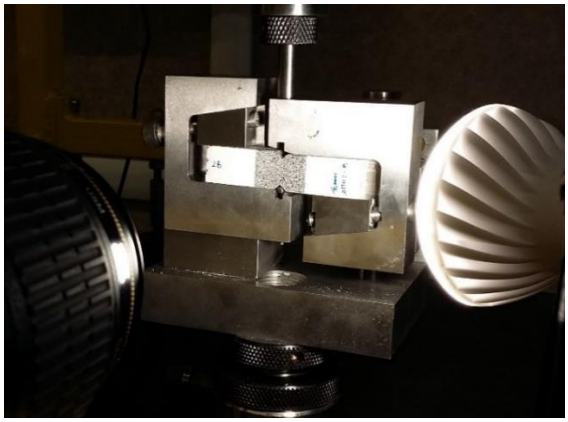

Figure 87: Iosipescu and Digital Image Correlation set-up

3.2.3 Digital Image Correlation set-up

In this PhD work, I used the Digital Image Correlation (DIC) method to measure the shear strain on the sample's surface to evaluate the corresponding modulus of the particleboard's core and compare it with values evaluated by TBPVS.

The hardware setup is composed of:

- Canon Reflex Camera EOS-400 (DS126151) with 10Mpixel of spatial resolution
- Canon Macro Lens EF 100mm 1:2.8 USM
- Canon Remote control camera
- Tripod Manfrotto 074
- LED Lighting REXER 10W 940lm with colour temperature equal to 4000K
- Lamp holder Minilite S-V

Figure 87 shows the DIC's hardware components set for the Iosipescu test, and Figure 88 shows the DIC performed on Three Points Bending Test.

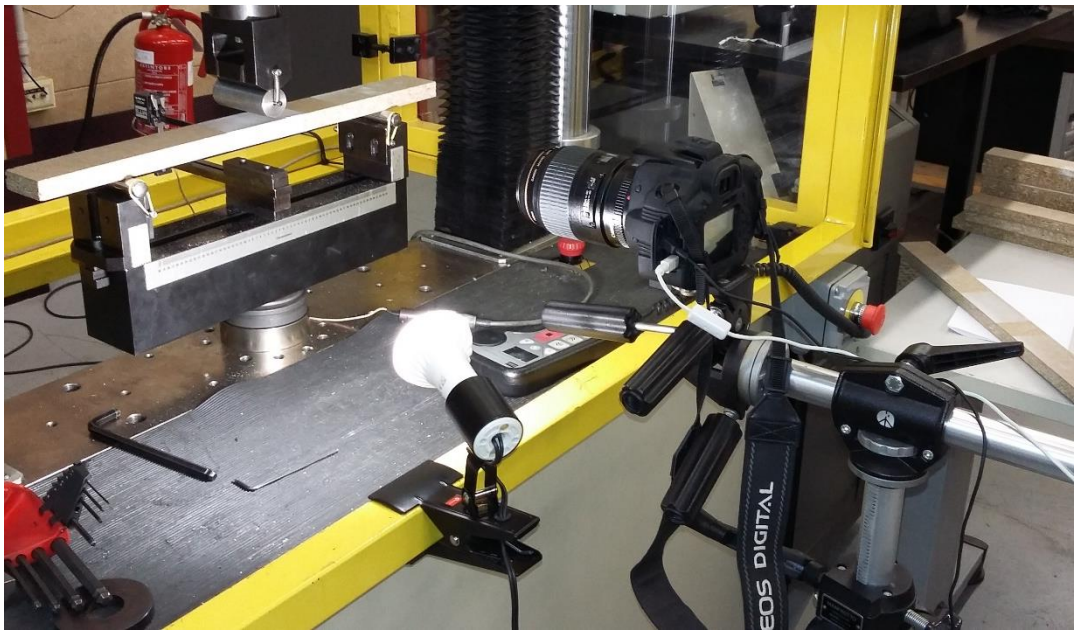

Figure 88: DIC set-up prepared to TPBT

The procedure of DIC measurement method requires to acquire the reference image of the interested zone of the sample, maximising the active zone of the picture. This first image is normally recorded at begin of the test. It is crucial that the light condition, camera's position and zoom are maintained unvaried during the consequent images acquisition until the end of the test. In this manner, only the changes due to the imposed displacement are recorded in the following images and can be detected by the correlation algorithm. I acquired pictures for the whole duration of the tests increasing the number of images in the proportionality zone for both Iosipescu and Three Points Bending tests. There are two factors to take into account:

- At every image, the load generated from the particleboard's sample must be recorded
- At the instant that the picture was acquired the machine's crosshead must be held to prevent that the image result blurred.

In order to evaluate elastic constants, the linear elastic zone limits for each type of tests had to be identified.

For the Iosipescu test, the standard (98) prescribes that the proportionality zone between load and deformation has lower shear strain limit in the range of 1500 to 2500με and an upper limit of 4000±200με must not be exceeded. Observing the material's nature and taking into account the load resolution required to remain below the upper limit, I decided to check directly the linearity of the curve load-deformations. To accomplish these acquisitions for Iosipescu test, in agreement with the

control software of the machine, I took pictures in the linear elastic zone every 10N load steps up to the maximum value of 120N, then the step was increased to 30N until sample's failure. For all the test duration, the crosshead's speed was set equal to 0.1mm/min.

The three Points Bending Test standard (96) prescribes that the linearity limits are in the range from 0.2mm to 1.2mm of deflection acquired. To perform the images acquisition, I set the load step equal to 25N until reaching the sample's failure. The crosshead speed was set to 0.5mm/min. The environment conditions of the laboratory are identified by temperature equal to 26°C and humidity equal to 35%.

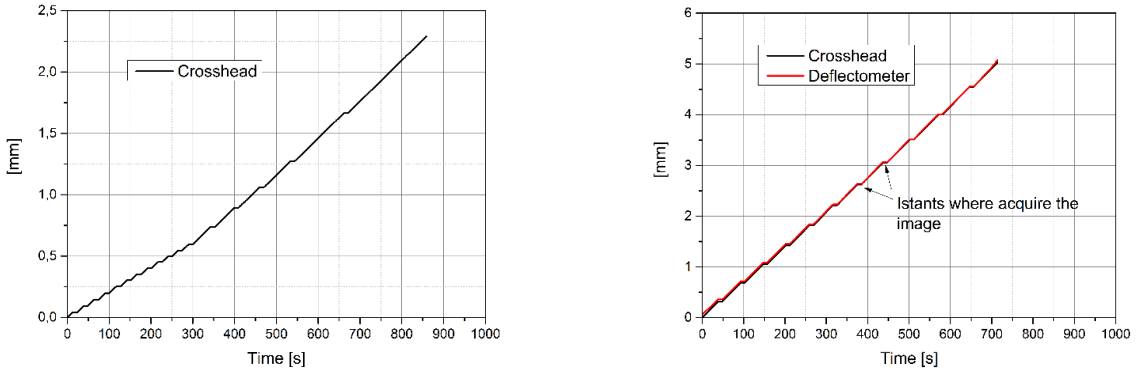

a b

Figure 89: Designed procedure to govern properly the electro mechanic machine to allow the image acquisition. a) Iosipescu test procedure; b) three points bending test procedure

For both IT and TPBT, the crosshead hold time between acquisitions was set to 10s to allow for the sample's relaxation and perform the picture acquisition correctly. The test procedures are displayed respectively in Figure 89a and Figure 89b for Iosipescu and Three Points Bending.

The image and camera characteristics are listed in Table 28*: Picture and Camera features*.

Table 28: Picture and Camera features

Pictures	
Dimensions	3888 x 2592
Width	3888 pixels
Hight	2592 pixels
Horizontal resolution	72 dpi
Vertical resolution	72 dpi
Depth	24bit
Disk's space required	5.75MB
File extension	.*raw
Camera	
F-Stop	f/8
Time exposure	1/6s
ISO	100
Focal distance	100mm

As presented in the last Section of Chapter 1, the software used in this thesis to process the images and measure the displacements and strains of the sample-framed zone is N-Corr, a free open source subroutine that runs in Matlab's environment. This program has a very user-friendly Graphic User Interface (Figure 90) that guides the operator step by step to complete the analysis.

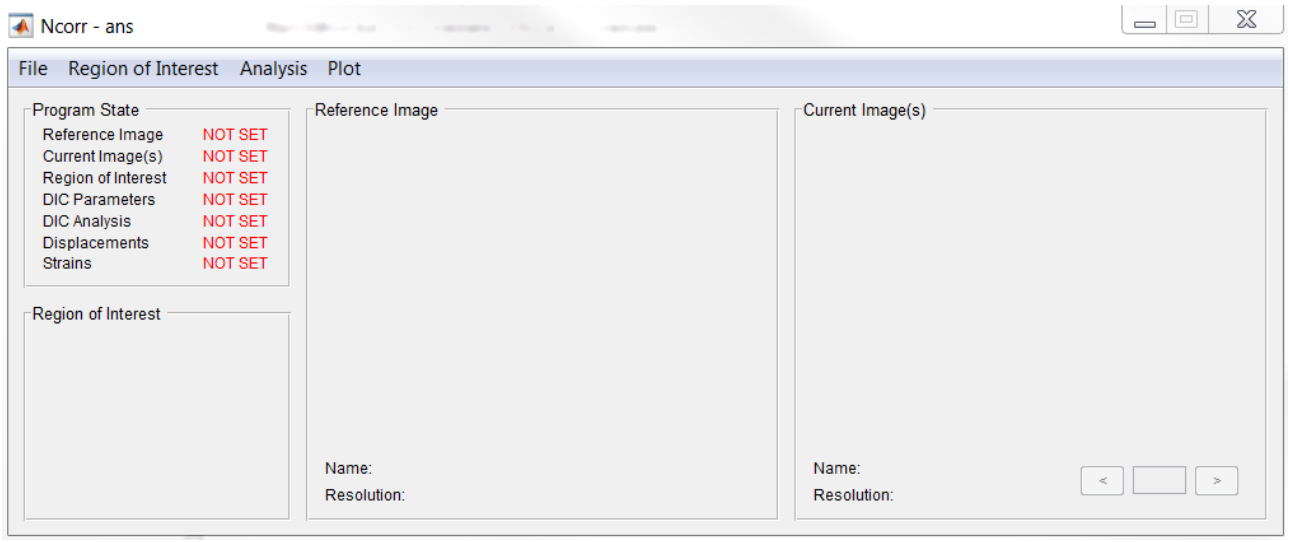

Figure 90: N-Corr Graphic User Interface

To obtain the displacements and the strains by DIC analysis using N-Corr software, the workflow includes the follow passages:

1) Set the reference image
2) Set the current images
3) Set the region of interest (ROI) drawing it directly on the picture
4) Set the DIC parameters
5) Perform the DIC analysis
6) Format displacement
7) Calculate strains

Step number four is the most important; where the operator can set the main parameters of the DIC analysis like subset spacing, DIC-radius and perform the pixel/mm calibration. The spacing component influences the computational load; however, the most important option is DIC-Radius. About this last point, there is wealth of literature available for the right selection of the subset size and related effect on the results. The main idea is to select the smallest subset possible which does not result into noisy displacement data, as larger subsets tend to have a smoothing effect (99). To test rapidly the measuring chain and to reach a good compromise between the computational cost and good displacements results, many calibration attempts were performed by tensile test on samples of

polyamide 66 with 30% glass fibre as a reinforced (PA66GF30) parallel to their longitudinal direction.

These attempts were performed to evaluate the best DIC parameters, lighting source and speckle density comparing the strain results by N-Corr with the values measured with an extensometer of 50mm gage length.

3.2.4 DIC Calibration

In order to calibrate the DIC system and define the most appropriate parameters, four different conditions were investigated by means of the tensile samples shown in Figure 91:

i) The sample prepared by black on white speckle, created by spray paint and tested with led lamp positioned to reach the sample by raking light (Figure 92a).

ii) The sample prepared by black on white speckle created by airbrush and tested with led lamp positioned to reach the sample by raking light (Figure 92b).

iii) The sample prepared by black on white speckle created by spray paint and tested without led lighting (Figure 92c).

iv) The sample prepared by black on white speckle created by airbrush paint and tested without led lighting (Figure 92d).

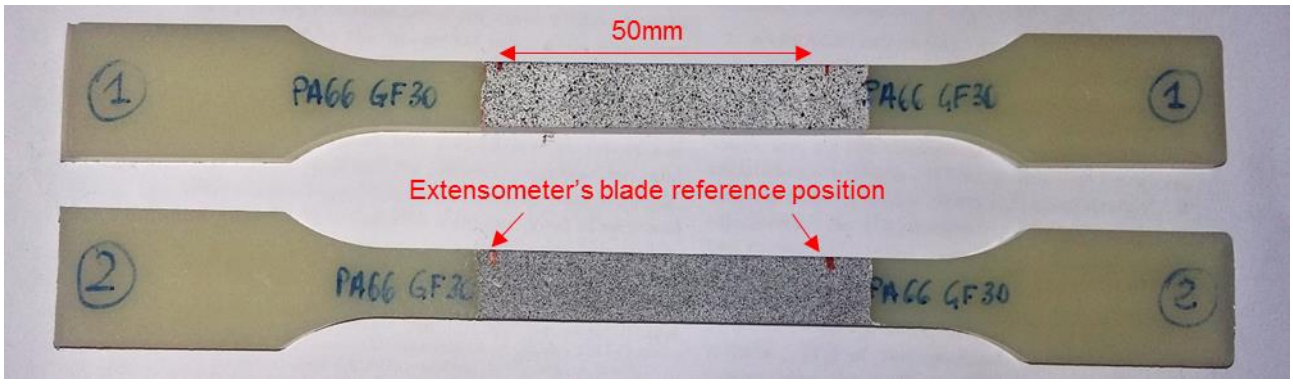

Figure 91: DIC calibration samples. 1) Black spray paint speckle; 2) black airbrush paint speckle

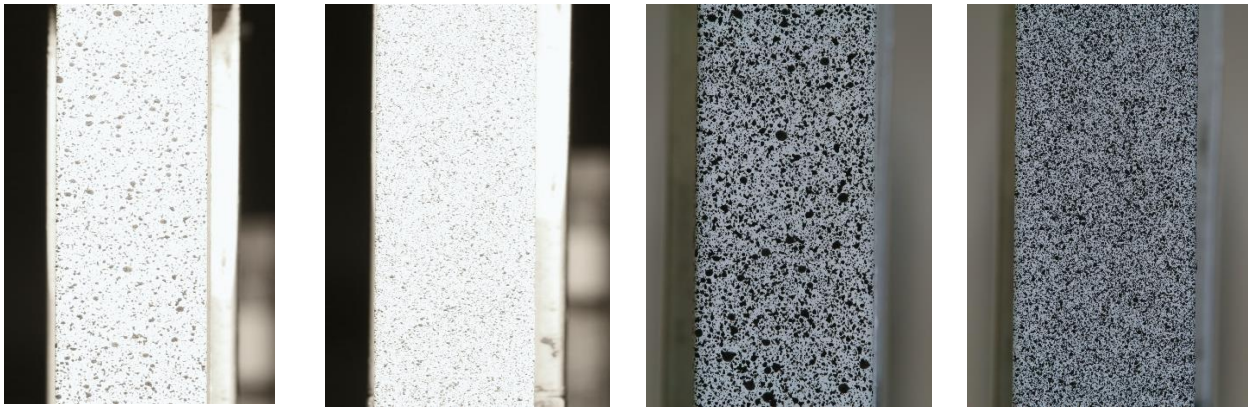

a b c d

Figure 92: Calibration test performed on samples of polyamide 66 with 30% glass fiber as a reinforce parallel to their longitudinal direction. a)=i); b)=ii); c)=iii; d)=iv.

Using an electro mechanic machine (Figure 81), twelve load levels equal to 100N from 0N to 1200N were imposed, without exceeding the linear elastic zone of the reinforced material. For every step, the strain measured by an extensometer was recorded, to compare it with the DIC results.

The DIC-Parameter imposed in N-Corr are respectively a DIC-Radius equal to 50 pixels and a Subset spacing equal to 5 pixels. The results and the difference between experimental measurements and DIC are shown in Figure 93. The best agreement between DIC average strain and strain acquired by the extensometer is obtained using the specimen with black on white speckle created by spray paint and illuminated by LED lamp (Figure 93a). In this configuration, the difference between the two curves (DIC average longitudinal strain and Extensometer) is 1.6%. The following validation tests on particleboard were performed using this configuration.

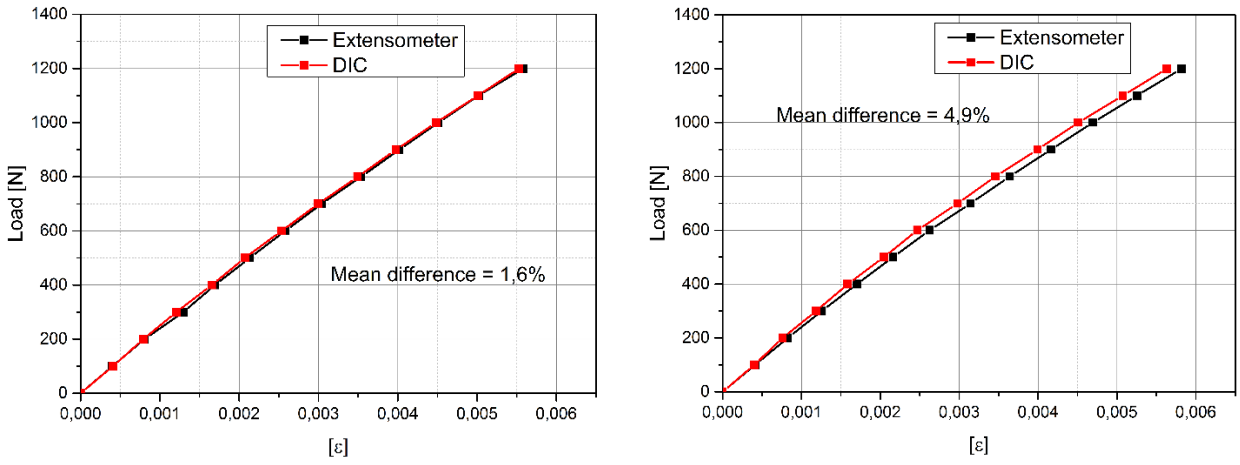

a b

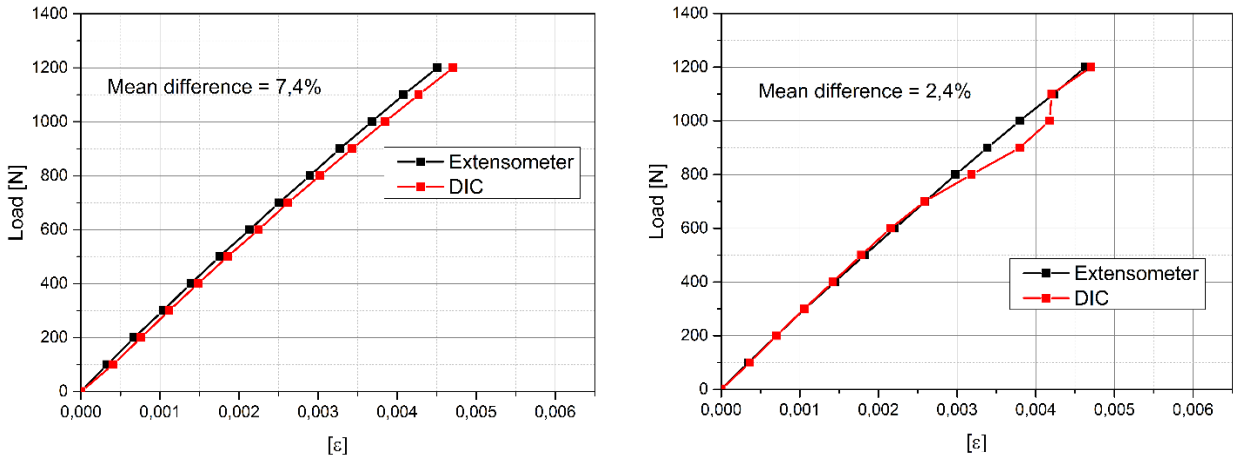

c d

Figure 93: Deformation-Load curves of the PA66GF30 samples tested in their longitudinal direction considering DIC-Radius equal to 50pixels and Subset spacing equal to 5 pixels. a) Black on white speckle, produced by spray paint and tested with led lamp positioned to reach raking light on the sample; b) black on white speckle produced, by airbrush and tested with led lamp positioned to reach raking light on the sample; c) black on white speckle produced by spray paint and tested without led lighting; d) black on white speckle produced by airbrush paint and tested without led lighting.

3.2.5 Particleboard's sample preparation

To perform the Three Points Bending Tests with variable (TPBTVS) and fixed span (TPBT) (this one for the elastic constant validation), and Iosipescu test, several particleboard's samples had to be prepared. In general, for the first evaluation of the elastic constants by TPBTVS, the DIC field method was not applied and the sample's deflection was simply measured by a deflectometer as reported in the previous section. In this case, samples of thickness equal to 8mm, 18mm and 38mm were extracted from the board with their longitudinal coinciding with the lamination direction of the panel. In this manner, the elastic constants evaluated for the panel's skins and core refer to the principal direction of the main board (direction 1 of Figure 94). No other treatments were applied to these samples for this first elastic constants identification procedure. Table 29: Three points bending tests sample's dimensions and geometry.

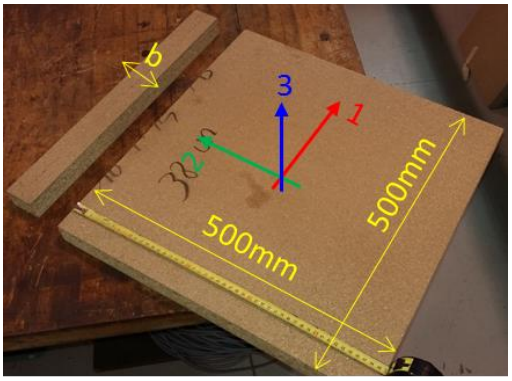

Figure 94: Three points bending test sample extraction

Table 29: Three points bending tests sample's dimensions

Sample's thickness [mm]	Length [mm]	Width (b) [mm]
8	250	50
18	500	50
38	500	50

For the validation procedure performed by Iosipescu test, two types of sample's geometry were extracted only from panels having thickness greater than 10mm. The standard geometry proposed in (98) is shown in Figure 95a and the geometry without notch is reported in Figure 95b.

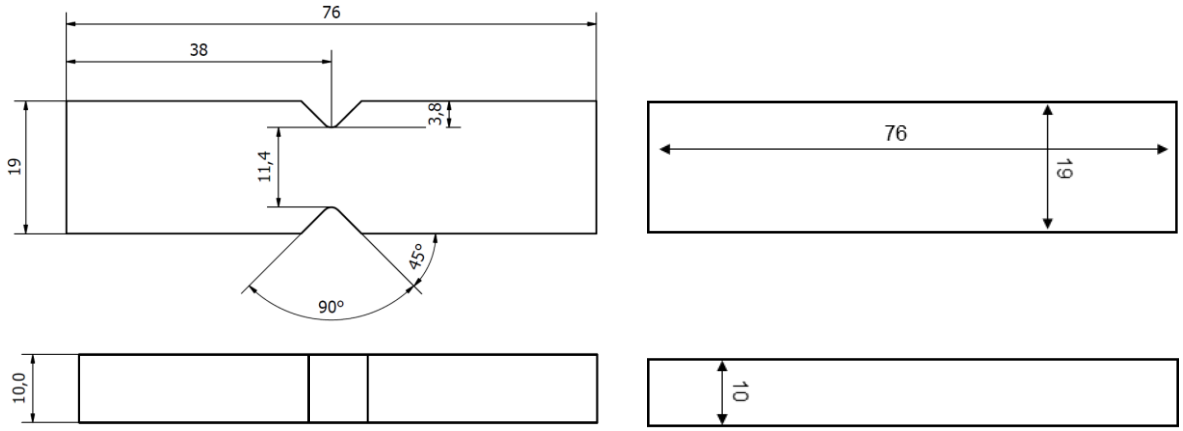

a b

Figure 95: Iosipescu's sample. a) Standard geometry (98)*; b) Sample without notch*

In agreement with the reference system proposed in Figure 94, the Iosipescu samples are extracted along the 1 direction of the particleboard, as reported in Figure 96. To validate the values of the core's shear modulus obtained by TPBTVS, the boards tested had 18mm and 38mm thickness. Panels of 8mm thickness are not suitable for the Iosipescu's load system, where only specimens with thickness equal to 19mm±1mm can be tested.

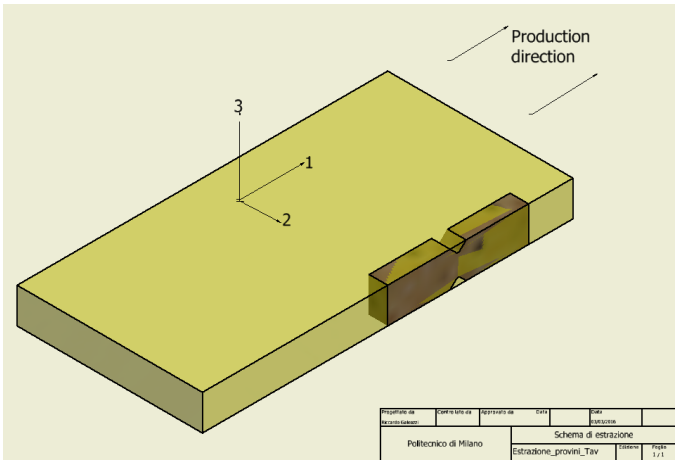

Figure 96: Iosipescu's samples extraction from the main board

Considering this prescribed value of thickness, the panel with thickness equal to 38mm had to be modified. Given the interest for the shear modulus of the core's particleboard, the skins of the 38 mm panels were removed in favour of the core in agreement with the Iosipescu device (maximum 19mm). The skins were mechanically removed using a planer. The geometry of the Iosipescu's sample with the thickness core equal to 19mm starting from 38mm after machining is reported in Figure 97. For the samples extracted from particleboard of 18mm of thickness, the planer's procedure was not necessary because the thickness was in agreement with the device and the thickness of the core was considered after post elaboration.

a b c

Figure 97: Iosipescu samples. a) Original raw geometry of 38mm; b) After the skin's discharge; c) Iosipescu core sample starting from panel with thickness equal to 38mm.

To perform Digital Image Correlation (DIC) measurements of the displacement and strain for the validation procedure of the particleboard core's shear modulus, it is necessary that the framed region of interest of the sample has:

- High contrast obtained by deposing the black speckle on the white surface
- Planarity.

For the Three Points Bending Test the ROI framed includes the load nose and the deflectometer and extends to the support, while the Iosipescu's ROI frames the entire central portion around the notches.

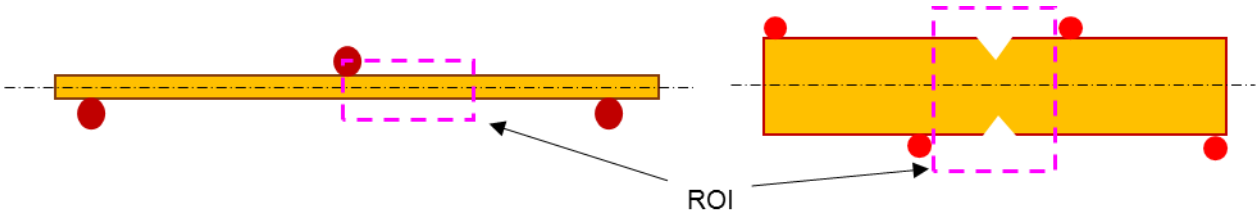

Figure 98: TPBT and Iosipescu tests ROIs

To maximise the surface's planarity, the surface voids had to be filled by deposing a thin layer of wood plaster. Then the surface was abraded using by sandpaper of 60 and 120 grit size to control the planarity. After this, I painted the ROI by two layers of white spray-paint (RAL9005OP). Finally, I created the black speckle in agreement with the DIC calibration performed in the previous Section using black spray-paint (RAL9010OP) on the previously obtained white layer. The workflow proposed it is shown in the diagram in Figure 99.

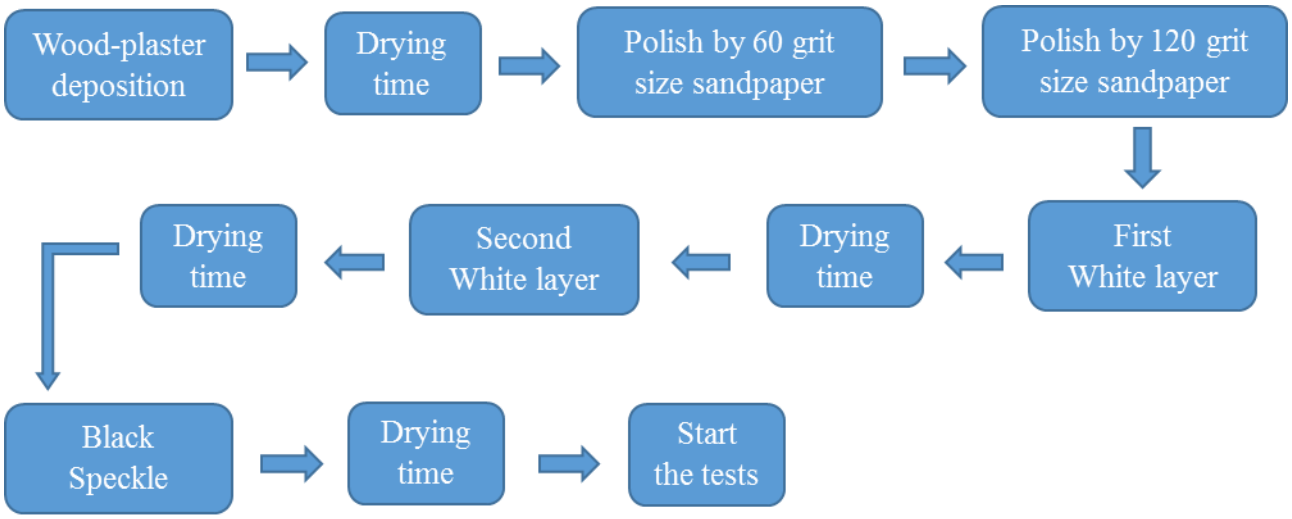

Figure 99: Workflow to produce the suitable ROI of the specimen for DIC measurement

Figure 100 reports the ROI surfaces of the samples after the steps reported in Figure 99.

a b

Figure 100: DIC Samples. a) Iosipescu test; b) TPBT test

Figure 101 a) and b) reports the reference images acquired at the beginning of the Iosipescu and Three Points Bending Tests, respectively.

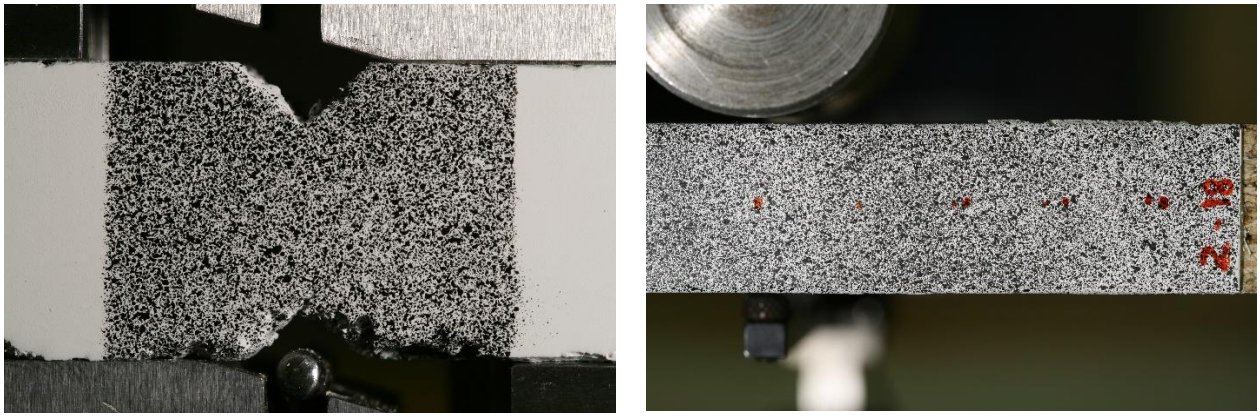

a b

Figure 101: Reference images to DIC acquired to perform particleboard core's shear modulus validation. a) Iosipescu Test; b) Three Points Bending Test.

3.3 Elastic constants determination by Three Point Bending Test

In order to determine the elastic constants by TPBT, the particleboard samples were modelled as a sandwich panels in agreement with the Vertical Density Profile shape. In this manner, the total deflection generated by the three points bending load condition can be expressed by two factors: pure shear and pure bending contributions. The shear deformation is related to the shear modulus of the core (considering negligible the shear contribution of the skins), while the flexural deformation is governed by the longitudinal modulus (assuming no difference between tensile and compression) of the skins, as reported in (34). The related theoretical stress distribution in the skins and in the core of the particleboard treated as a sandwich are schematically reported in Figure 102.

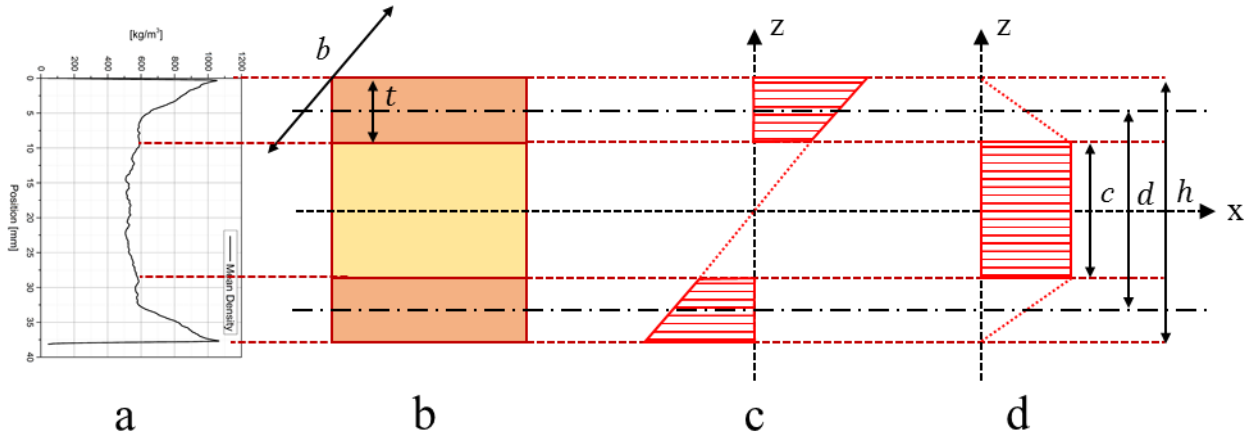

Figure 102: Bending stresses theoretical distribution. a) Vertical Density Profile; b) Sandwich model of the particleboard; c) Normal stress in the skins; d) Shear stress in the core

It is clear that exact knowledge the skins and core thicknesses, respectively *t* and *c* in Figure 102a and in Figure 102c, becomes crucial to well estimate the elastic constants. To define correctly the thicknesses *t* and *c*, qualitative and statistical analyses were performed on the Vertical Density Profiles (VDP) proposed in Figure 77. It is reasonable to postulate that the thickness of the skins is reached when the gradient of the density changes, as it is observed in the core. To identify the point of change, VDP's are statistically analysed approximating the skins density by a linear regression and the core's density by a quadratic interpolation.

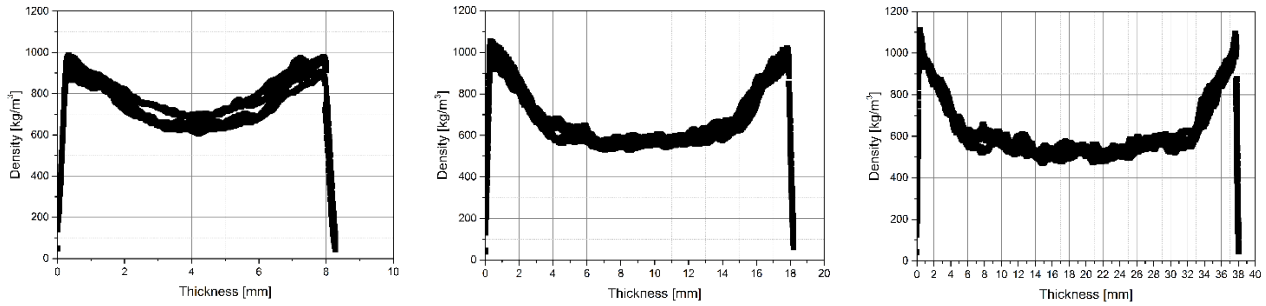

a b c

Figure 103: Density clouds from industrial measurements. a) 8mm; b) 18mm; c) 38mm

To perform these analyses (for the sake of brevity only the one performed for 38mm panel will be reported), the VDPs measured in Chapter 2 was saved as a cloud of points for every thickness measurement as shown in Figure 103. To interpolate linearly the skin zones profiles, a Matlab's algorithm was implemented to calculate the coefficient of determination R^2 (100) iteratively, by increasing at every iteration the number of density points considered.

$$R^2 = 1 - \frac{SS_E}{SS_T} \qquad \text{eq. 30}$$

where SS_E is defined as error sum of squares (Eq.31) and SS_T is the total sum of squares (Eq.32)

$$SS_E = \sum_{i=1}^{n}(y_i - \hat{y}_i)^2 \qquad \text{eq. 31}$$

where $\hat{y}_i$ are estimated value by linear or quadratic relations, and y_i are the real data points.

$$SS_T = \sum_{i=1}^{n}(y_i - \bar{y})^2 \qquad \text{eq. 32}$$

where the $\bar{y}$ is the mean value.

The estimation $\hat{y}_i = \widehat{\beta_0} + \widehat{\beta_1} x_i$ evaluated by linear regression for each skin corresponds to the maximum R^2 reached. In a similar way, the core region is treated by polynomial regression directly considering all density points available in the core thickness.

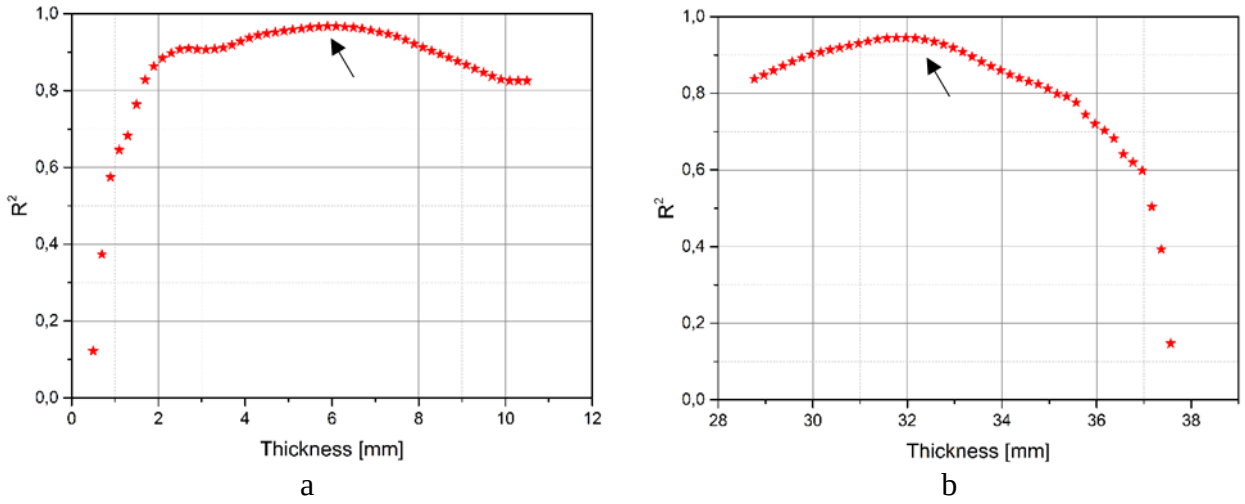

Figure 104: R^2 to select the suitable linear equation to interpolate the density of the skins (black arrows). a) Upper skin; b) lower skin.

Observing Figure 104, it clearly appears that the linear equations that relate the density to the thickness that maximise the R^2 is defined over 6mm for both upper and lower skins. However, it may happen that the intersection between the quadratic interpolation of the core and the linear interpolations of the skins are symmetric, as reported in Figure 105 (see the red arrows).

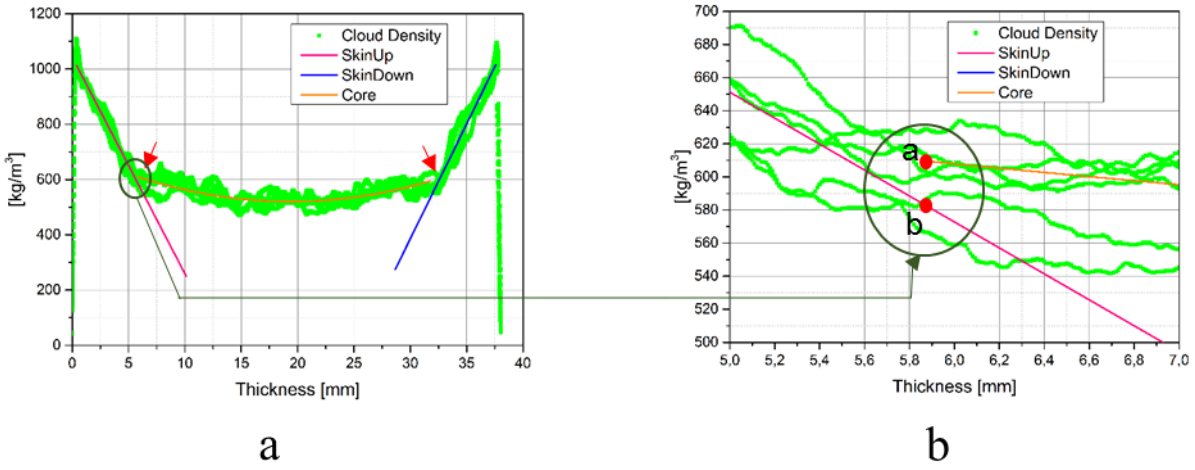

Figure 105: a) first tentative interpolation of the skins and core; b) magnification

To define a unique, symmetric position of the intersections between the two regression curves, I assumed a mean density value between densities *a* and *b* for each skin (referring to Figure 105b). This assumption cause a small decrease of the R^2 value of the linear regressions of the skins and quadratic interpolation of the core density but guarantees a symmetric intersection between the approximating curves, as shown in Figure 106.

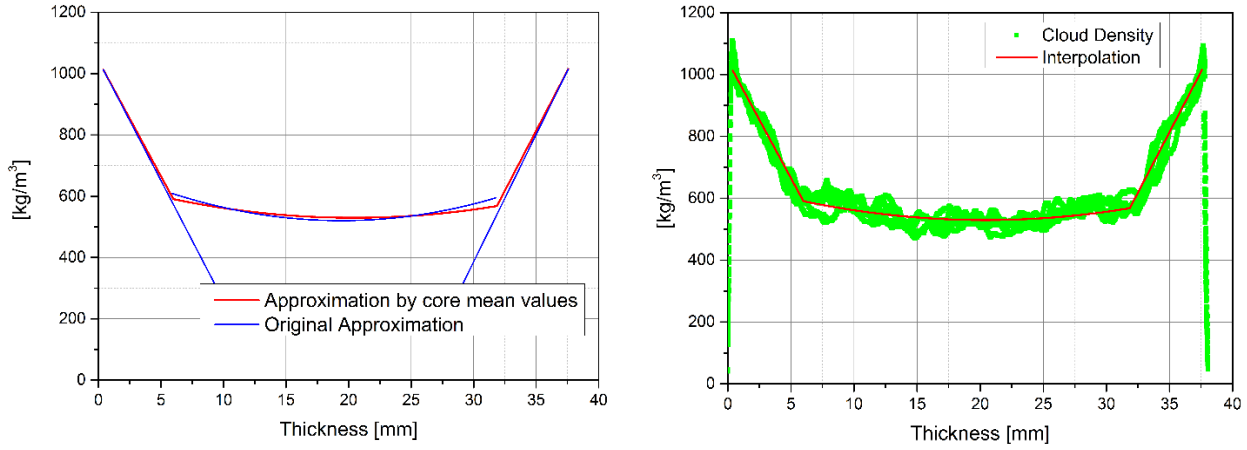

Figure 106: Density profile interpolation. a) Comparison between the approximations; b) final results.

These analyses were repeated for 18mm and 8mm thick samples, to obtain the thickness of the skins and cores reported in Table 30. Herein the qualitative values of the skins and core thicknesses obtained superimposing the millimeter paper on the board thickness and using a vernier caliper are confirmed by the values in the brackets obtained by statistical analyses.

Table 30: Geometrical dimensions of skins and cores for each panel. In the brackets there is the thickness evaluated by statistical analysis

Board Type [mm]	Skins Thickness [mm]	Core Thickness [mm]	Real board thickness [mm]
38	6 (6.1)	25.8 (25.6)	37.8
18	4 (4.005)	10 (9.89)	17.9
8	3 (2.95)	2 (2.1)	8.0

Knowing all the geometrical dimensions of the boards modelled as a sandwich panel, it was possible to run the identification algorithms to evaluate the elastic constants of the different types of particleboard samples, in particular:

- Elastic longitudinal modulus of the skins: E_f
- Elastic longitudinal modulus of the core: E_c
- Elastic shear modulus of the core: G_{13}

This first elastic constants evaluation was performed following the diagram reported in Figure 107, starting to collect the load-strain data by the set-up proposed in Section 3.2.1 (Figure 108).

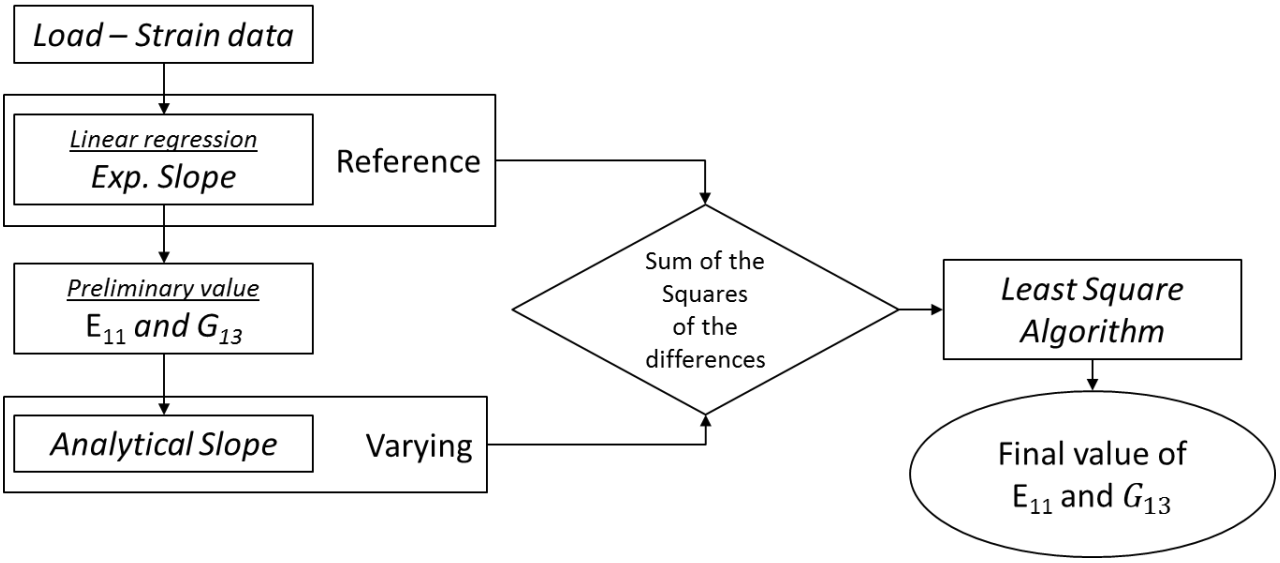

Figure 107: Elastic constants evaluation algorithm.

This algorithm is normally applied to determine the elastic constants of the sandwich panels or CFRP composites as reported in (37), (39) or (42). However, a similar technique is applied to the solid wood characterization as a reported in (101) where the authors verified the applicability of the Timoshenko bending theory by TPBT and proposed an empirical relationship to derive values of the shear modulus of solid woods.

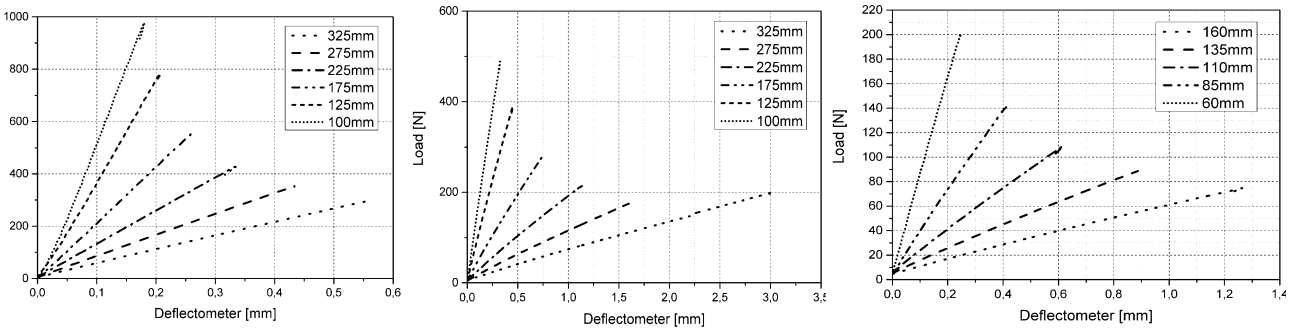

a b c

Figure 108: TPBTVS load-strain curves. a) 38mm; b) 18mm; c) 8mm

Treating the particleboard as an orthotropic material, by a series of Three Points Bending Tests (TPBTVS) with varying span between the supports, it is possible to determine, by a proper optimization algorithm, the values of the relevant elastic constants listed above (E_c; E_f and G_{13}). The scope of varying the span is to enhance the shear contribution of the core of the panel on the total deflection measured by deflectometer, obtaining a transition of the behavior of the beam from that of a slender beam to than of a thick beam, as the distance between the supports decreases. In agreement with the internal forces reported in Figure 83, the tests are conducted imposing a crosshead speed equal to 12mm/min. The load *P* was increased proportionally to the distance between the supports,

in order to keep maximum bending moment constant, although taking care of remaining in the strain range corresponding to the linear elastic behavior of the material (Table 31).

Table 31: maximum load and related strain for the TPBTVS

Span [mm]	38mm		18mm		8mm	
	P[N]	δ_{exp} [mm]	P[N]	δ_{exp} [mm]	P[N]	δ_{exp} [mm]
325	300.5	0.566	150.1	2.089	-	-
275	355.5	0.437	177.0	1.495	-	-
225	433.5	0.339	217.1	1.053	-	-
175	558.3	0.262	279.3	0.690	-	-
160	-	-	-	-	75.1	1.092
135	-	-	-	-	89.1	0.762
125	782.5	0.207	390.6	0.414	-	-
110	-	-	-	-	109.3	0.527
100	977.5	0.180	489.12	0.304	-	-
85	-	-	-	-	141.4	0.348
60	-	-	-	-	200.8	0.210

Considering the linear elastic curve segments in agreement with standard (32), it is possible to calculate the experimental slope Δ_{exp} with the relation expressed in Eq. 33:

$$\Delta_{exp} = \frac{P_1 - P_2}{\delta_1 - \delta_2} \qquad \text{eq. 33}$$

where P_1 and P_2 are respectively the loads higher (40% of P_{max}) and lower (10% of P_{max}) limits of the linear elastic zone on the load-strain curves and δ_1 and δ_2 are the corresponding deflections.

This experimental slope values (Eq.33) are compared with the analytical ones expressed in Eq. 34

$$\Delta_A = \frac{P_1}{\delta_A} \qquad \text{eq. 34}$$

The analytical deflection is composed of two contributions flexural and shear components $\delta_A = \delta_{fl} + \delta_{sh}$. Pure flexural deflection is major governed by the elastic longitudinal modulus of the skins of the panel and can be expressed by Eq. 35:

$$\delta_{fl} = \frac{P_1 * L^3}{48 * D} \qquad \text{eq. 35}$$

where L [mm] is the distance between the supports and D [N/mm^4] is the flexural stiffness of the specimen. Pure shear deflection is governed by the shear elastic modulus G_{13} of the core and it is expressed by Eq. 36:

$$\delta_{sh} = \frac{P_1 * L}{4 * G_{13} * A} \qquad \text{eq. 36}$$

where A [mm^2] is area of the core's cross section, expressed by b x c (Figure 109a). For a sandwich beam, the real shear stress distribution is slightly parabolic in the core portion and linear in the skins portion (Figure 109b). It is reasonable to consider that in the core portion the stress is modelled by the relationship $\frac{P}{b*c}$ that assumes the shear trend constant along the core thickness, as a reported in Figure 109c (102). Observing the shear stress in the core is considered constant and the shear value at the red points (see Figure 109c) not null, the shear factor is reasonably assumed equal to one. To define completely the analytical deflection it is necessary to express the flexural stiffness D of the particleboard's beam treated as a sandwich panel. To define this value D, three different sandwich models were proposed, characterized by a different degree of approximation to the real density profile (35):

- Pure Sandwich Model (PSM) → D
- Bi-linear Sandwich Model (BSM) → $D_{Bi\text{-}Lin}$
- Quadratic and Bi-linear Sandwich Model (QSM) → $D_{Quad\text{-}Bi\text{-}Lin}$

In the PSM model, the modulus of the skins is assumed to be constant through their thickness, equal to the average value of the actual linear distribution. The flexural stiffness D is expressed by Eq. 37 in agreement with (34); (96); (102) and (103):

$$D = 2 * \frac{E_{f11} * b * t^3}{12} + 2 * \frac{E_{f11} * b * t * d^2}{4} + \frac{E_{c11} * b * c^3}{12} \qquad \text{eq. 37}$$

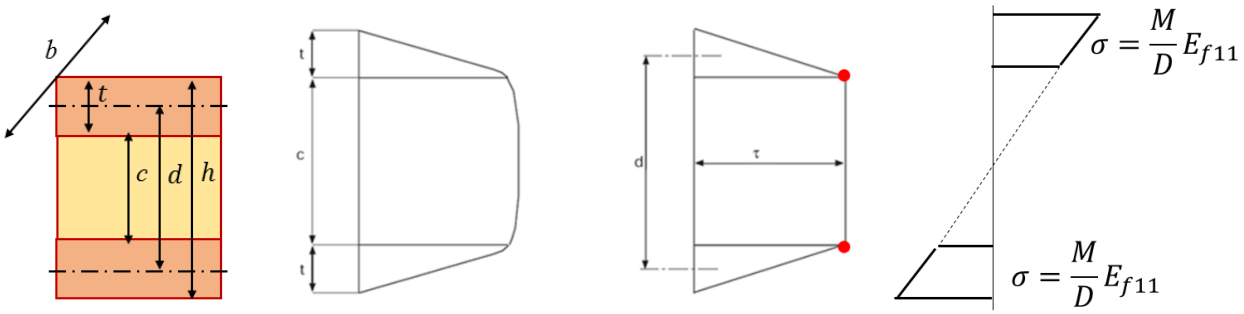

Figure 109: a) geometrical quantities of particleboard's model; b) real shear stress distribution in a sandwich beam; c) Modelled shear stress in a sandwich beam; d) Modelled normal stress in a sandwich beam

where geometrical quantities *b; t; d* and *c* considered in [mm] are shown in Figure 102 Figure 109a.

This relationship is normally used to model flexural behavior of real sandwich panels, where the skins are homogenous materials and the E modulus is constant and does not varies linearly as in particleboard's skins case. Using the relationship of Eq. 37, means modelling the skin's stiffness of the particleboard considering E_{f11} as the mean value of Young modulus over the skins' thickness (neglecting the linear variation of the E_{f11}) and E_{c11} as the mean value of the Young modulus of the core, as reported in Figure 110a.

Knowing the density profile shape and using the relationship $E = 5494.2 * \rho - 1845.4$ from the available literature (35), it is possible to visualize the expected shape of the curve representing the variation of the elastic modulus with the position through the thickness (Figure 110).

To better reproduce the E-modulus shape, a second model has proposed, the BSM. In this model, a bi-linear symmetric relationship between the Young modulus and the position through the thickness was assumed. Considering this assumption, the elastic modulus trend in the particleboard skins now becomes linear, as reported in Figure 110b. To implement the BSM it is necessary to redefine the expression of the flexural-stiffness D in $D_{Bi\text{-}Lin}$ to represent the linear variation of E-modulus through the thickness of the skins. It is also necessary to express the linear equation between the elastic modulus in the core E_c (still constant), and maximum elastic modulus in the skins E_{max}. The new mathematical expression of $D_{Bi\text{-}Lin}$ becomes (Eq.38):

$$D_{Bi-Lin} = \frac{1}{12} * E_{c11} * c^3 * b + 2 * b * \int_{\frac{c}{2}}^{\frac{h}{2}} (q + my) * y^2 dy \qquad \text{eq. 38}$$

where q is the intercept and m is the slope of the linear segment between E_{c11} and E_{max11}. The free coordinate along the skins thickness is y and $\frac{c}{2}$ and $\frac{h}{2}$ are the two extremes that represent the skins' thickness.

The third model, the QSM, takes in to account the parabolic shape of the density profile, and correspondingly that of the elastic modulus of the core. This new stiffness shape of the core is obtained writing the second order polynomial equation through two Young modulus points E_{c11} and E_{min11}, and symmetrical about the middle axis of the panel (Figure 110c). The new mathematical expression of flexural stiffness $D_{Quad\text{-}Bi\text{-}Lin}$ now becomes (Eq.39):

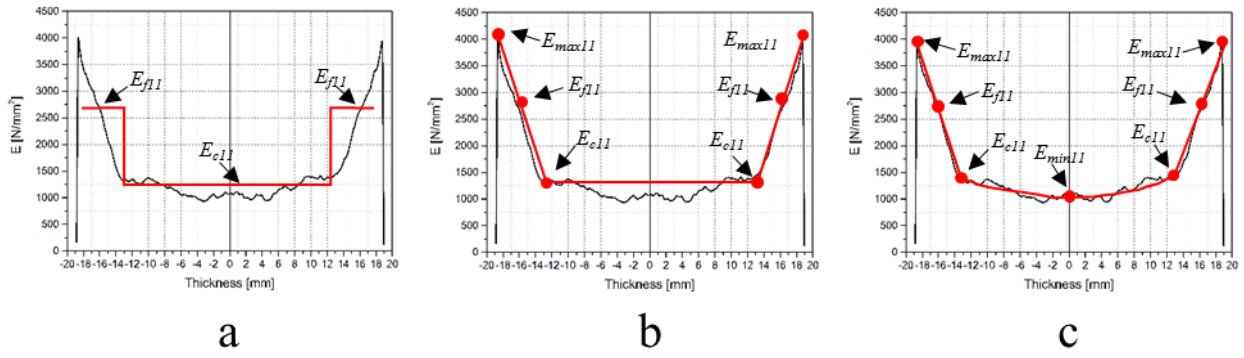

Figure 110: three sandwich models to express the flexural stiffness. a) Pure sandwich model (PSM); b) Bi-Linear sandwich model (BSM); c) Quadratic-Bi-Linear sandwich model (QSM)

$$D_{Quad-Bi-Lin} = b * \int_{-\frac{c}{2}}^{\frac{c}{2}} (ky^2 + wy + n) * y^2 dy + 2 * b * \int_{\frac{c}{2}}^{\frac{h}{2}} (q + my) * y^2 dy \qquad \text{eq. 39}$$

where *k*, *w*, and *n* are quadratic function's constants between E_{c11} and E_{min11} and the free coordinate *y* along the core thickness varying from $-\frac{c}{2}$ to $+\frac{c}{2}$.

The different expressions of the deflection δ_A were used to evaluate the analytical slope reported in Eq. 34. Then the difference between the experimental slope, considered as a reference, (Eq.33) and the analytical slope was minimized by varying the value of the in-plane elastic modulus of the skins (E_{f11}) and core (E_{c11}; E_{min11}), and out of plane shear modulus of the core (G_{13}), to reach the optimum solution and determine elastic constants of the particleboard. This optimization was performed for every model (PSM; BSM; QSM) using the Generalized Reduced Gradient implemented in Excel.

The next tables report the elastic constant results from this optimization algorithm performed on PSM (Table 32), BSM (Table 33) and QSM (Table 34); the mean values and standard deviations are calculated on five particleboard' samples extracted along the 1 direction of particleboard panels in agreement with the reference system shown in Figure 94.

Table 32: Particleboard's elastic constants results by Pure Sandwich Model (PSM) (Temperature equal to 26°C and humidity equal to 35%).

Board Tick.	E_{f11} [MPa]		E_{c11} [MPa]		G_{13} [MPa]	
[mm]	Mean	St. Err.	Mean	St. Err.	Mean	St. Err.
38	2631	19	1034	2	137	5
18	2466	76	1020	3	224	4
8	2986	160	1092	9	476	51

Table 33: Particleboard's elastic constants results by Bi-Linear Sandwich Model (BSM) (Temperature equal to 26°C and humidity equal to 35%).

Board Tick. [mm]	E_{f11} [MPa]		E_{c11} [MPa]		E_{max11} [MPa]		G_{13} [MPa]	
	Mean	St. Err.	Mean	St. Err.	Mean	St. Err.	Mean	St. Err.
38	2337	31	1424	73.3	3250	126	137	4
18	2218	62	1111	15	3324	110	223	5
8	2419	123	1287	37	3550	211	520	31

Table 34: Particleboard's elastic constants results by Quadratic and Bi-Linear Sandwich Model (QSM) (Temperature equal to 26°C and humidity equal to 35%).

Board Tick. [mm]	E_{f11} [MPa]		E_{c11} [MPa]		E_{max11} [MPa]		G_{13} [MPa]	
	Mean	St. Err.	Mean	St. Err.	Mean	St. Err.	Mean	St. Err.
38	2450	59	1309	15	3503	36	139	4
18	2320	106	1531	20	2927	122	228	5
8	2551	170	1790	17	3189	170	628	32

The results of the PSM model appear to be not in agreement with those of the BSM and QSM models, that gave results in better agreement with each other. The deviations of BSM results for QSM ones are reported in Table 35. The maximum difference is for E_{c11}, while for the other constants, the difference between the two models is lower than 15%. G_{13} for the 18mm panels has a difference equal to 2.2%.

Except for E_{c11}, for the others elastic constants, there is compatibility between Bi-linear and Quadratic-Bi-linear sandwich models, in particular for G_{13} of 38mm and 18mm of board's thickness. Particleboard with 8mm of thickness is not included in the comparison listed in Table 35 due to the core thickness slightest.

Table 35: Deviation between BSM and QSM

Board Tick. [mm]	E_{f11} [%]	E_{c11} [%]	E_{max11} [%]	G_{13} [%]
38	4.6	34.6	7.2	1.1
18	4.4	12.8	13.6	2.2

The values of the elastic constants obtained by the TPB method with varying span were then validated by the DIC technique, especially for the most diffused type of panels of thickness equal to 18 and 38mm, as is reported in the next Section.

3.4 Analysis of the relationship between panel density and Elastic longitudinal modulus profiles

Considering the elastic constants reported in Table 33 and in Table 34 in particular, E_{c11}, E_{f11} and E_{max11} (in the longitudinal direction) and relating these quantities to the correspondent density measured in Section 2.5.2 by the industrial density detector, I derived the relationships that expresses the elastic modulus as a function of the known density. It is important to remember that the longitudinal modulus is obtained considering a linear relationship with the position through the thickness in the skins (BSM approach). The *E*-modulus of the core was treated considering it constant or quadratic (QSM approach) through the thickness of the core.

Figure 111 reports two regressions, one linear and another quadratic, between density and the elastic modulus of particleboard for 8mm, 18mm and 38mm thicknesses. These regressions were compared with the statistical relationships found in the literature (35), where the authors derived the E-ρ relation for a virgin wood particleboard. This relation is one of the few statistical relationships found in literature derived for similar particleboard to that studied in this thesis.

The statistical relationships obtained using experimental data reported in this thesis are reported in Eq.40 to Eq. 45, where the elastic moduli used are those calculated considering a constant value in the core (BSM model). In particular, Eq. 40; Eq. 41 and Eq. 42 are obtained considering a linear relationship of E with density for every panel's thicknesses, while Eq. 43; Eq.44 and Eq. 45 are developed considering a quadratic regression imposing the intercept equal to zero, to ensure that for a density of the panel equal to zero, the elastic modulus is actually zero. Concerning the linear relationships (the intercept is different from zero), it will be necessary to define the range of applicability appropriate for particleboard.

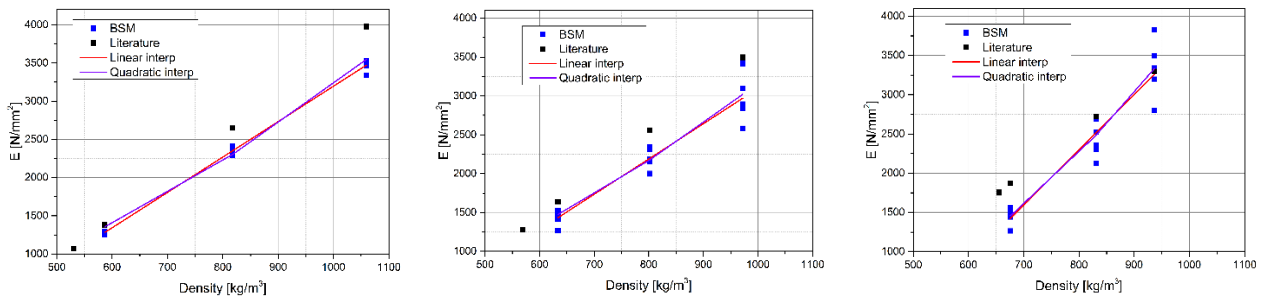

a b c

Figure 111: Density – E11 modulus relationship starting from elastic constants determined by TPBTVS and Bi-Linear Sandwich Modulus (BSM). a) 38mm; b)18mm; c) 8mm.

$E11 = 4.64 * \rho - 1439$ (R^2=0.997) *Thickness equal to 38mm* eq.40
$E11 = 4.54 * \rho - 1442$ (R^2=0.922) *Thickness equal to 18mm* eq.41
$E11 = 7.07 * \rho - 3359$ (R^2=0.903) *Thickness equal to 8mm* eq.42
$E11 = 0.0022 * \rho^2 + 1.0175 * \rho$ (R^2=0.991) *Thickness equal to 38mm* eq.43
$E11 = 0.0023 * \rho^2 + 0.8712 * \rho$ (R^2=0.919) *Thickness equal to 18mm* eq.44
$E11 = 0.0054 * \rho^2 - 1.4982 * \rho$ (R^2=0.911) *Thickness equal to 8mm* eq.45

where the *E11* modulus is expressed in *[MPa]* and the density ρ is expressed in *[kg/m^3]*.

In a similar way, similar relationships were obtained for sandwich models based on a quadratic though thickness variation of the elastic longitudinal modulus in the core of the panel (QSM model). Figure 112, reports the values of the elastic moduli as a function of the density for 8mm, 18mm and 38mm of thicknesses, the interpolating curves and the curves corresponding to the statistical relationship found in the literature (35). The new statistical relationships are reported in Eq. 46 to Eq. 51, where the elastic moduli were determined considering quadratic relation in the core (QSM model). In particular, Eq. 46; Eq. 47 and Eq. 48 are obtained considering a linear relationship with density, while Eq. 49; Eq. 50 and Eq. 51 are developed considering a quadratic trend imposing the intercept equal to zero, to ensure that for a density of the panel equal to zero, the elastic modulus is actually zero.

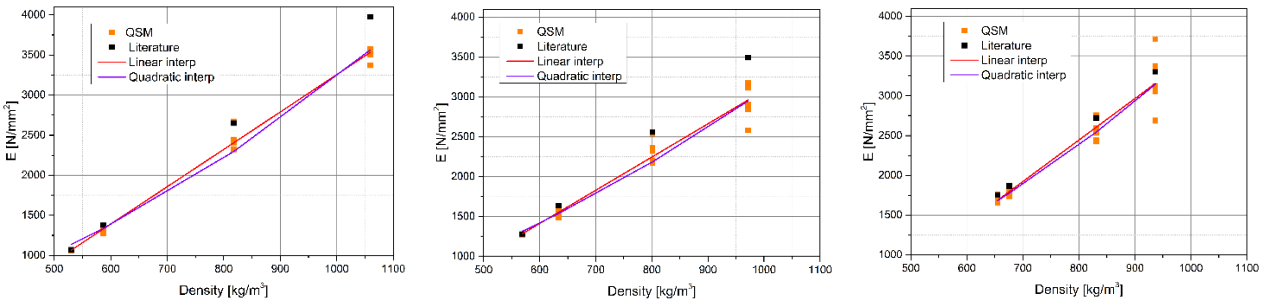

Figure 112: Density – E11 modulus relationship starting from elastic constants determined by TPBTVS and Quadratic-Bi-Linear Sandwich Modulus (QSM). a) 38mm; b)18mm; c) 8mm.

$E11 = 4.65 * \rho - 1405.1$ (R^2=0.994) *Thickness equal to 38mm* eq. 46
$E11 = 4.17 * \rho - 1086.9$ (R^2=0.960) *Thickness equal to 18mm* eq. 47
$E11 = 5.22 * \rho - 1730.4$ (R^2=0.913) *Thickness equal to 8mm* eq. 48
$E11 = 0.0023 * \rho^2 + 0.9263 * \rho$ (R^2=0.986) *Thickness equal to 38mm* eq. 49
$E11 = 0.0018 * \rho^2 + 1.886 * \rho$ (R^2=0.953) *Thickness equal to 18mm* eq. 50
$E11 = 0.0028 * \rho^2 + 0.7352 * \rho$ (R^2=0.915) *Thickness equal to 8mm* eq. 51

It is possible to observe in the charts reported in Figure 111 and in Figure 112 that the results from the literature are in agreement with the proposed relationships even if is possible to observe that the literature points are greater than the experimental obtained in this PhD thesis. This is reasonable if one thinks that the authors of ref. (35) worked on particleboard made of virgin wood, not recycled

like that used in this thesis, thus the properties found in this thesis (E-modulus) as a function of the density are likely to be lower.

3.5 Elastics constants validation: Iosipescu and TPBT coupled with DIC field method

The comparison between the values of the Young moduli obtained by TPBT and the relationships from the literature presented in the previous Section provided a certain degree of validation of results, although limited to values of E. Regarding the values of the shear modulus of the core (G_{13}) another type of validation was necessary, using the Iosipescu techniques and three points bending test experimental techniques coupled with Digital Image Correlation field method to measure the related strain. Moreover, it is important to remind that the panel's core is the zone where modifications are more likely to be introduced to reduce overall weight. For this reason, accurate validation of the core's elastic constant (G_{13}) is fundamental, in the perspective of possible future changes in the composition and the density of the core, also to be able to predict the effect of these changes on the particleboard's performances. The specimens tested are respectively 18mm and 38mm. The set-up used to perform this experimental campaign was reported in Section 3.2.

3.5.1 Iosipescu and DIC validation

The pictures acquired to measure the displacements and the strains in the region of interest of the Iosipescu's samples (Figure 98 and Figure 101a) in agreement with the procedure designed for DIC acquisition (Section 3.2.3) were processed by N-Corr Matlab's subroutine using a DIC-Radius and a Subset spacing equal to 50 and 5 pixels, respectively (Section 3.2.4). To perform this first validation by Iosipescu method, five notched samples were extracted from the first principal direction of the particleboard panels in agreement with reference system shown in Figure 96, are tested.

From Figure 113 to Figure 117 the DIC result for 18mm are presented. In particular, Figure 113 reports the Horizontal displacement U of the sample at four load steps, in similar way Figure 114 reports the vertical displacement V. Figure 115, Figure 116 and Figure 117 visualise respectively the strains ε_x; ε_y and ε_{xy}.

From Figure 118 to Figure 122 the DIC result for 38mm after mechanical removal of the skin, in order to test the core of the panel only, are presented. In particular, Figure 118 reports the Horizontal displacement U of the sample at four load steps. In a similar way Figure 119 reports the vertical

displacement V. Figure 120, Figure 121 and Figure 122 visualise respectively the strains ε_x; ε_y and ε_{xy}.

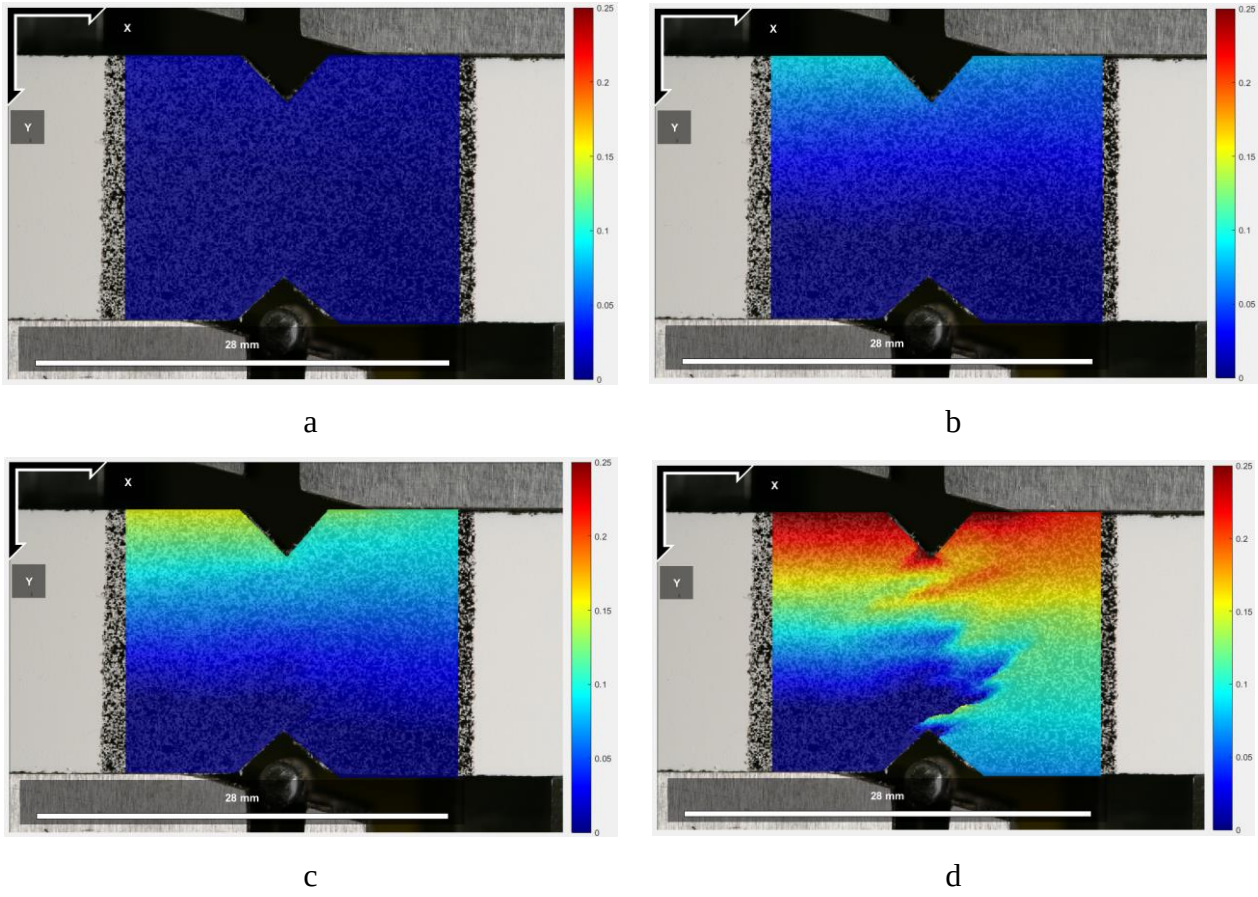

a b

c d

Figure 113: Iosipescu DIC results about Horizontal Displacement (U) reported in [mm] of 18mm sample. a) 10N; b) 100N; c) 210N; d) 360N.

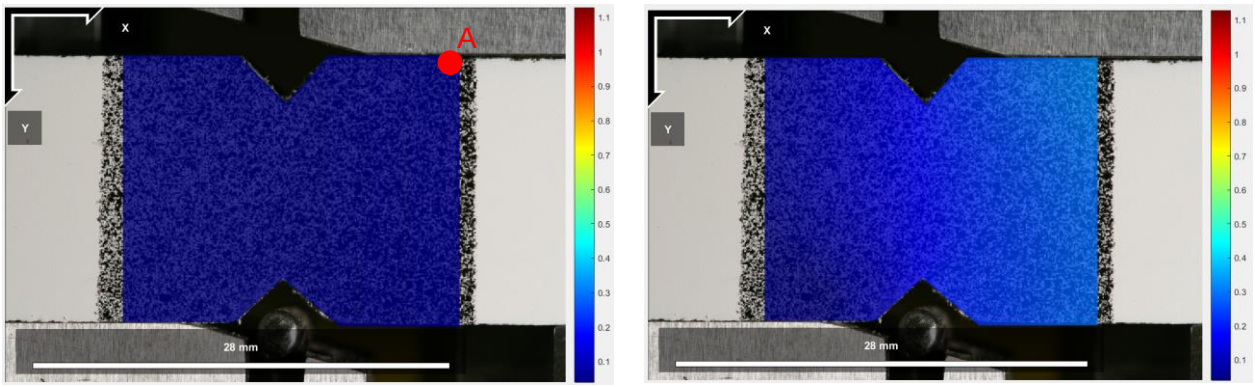

a b

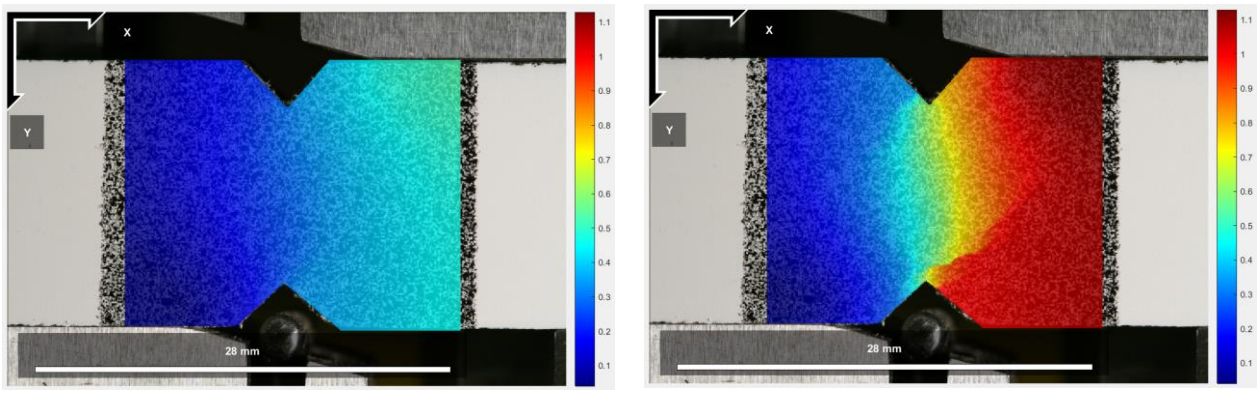

c d

Figure 114: Iosipescu DIC results about Vertical Displacement (V) reported in [mm] of 18mm sample. a) 10N; b) 100N; c) 210N; d) 360N.

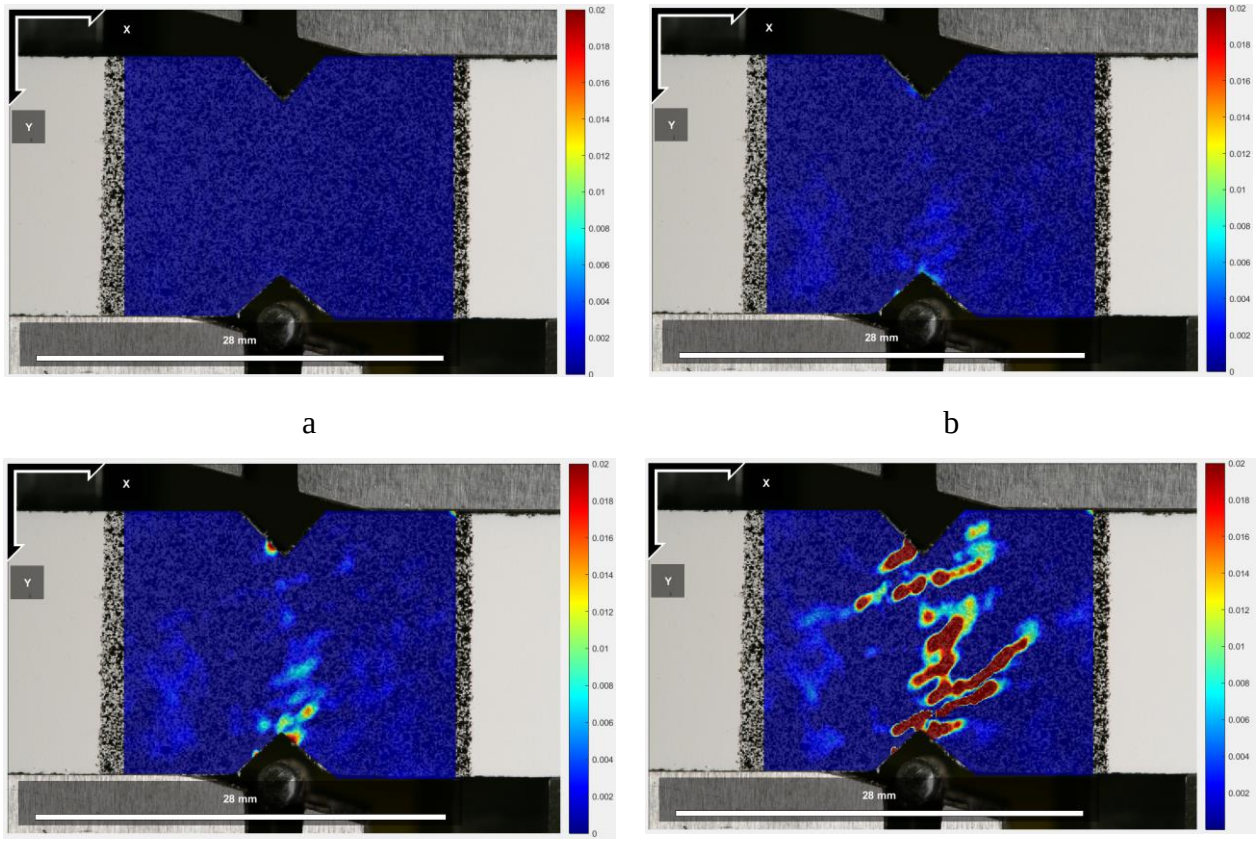

a b

c d

Figure 115: Iosipescu DIC results about ε_{xx} reported in [mm/mm] of 18mm sample. a) 10N; b) 100N; c) 210N; d) 360N.

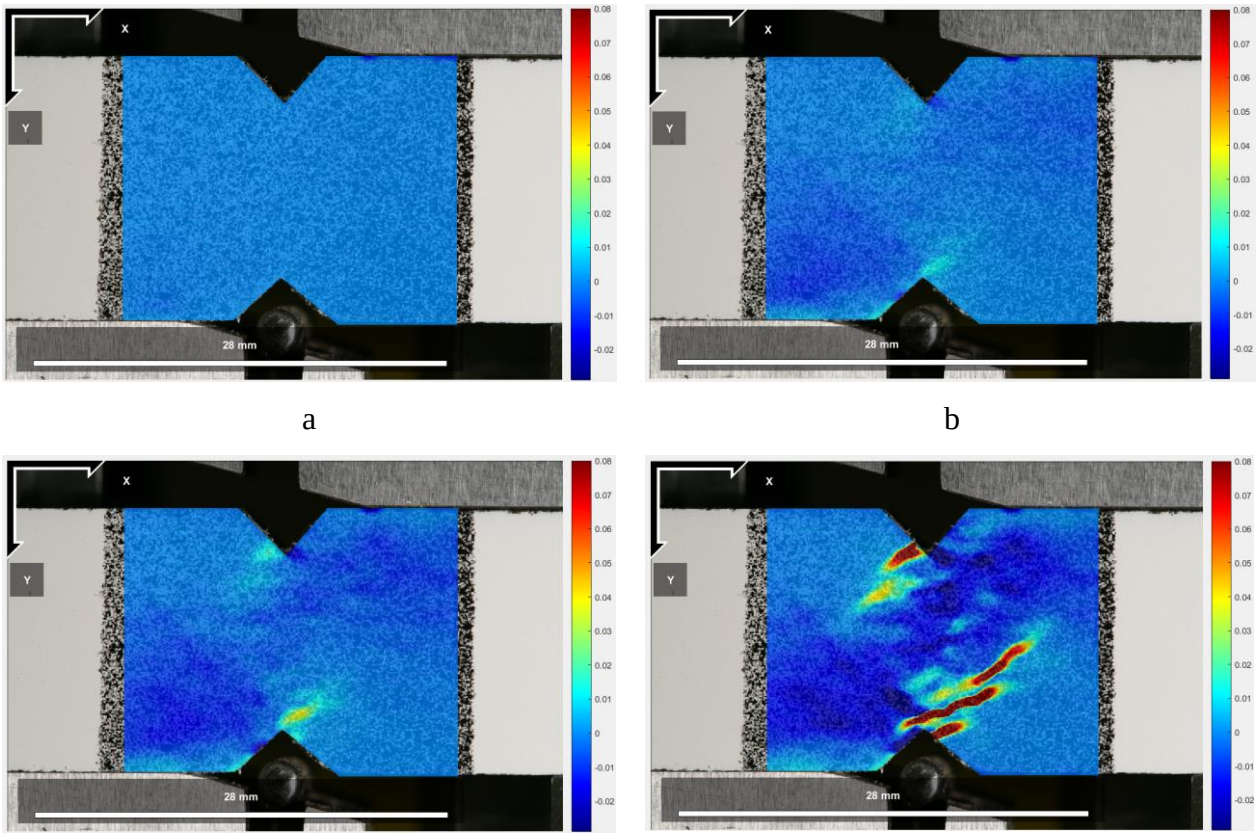

a b

c d

Figure 116: Iosipescu DIC results about ε_{yy} reported in [mm/mm] of 18mm sample. a) 10N; b) 100N; c) 210N; d) 360N.

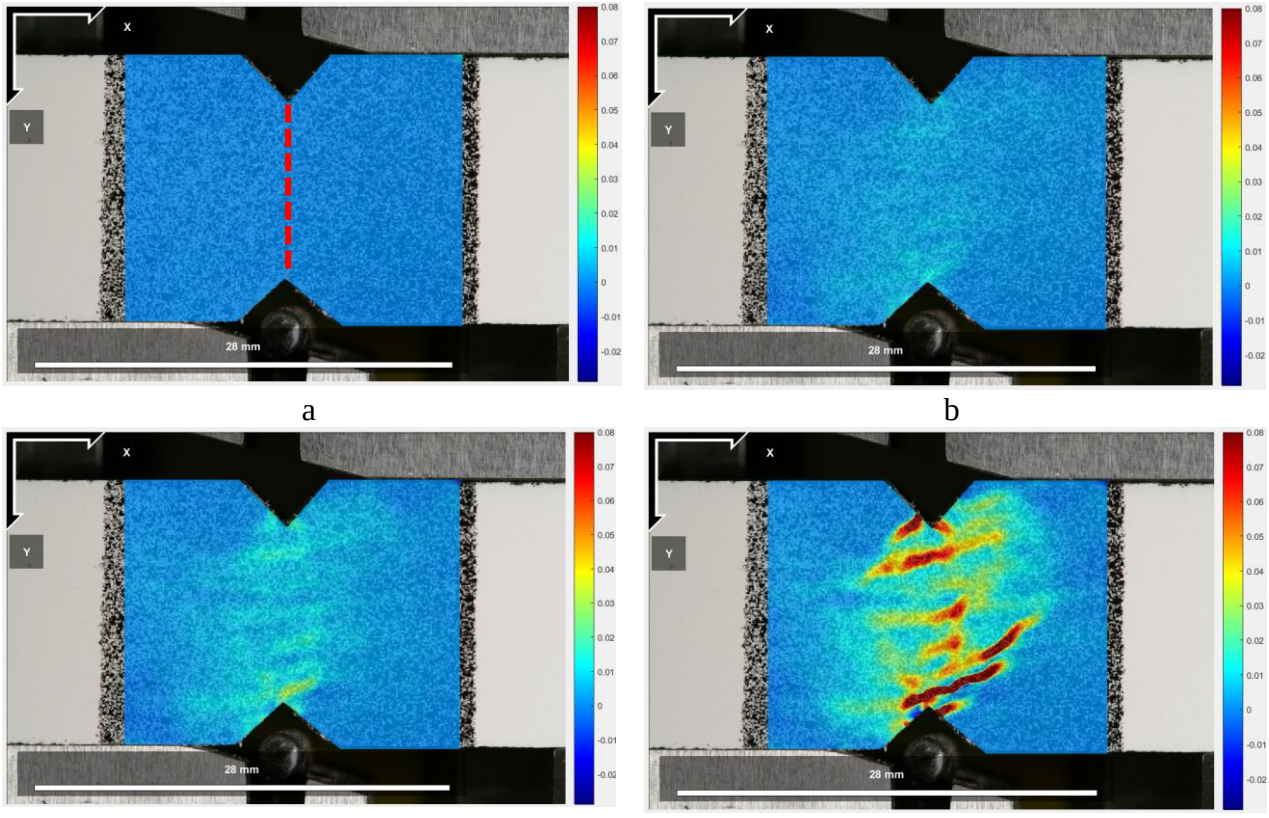

a b

c d

Figure 117: Iosipescu DIC results about ε_{xy} reported in [mm/mm] of 18mm sample. a) 10N; b) 100N; c) 210N; d) 360N.

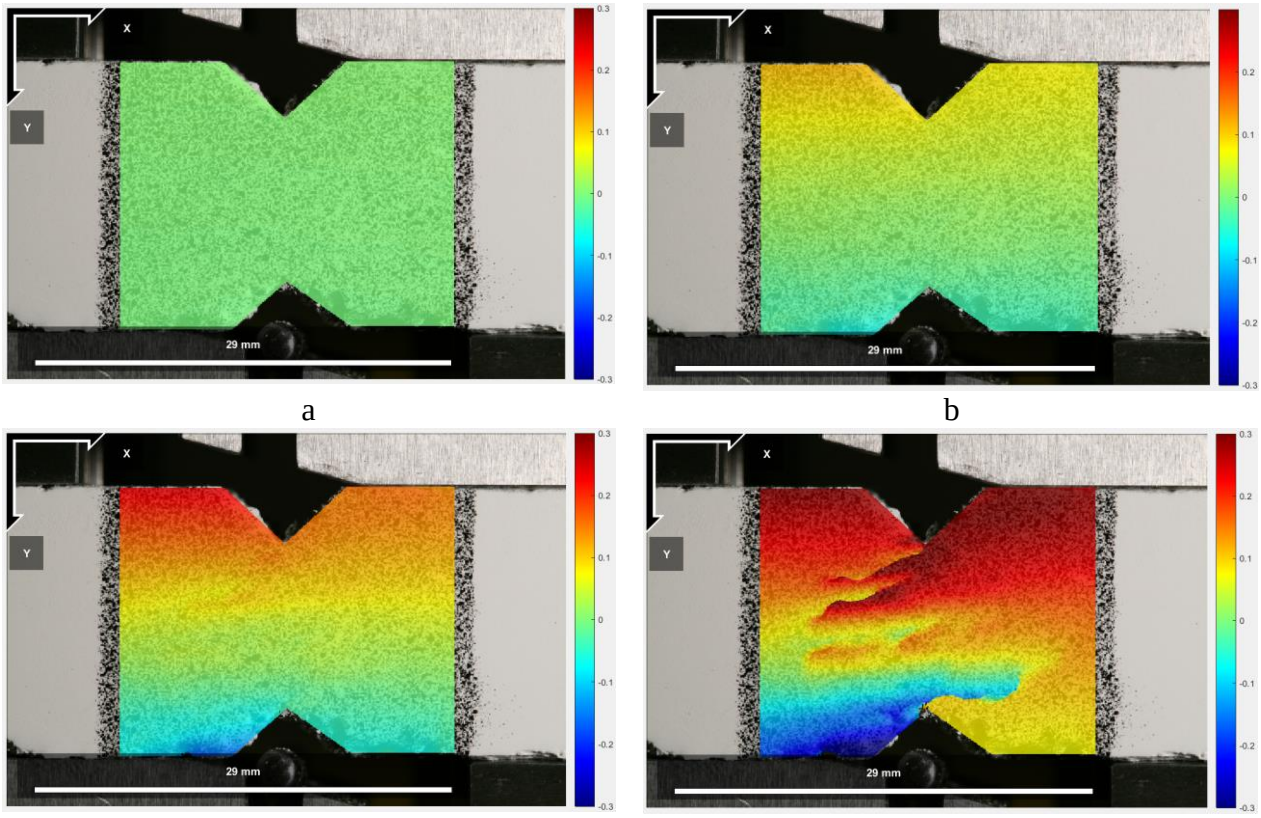

a b c d

Figure 118: Iosipescu DIC results about Horizontal Displacement (U) reported in [mm] of 38mm sample without skins. a) 10N; b) 100N; c) 210N; d) 288N.

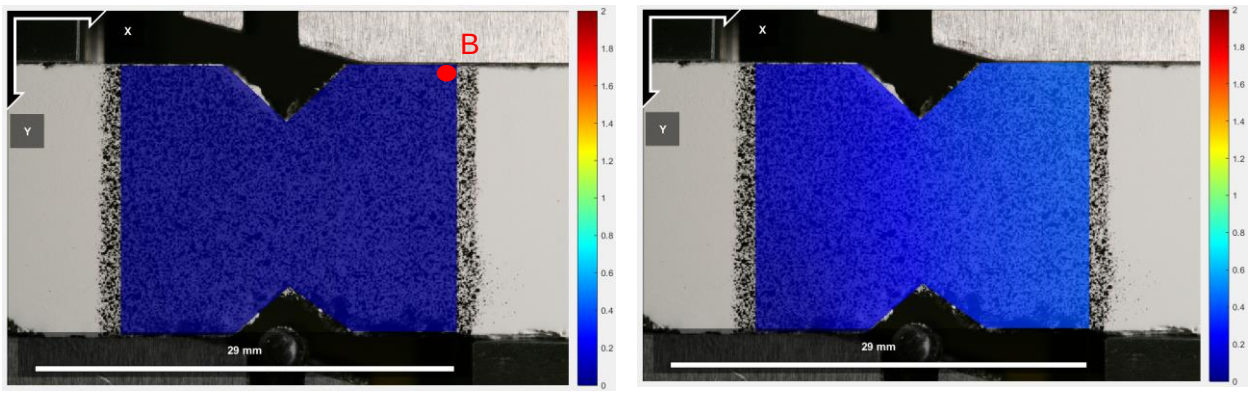

a b

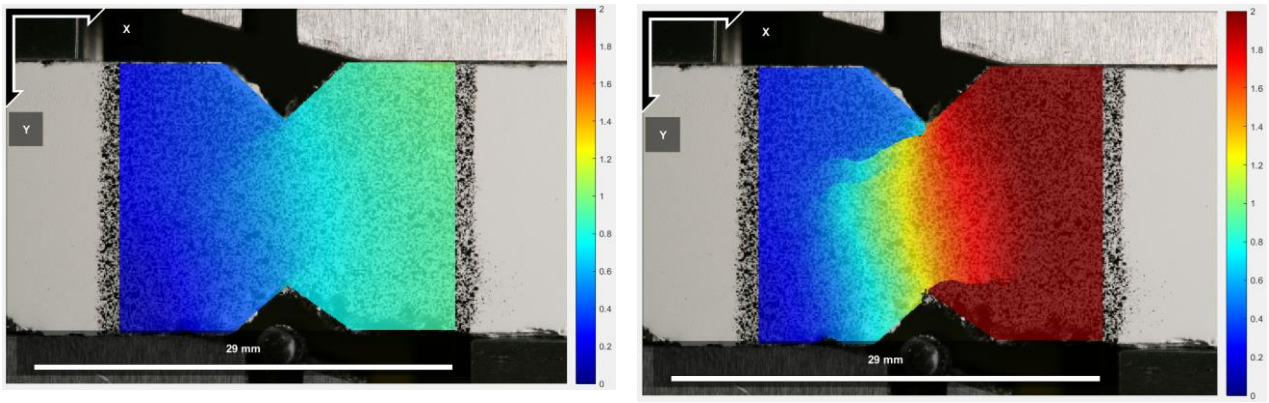

c d

Figure 119: Iosipescu DIC results about Vertical Displacement (V) reported in [mm] of 38mm sample without skins. a) 10N; b) 100N; c) 210N; d) 288N.

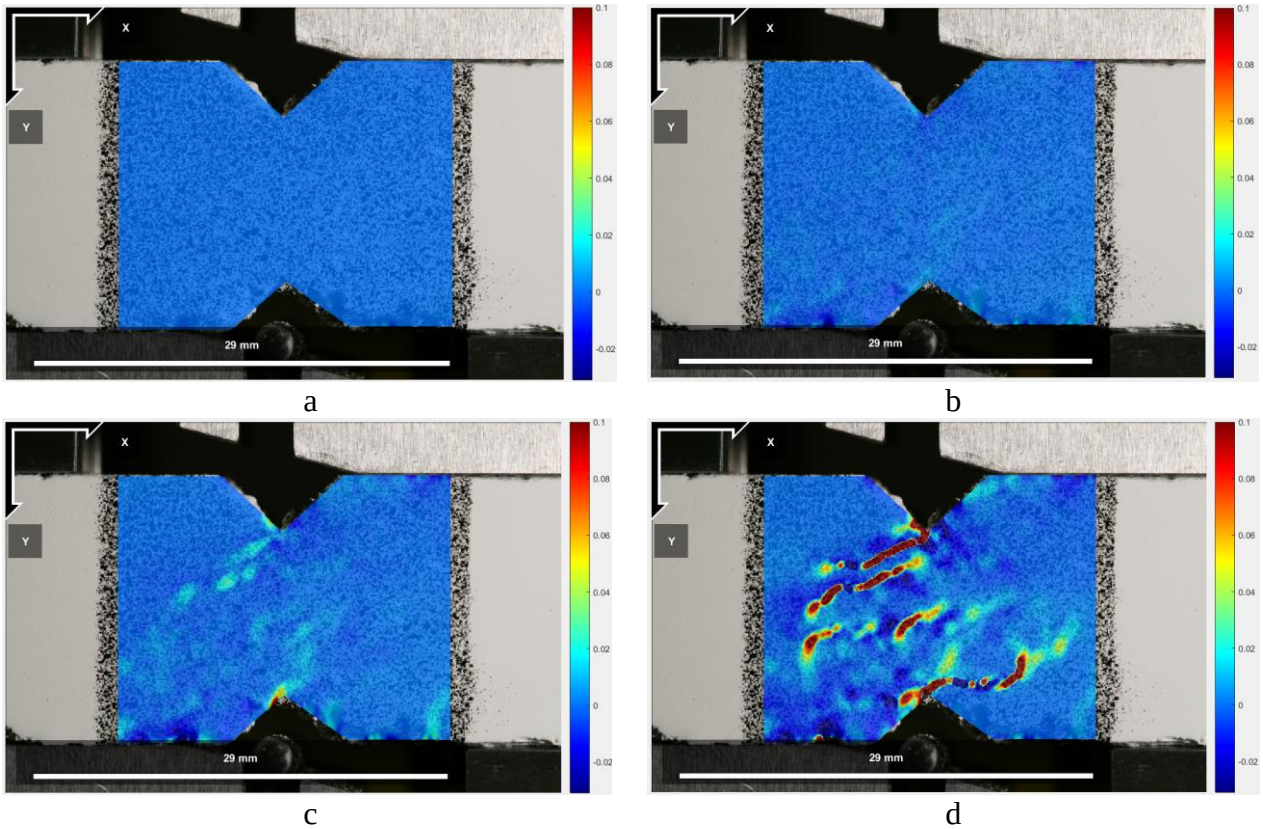

a b

c d

Figure 120: Iosipescu DIC results about ε_{xx} reported in [mm/mm] of 38mm sample without skins. a) 10N; b) 100N; c) 210N; d) 288N.

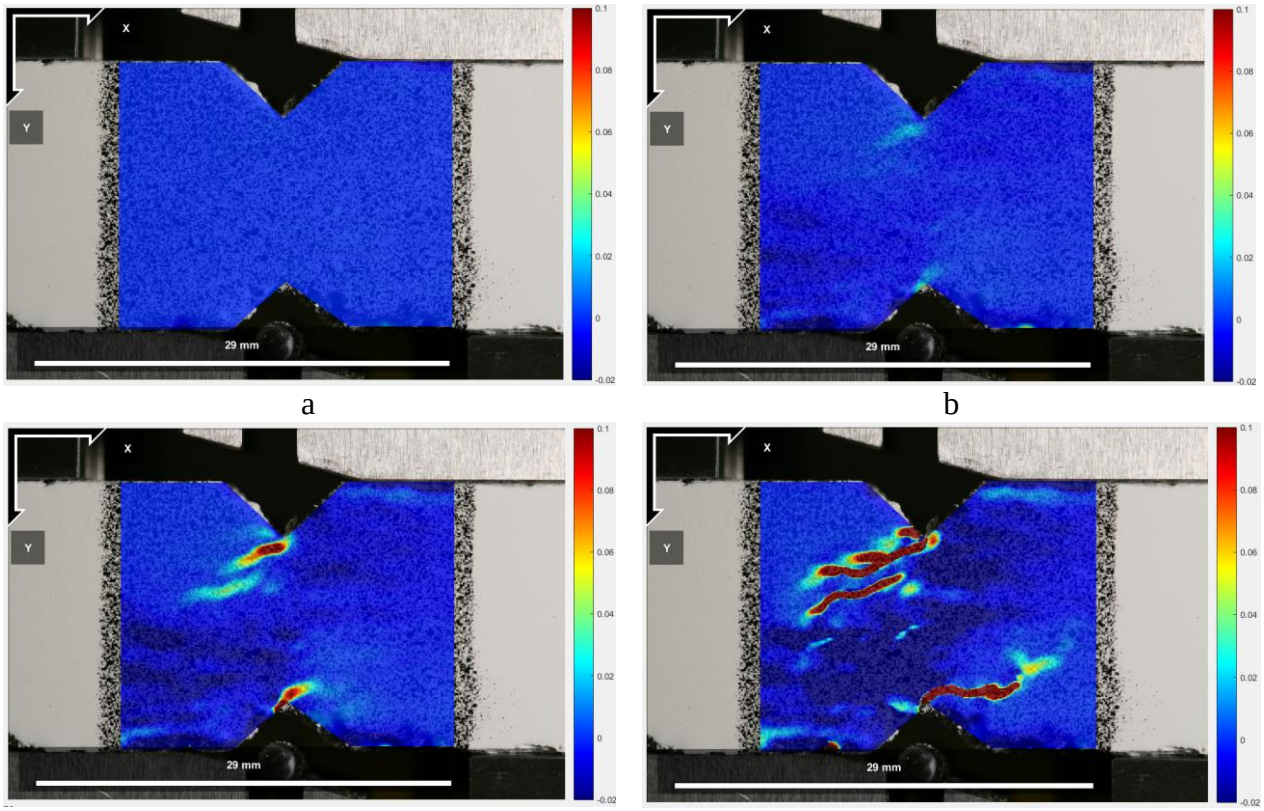

a b c d

Figure 121: Iosipescu DIC results about ε_{yy} reported in [mm/mm] of 38mm sample without skins. a) 10N; b) 100N; c) 210N; d) 288N.

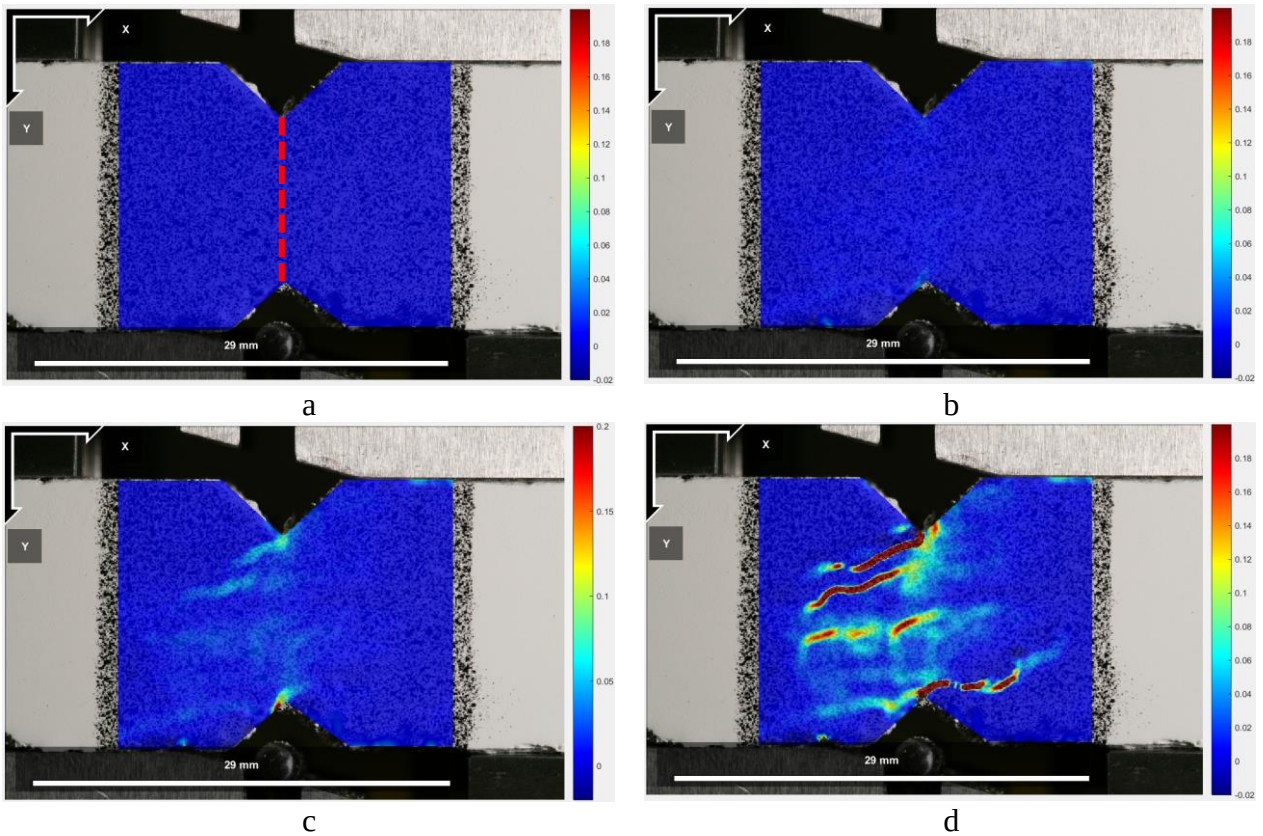

a b c d

Figure 122: Iosipescu DIC results about ε_{xy} reported in [mm/mm] of 38mm sample without skins. a) 10N; b) 100N; c) 210N; d) 288N.

The check the values of the vertical displacement measured by DIC, values measured at the red points *A* and *B* shown respectively in Figure 114a Figure 119a were compared with the vertical displacements of the machine's crosshead. Comparison is reported in Figure 123. Values are in good agreement, although some deviations are observed in the case of the 18mm sample, presumably because of the effect of the compliance of the machine when testing the 18mm sample (Figure 123a) which is stiffer than the 38mm (Figure 123b).

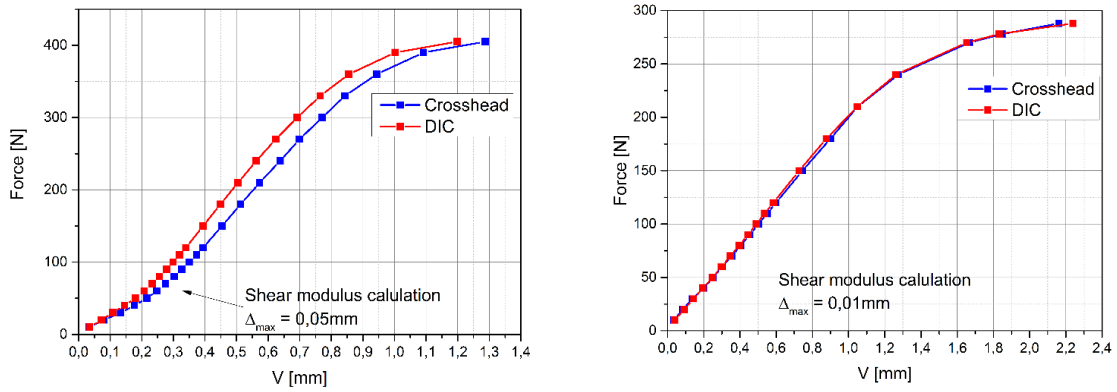

a b

Figure 123: Comparison between vertical displacements measured from DIC (red-line) and Crosshead of the machine (blue-line). a) 18mm particleboard's sample; b) 38mm particleboard's sample without the outer skins.

Values of the ε_{xy} strain were extracted point by point along the red dashed line of the Figure 117a for the 18mm samples and Figure 122a for the 38mm sample without the outer skins, and the engineering shear strain γ_{xy} (104) was evaluated by Eq. 52. The shear strain γ_{xy} is defined as the mean value over the line of extraction. Finally, it was possible to derive the stress-strain curve of the tests, where the shear stress is evaluated as the mean shear stress over the resistant area (98) (Eq. 53).

$$\gamma_{xy_i} = 2 * \varepsilon_{xy_i} \qquad \text{eq. 52}$$

$$\tau_{core} = \frac{P}{a*b} \qquad \text{eq. 53}$$

where P is the load in *[N]* obtained at each step of the test procedure presented in Section 3.2.3 and a and b are the dimensions of the gauge area in *[mm]*, as reported in Figure 124.

Samples	a [mm]	b [mm]	A [mm^2]
1-18	12.5	13.1	163.7
2-18	12.4	13.5	167.6
3-18	12.5	13.6	170.5
4-18	12.6	13.3	168.6
5-18	12.6	13.5	169.4
Samples	**a [mm]**	**b [mm]**	**A [mm^2]**
1-38	12.6	13.2	166.3
2-38	11.6	13.3	154.2
3-38	12.2	13.2	160.5
4-38	11.6	13.1	151.5
5-38	11.5	13.1	150.1

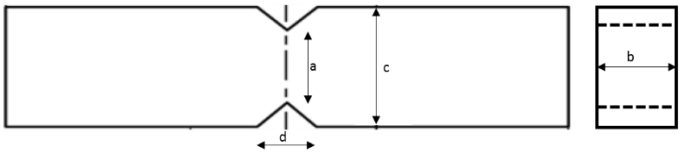

Figure 124: Iosipescu notches geometry.

The load-strain curves for one of the five Iosipescu' samples for 18mm and 38mm are reported respectively in Figure 125a and Figure 125c. In particular, considering the limits of proportionality prescribed in (98) and after having reduced the load range for the 38mm sample to guarantee the correct load resolution (see Section 3.2.3), it was possible to obtain the G_{13} modulus of the particleboard by linear regression between strain and load, see Eq. 54, Figure 125b and Figure 125d.

$$G_{13} = \frac{\Delta\tau}{\Delta\gamma} \qquad \text{eq. 54}$$

Table 36 lists the values of G_{13} obtained following this procedure.

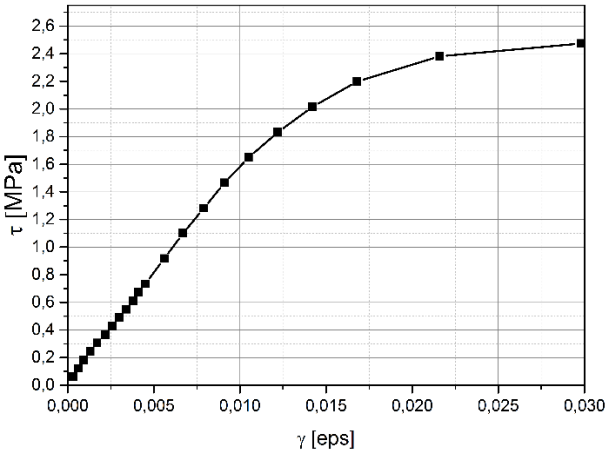

a

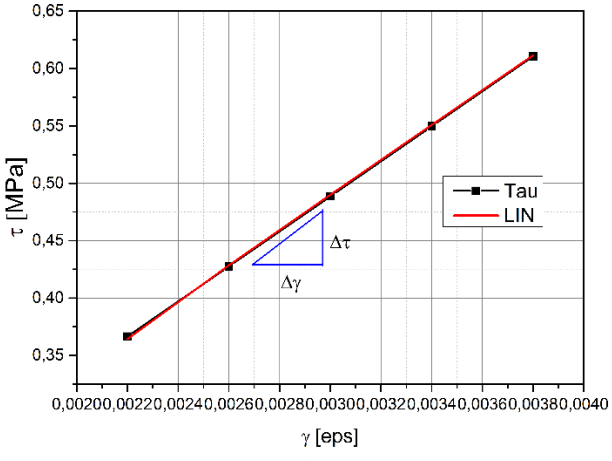

b

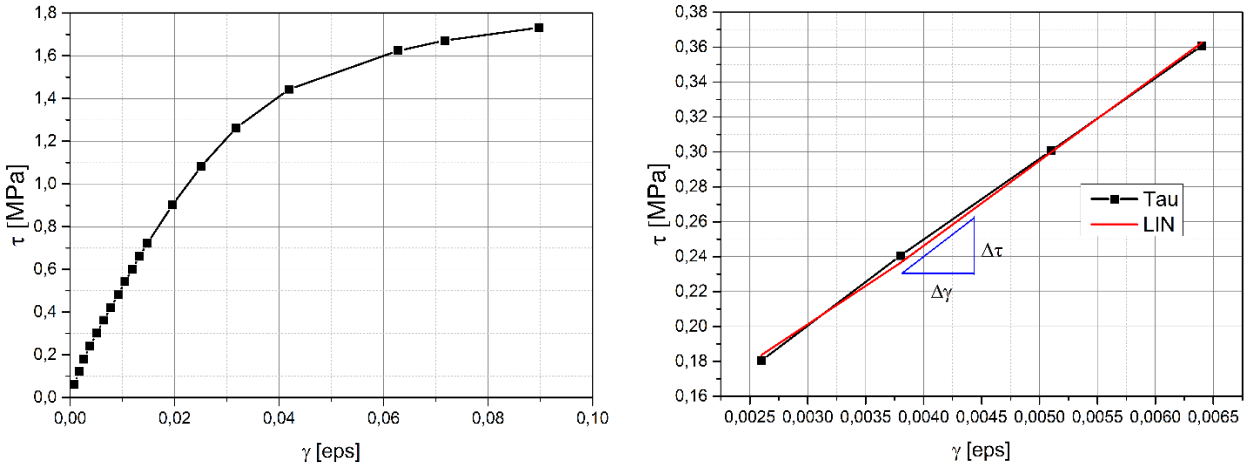

c d

Figure 125: Iosipescu Load-Stain curves obtained by DIC method. a) 18mm sample; b) 18mm proportionality zone to calculate the G_{13}; c) 38mm sample without the skins; d) 38mm proportionality zone to calculate the G_{13}.

Table 36: Iosipescu coupled with DIC results from five particleboard samples with notches.

Board Tick. [mm]	G_{13} [MPa]		F_{max} [N]		τ_{max} [MPa]		γ_{max} [eps]	
	Mean	Std. Err.	Mean	Std. Err.	Mean	Std. Err.	Mean	Std. Err.
38 (without skins)	105	16.1	262	11.6	1.67	0.06	0.0403	0.013
18	144	11.6	429	23.7	2.55	0.13	0.0362	0.0038

Table 37 the comparison between the shear modulus obtained by three points bending test with varying span, modelling the particleboard' samples by different sandwich models, and Iosipescu results is reported.

Table 37: Iosipescu and DIC results compared with three points bending test with varying span results about shear modulus.

Board Tick. [mm]	G_{13} [MPa]			
	Iosipescu + DIC	PSM	BSM	QSM
38	105	137	137	139
18	144	224	223	228

Calculating the difference between the results obtained by different experimental methods, it is possible to see that Iosipescu coupled with Digital Image Correlation produces a difference compared to the TPBTVS equal to 24% for the 38mm and equal to 36%. The cause of this shift between the various identification methods based on TPBTVS and Iosipescu with DIC can be due to notches on the Iosipescu' samples. The machining of notches is likely to have reduced the specimen stiffness.

Table 38: Difference between the methods about the shear modulus determination

Board Tick. [mm]	Iosipescu + DIC vs PSM	% Iosipescu + DIC vs BSM	Iosipescu + DIC vs QSM
38	23.5	23.5	24.5
18	35.7	35.4	36.8

To explore the effects of the notches on the Iosipescu' samples of this material, two samples without the notches, one for 18mm and another for 38mm, with the geometry reported in Figure 95b were tested under the same test conditions and DIC analysis parameters.

From Figure 126 to Figure 130 the results for 38mm particleboard' sample after the DIC analysis are shown for different load steps. In particular, horizontal U and vertical V displacements are reported in Figure 126 and Figure 127. The strains ε_{xx} ε_{yy} and ε_{xy} measured on the region of interest are reported respectively in Figure 128 Figure 129 and Figure 130.

In a similar way, from Figure 131 to Figure 135 the results for 18mm particleboard' sample after the DIC analysis for different load steps are reported. In particular, horizontal U and vertical V displacements are reported in Figure 131 and Figure 132. The strains ε_{xx} ε_{yy} and ε_{xy} measured on the region of interest are reported respectively in Figure 133, Figure 134 and Figure 135.

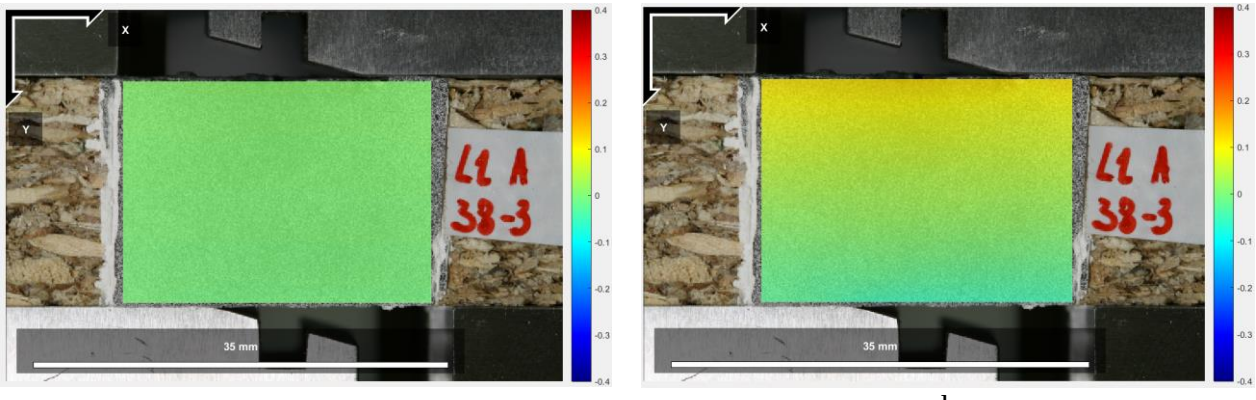

a b

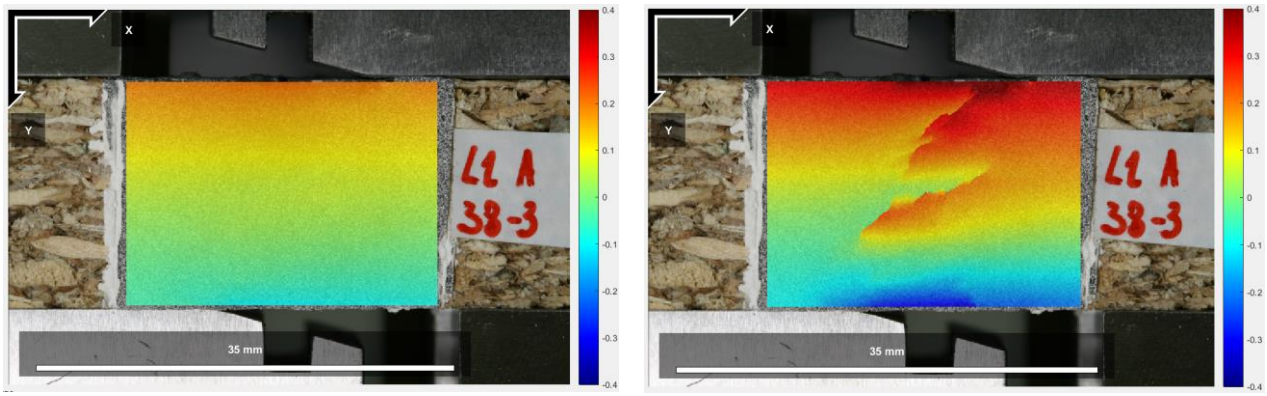

c d

Figure 126: Iosipescu DIC results about Horizontal Displacement (U) reported in [mm] of 38mm sample without skins and notches. a) 10N; b) 100N; c) 210N; d) 385N.

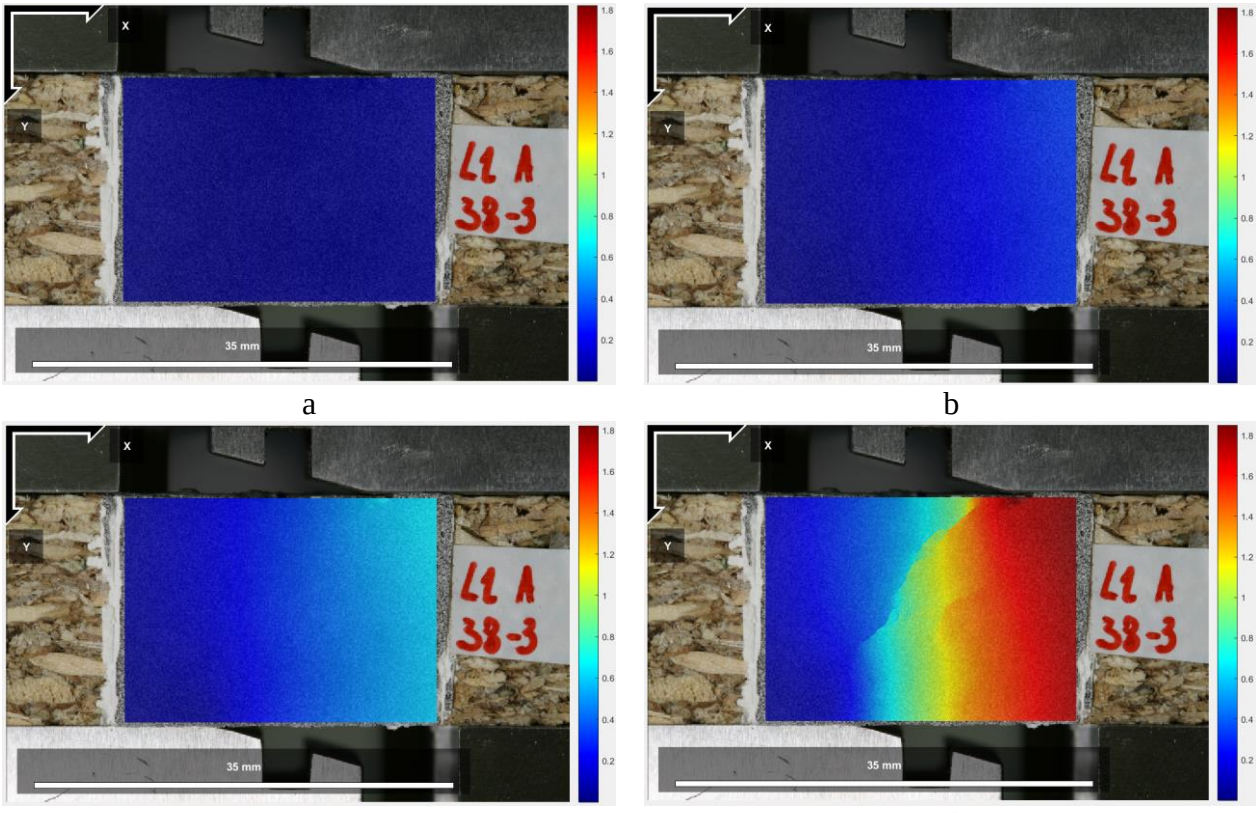

a b

c d

Figure 127: Iosipescu DIC results about Vertical Displacement (V) reported in [mm] of 38mm sample without skins and notches. a) 10N; b) 100N; c) 210N; d) 385N.

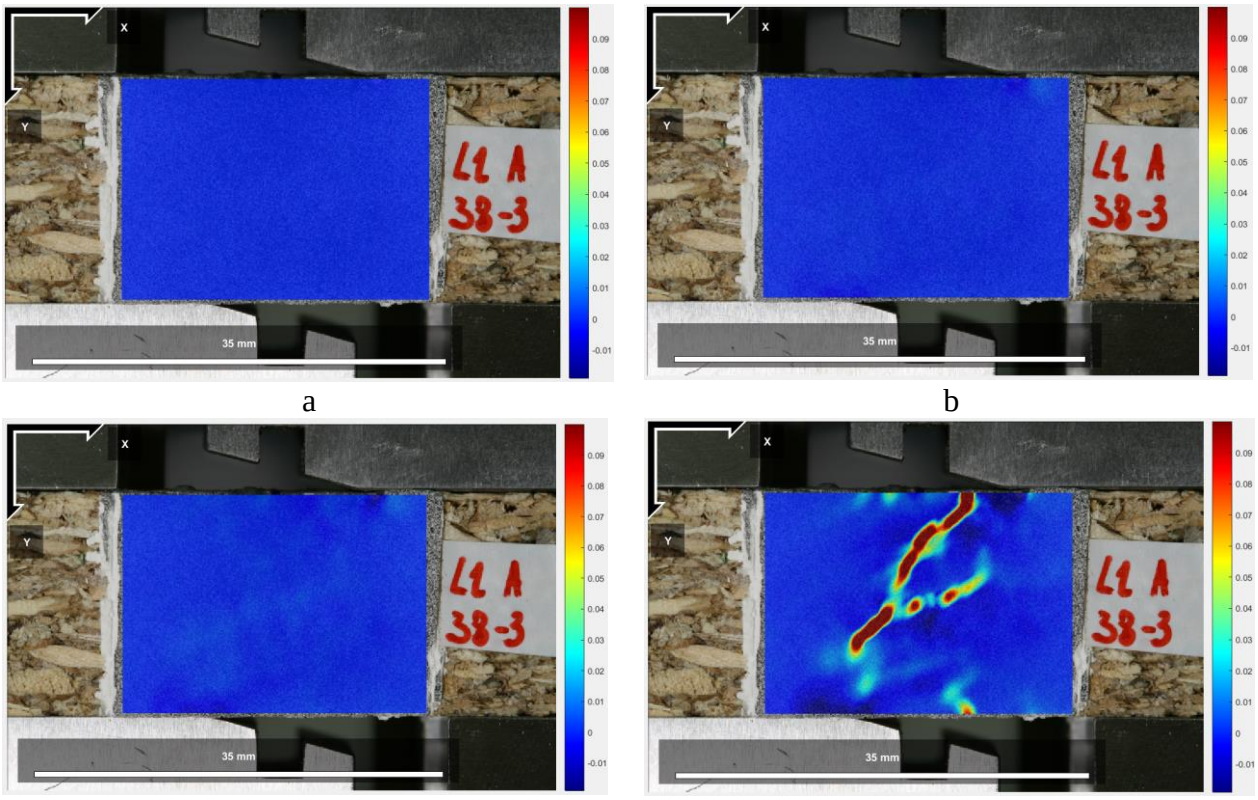

a b c d

Figure 128: Iosipescu DIC results about ε_{xx} strain reported in [mm/mm] of 38mm sample without skins and notches. a) 10N; b) 100N; c) 210N; d) 385N.

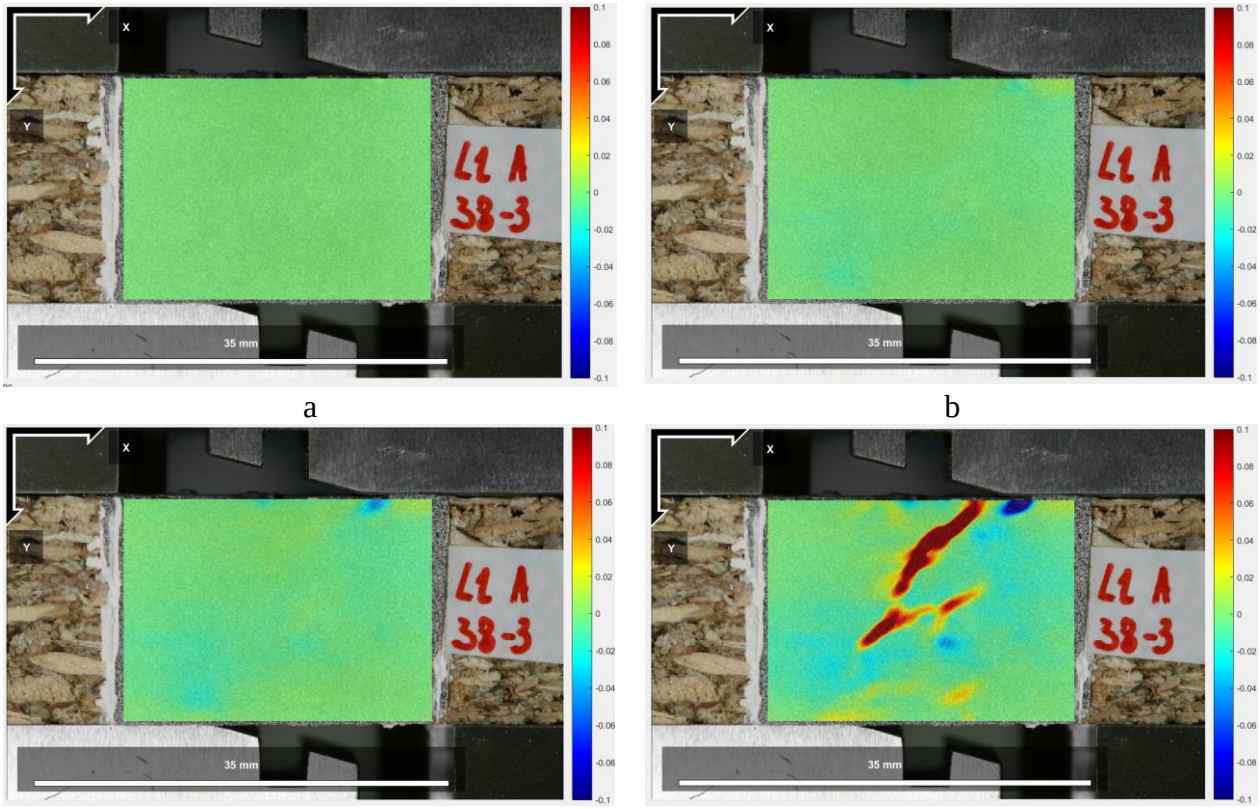

a b c d

Figure 129: Iosipescu DIC results about ε_{yy} strain reported in [mm/mm] of 38mm sample without skins and notches. a) 10N; b) 100N; c) 210N; d) 385N.

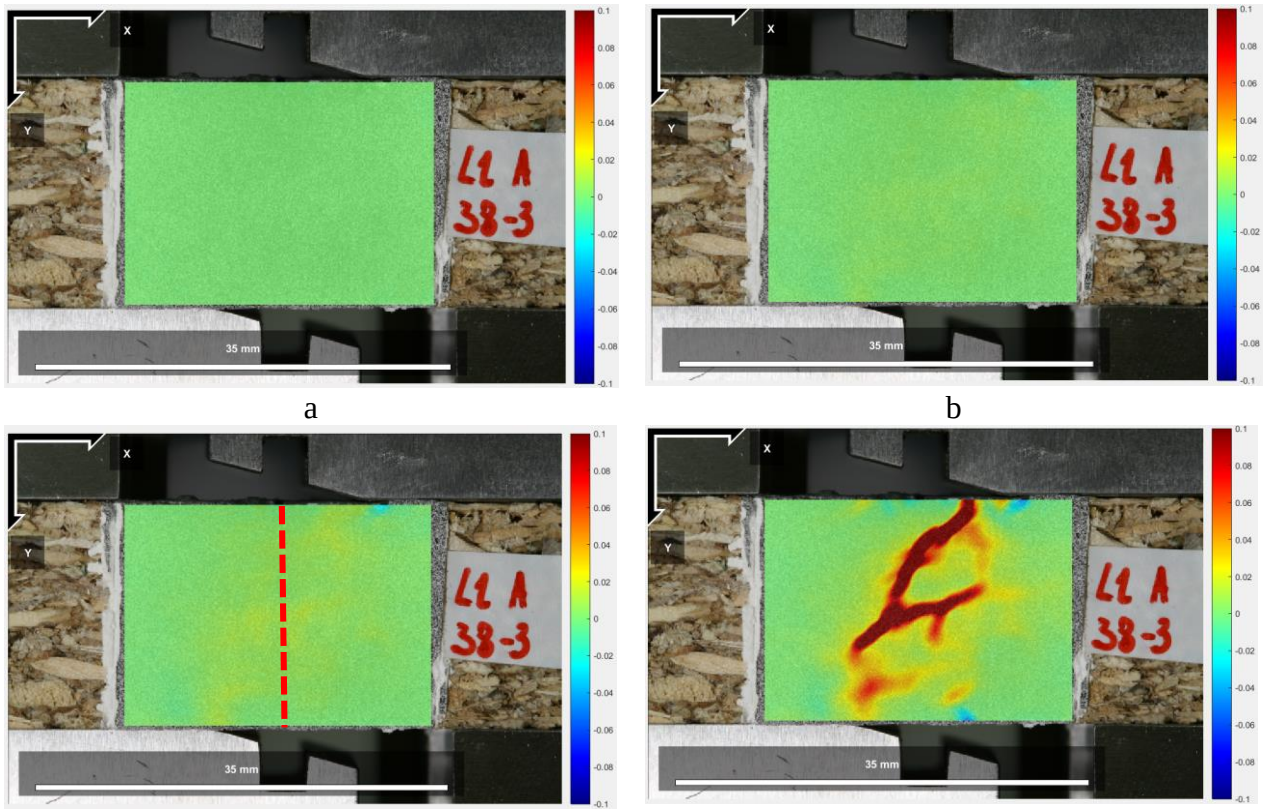

a b

c d

Figure 130: Iosipescu DIC results about ε_{xy} strain reported in [mm/mm] of 38mm sample without skins and notches. a) 10N; b) 100N; c) 210N; d) 385N.

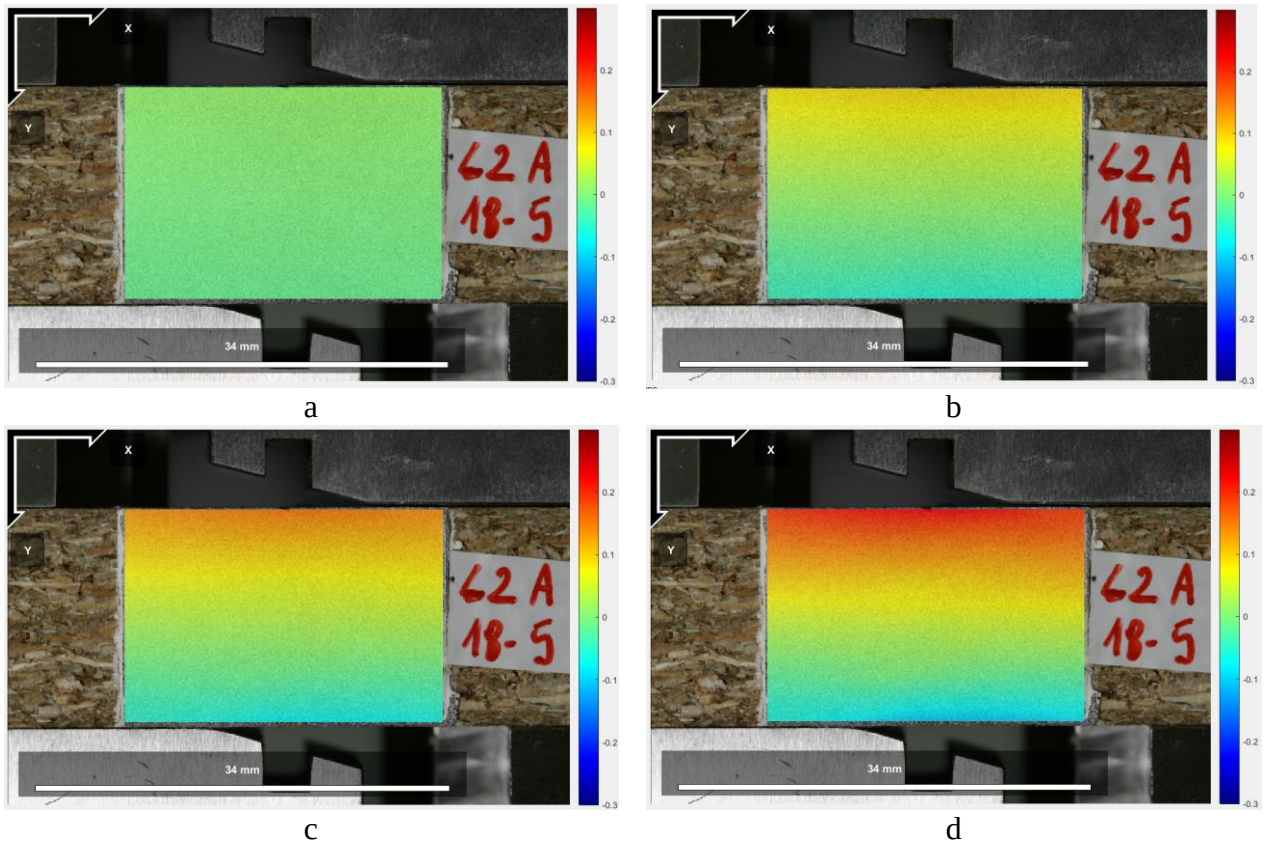

a b

c d

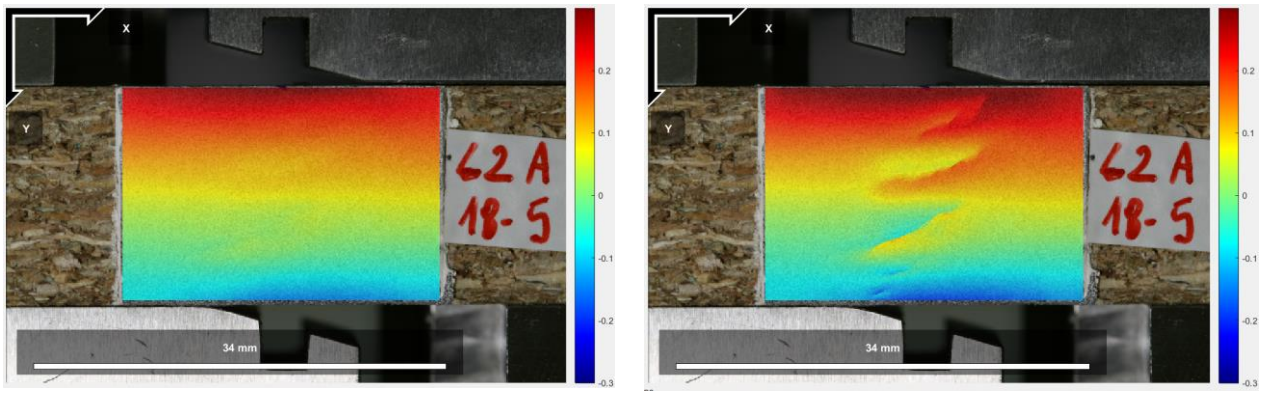

e f

Figure 131: Iosipescu DIC results about Horizontal Displacement (U) reported in [mm] of 18mm sample without notches. a) 10N; b) 100N; c) 210N; d) 360N; e) 510N; f) 540N.

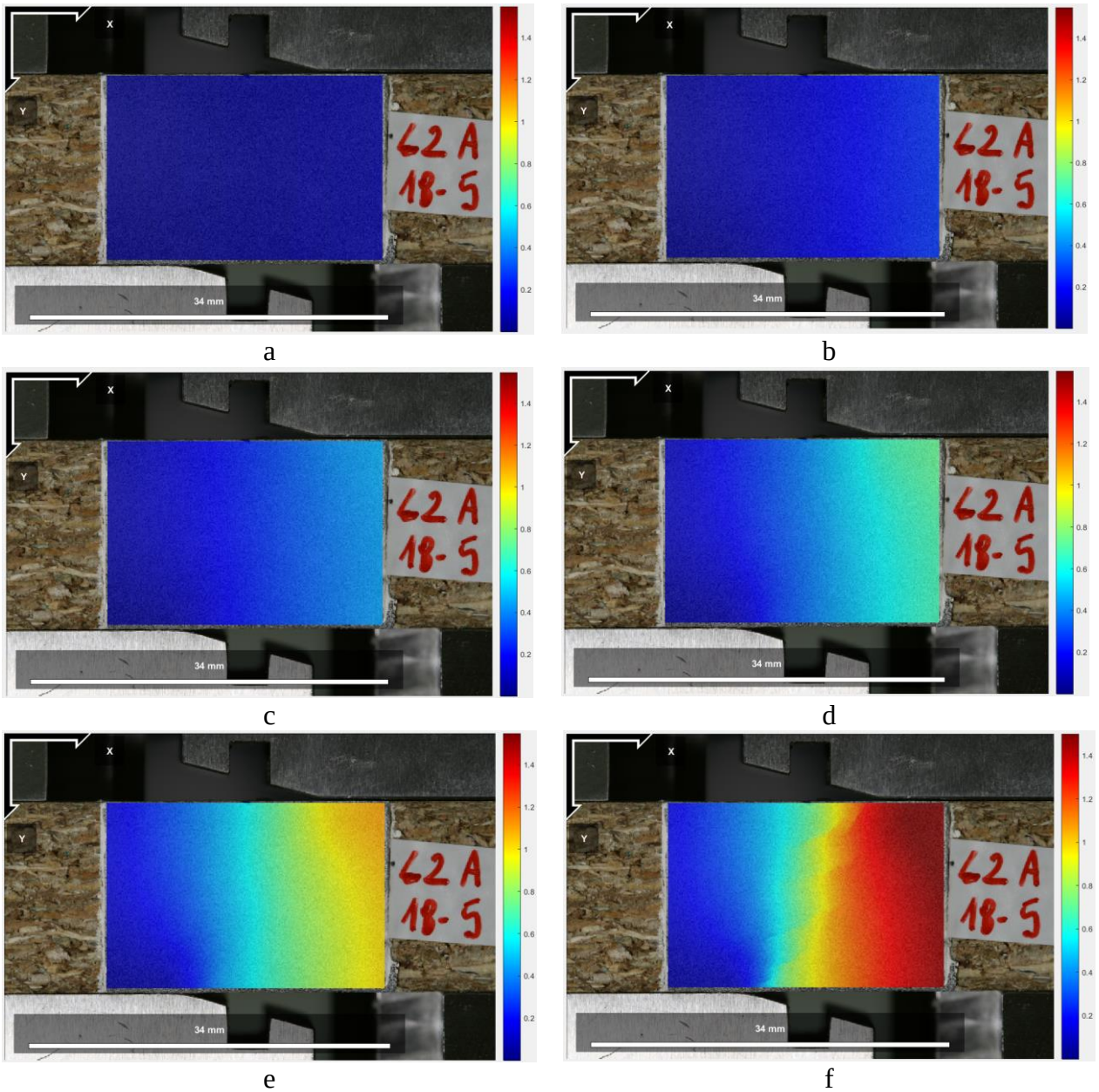

a b

c d

e f

Figure 132: Iosipescu DIC results about Vertical Displacement (V) reported in [mm] of 18mm sample without notches. a) 10N; b) 100N; c) 210N; d) 360N; e) 510N; f) 540N.

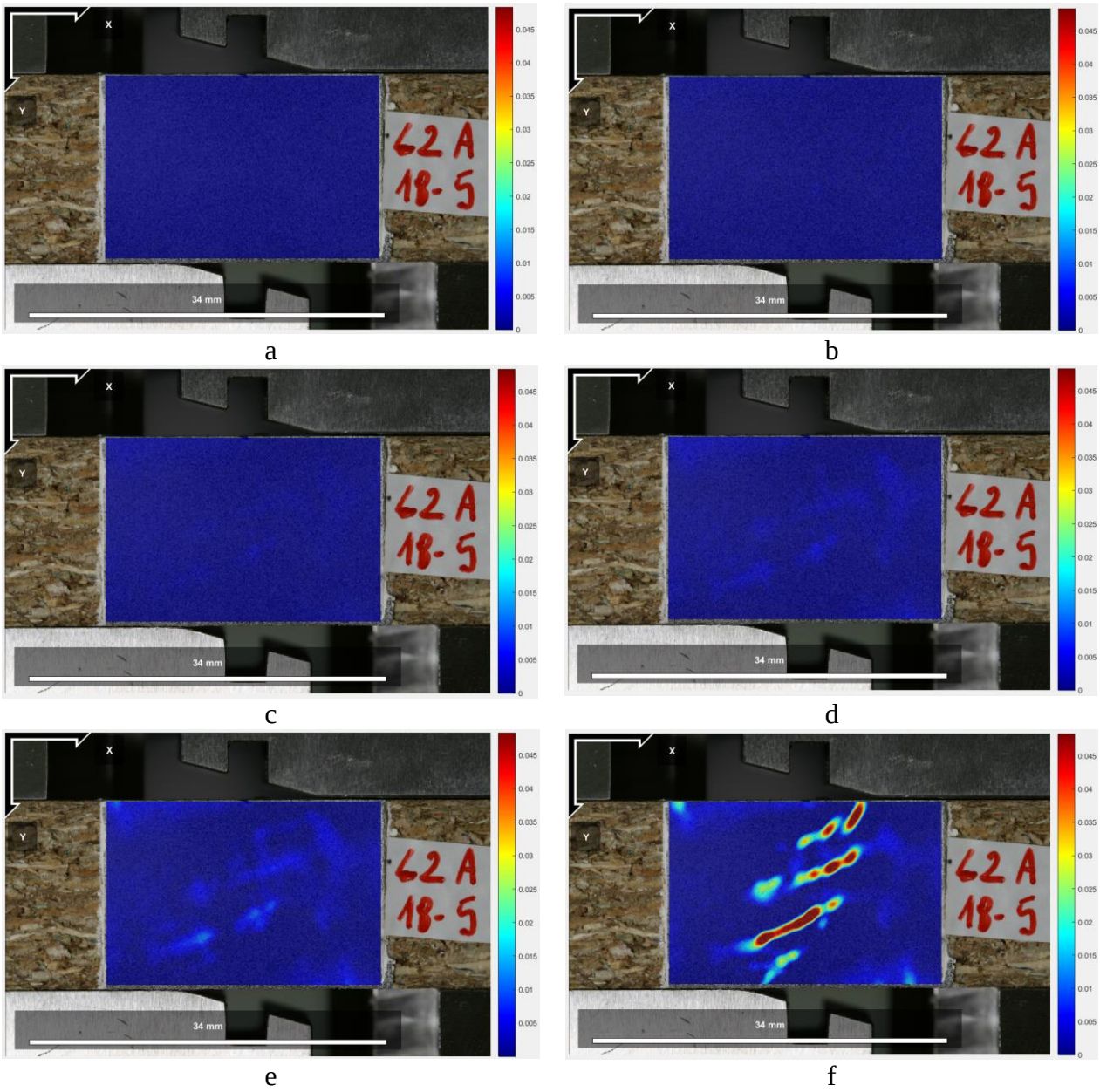

Figure 133: Iosipescu DIC results about ε_{xx} strain reported in [mm/mm] of 18mm sample without notches. a) 10N; b) 100N; c) 210N; d) 360N; e) 510N; f) 540N.

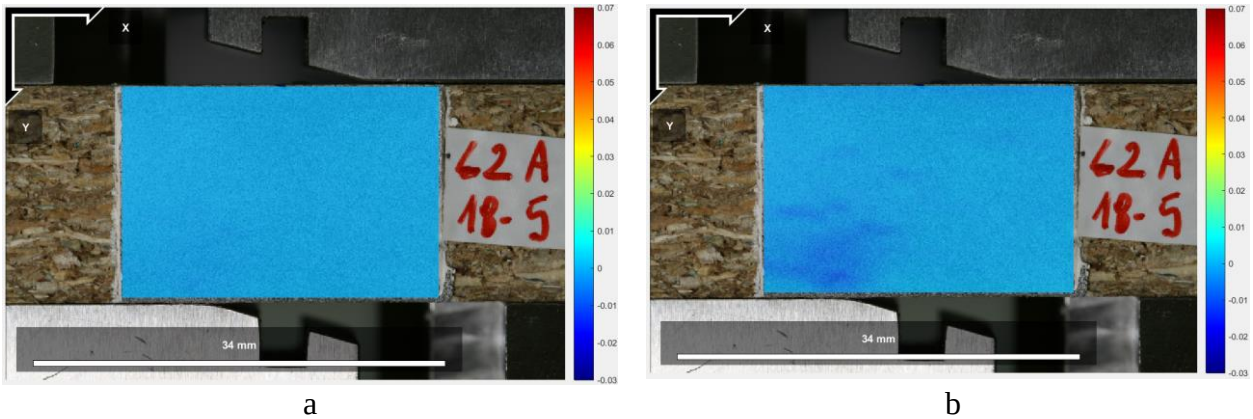

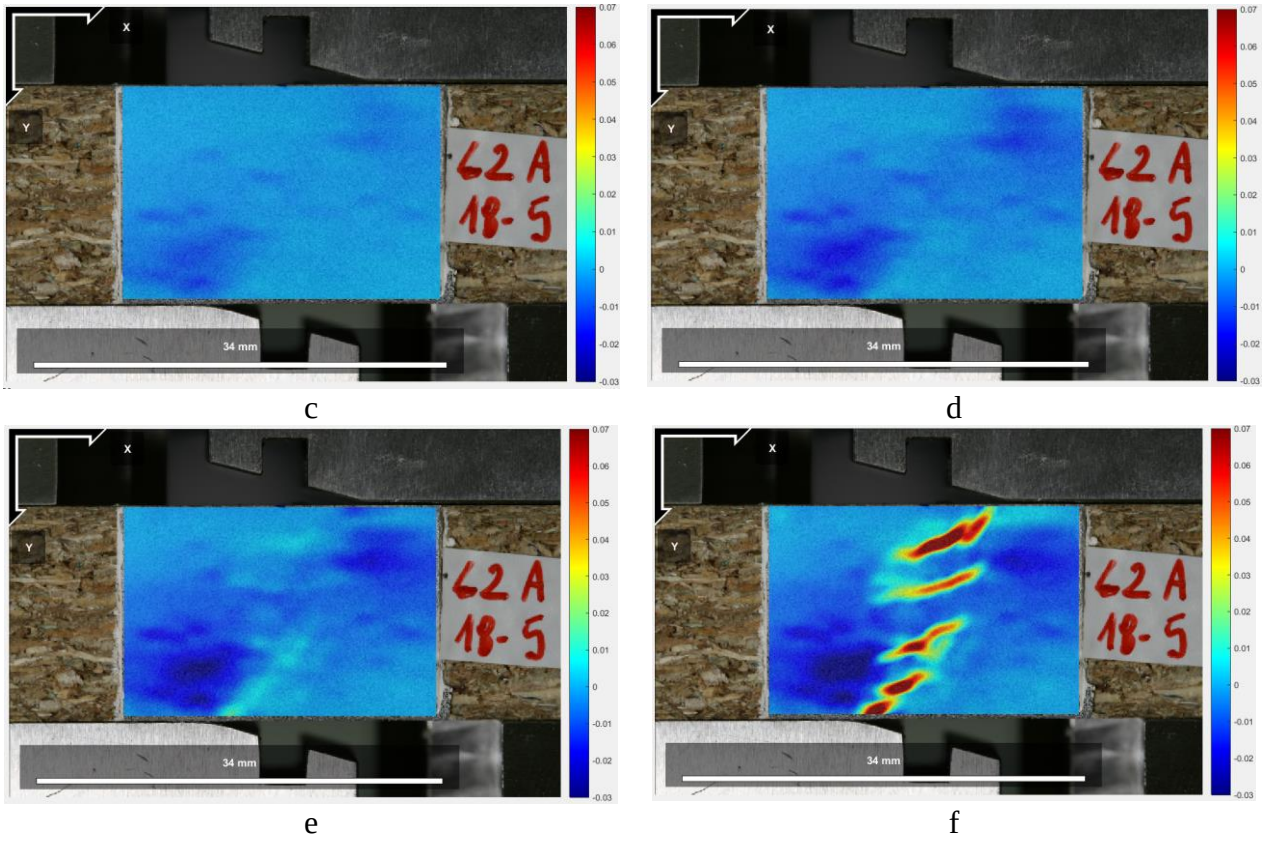

Figure 134: Iosipescu DIC results about ε_{yy} strain reported in [mm/mm] of 18mm sample without notches. a) 10N; b) 100N; c) 210N; d) 360N; e) 510N; f) 540N.

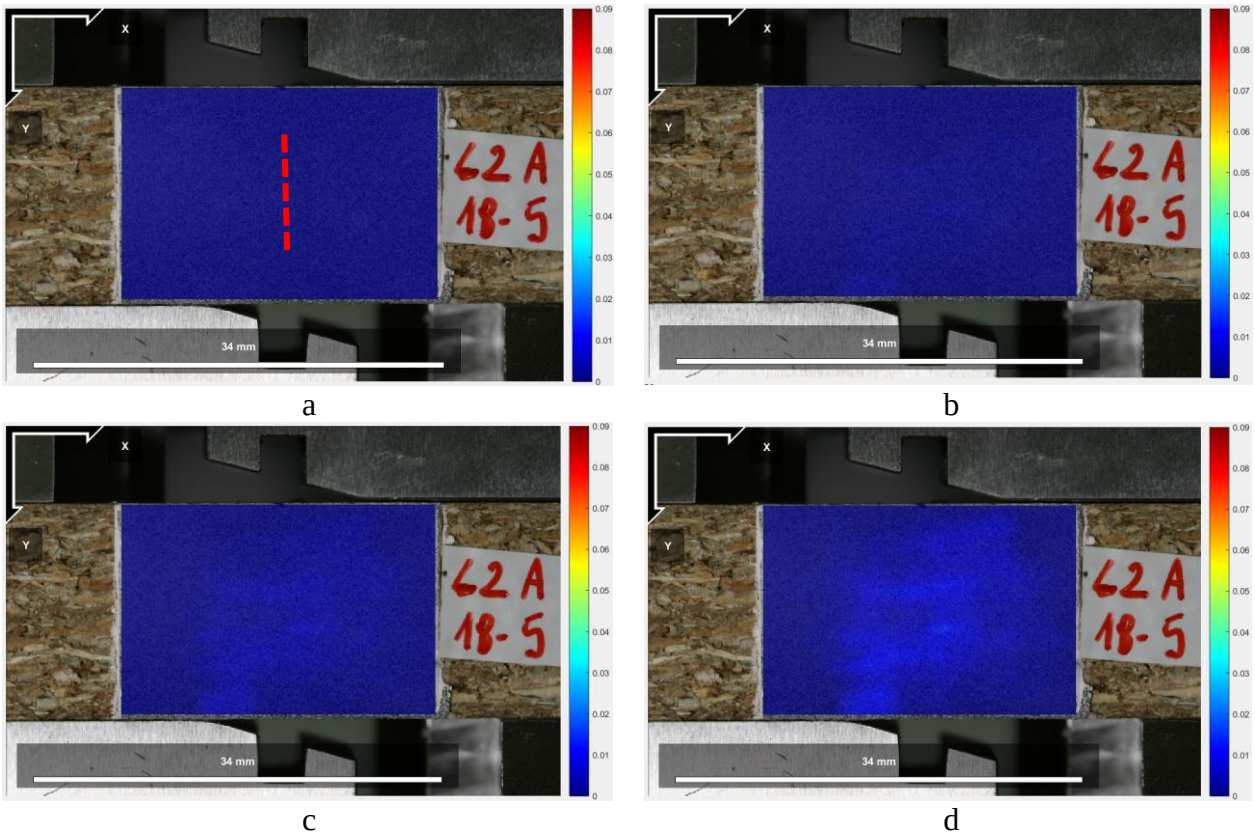

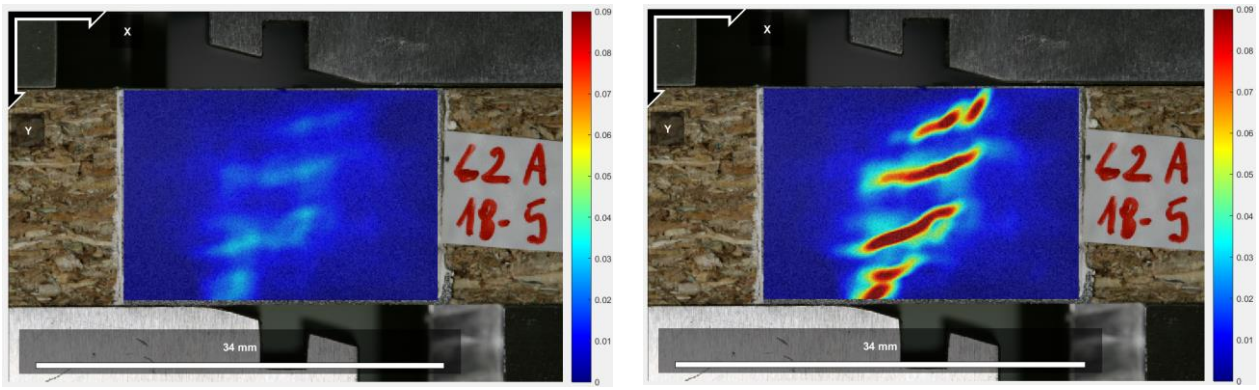

e f

Figure 135: Iosipescu DIC results about ε_{xy} strain reported in [mm/mm] of 18mm sample without notches. a) 10N; b) 100N; c) 210N; d) 360N; e) 510N; f) 540N.

Using the same procedure applied before to the notched particleboard samples, it was possible to extract point by point the shear strain ε_{xy} along the red dashed lines reported on Figure 130a and on Figure 135a for 38mm and 18mm samples, respectively, taking into account the same strain limits reported in Section 3.2.3 (2000 – 4000με for 18mm and 2000 – 6000με for 38mm). In this case, I modified the strategy to calculate the G_{13}. From the extraction line, I recorded the shear strain values along the core's thickness. Then, knowing the shear stress calculated in the core's thickness using Eq. 53, it was possible to determine the shear modulus G_{13} at every point along the extraction line for every step as $\frac{\tau}{\gamma_{xy\_i}}$ where the i-subscript indicate the shear strain along the extraction line (Figure 135a). It is important to remember that for the 38mm particleboard, the specimens were separated from the skins to testonly the core. Conversely, for the 18mm particleboard the Iosipescu specimens were left unchanged (skin + core + skin). For this, the extraction line for collecting the displacements and strains for 38mm are tracked along the entire thickness , whereasfor 18mm only in the center of the specimen, to exclude the skins.

As expected the G_{13} profile will be almost constant at every load step included in the proportionality range; the value of G_{13} was then calculated as the mean values of the G_{13} profile at every strain point. The shear modulus profiles estimated for the specimen core of 18mm and 38mm are reported respectively in Figure 136a and Figure 136b and in Table 39. Herein, it is possible to observe the jagged shape of G_{13} profile, probably due to the heterogeneity of the microstructure and also to contribution of the single particles that may belong to different wood species, thus having different stiffness performances. Calculating the mean value of these profiles without considering the spikes, it was then possible to obtain the G_{13} values for the 18mm and the 38mm samples and compare them with the previously obtained values.

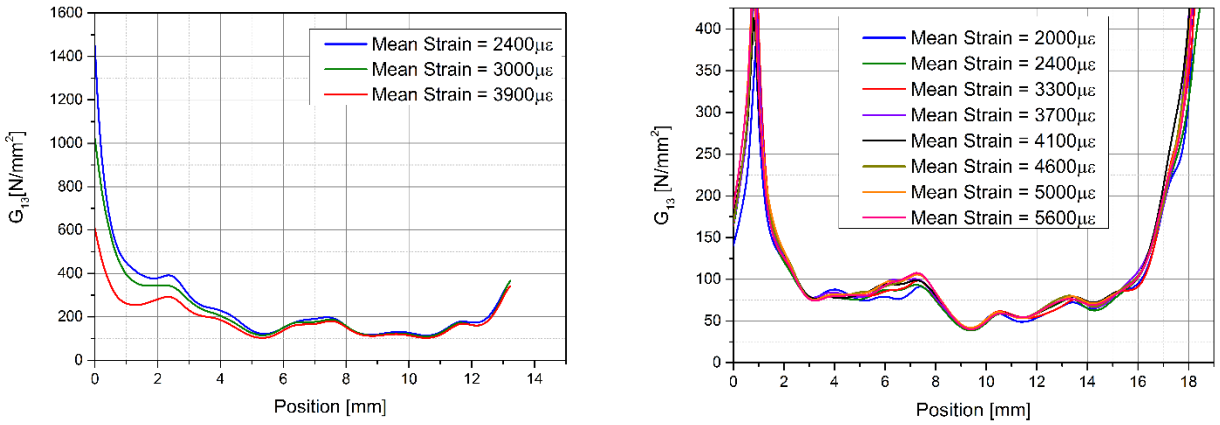

a b

Figure 136: Shear Modulus profile (G_{13}) calculated on the Iosipescu particleboard sample over the core. a) 18mm core sample; b) 38mm core sample (without the skins).

Table 39: Iosipescu coupled with DIC results from one particleboard sample for each thickness, without notches.

Board Tick. [mm]	**G_{13} [MPa]**	**F_{max} [N]**	**τ_{max} [MPa]**	**γ_{max} [eps]**
38 (without skins)	125	385	1.52	0.0734
18	222	540	2.23	0.0352

In Table 40, there is the comparison between the shear modulus values obtained by three methods:

- TPBT with varying span, modelling the particleboard' samples by different sandwich models (PSM, BSM and QSM).
- Iosipescu coupled with DIC field method performed on notched samples.
- Exploration of the modified (without notched) Iosipescu experimental test coupled with DIC (tests performed on one sample only for each thickness).

Table 40: Iosipescu + DIC results and three points bending test with varying span results final comparison about G_{13}.

Board Tick. [mm]	**G_{13} [MPa]**				
	Iosipescu + DIC	**Iosipescu + DIC without notches**	**PSM**	**BSM**	**QSM**
38	105	125	137	137	139
18	144	222	224	223	228

Observing these new results (third column of Table 40), compared with the others method, it is possible to conclude that this last strategy seems a promising method to evaluate G_{13} by Iosipescu approach. Indeed, the difference between the others method is now equal to 9% for the 38mm and 0.9% for 18mm. However, the results were affected by a limited statistical base due to time

constraints. In the future, it will be necessary to confirm these results repeating the experimental test on almost five samples without notches, to have statistical significance.

3.5.2 TPBT with fixed span validation coupled with DIC field method

Displacement and strains were measured by DIC also during some TPB tests on 38mm and 18mm particleboard's samples with the DIC set-up illustrated in Section 3.2.3 (Figure 88). The region of interest was prepared to guarantee the planarity and the suitable contrast with a black on white speckle. For these tests, values of the span between the supports were chosen equal to 175 and 225 mm. Values of the applied loads and the corresponding bending moments are reported in Table 41. The environment conditions of the lab are maintained with the temperature equal to 26°C and the humidity equal to 35%.

Table 41: TPBT load conditions coupled with DIC field method

Board Tick. [mm]	Span [mm]	Bending Moment [Nmm]	Load [N]
18	175	7253	165
	275	7253	105
38	175	12263	280
	275	12265	180

Load step were set to 25N to reach the real maximum load reported in the last column of Table 41 which ensured remaining in the linear elastic zone of the particleboard. Pictures were processed by N-Corr subroutine using the same DIC parameter uses in other analyses. For the sake of brevity, the pictures shown from Figure 137 to Figure 146 represents only 18mm and 38mm for one span length equal to 175mm. In particular, for the sample with thickness equal to 18mm, the horizontal and vertical displacements U and V are reported in Figure 137 and in Figure 138. The strain patterns of ε_{xx} , ε_{yy} and ε_{xy} for 18mm sample, are shown in Figure 139, Figure 140 and in Figure 141, respectively.

Vertical and horizontal displacement of the 38mm particleboard sample are reported in Figure 142 and in Figure 143, while the strains ε_{xx} ε_{yy} and ε_{xy} are shown in Figure 144, Figure 145 and in Figure 146.

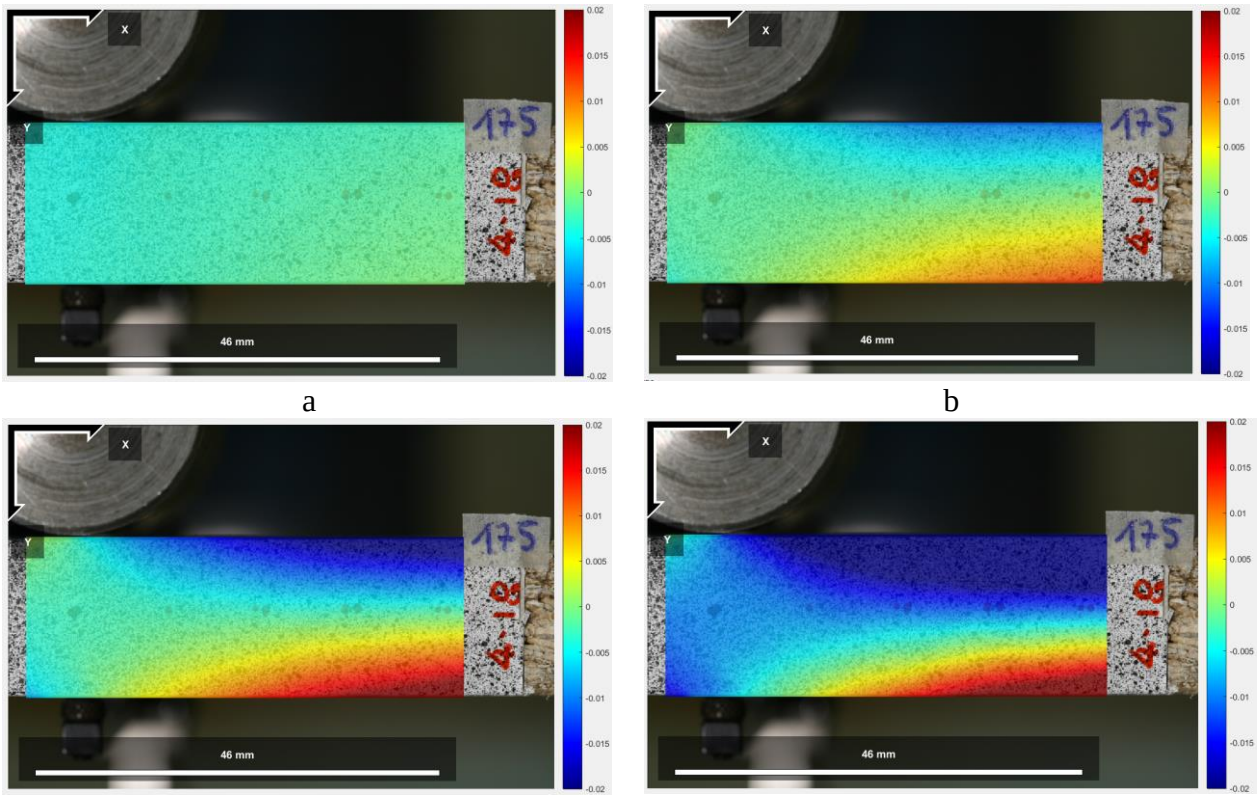

Figure 137: TPBT with fixed span coupled with DIC results about Horizontal Displacement (U) reported in [mm] of 18mm sample. a) 5N; b) 50N; c) 100N; d) 150N.

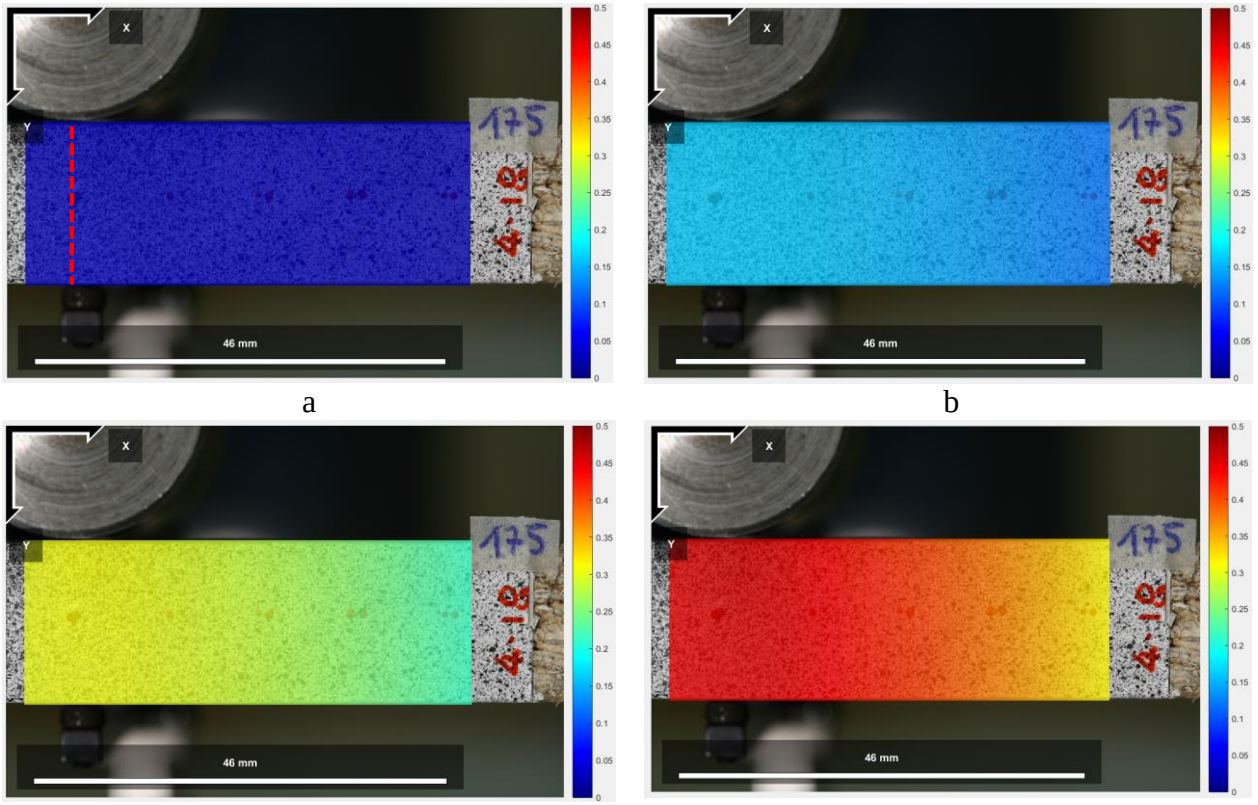

Figure 138: TPBT with fixed span coupled with DIC results about Vertical Displacement (V) reported in [mm] of 18mm sample. a) 5N; b) 50N; c) 100N; d) 150N.

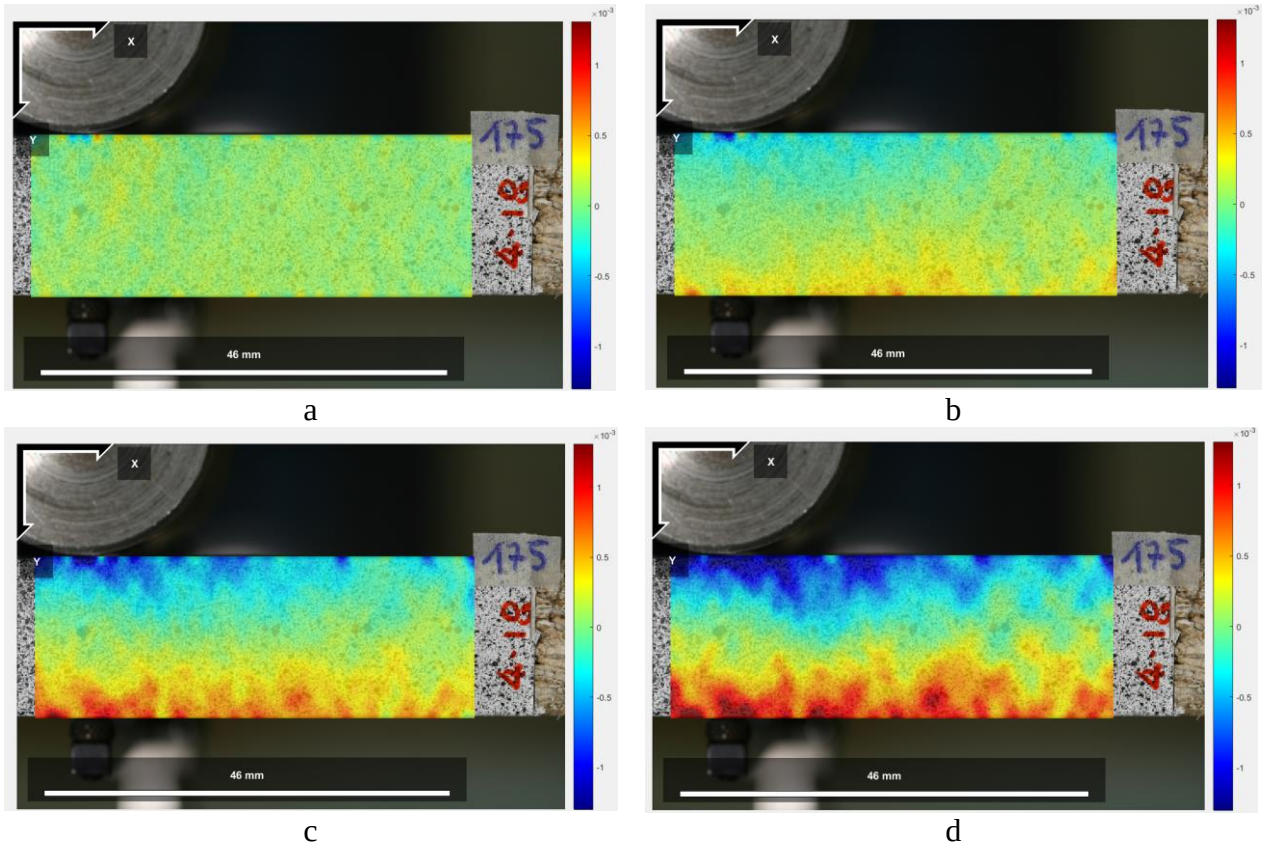

Figure 139: TPBT with fixed span coupled with DIC results about ε_{xx} strain reported in [mm/mm] of 18mm sample. a) 5N; b) 50N; c) 100N; d) 150N.

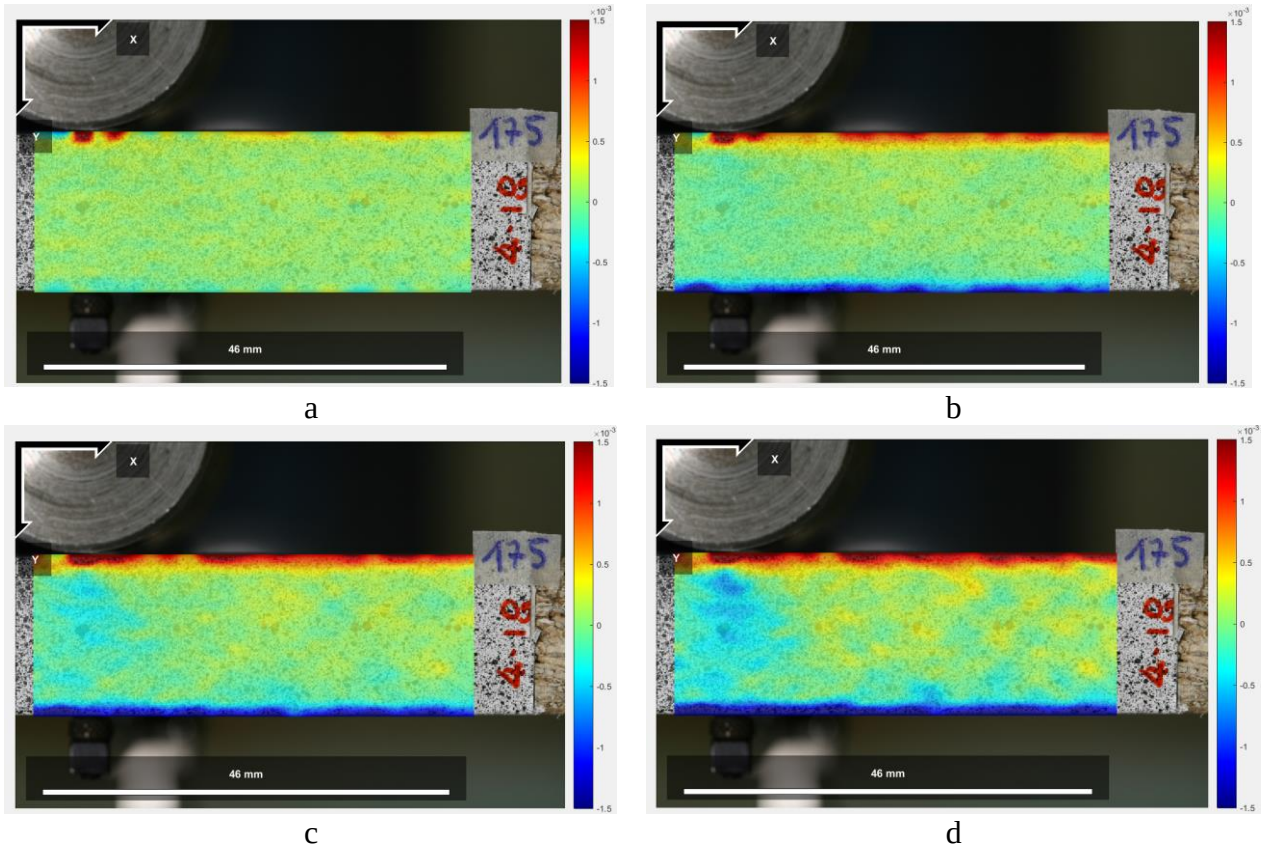

Figure 140: TPBT with fixed span coupled with DIC results about ε_{yy} strain reported in [mm/mm] of 18mm sample. a) 5N; b) 50N; c) 100N; d) 150N.

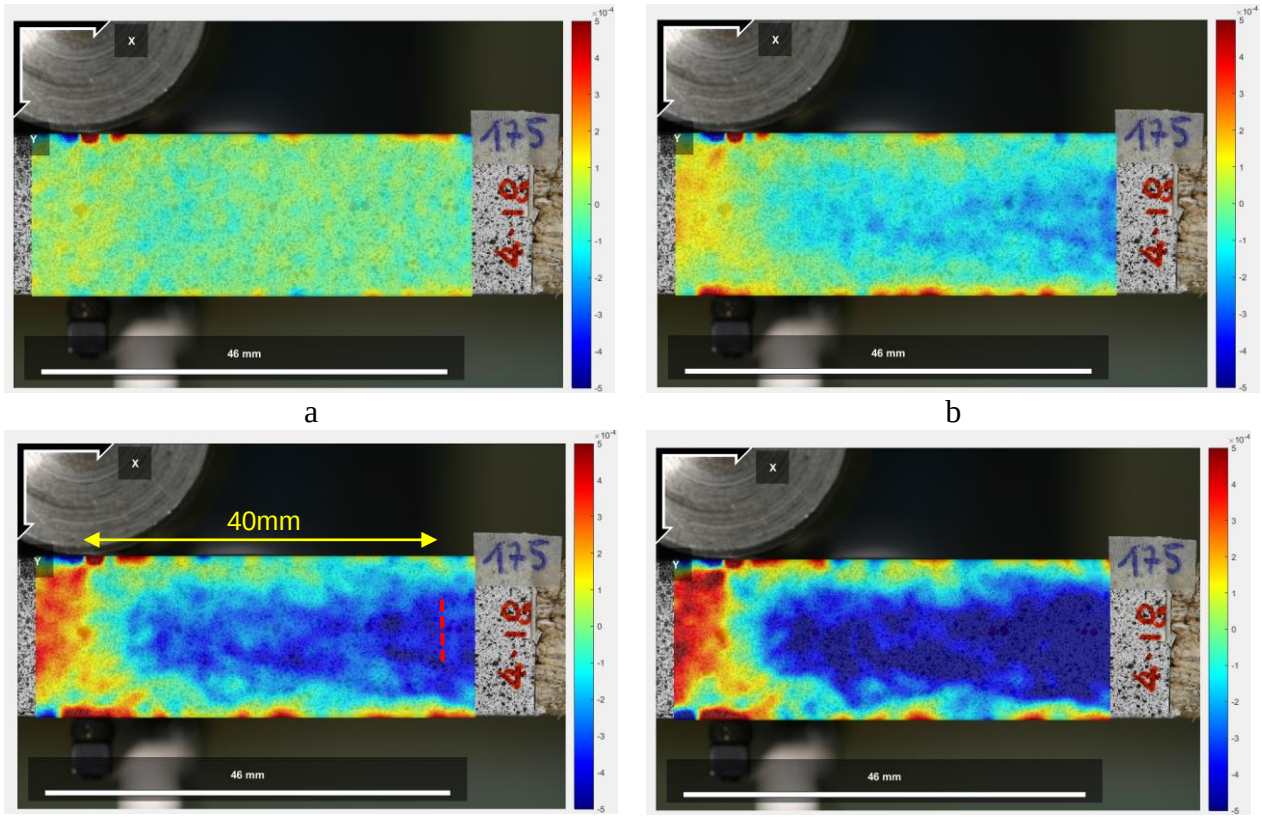

a b c d

Figure 141: TPBT with fixed span coupled with DIC results about ε_{xy} strain reported in [mm/mm] of 18mm sample. a) 5N; b) 50N; c) 100N; d) 150N.

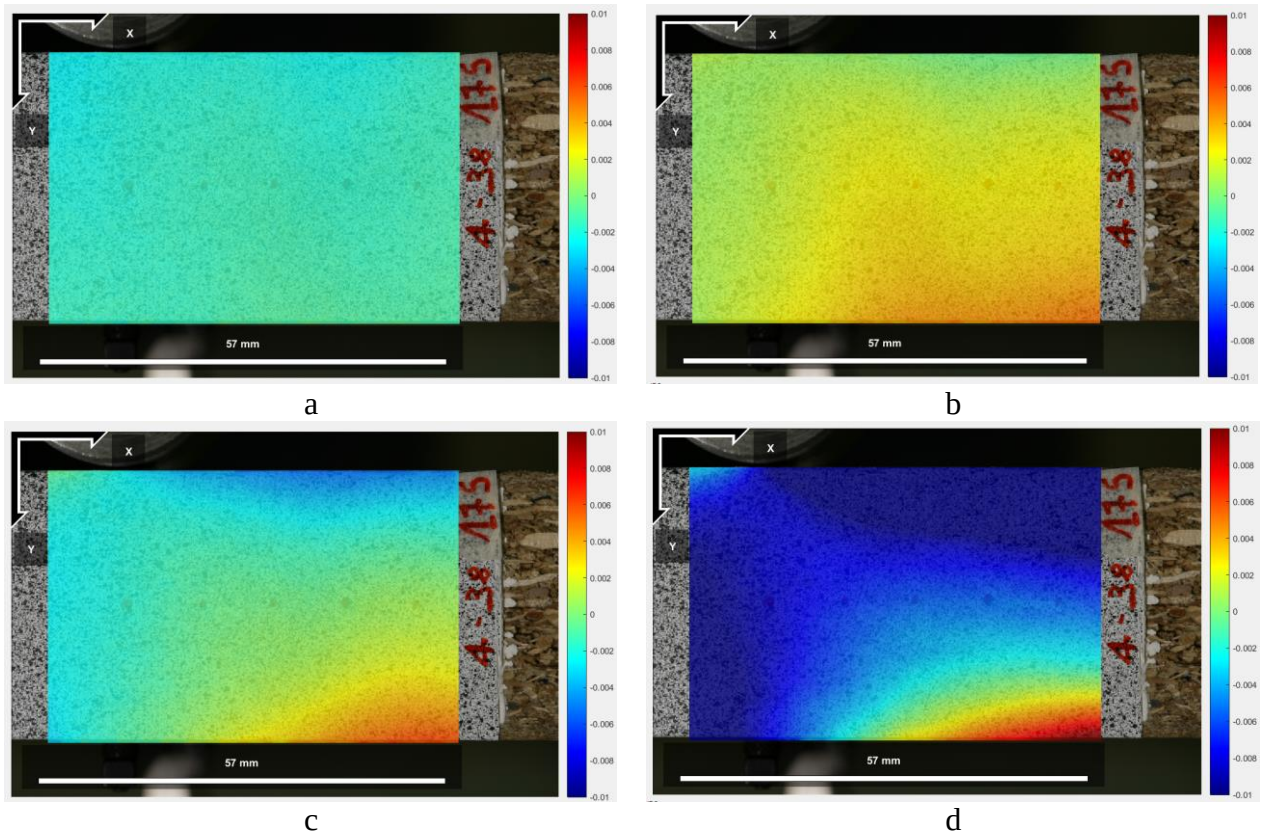

a b c d

Figure 142: TPBT with fixed span coupled with DIC results about Horizontal Displacement (U) reported in [mm] of 38mm sample. a) 25N; b) 75N; c) 125N; d) 280N.

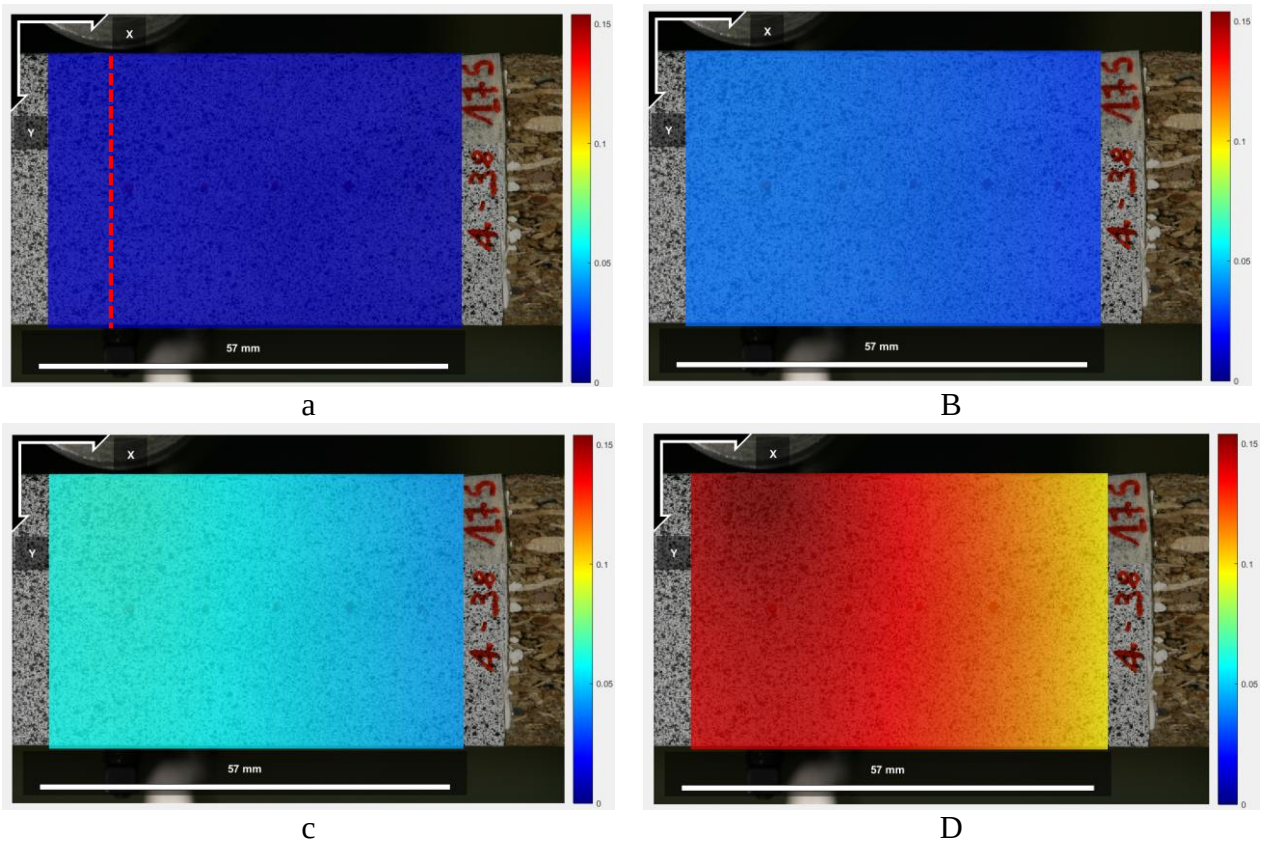

Figure 143: TPBT with fixed span coupled with DIC results about Vertical Displacement (V) reported in [mm] of 38mm sample. a) 25N; b) 75N; c) 125N; d) 280N.

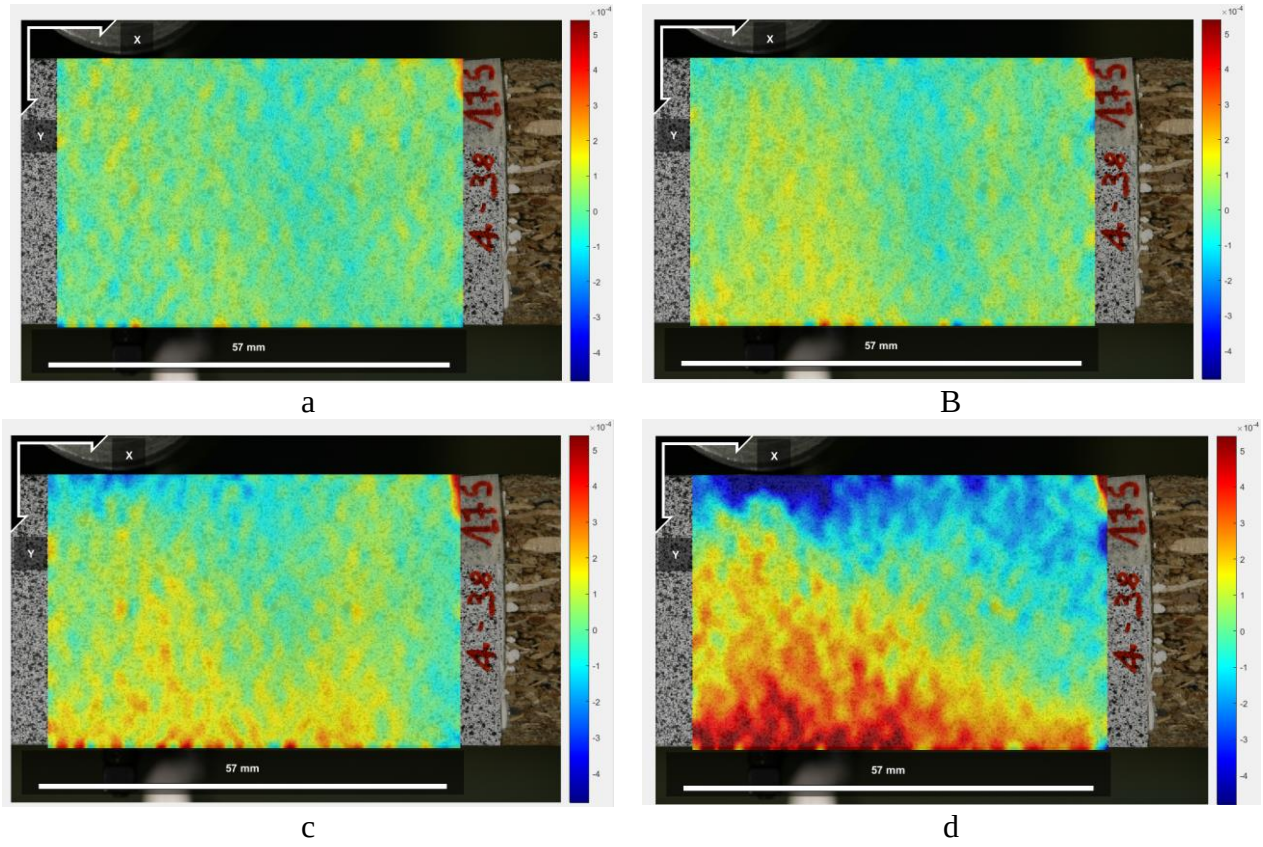

Figure 144: TPBT with fixed span coupled with DIC results about ε_{xx} strain reported in [mm/mm] of 18mm sample a) 25N; b) 75N; c) 125N; d) 280N.

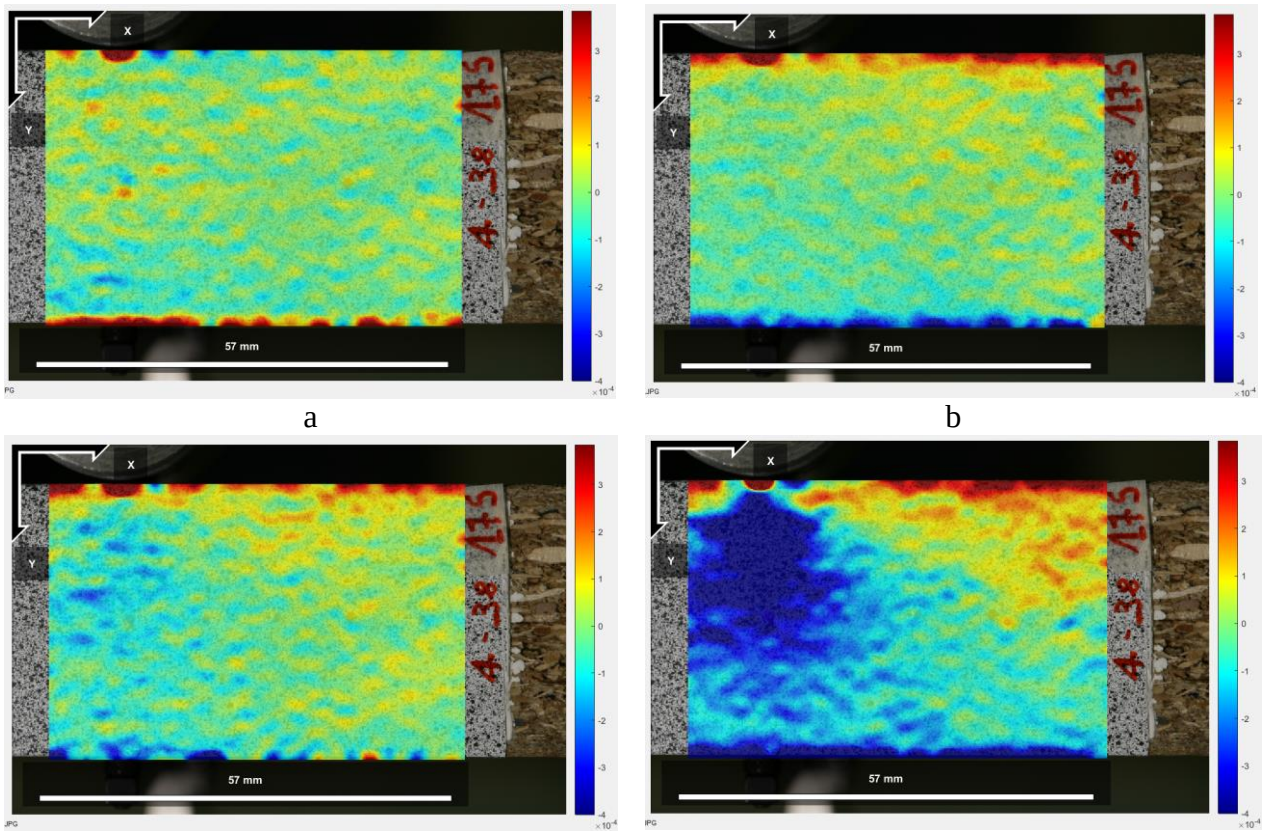

a b

c d

Figure 145: TPBT with fixed span coupled with DIC results about ε_{yy} strain reported in [mm/mm] of 18mm sample a) 25N; b) 75N; c) 125N; d) 280N.

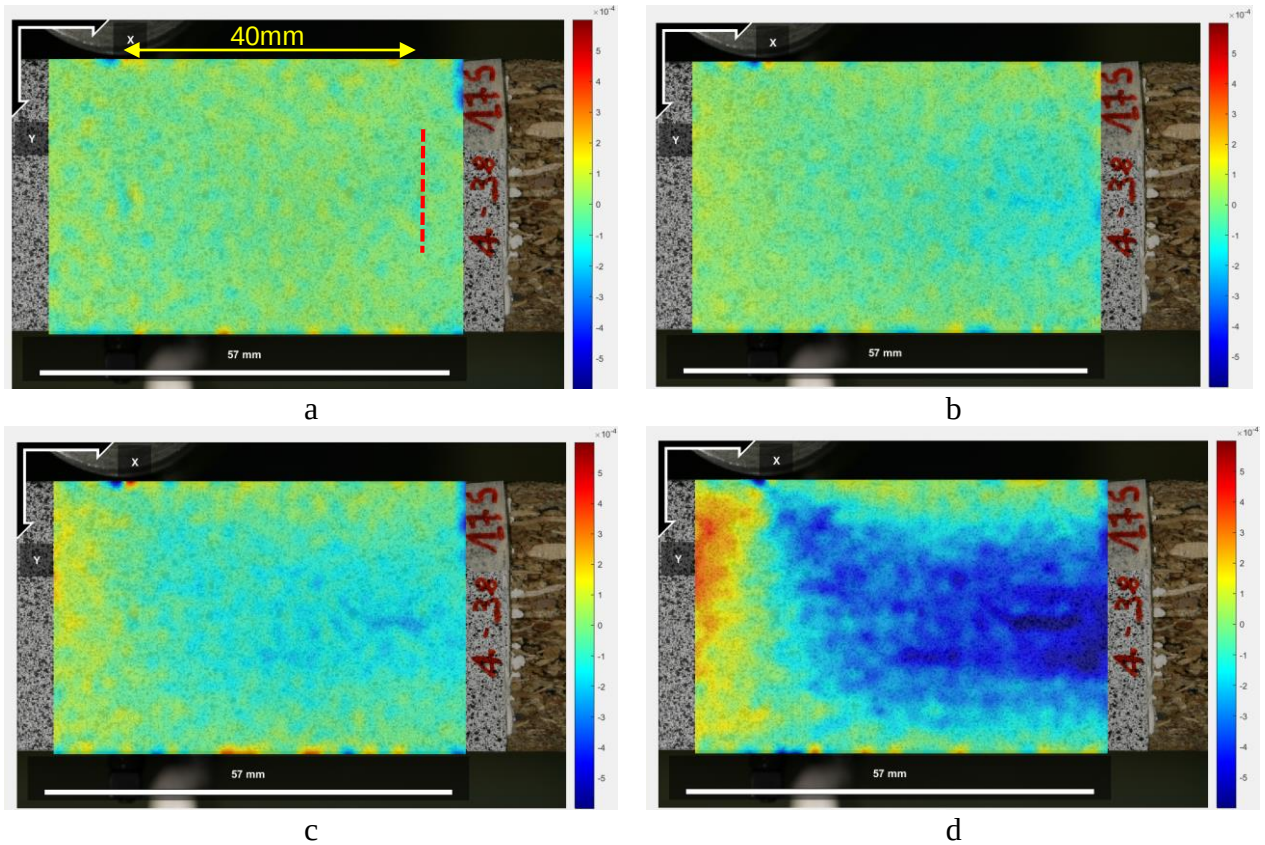

a b

c d

Figure 146: TPBT with fixed span coupled with DIC results about ε_{xy} strain reported in [mm/mm] of 18mm sample a) 25N; b) 75N; c) 125N; d) 280N.

During tests a deflectometer was used, thus it was possible to compare the experimental deflection of the sample with that measured by DIC. The deflectometer is not affected by the machine's compliance and therefore it was used to validated the vertical displacement measured by DIC. To perform this comparison, the mean vertical displacement of the 18mm and 38mm particleboard samples were extracted along the red-dashed lines shown in Figure 138a and in Figure 143a. The lines are precisely selected along the direction that joins the load point to deflectometer tip. In Figure 147a and Figure 147b it is possible to see comparison between the vertical displacements measured for 18mm and 38mm samples, respectively. The maximum difference between the deflectometer and DIC are equal to 6% for 18mm sample and 2% for 38mm sample.

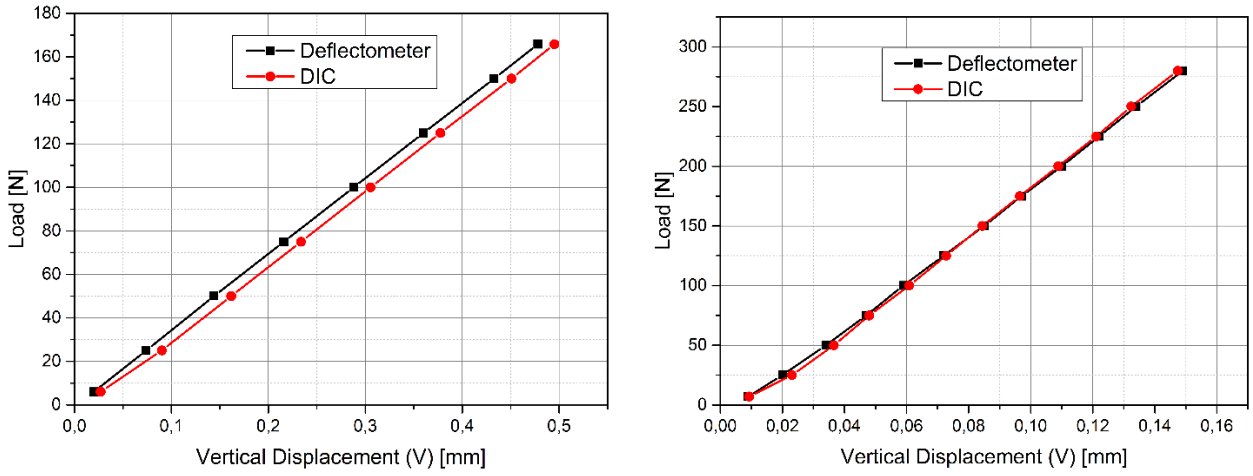

a b

Figure 147: Deflectometer and DIC vertical displacement comparison. a) 18mm particleboard's sample; b) 38mm particleboard's sample.

These tests allowed for further validation of G_{13} values obtained by indirect (TPB) and direct (Iosipescu test on particleboard samples without the notches) tests. In this case, the G_{13} of the particleboard's core of different thickness was evaluated by the relation reported in Eq. 55, extracting the shear strain from DIC results and determining the shear stresses distribution along the core's panel subject to TBP

$$G_{13\_i} = \frac{\tau_i}{\gamma_{xy\_i}} \qquad \text{eq. 55}$$

where G_{13_i} is the shear modulus calculated along the extraction line of strains γ_{xy_i} in the core of the particleboard and τ_i is the shear stress distribution.

It is crucial select accurately where to extract the shear strains to decrease the strain distortion due to the proximity of the load point to the supports. The extraction line was positioned 40mm away

from the load-nose (see Figure 141a and Figure 146a for the sample with the thickness equal to 18mm and 38mm). Knowing the ε_{xy} strain, using Eq. 52, is possible to evaluate the engineering shear strain.

To calculate the shear stress distribution it is necessary to study separately the core and skins of the panel, imposing the equilibrium of an infinitesimally long segment of the beam as reported in Figure 148 (105). For the sake of accurateness, it is important to underline that the ratio of width and thickness for TPB specimen is 1.3 and 2.7, respectively for 38mm and 18mm. These calculations used to express the shear stresses, are based on Jourawsky formula where, for a uniform rectangular section, it has an error compared to the maximum shear stress exact solution of almost 40% for a ratio equal to 2. This further comparison is just an estimation from three points bending test. Equations were derived under the assumption of constant Young modulus in the skins and in the core, according to the PSM model.

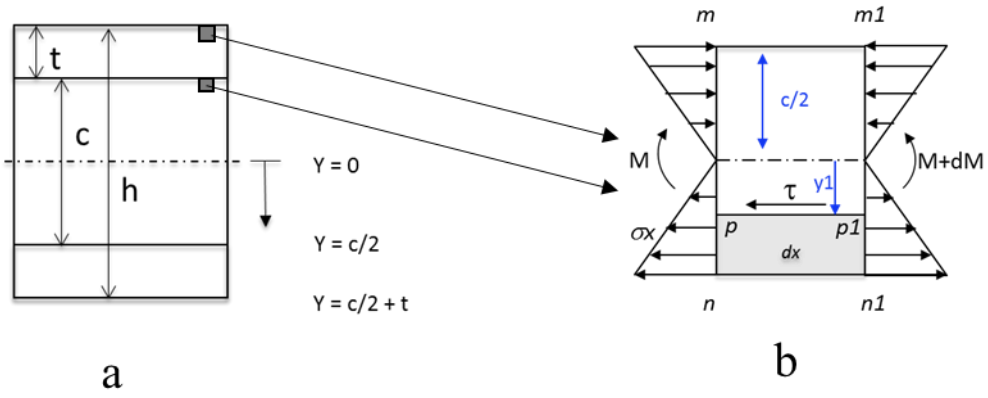

Figure 148: Shear stress distribution by horizontal equilibrium. a) Sandwich panel scheme; b) calculation scheme.

Considering all the contributions shown in Figure 148b and integrating the equilibrium equation along the free coordinate *y* reported in Figure 148a, it is possible to derive the expressions of the shear stresses for the skin (τ_f) and core (τ_c) exploiting the symmetrical geometry of the sandwich model applied to the particleboard. Eq. 56 and Eq. 57 are the two equations that express the shear stresses:

$$\tau_f = \frac{P}{D} * E_{f11} * \frac{1}{2} * \left[\left(\frac{h}{2}\right)^2 - y^2\right]_{c/2}^{c/2+t} \qquad \text{eq. 56}$$

$$\tau_c = \tau_f\left(y = \frac{c}{2}\right) + \frac{P}{D} * E_{c11} * \frac{1}{2} * \left[\left(\frac{c}{2}\right)^2 - y^2\right]_0^{c/2} \qquad \text{eq. 57}$$

where P is the applied load, D is the flexural stiffness expressed by Eq. 37; E_{c11} and E_{f11} are respectively the longitudinal elastic modulus of the core and of the skins determined by BSM in Section 3.3(Table 33); c and t are the thicknesses of the skins and of the core and y is the free coordinate along the particleboard thickness (Figure 148a).

Combining Eq.56 and Eq.57 is possible to obtain the shear stress profiles for 18mm and 38mm, plotted in Figure 149a and Figure 149b, respectively.

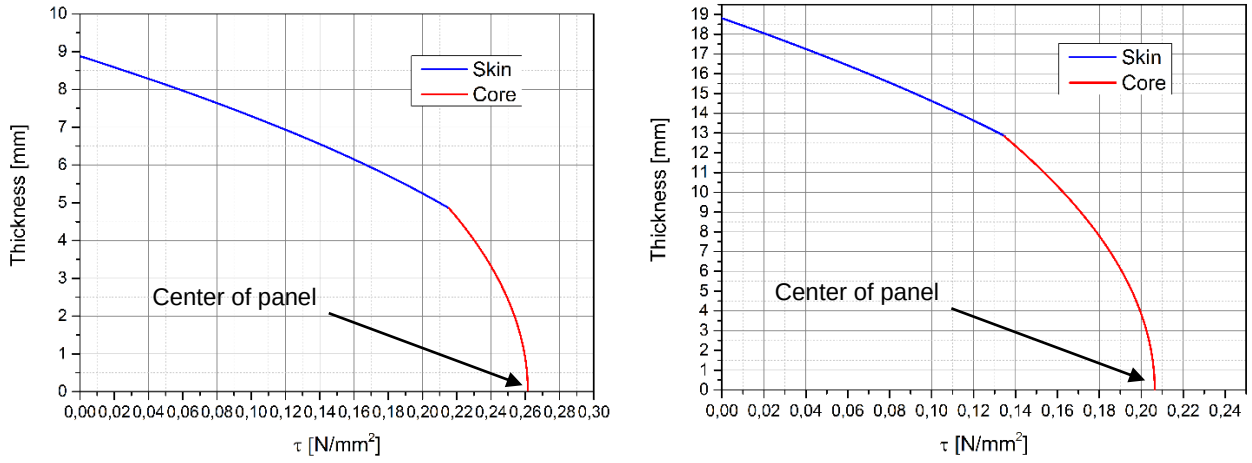

Figure 149: Shear stress distribution in the skin and in the core (only one side is shown, the other is symmetrical). a) Particleboard specimen of 18mm; b) particleboard specimen of 38mm.

Combining the τ distribution with the strain profile extracted from DIC measurements, it was then possible to calculate the shear modulus for the core portion by Eq. 55. The final value of G_{13} was evaluated as the mean value of the profile reported in Figure 150.

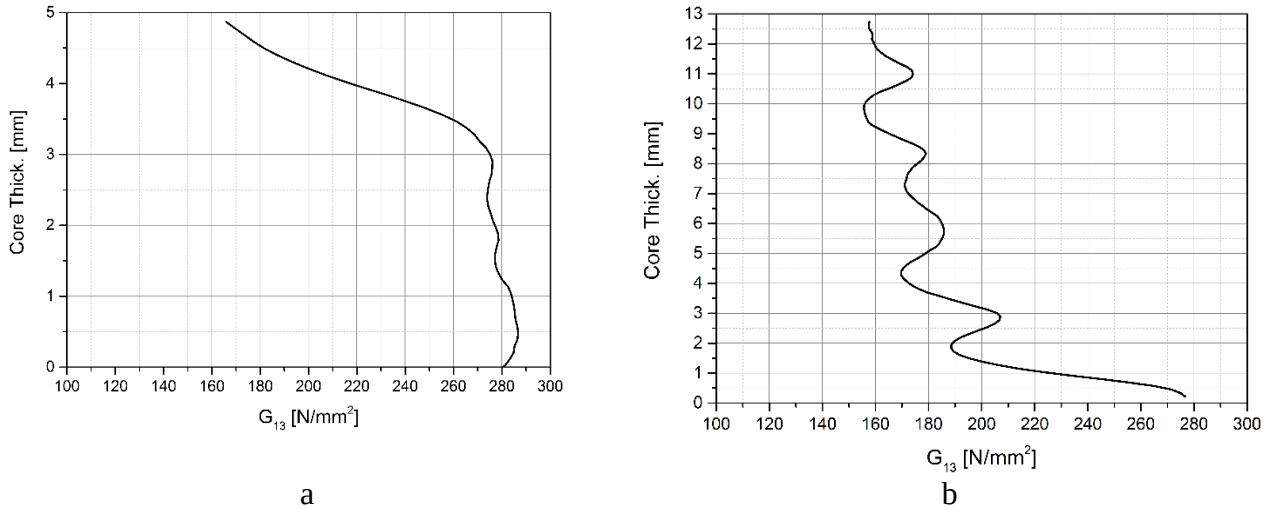

Figure 150: G_{13} profiles determined knowing the shear stress distribution and shear strain from DIC analysis. a) Shear modulus profile of 18mm core panel; b) shear modulus profile of 38mm core panel.

Shear modulus results are reported in Table 42 as mean value of three sample tested for 18mm and 38mm at 175mm and 275mm of distance between the three points bending supports. As you can see, there is a considerable scatter between the values of shear modulus, probably due to the variable planarity of the surface framed prepared manually by sanded plaster.

Table 42: G_{13} results by Three Points Bending Test coupled with DIC field method determined at environment condition of temperature and humidity equal to 26°C and 35%.

Board thick. [mm]	Span [mm]	G_{13} [MPa]	
		Mean	Std. Err.
38	175	245	18.02
	275	219	9.03
18	175	212	15.03
	275	225	16.95

Table 43 compares all the G_{13} modulus values obtained by the various identification methods applied to the particleboard. Leaving aside the second column that represents the Iosipescu results from notched samples, it is possible to see that for 18mm samples all the other methods are in good agreement. It is not possible to come to the same conclusion in the case of the 38mm particleboard: the results obtained by TPBT and DIC (fourth column of Table 43) are higher than PSM, BSM and QSM. To try to reduce this difference, I thought that the proximity of shear strain extraction line to the load point could produce a strain distortion that can be the cause of the higher value of shear modulus of 38mm.

Table 43: Final comparison between macroscopic methods

Board Tick. [mm]	G_{13} [MPa]					
	Iosipescu + DIC	Iosipescu + DIC without notches	TPBT +DIC	PSM	BSM	QSM
38	105	125	219	137	137	139
18	144	222	225	224	223	228

I prepared new 38mm particleboard samples, modifying the region of interest to guarantees a right distance from the load point to extract the shear strain. I selected the extraction zone 80mm (twice than before) away from the load point, but repeating the same procedure I obtained the same results for 38mm. This time the extraction line was probably too close to the supports.

3.6 Conclusions

To summarise at the end of this chapter, I presented different methods for estimating the elastic constants by indirect (TPBT with variable span) and direct methods (TPBT and IT coupled with DIC) of particleboard made of recycled wood, comparing the results in particular for shear modulus G_{13} of the core of the panel. Starting from three point bending test with varying span, I determined the longitudinal elastic modulus of the skins and core and shear modulus of the core, by studying the particleboard with different sandwich models. Focusing on shear modulus G_{13} I tried to validate it, by different experimental method coupled with DIC to measure the shear strains on the samples. It was found that (referring to the Table 43):

- Iosipescu method performed on notched samples, produce results about shear modulus of the core's panel not in agreement with the TPBTVS results. This difference is presumably due to the machining of the notches in the sample, that may have produced a stiffness loss already in proportionality zone between load and strain. For this, the shear modulus resulted lower than values obtained by other methods.
- Iosipescu approach performed on samples without notches yielded a G_{13} modulus of the particleboard's core in agreement with the TPBTVS and TPBT coupled with DIC. The shift between the methods is less than 5% for 38mm and practically the same for 18mm samples.
- The TPBT was coupled with Digital Image Correlation to estimate another time the shear modulus of the core's panel. For 18mm, the results are in agreement with other methods, but for 38mm there is a deviation greater than 30%, probably because of the proximity of the strain extraction line to the loading nose. However, moving the extraction line far from the loading point up to 80mm caused the extraction line fall too near to the supports (remember the span equal to 175mm and 275mm) producing the same distortion effect on the strain. Another cause could be the presence of not negligible out of plane displacements for 38mm samples, due to anticlastic bending. This type of displacement is not possible to be recorded by DIC method that observes 2D deformations of the surface framed and can affect the accuracy of in-plane measurements. In the future, particleboard samples of 38 mm thickness should be tested using a much greater distance between the supports. However, a completely different setup is needed, being the maximum span of the actual rig limited to 400 mm, as well as different DIC setup, allowing for framing a much wider area.

Chapter 4 – Micro-mechanical model of particleboard wood based material.

4.1 Outline

In the previous chapters, the elastic longitudinal and shear moduli of the skins and of the core were determined indirectly, by three point bending tests with variable span and Iosipescu tests. However, some discrepancies were evident between the values of the elastic moduli determined with different methods. The main difficulties were encountered in the case of the out of plane shear modulus of the core. In this chapter, starting from image analysis results performed on Micro-CT images (Chapter 2), micro-mechanical modelling of particleboard is attempted, in order to confirm the results obtained by macroscopic testing. Moreover, in the perspective of designing improved lightweight panels, the development of a micromechanical model of the core layer should provide a design tool for evaluating the impact of microstructural modifications of the core's properties, thus allowing for virtual experiments before any modification of the manufacturing process.

The micromechanical model developed in this thesis is a FE model of a Representative Volume Element (RVE) of the material, which will lead to the evaluation of the elastic constants at the macroscale by homogenization. These results were finally compared with the elastic constants obtained before with the experimental methods (see Chapter 3).

To obtain the input data required for the FE environment it was necessary to analyze the particleboard with a series of different techniques. One of those is the analysis of the Micro-CT images, necessary to inspect the geometrical characteristics and orientations of the particles. These images was also useful for a thresholding algorithm that was applied in order to evaluate the particleboard volume fractions. In addition, an automatic detection algorithm of the geometrical characteristics of the raw wood fibres before the particleboard production process was applied.

Finally, considering the Vertical Density Profile (VDP) of the material determined by the methods presented in Chapter 2, the core of the 18 mm thick panel was identified as a region of large thickness, characterized by a relatively uniform density profile, suitable for being modelled using the FE package of Digimat®. This micro-model is based on the input data about the properties of the wood particles, starting from Micro-CT image analysis, but also taking into account also data from

the analysis of unprocessed particles. Both RVEs were built considering the UF-adhesive or without it.

The results of the analysis consisted in the homogenized elastic constants of an equivalent othotropic material. They were obtained by an appropriate configuration of the Digimat software to select the right Representative Volume Element dimensions and generation algorithm. Finally, the results obtained with the different RVE models were compared with the elastic constants derived experimentally.

Part of the last Chapter was developed in the framework of the Master thesis (106) that I co-supervised.

4.2 Digimat software

The generation and analysis of particleboard RVE was performed using Digimat software, a nonlinear multi-scale and structure modelling platform that allows the users to perform several tasks, including homogenization by different techniques. In particular, using Digimat it is possible to investigate and predict the behaviour of a large mix of composite materials, optimising the weight of the parts and reducing the material testing and prototyping, all this features taking into account the material's manufacturing process (107). To perform the analysis, Digimat provides many modules like (107):

- Mean Field (MF); generally adopted in the engineering plastics area, where Digimat is used to model the composite materials as short fibre reinforced thermoplastic injection moulded parts, to predict their behaviour. Normally, MF analysis requires the fibre orientation estimated by injection moulding software, besides the mechanical characteristics of the constituents.
- Finite Element (FE); used to generate a realistic Representative Volume Element (RVE) of different material microstructures as reinforced plastics, rubbers, metals or others and build the corresponding finite element model. By imposing appropriate boundary conditions and loads, the resulting finite element problem can be solved using various FEA codes and results are processed to extract the values of the elastic constants of the homogenized material.
- Material eXchange (MX); a material database that contains the data for each phase of the composite as well as microstructure data in terms of constituents and morphology.
- Material MAPping (MAP); it is used to transfer fibre orientations, residual stresses, temperatures, weld lines, porosity or volume fraction between different injection moulding, helping the engineers to generate the optimal mesh refinement and element types to capture the real material behaviour.
- Structural Analysis (CAE); it enables an integrative and accurate approach to multi-scale modelling of the final part structures.

In particular, Digimat offers a series of interfaces where it is possible to define every characteristic of the material that is being modelled.

Considering the purpose of this Chapter focused on RVE generation of the particleboard, the Finite Element module was used. Figure 151 reports the control panel and FE model tree of the FE-Module of Digimat.

When the user opens the FE-Module, the software offers a series of interfaces where it is possible to define every characteristic of the composite material studied (Figure 151b). First, is necessary to define the composite's constituents inputting the material's density and its elastic constants. Then it is necessary to define the different phases that could be voids, inclusions or matrix,

by inserting for each component its volume fraction and, for the inclusions, their geometrical characteristics as dimensions, orientation and aspect ratio.

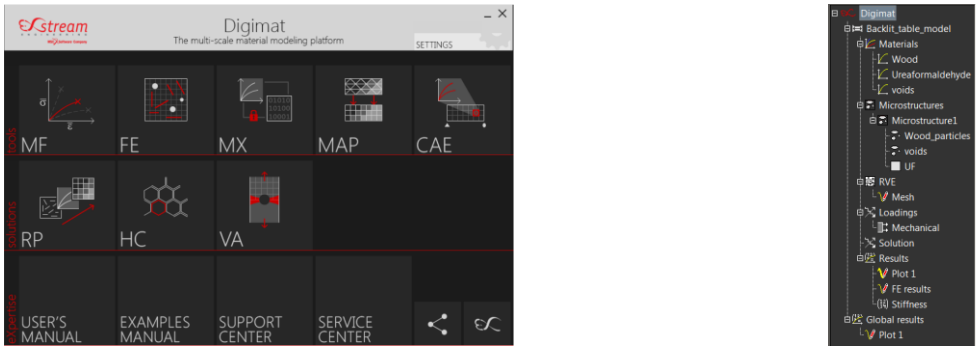

a b

Figure 151: Digimat interface. a) Digimat's control panel; b) Digimat FE model tree.

Then it is possible to select the generation algorithm to produce the RVE, selecting its dimension and the type of mesh to be used. Digimat provides two algorithms for generating the RVE named *Classical FE Algorithm* and *Stacking Algorithm* , that were studied in the next section where all the advantages and limitations are presented. It is important to underline that the choice of the algorithm is decisive to model correctly the material.

The loading selection includes mechanical, thermal, electrical or thermo-mechanical loadings and can be selected a loading cycle monotonic, cyclic or custom. Moreover, Digimat offers additional loading source named uniaxial, biaxial, shear, general 2D or 3D and Automatic properties evaluation (107).

The available boundary conditions (BC) in this platform are Dirichlet BC, Mixed BC and Periodic BC (107). Once the periodic boundary condition and loadings have been defined, it is possible to launch the analysis to build the RVE of the material and evaluate the corresponding elastic constants.

In the literature is possible to find many works that using FE micro modelling to evaluate properties of different materials. For example, in (108) the authors predicted the biaxial yield behaviour, hardening and plastic flow of composite materials made of an elastoplastic matrix reinforced with misaligned short fibre using mean-field homogenization method and RVE generation by Digimat FE-module. Figure 152a report the unit cell of the composite material aligned in the longitudinal direction, while Figure 152b shows the RVE of randomly oriented short fibre reinforced composites.

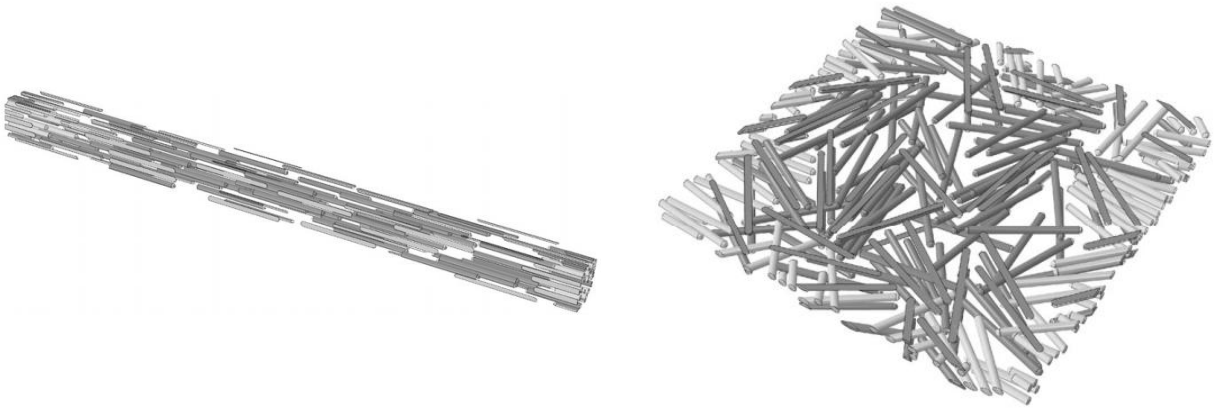

a b

Figure 152: Typical unit cells resulted from the FE simulations. a) 166 aligned fibers in the longitudinal direction 1. The volume fraction of fibers (v) and their aspect ratio (FAR) are respectively v=15.7% and FAR = 15; b) 245 randomly oriented fibres in the 1-2 plane. v=15.7% and FAR = 15 (108).

Another example reported in (109) is focused on multi-scale modelling of epoxy-based composites with polydisperse SiC nanoparticles. Herein the authors use the Digimat-FE module to generate the RVE reported in Figure 153, where the unit cell represent the microstructure of the material modelled as a three-phase scheme composed of nanoparticles, matrix and interphase zone to derive the elastic constants as a function of the characteristics of the particles.

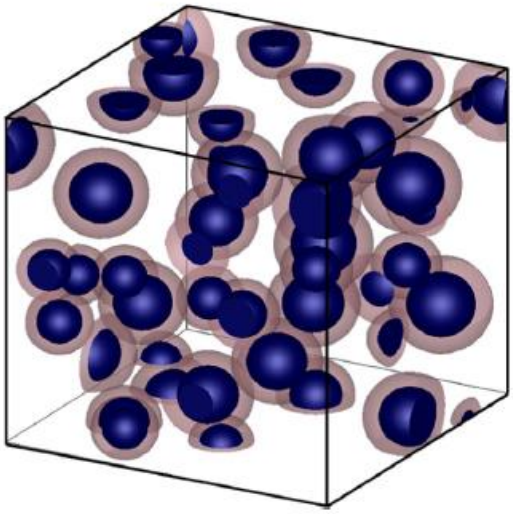

Figure 153: RVE of Nano-composite containing 24 nanoparticles. Is possible to see the surrounding interphase of the particles generated by Digimat-FE.

4.3 Backlit wood-particles geometrical measurement set-up

As we will see in the next sections of this Chapter, the dimensional data of the wood particles of the particleboard can be determined by image analysis starting from Micro-CT images or images of the fibres before the production process. In particular, these particles that come from the grinding step, are provided by Mauro Saviola Group and are have undergone drying only, but no compaction or adhesive spraying. As presented in Chapter 2, the Micro-CT images were obtained from particleboard's samples with dimensions equal to 10x10x18mm, then it is possible that the particles were cut and their original dimensions modified. Observing the wood particles before the hot-pressing phase it will be possible to detect their true geometrical characteristics. This will be useful to understand the differences on the resultant RVE if the dimensions of the particles are collected from the Micro-CT images or from analysis of the fibres before the final processing.

To obtain the pictures of the raw particles and in order to have images with maximum contrast to perform efficiently particle's detection, pictures of a sample of fibres were taken using digital camera and spreading the wood particles on a backlit table. The digital camera, its optics and tripod stand are the same of which utilised in Chapter 3 to perform DIC analysis, and the backlit table is shown in Figure 154.

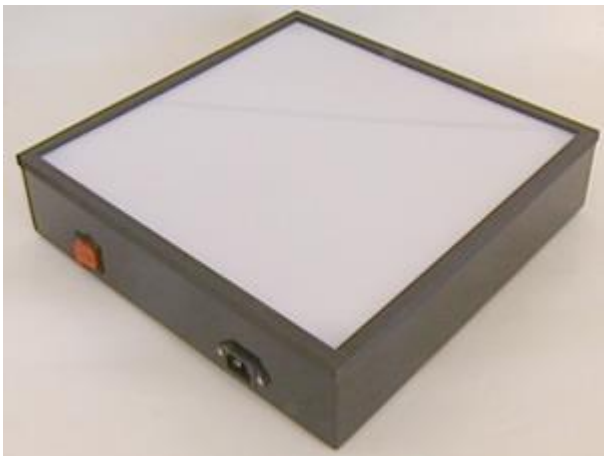

Figure 154: backlit table to visualize the slides, transparencies or X-Ray plate.

The camera was placed exactly above to the light table, reaching as much as possible the perpendicularity with the table, by a spirit level. Lastly, in order to perform the spatial calibration of the image, it was necessary to frame in every picture a transparent ruler as length reference. Figure 155 shows the set-up to perform the acquisition of the images of the wood particles before the adhesive spreading and hot-pressing phase.

Figure 155: a) Backlit table set-up; b) wood-particles ready to be framed

Figure 156 reports the particles classified in agreement to the production process in fine (Figure 156a), used for the skin layers, and coarse (Figure 156b), used for the core, placed onto the backlit table.

a b

Figure 156: a) fine wood-particles; b) coarse wood-particles.

By the backlit table set-up, it is possible to acquire the images and measure the particle's dimensions. Figure 157a report high-contrast image of coarse particles and Figure 157b shows fine particles. It is important to underline that the particles disposition is very important to have good measurements. The particles must be well separated, without superposition that can lead to an incorrect detection. Moreover, by backlit images, it is impossible to acquire meaningful data about the particle's orientation because these are spread by the operator. To take into account the orientation

obtained during the particleboard production process, the Micro-CT images were used, as described later.

The analysis of the fine particles was conducted with the sole purpose of obtaining data useful for the setup of the algorithms for image processing. No modelling of the skins that are made of these fine particles is attempted in this thesis, due to their non uniform density profile, which constitute a problem characterized by higher level of complexity with respect to the modelling of the more homogeneous core layer.

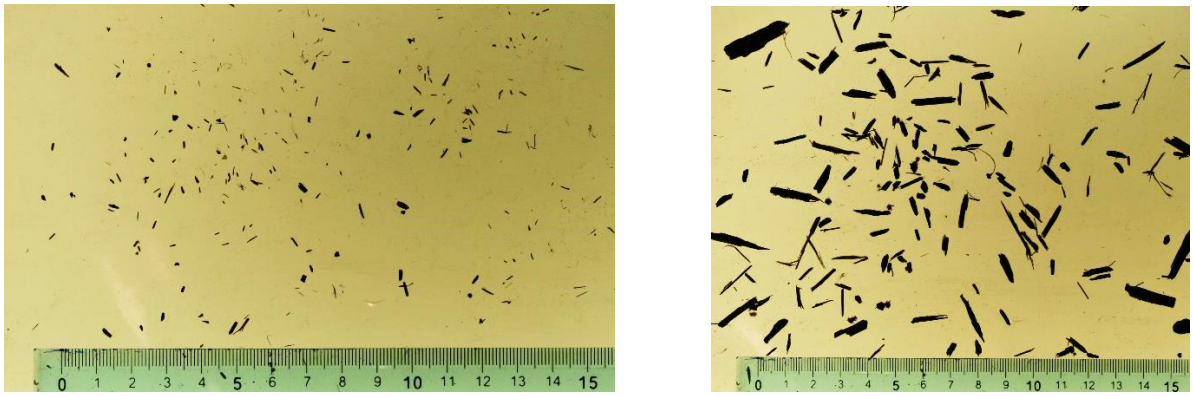

a b

Figure 157: backlit images. a) Fine particles; b) coarse particles.

4.4 Particleboard Micro mechanical model building input data collecting

After briefly explaining the main software tool (Section 4.2) and simple experimental set-up (Section 4.3) used in this last part of my PhD thesis, the next sections will be dedicated to present all the steps taken to generate the particleboard RVE and obtain the elastic constants of the material by micromechanical analysis developed by Digimat-FE.

4.4.1 Manual detection of the geometrical properties of the wood particles

In order to build an RVE model of particleboard of thickness equal to 18mm, the main sources were Micro-CT images, used to identify the characteristic parameters of the particles as input for Digimat-FE, namely the orientations and the dimensions. From this point onwards, the wood particles will be defined as fibres.

Fibres were assumed to have a planar distribution in the longitudinal plane of the panels and therefore their geometrical characteristics were obtained by the analysis of Micro-CT slices that are parallel to that plane. The assumption of a planar distribution was confirmed qualitatively by the observation of the transverse views of the reconstructed sample. Several slices of the reconstructed volume were processed to obtain a statistical sample of fibre length (main fibres axis), fibre width or equivalent diameter (secondary fibres axis) and Fibre Aspect Ratio (F.A.R) defined by Eq. 59.

$$F.A.R. = {}^{Length}/_{Width} \qquad \text{eq. 59}$$

It is important to remark that for the nature of wood microstructure and productive process in the grinding phase, the geometry of the particles are in agreement to the minor strength axis. It is then reasonable to suppose (it is qualitatively verified) that the length and the width of the single particle are higher than the thickness. Others important characteristics are the orientations and the estimated area. The fibres' area will be an estimation because it is defined as the equivalent ellipse that contains the fibres. This ellipse is defined considering its two axes equal respectively to main fibres axis and secondary fibre axis.

I used the tool presented in (110) where the authors developed a Matlab subroutine named *Fiberstat* to measure the geometrical quantity of glass fibres reinforced polymer. It is important to underline that this subroutine works by manual detection of the geometrical quantities of the fibres,

then the procedure can be affected by the subjectivity of the operator. An automatic segmentation tool, using the images obtained by the Micro-CT technique, would be useless because images are too rich of details and particles are often too close to each other.

The *Fiberstat* algorithm works with 8-bit images. The image's contrast was enhanced to best visualise the fibres in every slice observed. It is fundamental to remember that this contrast enhancement operation must be performed in an equal manner for every slice in order not to shift grey levels, for the volume fraction detection performed in next Section. After this equalisation step performed by FIJI (83), the slices appears as reported in Figure 158.

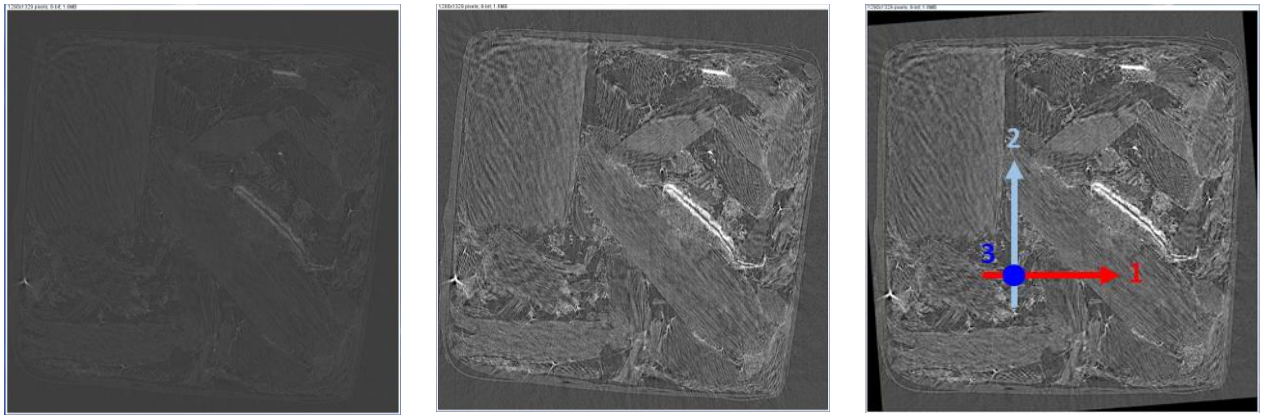

a b c

Figure 158: Equalization procedure and rigid rotation performed on 8-bit Micro-CT slices. a) Original Image after conversion from 32bit to 8bit; b) slice processed by equalization; c) slice after rigid rotation with the material reference system.

In similar way as presented in Section 2.3, the spatial calibration of the images is required in order to have a reference to express the fibres' geometrical quantities. As presented before, each side of the particleboard samples scanned by tomography have dimensions reported in Table 21, so it is easy to achieve spatial calibration.

Observing Figure 158b it is possible to see that the slice is not oriented parallel to X and Y axes, so to obtain the reference, it was necessary to rotate to reach parallelism with horizontal and vertical directions (Figure 158c)

After these settings, it was possible to start the analysis of the fibres. The first required dimension is the principal axis of the fibre. After that, 5 diameters are required. The resultant fibre width is the average value of the previous 5 diameters collected. The fibre orientation is expressed comparing the principal axis orientation with the horizontal one. An example of this type of fibre identification and analysis is reported in Figure 159, in which the red line represents the selection of the fibre principal axis (main axis) and the 5 light blue lines (for each fibre) are the selection necessary for the detection of the secondary fibre axis. As said before, this is a subjective procedure because the identification and selection of the fibres can slightly changes if the operator that analyse the image

changes. However, a lot of details are present in the available images (see Figure 158 and Figure 159) that make it impossible to apply standard automatic techniques.

At the end of the particle detection step, all the obtained fibre characteristics (principal and secondary axes, *F.A.R.*, orientations and estimated area) are stored in a Matlab matrix that can be exported to a Microsoft Excel file for the next analysis steps.

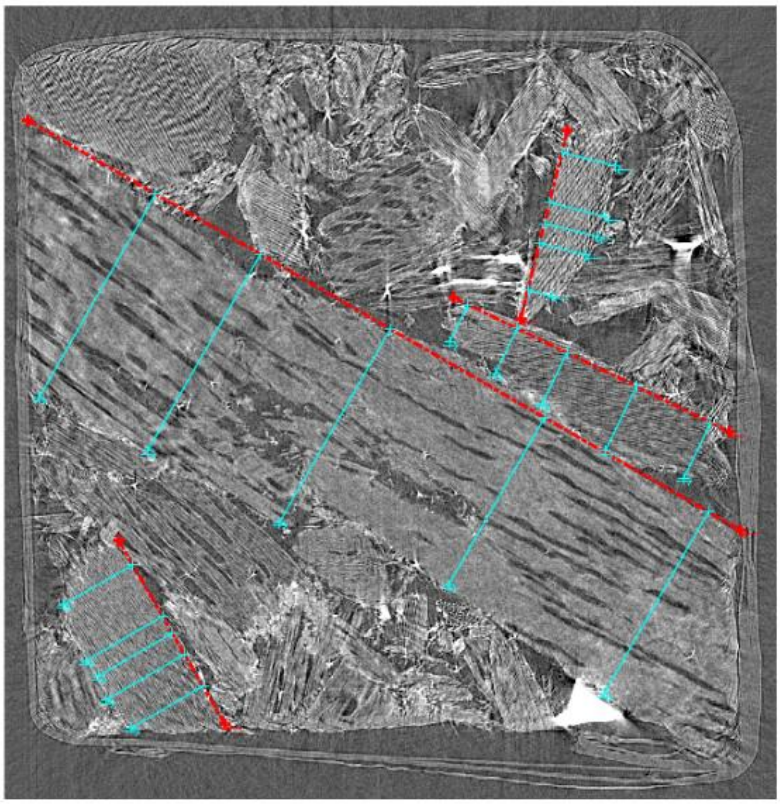

Figure 159: Fibre detection procedure. The red-dashed lines represent the principal axis while the light blue lines individuates the secondary axis.

Performing manual detection on 37 slices extracted from the core and from the skins of the 18mm particleboard's Micro-CTs allowed for obtaining the mean results reported in Table 44 and Table 45 for the core and skins, respectively. The values reported are the average results calculated without applying any weighting on the particles information; every particle has the same importance on the final mean value for every quantity (principal and secondary axes, area and F.A.R). As reported in (111) the modern particle scientists often choose to describe the entire size distribution as opposed to just a single point on it. For image analysis results, it is common to report the distribution width or, as performed here, the mean values must be followed from the standard deviation of the particles distribution (111). Figure 160 reports the principal axis length distribution of the core's fibres included in every class and Figure 161 reports the same percentage distribution of the fibre length of the skins.

Table 44: Geometrical characteristics of the core fibres.

	Fibre length [µm]		Area [µm²]	F.A.R. (Particle Aspect Ratio)
	Principal axis	Secondary axis		
Mean value	2920	1060	2922409	3.13
Max	11120	4870	33465627	11.5
Min	650	130	109828	1.01
Std. Dev	1778	627	3827017	1.77

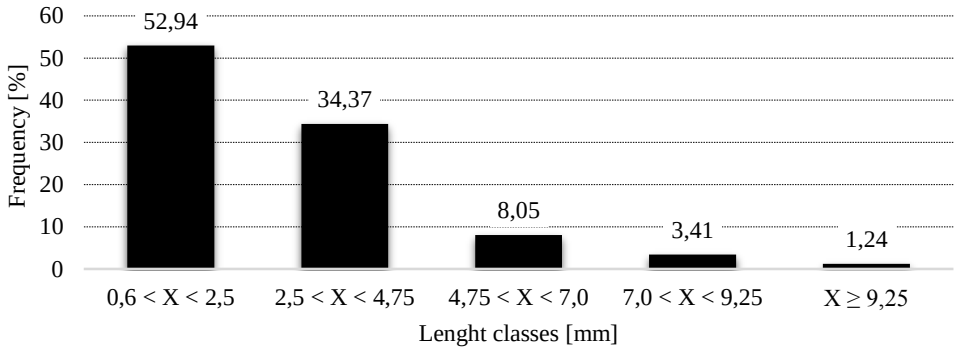

Figure 160: Principal axis length distribution of the core's fibres for each class length.

Table 45: Geometrical characteristics of the skin fibres.

	Fibre length [µm]		Area [µm²]	F.A.R.
	Principal axis	Secondary axis		
Mean value	1420	480	555583	3.24
Max	4330	1100	2235351	14.09
Min	510	170	83243	1.04
Std. Dev.	726	194	412601	1.83

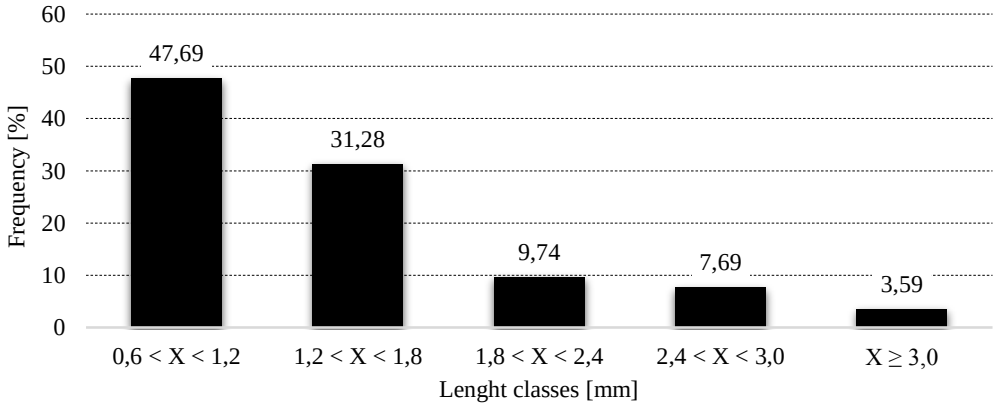

Figure 161: Principal axis length distribution of the skin's fibres for each class length.

The reference system used in this thesis to characterise the particles orientations is shown in Figure 158c where the direction 1 is the direction of the hot-pressing considered it as the principal panel direction to refer the fibres orientation. In particular, to build RVE of the material in Digimat-FE the components of the orientation tensor of the fibres are required. Assuming a planar distributions, the components are defined by Eq. 60 and Eq. 61 (112) (107):

$$a[1,1] = \frac{\sum_{i=1}^{n} \cos^2(\theta_i)}{n} = \langle \cos^2(\theta_i) \rangle \qquad \text{eq. 60}$$

$$a[2,2] = \frac{\sum_{i=1}^{n} \sin^2(\theta_i)}{n} = \langle \sin^2(\theta_i) \rangle \qquad \text{eq. 61}$$

where θ_I are every particle's orientation obtained comparing its principal axis to the direction 1 shown in Figure 158c and *a[i,j]* are the tensor components. Also, the quantities a[1,3]; a[2,3] and a[3,3] are required but these three values are assumed to be null because, during the production of the panel, the particles are disposed on top of each other and they don't show a relevant out of plane orientation, as confirmed by micro CT.

The results about orientation distribution and orientation tensor for the skins and core of the panel are listed in Table 46 and in Figure 162. It is possible to observe from polar diagrams that in particular for the skins, the preferential disposition is parallel to the direction 1 in the skins, whereas in the core a lower degree of alignment is found even if a predominance of 0° (dir. 1) and 90° (dir. 2) orientation is visible.

Table 46: Orientation tensor components for the core and skins of the panel.

Core		**Skin**	
a[1,1]	**a[2,2]**	**a[1,1]**	**a[2,2]**
0.5	0.5	0.6	0.4

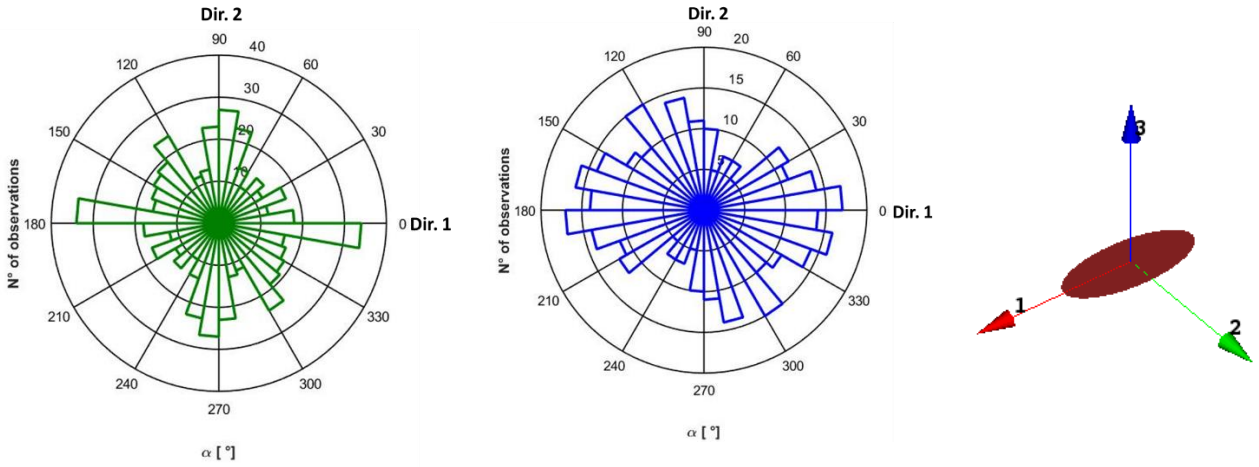

a c d

Figure 162: Polar diagrams and tensor display. a) core particles orientation distribution; b) skins particles orientation distribution; c) orientation tensor display.

Another important geometrical quantities that is required for the definition of the RVE is the wood fibres thickness. To determine the fibre thickness, it was necessary to stack up the particleboard's Micro-CT slices to reconstruct a 3D volume by the "Volume viewer" subroutine of FIJI (see Chapter 2). Thus, it was possible to observe the volume from different planes (in particular X-Z plane) as reported in Figure163c and Figure 163d respectively. Taking the snapshots of the core and skins zones in these planes (respectively Figure 164a and Figure 164b) it was possible to detect the fibre's thicknesses using the same procedure presented before. The X-Z images were collected along Y axis from the reconstructed volume, treating the thicknesses as the secondary axis measurements. The resultant fibre thickness is the average value of the 5 lengths collected on X-Z image (Figure 164a). The total number of snapshots processed was equal to 20, 10 for the core and 10 for the skins to acquire a total of 120 fibre's thickness values. Table 47 reports the results.

Table 47: Fibre's thicknesses.

	Fibre thickness [µm]	
	Core	**Skin**
Mean value	349	234
Max	913	326
Min	132	133
Std. Dev.	177	68

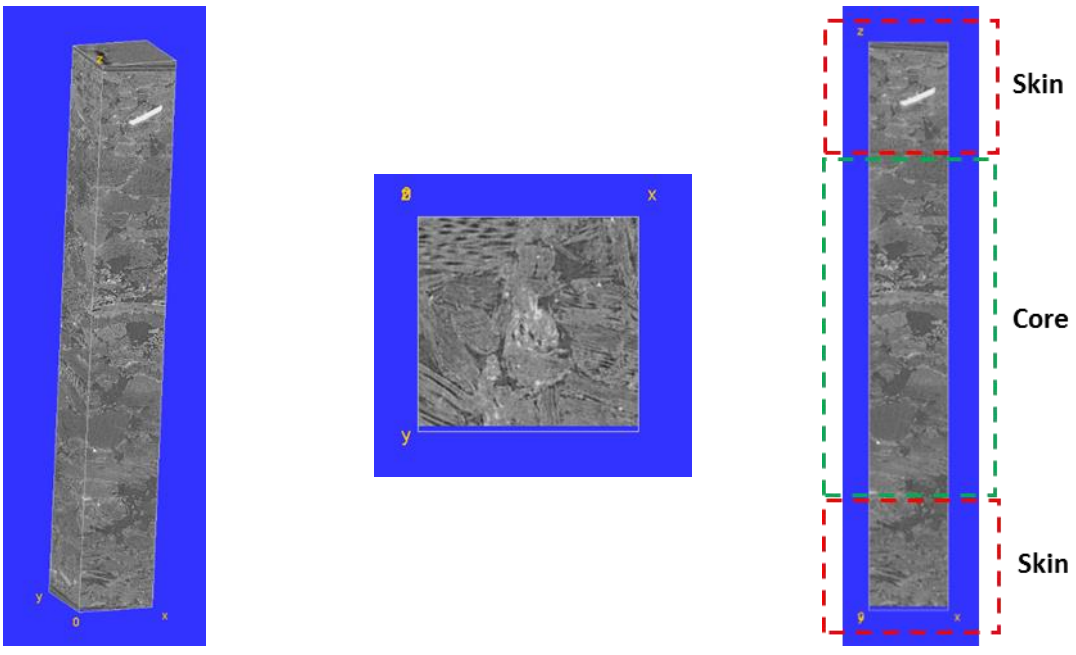

a b c

Figure 163: Particleboard 3D reconstructed volume observed from different views. a) 3D; b) X-Y plane; c) X-Z plane.

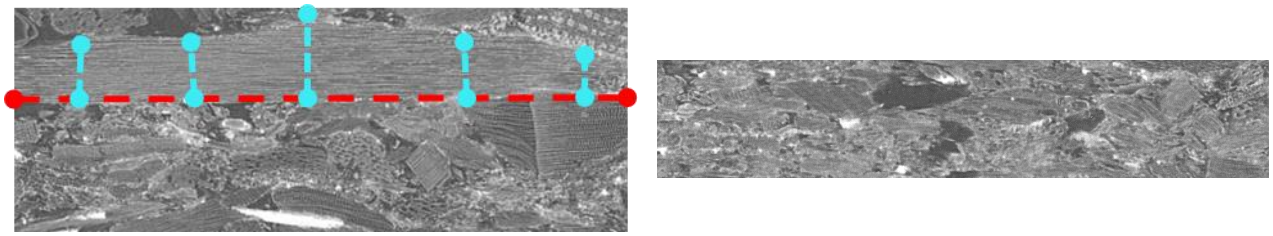

a b

Figure 164: two snapshots. a) X-Z plane view of the core zone (red dashed line is the principal axis, and the five light blue dashed lines represents the five thicknesses of the particle); b) X-Z plane view skin zone.

These results will be applied to build the RVE of particleboard named *μCT-RVE*. The definition comes from the origin of the geometrical fibres data. An alternative way to get the fibres dimensional data was by measurement on the fibres used for manufacturing before glueing and hot-pressing phase and not extracted from Micro-CT specimen images except the fibres thickness.

4.4.2 Particles wood automatically detection using particles before glued spreading and hot-pressing phase

The set-up described in Section 4.3 allows for detecting the true fibre dimensions because fibres are not cut during the specimen extraction from the main panel unlike the particles of the Micro-CT images. However, by this method, it will be impossible to acquire meaningful data about the fibre orientations and, obviously, their thicknesses.

In addition, this method is a good alternative, with respect to the previous one, because it allows detecting the particles characteristics in an automatic way, reducing the necessary time and the operator dependence.

Starting from fibre's images reported in Figure 157 and Figure 165a (six pictures acquired for both fine and coarse fibres) the automatic segmentation was performed by Matlab Image toolbox. In particular, the two subroutines used are Image-Segmenter (IS) and Image-Region-Analyser (IRA). As usual, the images must be prepared before applying the geometrical quantities detector IRA, separating foreground object from the background. To do this, I used the IS subroutine that works on the 8-bit image by the active contours algorithm (113), (114) to reach the separation of the foreground from the background. The final results can be manually improved by modifying the sensitivity or the threshold. Using this tool, the output image is a binary image where the foreground is white (logical true) and the background is black (logical false), see Figure 165b.

a b c

Figure 165: a) Original image of core fibres; b) binary image after IS analysis; c) inverted image.

However, IRA recognises background as black (logical false) and objects as white (logical true), thus the next step was inversion (Figure 165b). The resulting image is reported in Figure 165c. Then, by the IRA algorithm it was possible to obtain all the measurements of the wood fibres. i.e. the principal axis length, the secondary axis length and the area of the fibres. Although the scatter of the particles onto the backlit table was good, due to the small dimensions of the fibres compared to the backlit surface, it was impossible to avoid clusters, as shown in Figure 166.

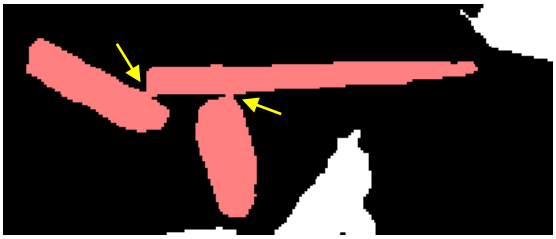

Figure 166: Example of superposition of the fibres (see the yellow arrows)

To reduce this problem, IRA provides a series of filters that can help to eliminates many incorrect detections. The most effective are listed below:

- Area > *N* pixels. Imposing this filter, subroutine preserves the detected surface with the greater area and eliminates small white pixels coming out from the thresholding.
- Solidity > α. The solidity describes the proportion of pixels in the convex hull that are also in the region defined as *Area / Convex Area* (115). It allows to detect and eliminate superimposed and fictitious fibres
- Euler Number > β. Euler Number is a topological feature of a binary image which is the difference between the number of contiguous parts and the number of holes (116). $Eul = N° \, of \, contiguous \, parts - N° \, of \, holes$. It allows detecting and eliminating superimposed and fictitious fibres.

N; α and β are the parameters that can be evaluate repeating the analysis to reach the best tradeoff. The values found are *N = 100px;* α = 0.65 and β = 0.The automatic detection results for the core and

skin fibres by IS and IRA subroutine provided from Image Analysis Toolbox available in Matlab are report in Table 48 and in
Table 49, respectively.

Table 48: Geometrical characteristics of core particles by backlit image analysis.

	Fibre length [µm]		Area [µm²]	F.A.R.
	Principal axis	Secondary axis		
Mean value	7561	1745	16729906	5.3
Max	51414	10816	355432276	49.3
Min	1071	268	900240	1.1
Dev. St.	5910	1157	25647130	3.7

Table 49: Geometrical characteristics of skin particles by backlit image analysis.

	Fibre length [µm]		Area [µm²]	F.A.R.
	Principal axis	Secondary axis		
Mean value	1872	466	1005780	4.9
Max	6178	1716	7538250	20.4
Min	412	135	103123	1.1
Dev. St.	1049	308	1130626	3.1

The principal axis fibre length distribution for the core and the skin are shown in Figure 167 and in Figure 168, respectively.

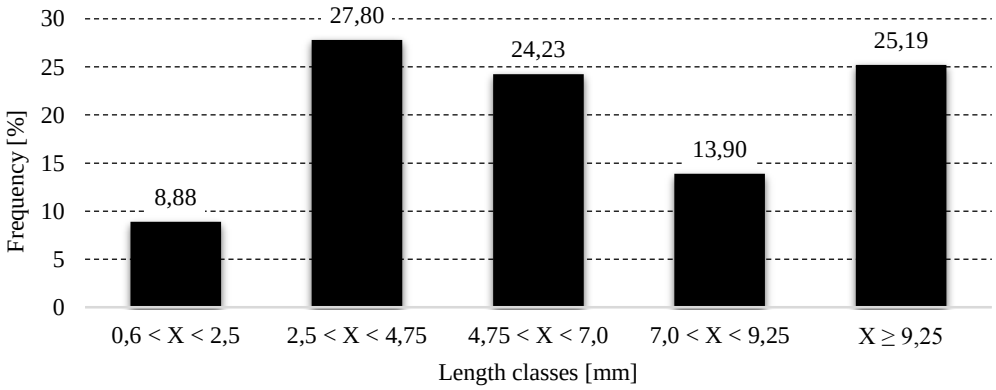

Figure 167: Principal axis length distribution of the core's fibres from backlit image analysis.

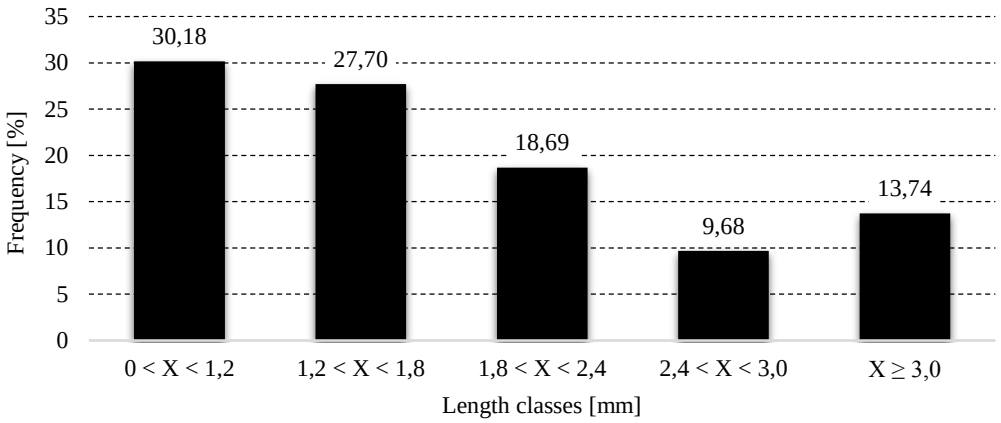

Figure 168: Principal axis length distribution of the skin's fibres from backlit image analysis.

By automatic detection using the backlit table, it is physically impossible to measure the thickness of the particles due to the nature of the procedure. To build the RVE using this geometrical information collected by the backlit method, it was necessary to make a strong assumption about the particles' thickness: it was considered invariant before and after the production process. In this manner, the RVE was performed considering the particles length and width before the production process (from the backlit table) and the particles thickness after the production process (from the Micro-CT image analysis). In the future, it will be important to verify if this assumption is correct or not.

4.4.3 Wood fibres geometry comparison

Measurements performed on the Micro-CT and on the backlit images for the core and skin fibres are reported respectively in Figure 169a and in Figure 169b for comparison purposes.

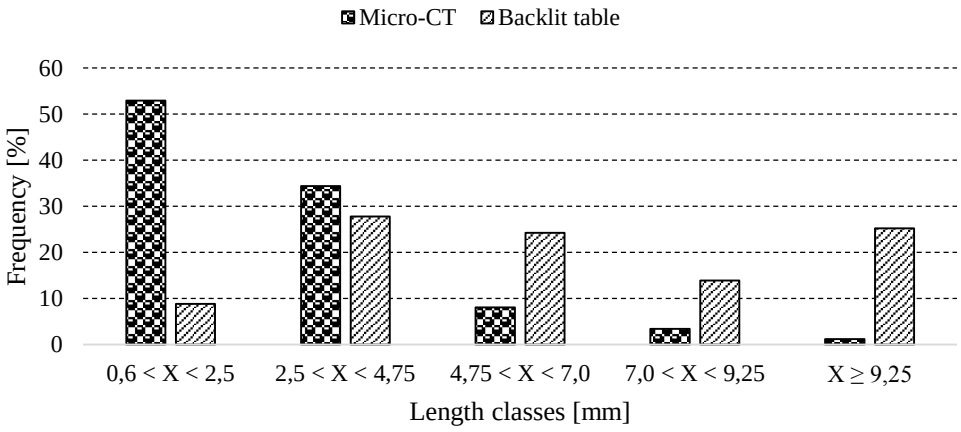

a

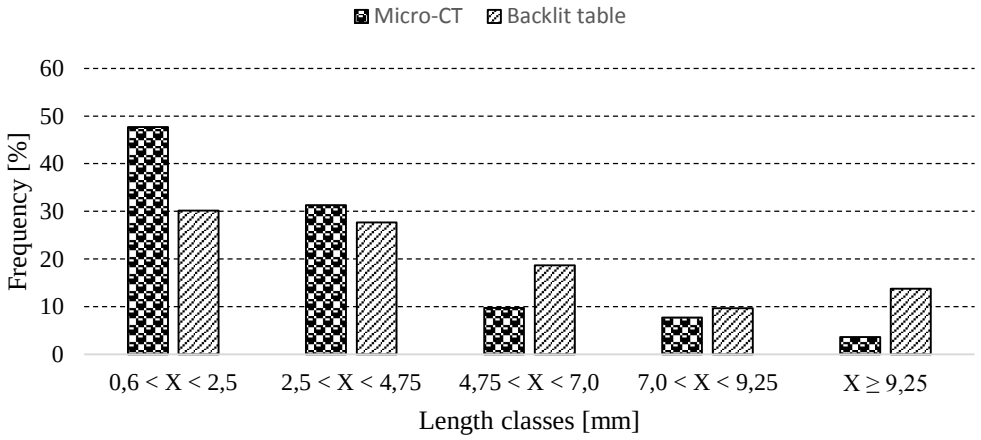

b

Figure 169: Principal axis length comparison between Micro-CT and backlit image analysis. a) core's fibres; b) skin's fibres

Observing Figure 169b, it appears that the fibre length distribution in the skins obtained processing the Micro-CT images and by the automatic segmentation performed on backlit images are quite similar. In fact, their length distribution are in good agreement as reported in Table 50 where the shift between the principal axis length is equal to 24% and 2% for the secondary axis. Conversely, for the core fibres (see Figure 169a) the difference between the two methods is much larger Table 50 shows a shift equal to 61% regarding the principal fibre's axis and 39% for the secondary axis. This mismatch between the core's fibres lengths observed on Micro-CT and backlit images is likely to be due to the fact that the dimensions of the sample used for the X-ray tomography acquisition (cross section equal to 10x10mm) are not sufficient to detect entire fibres, especially for the core particleboard portion, in which the longest ones are found. At this time, there are not elements to say that the fibres breakage after the deposition, are due to the pressing phase. The second one is about the slice analysis. Instead, by the backlit method images mainly include entire fibres.

Table 50: Comparison between fibres geometrical quantities acquired from Micro-CT and backlit images.

	Core's fibres mean length [µm]		**Mean Area**	**Mean**
	Principal axis	**Secondary axis**	**[µm²]**	**F.A.R.**
Backlit	7561	1745	1.67E+07	5.34
Micro-CT	2920	1062	2.92E+06	3.13
%	61	39	82	41
	Skin's fibres mean length [µm]		**Mean Area**	**Mean**
	Principal axis	**Secondary axis**	**[µm²]**	**F.A.R.**
Backlit	1873	467	1.01E+06	4.93
Micro-CT	1421	478	5.56E+05	3.24
%	24	-2	45	34

Once obtained the fibre length and orientation distributions, the particleboard's volume fraction was required for the construction of the RVEs.

4.4.4 Particleboard volume fraction determination

In general, when it is required to study composite materials from mechanical point of view, one of the most important data is the volume fraction of the components involved. From volume fraction of the reinforcing fibres depend all the mechanical elastic constants of the material. In a similar way, considering particleboard as a composite sandwich laminate, the volume fraction of the wood fibres is fundamental for the mechanical characterization.

To analyse and quantify the three-dimensional objects contained in the reconstructed particleboard volume by Micro-CT images the program Quant3D (117) was used. This software is largely used in literature. One example is reported in (118) where the authors, starting from Micro-CT image of carbon fibres reinforced polyamide composite, determined the fibre's volume fraction. Another example is (119), where the authors derived the orientation tensor of the short glass fibres reinforcement in a polyamide 6 composite by Quant-3D.

The software takes as input a series of 8-bit grayscale Micro-CT images that describe, in this case, the particleboard's reconstructed volume. In particular, core and skin 3D volumes will be analysed separately. After that, it allows specifying a grayscale range that corresponds to the material of interest and separates it from the rest of the data. Some preliminary tasks were necessary, like brightness and contrast adjustment and cropping the volume image from not interesting parts as reported in Figure 170.

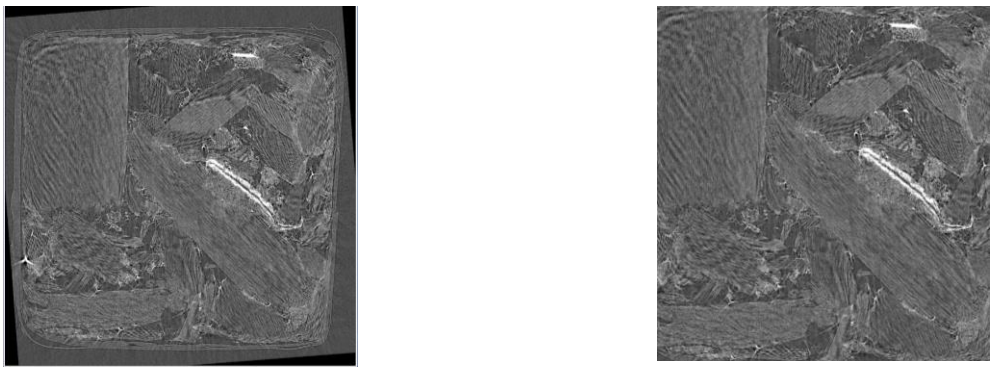

a b

Figure 170: 3D Image saw from XY plane before (a) and after (b) cropping procedure to prepare it to the Quant3D analysis.

Figure 171 shows the core 3D volume portion used as input data to Quant3D. A similar volume was prepared for the skins of the particleboard. The thicknesses of the two portions are in agreement with the quantities reported in Table 30.

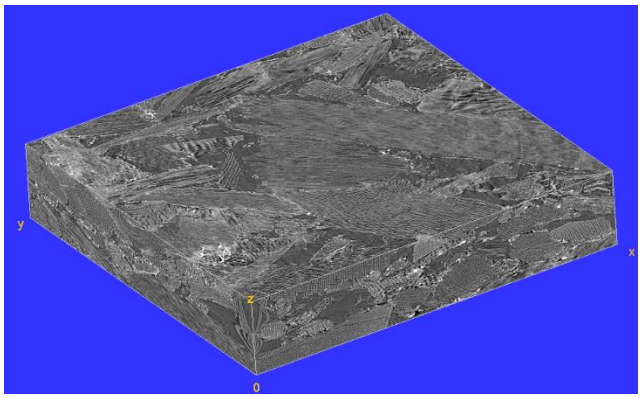

Figure 171: Particleboard core 3D reconstructed volume as input of Quant3D software.

The slices were then ready to be analysed with Quant3D software. In order to separate the wood fibres from others material present in the volume, Quant-3D requires the grey level threshold with lower and upper limits. It is important to underline that the volume fraction evaluation is based on the assumption that the input data represent two-phase system (fill/voids), so if there is a third material, the results may be less reliable (120). The UF-Adhesive, in this case, was treated as part of the wood fibres as well as the impurities These assumptions fix the upper threshold limit equal to 255 (8-bit images).

However, individuating the right grey level threshold lower limit is crucial for reaching the meaningful volume fraction of the fibre. To perform this identification, a preliminary analysis was made to control the sensibility of the volume fraction varying the fibre's wood grey level. Figure 172 visualise the dependency of these two variables on the panel's core.

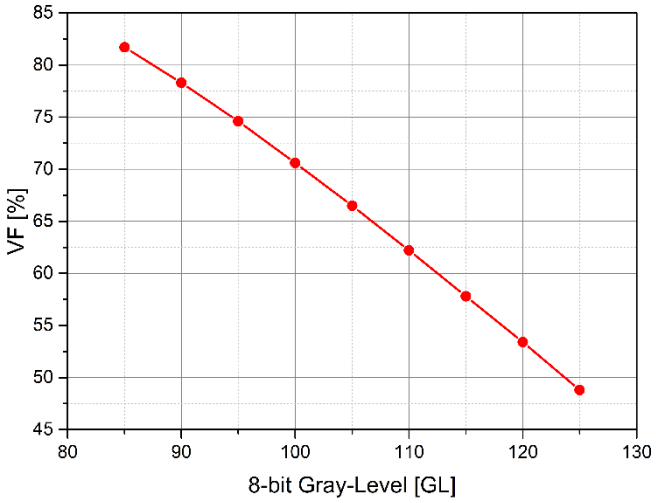

Figure 172: Fibre's wood volume fraction in function of the grey level changing

As Figure 172 shows, changing the grey level from 85 to 125, the volume fraction of the fibre changes from 82% to 49%, so it is very important to select accurately the appropriate lower threshold limit required to individuate effectively the fibre wood volume fraction. Similar results are found in (121) where the authors studied the morphological aspect of the voids in Oriented Strand Boards (see Chapter 1) scanned by tomography techniques. The dependence of the measured volume fraction of the voids upon threshold and mean density of the OSB sample is shown in Figure 173.

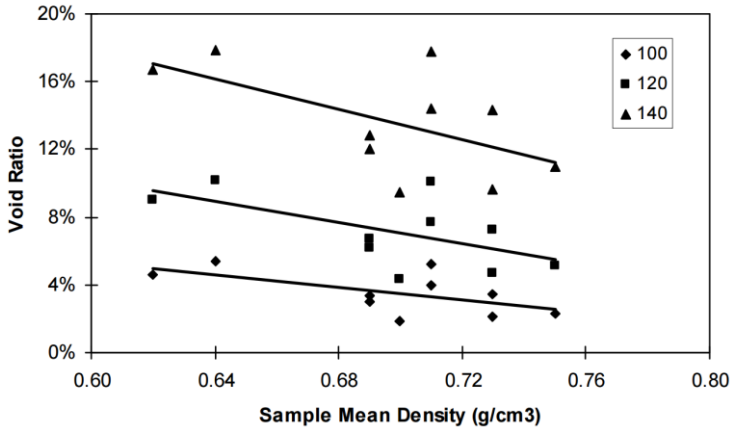

Figure 173: Measured void ratio in relation with OSB mean density and threshold level (121).

Observing Figure 173 , it is possible to observe that changing the threshold lower limits from 100 to 140, void volume fraction in OSB change from 4% to 16%.

It is possible to conclude that a method for the identification of the best lower limits threshold must be used.

In this PhD thesis, the Otsu method (122) was applied to reach the optimum value of grey level threshold lower limits. This method was selected because it evaluates the goodness of the threshold *k** found automatically. The goodness evaluation is performed by only zeroth and first-order cumulative moments of the grey level histograms.

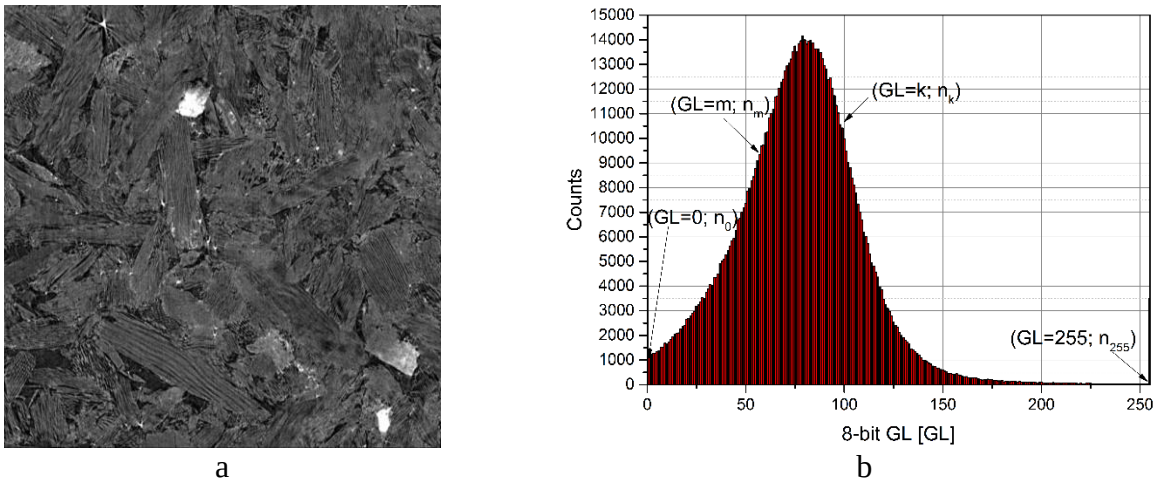

a b

Figure 174: a) 8-bit slice; b) grey-level histogram

To describe briefly the Otsu method (122), let's suppose to indicate with n_i the number of pixels at a certain level i and to have GL (0; 1; …… ; 255) grey levels for 8-bit images (referring to Figure 174). Then the total number of pixel for a particular image is expressed by the sum of every n_i as reported in Eq. 62:

$$N = n_1 + n_2 + \cdots + n_{255} \qquad \text{eq. 62}$$

The histogram is now normalized considering the reference the total number of pixel *N*, see Eq. 63:

$$p_i = {}^{n_i}/_{N} \qquad \text{eq. 63}$$

where p_i is probability distribution to find a pixel at certain grey level over total number *N*. The total summation of every p_i is equal to 1 as reported in Eq. 64:

$$p_i \geq 0, \quad \sum_{i=1}^{L} p_i = 1 \qquad \text{eq. 64}$$

Supposing to divide pixels in to classes called C_0 corresponding to the void and C_1 corresponding to the wood's fibres, individuating a first tentative threshold level *k* it is possible to define:

- $C_0 \in [0; \ldots; k]$ *(pixel's levels)*
- $C_1 \in [k+1; \ldots; 255]$ *(pixel's levels)*

The probabilities of the class occurrence, the class mean levels μ_i and class variances σ_i^2 are given by equations 65 and 66, where ω_0 is the probability to have a pixel in the C_0 class and ω_1 is the probability to have a pixel in the C_1 class:

$$\omega_0 = Pr(C_0) = \sum_{i=0}^{k} p_i; \qquad \mu_0 = \sum_{i=0}^{k} i \cdot \frac{p_i}{\omega_0}; \qquad \sigma_0^2 = \sum_{i=0}^{k} (i-\mu_0)^2 \cdot \frac{p_i}{\omega_0} \qquad \text{eq. 65}$$

$$\omega_1 = Pr(C_1) = \sum_{i=k+1}^{255} p_i; \quad \mu_1 = \sum_{i=k+1}^{255} i \cdot \frac{p_i}{\omega_1}; \quad \sigma_1^2 = \sum_{i=k+1}^{255} (i-\mu_1)^2 \cdot \frac{p_i}{\omega_1} \qquad \text{eq. 66}$$

In order to evaluate the "goodness" of the threshold at level *k*, it is necessary to introduce the following variances normally used to define the class separability, called also discriminant criterion

measures used in the discriminant analysis. In particular Eq. 67 and Eq. 68 reports respectively the within-class variance of grey levels (σ_w^2) and the between-class variance of grey levels (σ_b^2):

$$\sigma_w^2 = \omega_0 \cdot \sigma_0^2 + \omega_1 \cdot \sigma_1^2 \qquad \text{eq. 67}$$

$$\sigma_b^2 = \omega_0 \cdot \omega_1 \cdot (\mu_1 - \mu_0)^2 \qquad \text{eq. 68}$$

Then the problem is to search the threshold *k* that maximise one of the object functions reported in Eq. 67 or Eq. 68. Otsu explains that the best object function is σ_b^2 because is based on first-order statistics (class means). Instead, σ_w^2 is more complex because is based on the second-order statistics (class variances), then the optimal threshold *k** is the value that maximises σ_b^2 as reported in Eq. 69:

$$\sigma_b^2(k^*) = max_{0 \le k < 255}\ \sigma_b^2(k) \qquad \text{eq.69}$$

Using Matlab, it is possible to write a subroutine to calculate σ_b^2 for each *k*, analysing alternatively the core and skin 3D-portions in an iterative way, displaying the σ_b^2 value for each iteration to best visualise the trend and detect *k**. Appling the Otsu method, the obtained histograms for the core and skin 3D volume are reported in Figure 175a and in Figure 175b, respectively, where the ordinate axis represents the number of the pixel with the same grey level for all the slices of the volume.

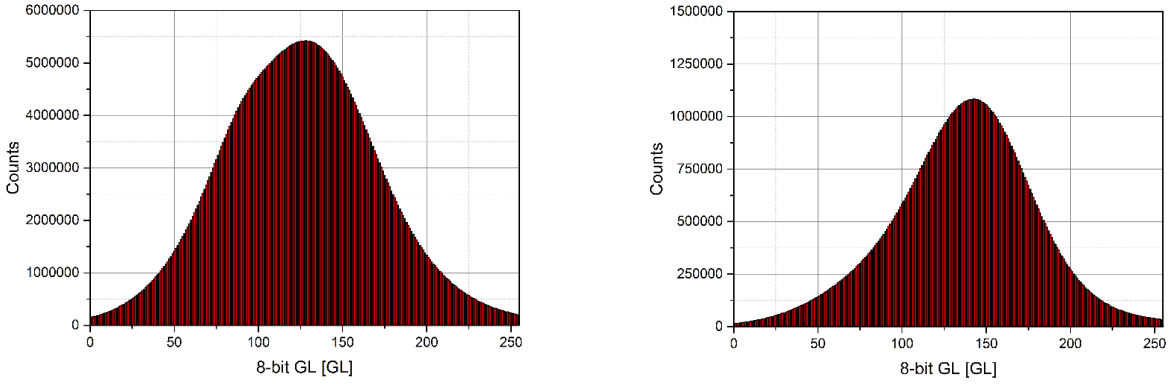

a b

Figure 175: Grey level histogram of the 3D reconstructed volume of particleboard's portions. a) core's portion; b) skin's portion.

By changing in an iterative way the threshold k, it is possible to compute the probabilities of class occurrence (Figure 176a and Figure 176c) and the class mean levels (Figure 176b and Figure 176d) respectively for core and skin portions.

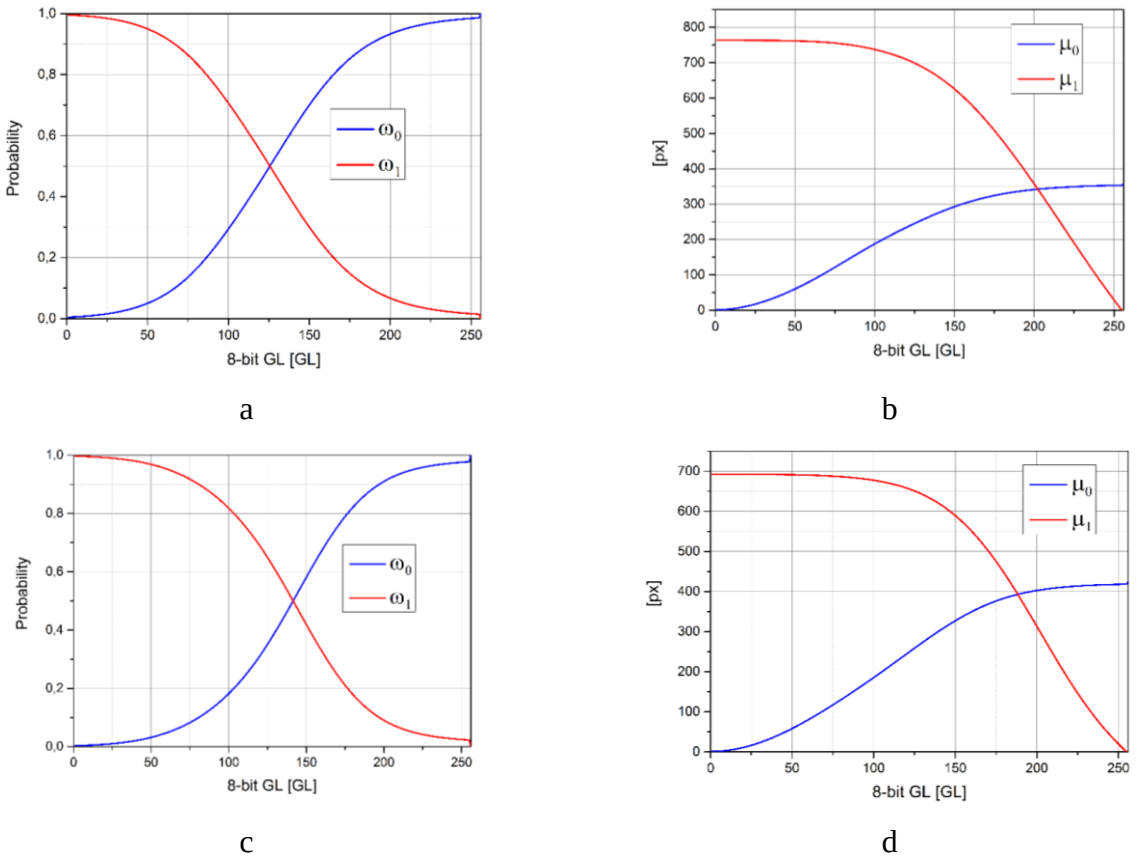

Figure 176: a) Probabilities for the C_0 class (ω_0) and for C_1 class (ω_1) for the panel's core; b) Mean levels for C_0 class (μ_0) and for C_1 class (μ_1) for the panel's core; c) C_0 class (ω_0) and for C_1 class (ω_1) for the panel's skin; d) Mean levels for C_0 class (μ_0) and for C_1 class (μ_1) for the panel's skin.

The between-class variance σ_b^2 for the core and skin 3D portions are reported in the following Figure 177.

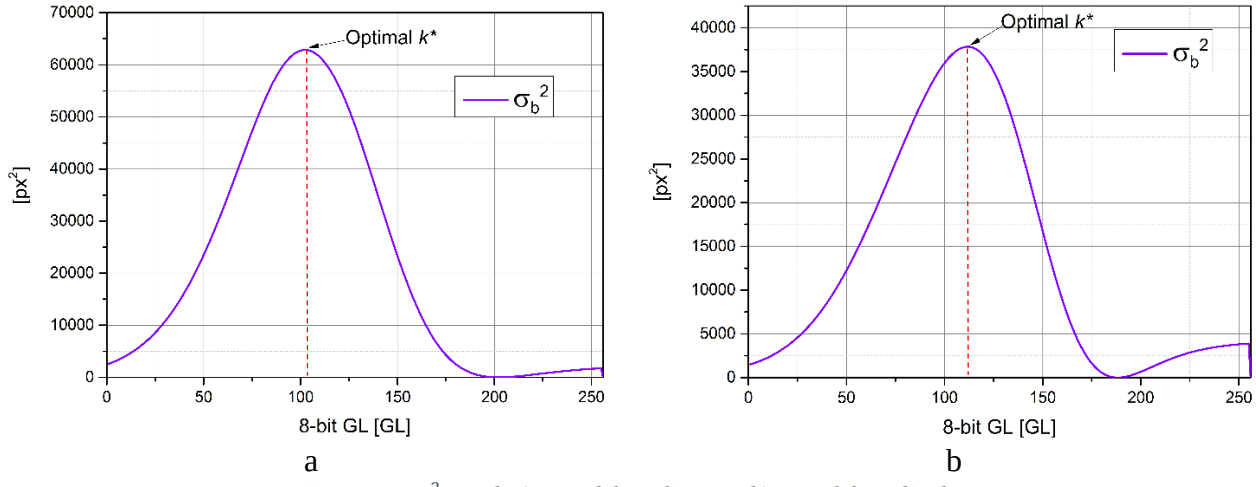

Figure 177: σ_b^2 trend. a) particleboard's core; b) particleboard's skin.

Observing Figure 177a, the optimal threshold value k^* for the particleboard's core portion is equal to 101, otherwise for the skin portion the optimal k^* is 111 (Figure 177b). In this manner, it is possible to define the classes C and related lower limits, reported in red for core and skin

particleboard, see Table 51. Herein it is possible to see the results after Otsu's analysis performed on two Micro-CT reconstructed volume of Reference particleboard's samples with dimensions equal to 10x10x18mm (see Table 14).

Table 51: fiber/voids class definition.

	C_0 (voids class)	**C_1 (fibre's class)**
Core	[0; …. ; 101]	[102; …. ; 255]
Skin	[0; …. ; 111]	[112; …. ; 255]

Considering the lower limits for core and skin respectively equal to 102 and 112, Quant3D provided the volume fractions reported in Table 52.

Table 52: fibers volume fractions.

	Fibre volume fractions	**St. Dev**
Core	0.699	0.011
Skin	0.762	0.022

The values thus obtained will be used in Digimat-FE to build the RVE of particleboard's skin and core.

4.4.5 Mechanical characteristics of particleboard constituents: Wood

One of the most important steps required to build the RVE model of the particleboard is the definition of the materials that compose it. This is a tough task because the particleboard is composed of recycled wood, so the exactly wood types are unknown. This Section will be dedicated to understanding which is the best type of wood to be considered as the mean material involved in the production and find the main properties of this material.

As reported in (123), wood can be considered as a transversely isotropic material. In general, this wood's definition is a special class of materials that have the same properties in one plane (e.g. the X-Y plane) and different properties in the direction normal to this plane (e.g. the Z axis). To describe a transverse isotropic material is necessary only five independent elastic constants, instead of nine for the orthotropic material (34). These elastic constants are Young modulus and Poisson's ratio on the X-Y plane (E_{xy} and ν_{xy}); out-of-plane along the Z axis (E_z and ν_{xz}) and shear modulus on

the X-Z plane (G_{xz}). Wood can be considered as a transversely isotropic material because the coefficients of two of the main directions are similar. In fact, from the wood structure, it is possible to define three main directions (124) as reported in Figure 178.

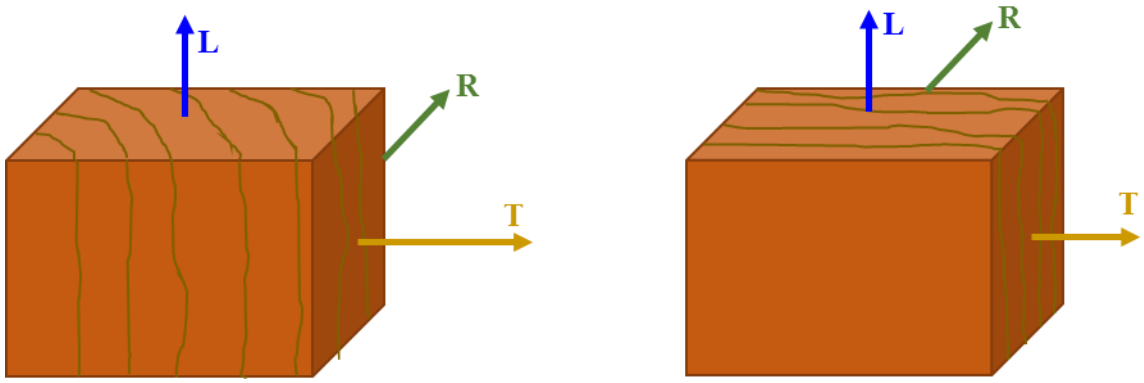

Figure 178: wood orientation of two different extracted samples.

Longitudinal direction (*L*) is parallel to the log's tree axis, Radial direction (*R*) orthogonal to the *L* direction and parallel to the tree growth circles and Tangential direction (*T*), tangential to the growth circles. Knowing these reference directions, it is possible to express the stress-strain constitutive law, in agreement with (125) and reported in Eq. 70:

$$\begin{Bmatrix} \varepsilon_T \\ \varepsilon_L \\ \varepsilon_R \\ \gamma_{LR} \\ \gamma_{TR} \\ \gamma_{TL} \end{Bmatrix} = \begin{bmatrix} \frac{1}{E_T} & -\frac{\nu_{LT}}{E_L} & -\frac{\nu_{RT}}{E_R} & 0 & 0 & 0 \\ -\frac{\nu_{TL}}{E_T} & \frac{1}{E_L} & -\frac{\nu_{RL}}{E_R} & 0 & 0 & 0 \\ -\frac{\nu_{TR}}{E_T} & -\frac{\nu_{LR}}{E_R} & \frac{1}{E_R} & 0 & 0 & 0 \\ 0 & 0 & 0 & \frac{1}{G_{LR}} & 0 & 0 \\ 0 & 0 & 0 & 0 & \frac{1}{G_{TR}} & 0 \\ 0 & 0 & 0 & 0 & 0 & \frac{1}{G_{TL}} \end{bmatrix} \cdot \begin{Bmatrix} \sigma_T \\ \sigma_L \\ \sigma_R \\ \tau_{LR} \\ \tau_{TR} \\ \tau_{TL} \end{Bmatrix} \qquad \text{eq. 70}$$

As it is possible to find in the literature (126) the mechanical characteristics of the wood can be varied in function of different parameters, for example, temperature or moisture content. However, the modulus ratios about the *R; T* and *L* directions can be found in Eq. 71; Eq.72 and Eq.73 and are valid for the most of the wood species:

$$E_L : E_R : E_T \approx 20 : 1.6 : 1 \qquad \text{eq. 71}$$

$$G_{LR} : G_{LT} : G_{RT} \approx 10 : 9.4 : 1 \qquad \text{eq. 72}$$

$$E_L : G_{LR} \approx 14 : 1 \qquad \text{eq. 73}$$

Observing the ratio's values reported in the previous equations, it is possible to assume that the direction *R* and *T* can be considered as unique radial direction *R*. In this manner, the Young modulus parallel to the *R* direction will be called E_R and those parallel to the *L* direction will be defined as E_L. Finally, there will be only one shear modulus *G* since the fibres have been modelled as a transversely isotropic. Figure 179 reports the Digimat panel to input the wood properties.

Considering the wood raw material provenience (referring to Section 1.2.6), to identify the right wood species involved in particleboard production is practically impossible. However, it is reasonable to suppose that in dumps or wood waste collection centres it is difficult to find precious wood species, but it is simpler to find used particleboards or pieces of softwood. Checking the literature, as expected the authors of (127) found that the panels are mainly made of pine, fir, larch, and more in general conifer wood, sometimes poplar wood.

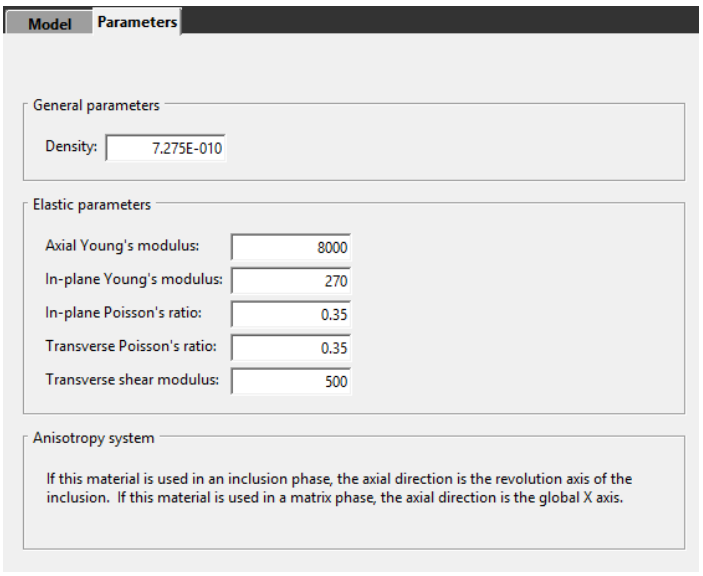

Figure 179: Digimat panel to input the wood transversely isotropic properties.

Then the hypothesis to consider wood's fibres made of conifer wood was made. However, this assumption is not enough, because the conifer species are different and then the mechanical properties differs. To select the right wood type reference (128) was examined, where different classes of strength and wood conifer species belonging to the *C class* are reported. In particular, the chosen one is the *C16* because is one of the less precious wood type. Poisson ratio can be obtained in agreement with (129). Table 53 list the mechanical characteristics assigned to the fibre's wood assumed to be originated from conifer wood.

Table 53: Conifer wood properties assigned to fibre's wood.

[MPa]				
E_L	E_R	G	ν_{LR}	ν_{TL}
8000	270	500	0.35	0.35

It is now fundamental assign these properties in agreement with the wood's fibres direction in order to correctly represent the wood behaviour. About this issue, a basic assumption is made. Observing the slices extracted from the particleboard's core, it was noted that the principal axis length of the fibers detected is parallel to the fiber-wood direction visualized on it, so I have assumed that the greater length of the fibres is parallel to the direction *L* and the shorter length is parallel to direction *R*. This assumption is supported considering that during the wood grinding phase; the material is likely to break parallel to the direction of minimum strength (direction *R*).

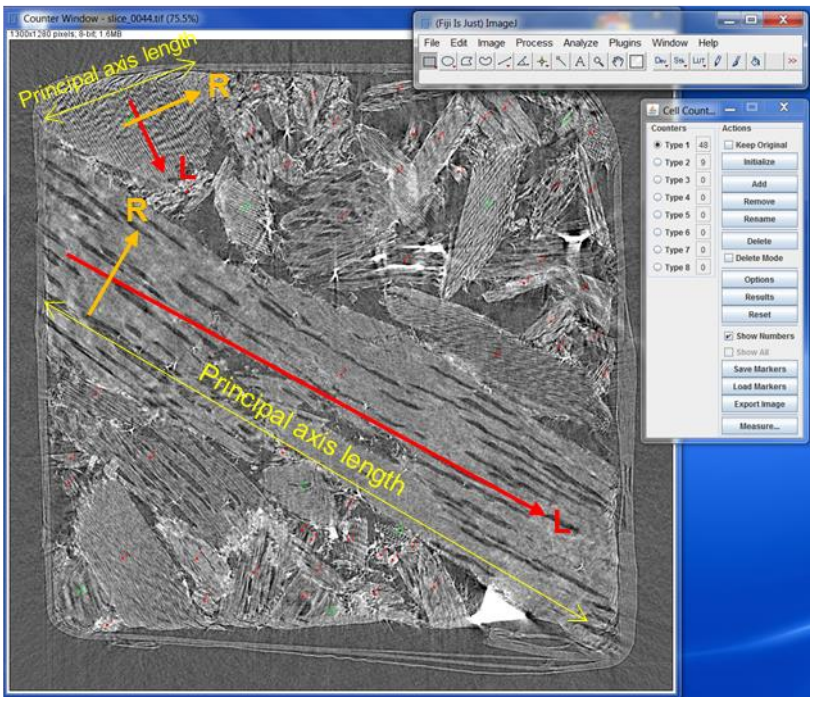

Figure 180: Fibre directions definition compared to the principal axis length.

Observing the core's slice reported in Figure 180, it is possible to see that over 57 fibres detected, 48 have the principal axis length parallel to the longitudinal direction *L* of the wood and only 9 are orthogonal. It is possible to conclude that 84% of the fibres detected in this slice are in agreement with the material directions and 16% are opposite to. Principal axis length will be parallel to the longitudinal direction *L* and secondary axis length will be parallel to the *R* direction.

4.4.6 Mechanical characteristics of particleboard constituents: Urea-Formaldehyde Adhesive

UF is a polymeric material used in many sectors, not only as particleboard bonding agent. For example moulded pieces, plate production, abrasive wheels, lacquers and coatings are obtained after a chemical reaction between the binder (thermoset resin), water, hardener and the paraffin (130). Urea-Formaldehyde adhesive is modelled as an homogenous and isotropic material considering its mechanical and physical properties reported in Table 54 (131) (132).

Table 54: Urea-Formaldehyde thermoset adhesive properties.

E [MPa]	ν	ρ [kg/m^3]	Volume fraction
9000	0.35	1500	0.1

4.4.7 Evaluation of Digimat-FE algorithms to build RVE's particleboard: Classical FE algorithm

The finite element module of Digimat gives the possibility to select two different options to build the RVE model. About particleboard modelling, it is crucial the selection of the right RVE's building algorithm that essentially defines the shape of the fibre and how to organise them to reach the required volume fractions.

By the Classical FE algorithm of Digimat, it is possible to model an RVE as a mixture of different phases, in particular the matrix and a set of inclusions. Since in the reality the Particleboard has no matrix, the matrix was define as composed of air. Wood fibres represent the inclusion phase with the parameters evaluated in Sections to 4.4. For the creation of the RVE. the geometrical shape selection can be made in two ways: using ellipsoids or parallelepipeds. These two methods generate feature that are the most similar to the wood particles true shape; but then, as explained in (107), these two geometries are the most time-consuming shapes during the RVE computation. For this reason, the final decision was to the third possibility: the sphere-cylinder elements. This geometry is composed of three parts: two hemispheres at the extremity and a central cylindrical part. This type of inclusion shape actually requires less computational time and it is still capable of representing the true fibre's shape in a acceptable way.

Using sphere-cylinders elements, it is necessary to define the mean aspect ratio (F.A.R.) to set the shape proportions of the inclusions using the results obtained in Section 4.4.3. The definition of

the size of the fibres assigning the principal axis length (Section 4.4.3) is probably the most critical step in order to obtain a meaningful RVE. This parameter affects the maximum volume fraction reachable by the generation algorithm. The classical FE algorithm works placing iteratively the sphere-cylinder elements inside the RVE. If the inclusion is in contact with another, the algorithm tries again to place it in another position until the volume fraction or the maximum attempts iterations number are reached. Then, if the principal axis dimension of the fibre is too large compared to the RVE volume, the algorithm does not succeed in positioning the inclusions without touching other fibres, thus preventing form reaching the volume fraction required in the iteration's number defined.

The Classical FE algorithm provides two different size definition methods to define the sphere-cylinder fibres dimensions in the RVE. They are the size distribution and the size reduction methods.

The size distribution approach requires the statistical distribution to define the fibre's shape to fill the RVE by its mean and variance. The representative volume of particleboard will be filled by fibres of geometry in agreement with the normal distribution defined by mean and variance of the principal axis length (Section 4.4.3). With the first solution (size distribution method), it is completely impossible to reach particles volume fractions higher than 0.4 - 0.45. The classical FE algorithm does not position the particles without interpenetration reaching the maximum number of attempts before the volume fraction desired (0.69 for the core). Therefore, this approach must be discarded.

The size reduction approach requires a starting size of the inclusion, the maximum number of steps reduction and the size reduction factor. The algorithm performs a progressive size reduction of the fibres in agreement with the maximum number of steps and reduction's factor when classical FE algorithm can no longer find space to place new fibre. This second method works better, reaching a volume fraction close to 0.7. However, analysing the obtained RVE (Figure 181a); the fibres size distribution does not adequately represents that evaluated by the Micro-CT identification (Figure 181b) and in particular from backlit particle's images (Figure 181c). As it can be clearly seen, too many small fibres were created. In fact, it is not simple to control the resulting size distributions with this method. In addition, the RVE generation was also very long in terms of computational time.

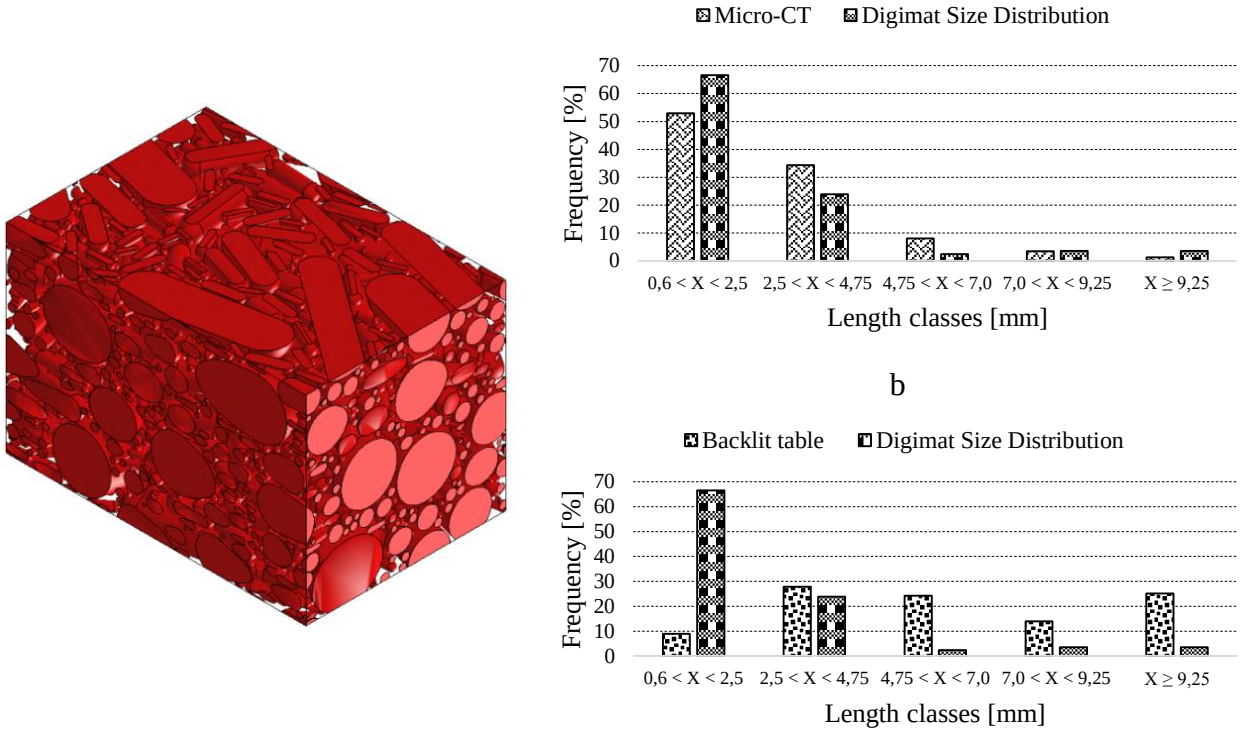

Figure 181: Classical FE Algorithm results. a) RVE of particleboard; b) Principal axis length comparison between Micro-CT and Digimat RVE; c) Principal axis length comparison between backlit table and Digimat RVE.

Summarising the negative aspects of the Classical FE algorithm compared to my scopes, it is possible to underline that one is the mandatory matrix definition (air for my case). Then, the sphere-cylindrical shape of the fibres is not similar to the real case geometry and the difficulty to generate an RVE that reproduce the data acquired from is not negligible. In particular, it was impossible to reach the proper volume fraction with the size distribution method and moreover the results are not satisfactory with size reduction method.

However, a positive feature of the classical RVE generation algorithm is the possibility to create a coating that surrounds the fibres. It is a good solution because, as seen in Chapter 2, the wood's fibres of the particleboard are covered by Urea-Formaldehyde adhesive.

Unfortunately, the resin layer it is very thin (only a few microns), thus it would require such a very fine mesh. The computational cost would increase in an exponential way, making the analysis unfeasible. Due to these negative aspects, this modelling approach was discarded the stacking algorithm used instead.

4.4.8 Evaluation of Digimat-FE algorithms to build RVE's particleboard: Stacking algorithm

This option is to be used when the high volume fraction of fillers is requested. The stacking algorithm inserts the fillers one by one. The newly inserted filler adapts its geometry in agreement with two constraints (107):

- Adapting the fibre geometry to the already inserted inclusions
- Filling all the space that is possible to fill.

Considering these two constraints, the algorithm work stacking inclusions onto each other, voids and adhesive, if defined, until the RVE is full. The meshing phase is done simultaneously.

By the stacking algorithm, the particleboard's RVE can be generated also without the use of the matrix. In fact, it is possible to define the representative volume just with inclusions and void elements, approaching to the real case. Another aspect regards the fibre's coating that of course can be modelled by using a cohesive phase but as said before for the Classical FE algorithm, the adhesive layer model would require a very high number of elements. This is due to the very thin adhesive layer that covers the fibre. In this PhD thesis, the micromechanical model of the particleboard's microstructure that contains Urea-Formaldehyde was performed only defining it as a matrix. A third relevant aspect of this algorithm is the fixed shape of the inclusions. In fact, they are parallelepipeds, which can be considered as a good approximation of the wood particles. Furthermore, using this algorithm it is possible to reach every desired volume fraction (from 0 to 1), so it is very suitable for the Particleboard's RVE generation.

In this case, the size definition of the fibres is different with respect to the classical algorithm. In fact, fixed sizes must be chosen and will be those measured by Micro-CT or backlit images analysis. Principal axis length, secondary axis length and the thickness of the fibres are reported in Table 47 and in Table 50. Figure 182 reports the comparison between the real wood's fibre and those modelled by stacking algorithm. This algorithm has the peculiarity to build the RVE and meshing it in one single step.

a b

Figure 182: Particleboard fiber's comparison. a) Real wood's particles; b) Model of the single fiber.

It is important to underline that this method, for the elastic moduli determination, considers loadings and stresses transmitted inside the RVE's structure through the contact points among the generated fibres, where they are merged together during the meshing process.

4.4.9 RVE generation strategies

Based on the previous analysis of the performances of the RVE generation algorithms, the RVE generation was performed for the 18mm particleboard by Digimat-FE using the stacking algorithm. At this stage, the focus was on the core only, because it is a large region of relatively uniform density. Modelling of the skin would mean considering also modelling the density variation across layers whose thickness is comparable with the dimensions of the RVE. Moreover, the analysis of the actual behaviour of the core is crucial for the set up of a modelling technique allowing for studying possible solutions in the perspective of reducing weight and improving mechanical bending behaviour.

Two different cases were taken into account, using fibre geometrical dimensions extracted from the backlit images and orientations extracted from the Micro-CT images:

- Core's RVE with the urea-formaldehyde adhesive considered as a matrix
- Core's RVE without the adhesive, with particles and voids only

The option of considering or not the adhesive inside of the representative volume of the particleboard is based on the qualitative image analysis results (Chapter 2). Herein, it was possible to see that the adhesive distribution is clearly different compared to the matrix in CFRP material for example. Then, this differentiation (with UF or without UF) is performed to evaluate the effects on the elastic moduli.

Table 55 reports the volume fractions of the components used as input to build the micro models considering the geometrical dimensions of the wood particles from different measurement methods. Herein is possible to see that the quantity of adhesive considered as a matrix is not comparable with what is found in polymer composites, where the matrix incorporates the fibres with a percentage greater than that of the fibres.

Table 55: Particleboard's constituents volume fractions.

Components	CORE Volume fractions [%]	
	Model with UF	Model without UF
Wood particles	60	70
Urea-Formaldehyde (UF)	10	0
Voids	30	30

4.4.10 RVE Convergence analysis

Every material can be associated to a representative volume element, which defines in a univocal way its macroscopic mechanical properties. Above the dimensions of that volume, the material can be considered homogeneous (133). For the most common materials or periodic microstructures, these dimensions of the RVE are already known (134). However, no data are available for the particleboard. Thus, in order to get reliable results, it was necessary to determine the correct RVE dimensions using the convergence analysis inspired by the approach reported in (57). Herein the authors, in order to generate the micromechanical model of short fibre reinforced composites that behave homogeneously, investigated the minimum representative volume element. For every tested RVE's sizes, the authors performed three repetitions, checking the longitudinal elastic modulus variation by the arithmetic mean, variance and confidence interval equal to 95%. The optimal sizes of the representative volume of the material was reached when the elastic modulus stabilised around its mean value.

The same approach was applied in the Master thesis (106) to particleboard, considering the core fibre's dimensions evaluated by backlit image analysis (Table 48) and their orientation by Micro-CT results (Table 46). In Figure 183 are visualised the convergence analysis results of 18mm particleboard's core modelled by Digimat-FE using stacking algorithm considering or no the presence of the UF adhesive by proper volume fractions (Table 55).

Results were obtained assuming values of the components of the orientation tensor $a_{11} = 0.7$ and $a_{22} = 0.3$ not based on fibre orientation measurement, because this convergence analysis was conducted before obtaining the fibre orientation distributions. Therefore, only the results in terms of RVE size can be retained, while values of the elastic constants corresponding to the correct values of the components of the orientation tensor are reported in the following sections.

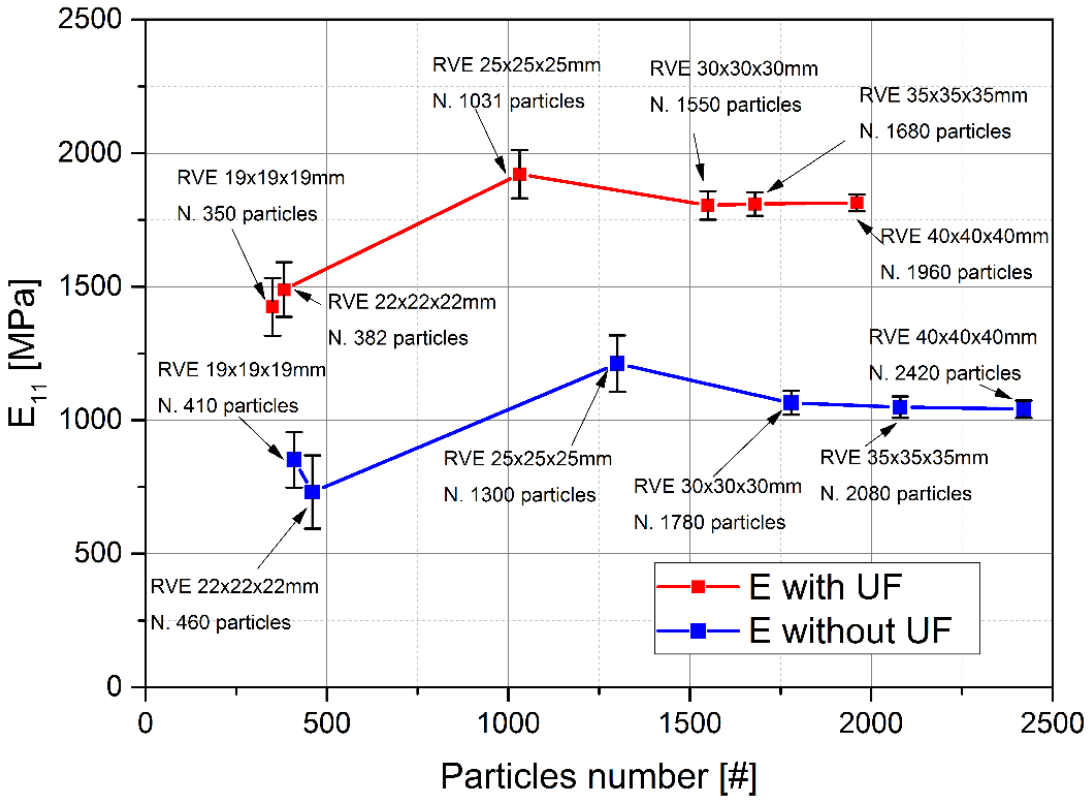

Figure 183: RVE convergence analysis of the 18mm particleboard's core using stacking algorithm and input data from Section 4.4.

Table 56 lists the mean values, variance and half width confidence interval of E_{11}. Observing Figure 183 and Table 56 it is simple to see that the mean values of E_{11} flatten if the number of wood's fibres is greater than 1550 for UF model and 1780 for the model without UF adhesive. These two quantities correspond to a RVE's size equal to 30x30x30 mm.

Table 56: Convergence analysis results

RVE particleboard's model <u>with</u> Urea Formaldehyde adhesive			
Number of fibres	**RVE dimensions [mm]**	**E_{11} [MPa]**	**$\sigma^2(E_{11})$ [MPa^2]**
350	19x19x19	1424.3	2911.6
382	22x22x22	1489.5	2593.2
1031	25x25x25	1921.8	2047.8
1550	30x30x30	1804.3	710.3
1680	35x35x35	1809.5	489.8
1960	40x40x40	1814.0	240.1
RVE particleboard's model <u>without</u> Urea Formaldehyde adhesive			
Number of fibres	**RVE dimensions [mm]**	**E_{11} [MPa]**	**$\sigma^2(E_{11})$ [MPa^2]**
410	19x19x19	851.3	2698.6
460	22x22x22	730.7	4708.9
1300	25x25x25	1212.3	2798.0
1780	30x30x30	1065.0	507.3
2080	35x35x35	1048.7	399.5
2420	40x40x40	1041.2	263.4

The described convergence analysis was performed with a cubic RVE, as suggested by (107). However, the core portion of the 18 mm thick particleboard panel has a thickness of 10mm, lower than the selected RVE thickness. For this reason, an analysis without UF-adhesive, using an RVE with the real core thickness was attempted. Warnings messages appeared (about a possible low accuracy of the results), computational time increased and most of the times the analysis failed. To increase the accuracy of the analysis's results and reduce the number of the analysis failures, it was necessary to increase the RVE side to 80mm. The E_{11} moduli obtained, using an RVE of 80x80x10mm which contains about 1760 particles (so almost the number evaluated before as the optimal one), are reported in Table 57.

Table 57: Comparison between different RVE dimensions.

RVE particleboard's model <u>without</u> Urea Formaldehyde adhesive			
Number of fibres	**RVE dimensions [mm]**	**E_{11} [MPa]**	**$\sigma^2(E_{11})$ [MPa^2]**
1780	30x30x30	1065.0	507.3
1760	80x80x10	1137.8	1180.8

Considering the difference between the E_{11} equal to 6.3% and, more important, the smaller variance of the larger (30x30x30 mm^3) RVE reported in Table 57, the decision was to perform all the following analyses with a cubic RVE with dimensions equal to 30x30x30 mm^3.

4.5 Results and discussion

As discussed previously, (Sections 4.4.1 and 4.4.2), the fibres geometrical characteristic identification was performed in two different ways. The first one is the manual analysis using the Micro-CT images and the second one is automatic processing of images of raw fibres on the backlit table. The results are used as input to create the micromechanical model and evaluate the elastic constants using Digimat FE package. Here are reported the model features implemented by software:

- *Boundary condition:* Periodic.
- *Interface behaviour (particle-particle or particle-voids-adhesive:* Perfectely bonded.
- *Properties of the air:* density and modulus almost zero (1E-12).

The modelling strategies for the core portion reported in Section 4.4.7 are summarised in the flowchart reported in Figure 184.

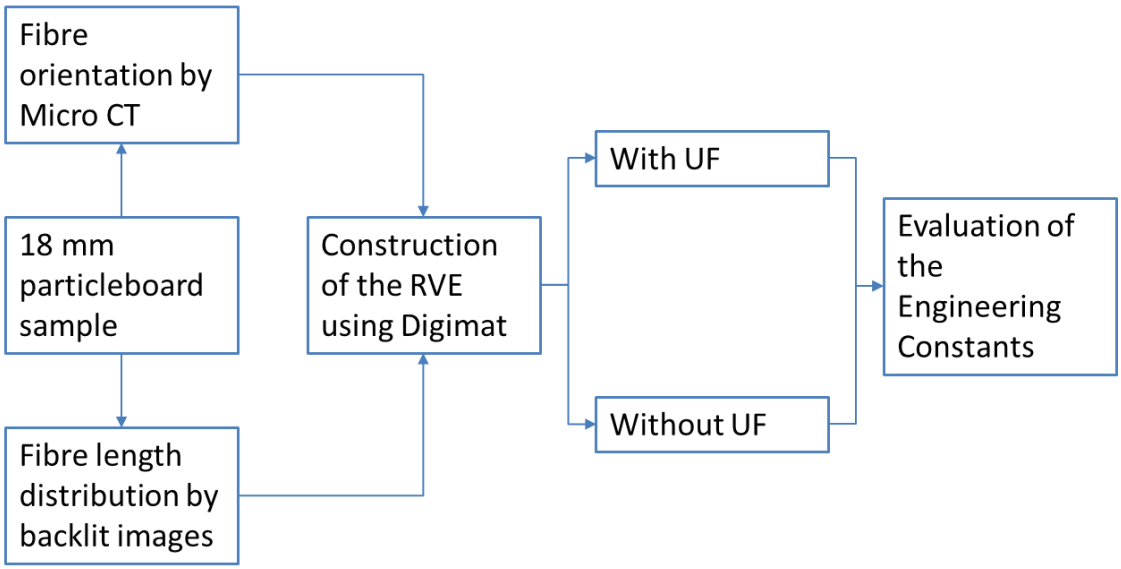

Figure 184: Micromodelling core strategies flowchart.

Starting from the micro model of the panel's core using fibre geometrical data from the backlit table source, Figure 185 reports the core's RVE built by the stacking algorithm without Urea-Formaldehyde adhesive. By homogenization analysis, Digimat-FE provided the elastic constants results reported in Table 58.

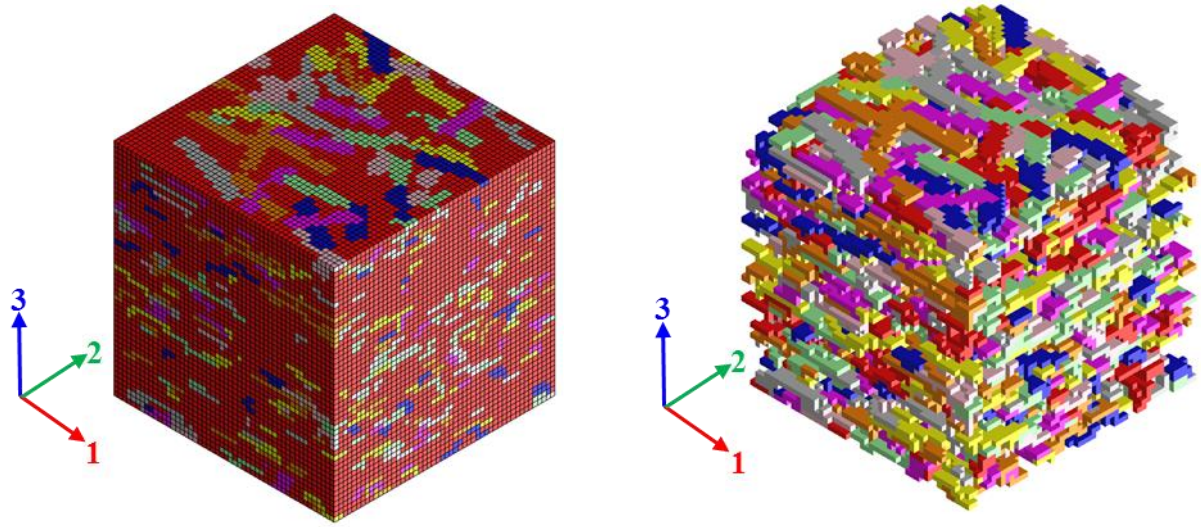

a b

Figure 185: Core RVE built by Stacking algorithm using fiber geometrical data from backlit table source and without UF-adhesive. a) Visible air (red voxel); b) without air visualization.

Figure 186 reports the Core's RVE built again by backlit table fibre's geometrical data but considering UF adhesive as a matrix. The elastic constants results after homogenization are reported in Table 58.

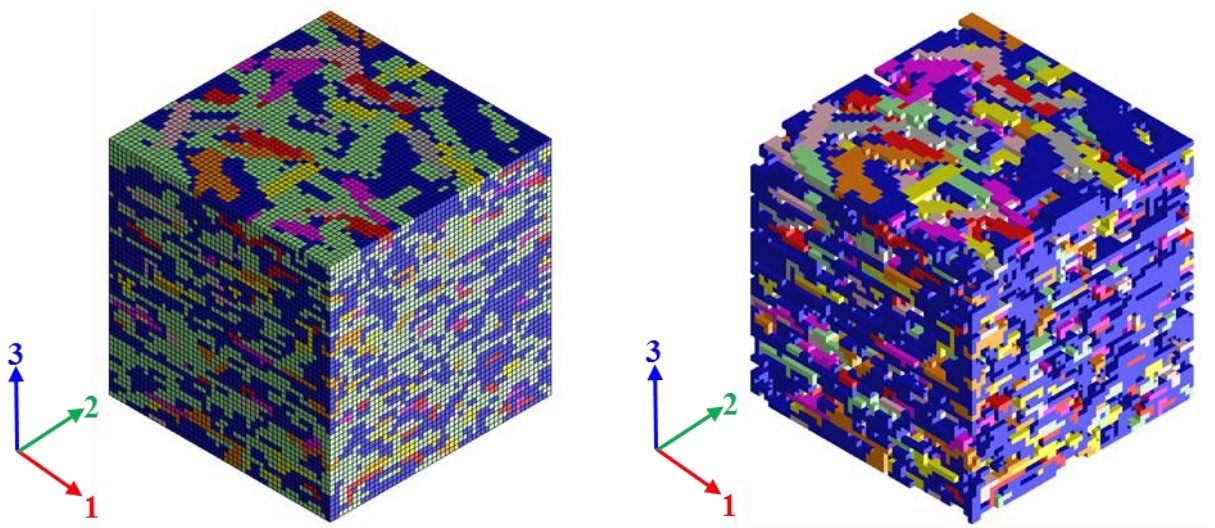

a b

Figure 186: Core RVE built by Stacking algorithm using fiber geometrical data from backlit table source and considering UF-adhesive. a) Visible air (green voxel); b) without air visualization.

The RVEs of the core generated starting from Micro-CT source data, determined the elastic constants after homogenization listed in Table 58. Images of the corresponding RVEs are not reported the RVE, being them practically the same as the previous one reported in Figure 185 and in Figure 186.

Table 58: Micromechanical model elastic constants results for core portion and comparisons

without UF-adhesive [MPa]		
E_{11}	**E_{22}**	**G_{13}**
599 (- 46% w.r.t. BSM)	580	77 (- 62 %w.r.t. BSM) (-47%% w.r.t. Iosipescu)
with UF-adhesive [MPa]		
E_{11}	**E_{22}**	**G_{13}**
1090 (-2% w.r.t. BSM)	1061	151 (-32 % w.r.t. BSM) (+5% w.r.t. Iosipescu)

It is now possible to compare the elastic moduli results obtained at micro level with the elastic constant obtained at the macro-level by TPBT and shear tests. Considering the macro-level elastic moduli results obtained by BSM for 18mm's panel (referring to Chapter 3, Table 33), it is possible to see the comparison between longitudinal core's modulus and shear moduli obtained by modeling at the micro level (Table 58 in the brackets).

From those results it is clear that the model containing particles and voids only (i.e. without UF-adhesive) underestimate the experimental longitudinal modulus (BSM results), being the

difference -58% for the longitudinal modulus and –72% for the out of plane shear modulus. Otherwise, if the UF adhesive is considered in the RVE's generation, the agreement between longitudinal moduli is improved because the generated model is more rigid due to the presence of Urea Formaldehyde. Nevertheless, values of G_{13} are still lower than experimental ones.

In order to improve the results regarding the value of G_{13}, an attempt was also made to include a certain degree of out of plane orientation. In fact, in previous analyses no out of plane orientation was assumed, but this assumption was not checked. Future work should concentrate on this aspect. Nevertheless, a simulation was conducted, assuming the following values of the principal components of the orientation tensor: $a_{11} = 0.5$, $a_{22} = 0.4$ and $a_{33} = 0.1$, with UF. Results are reported in Table 59. An increase of G_{13} is obtained, approaching better the BSM experimental data, with E_{11} maintaining a good agreement with experimental data.

Table 59: New micromechanical model elastic constants results for core portion and comparisons

with UF-adhesive [MPa]		
E_{11}	**E_{22}**	**G_{13}**
984 (-11% w.r.t. BSM)	740	175 (-20% w.r.t. BSM) (+20% w.r.t. Iosipescu)

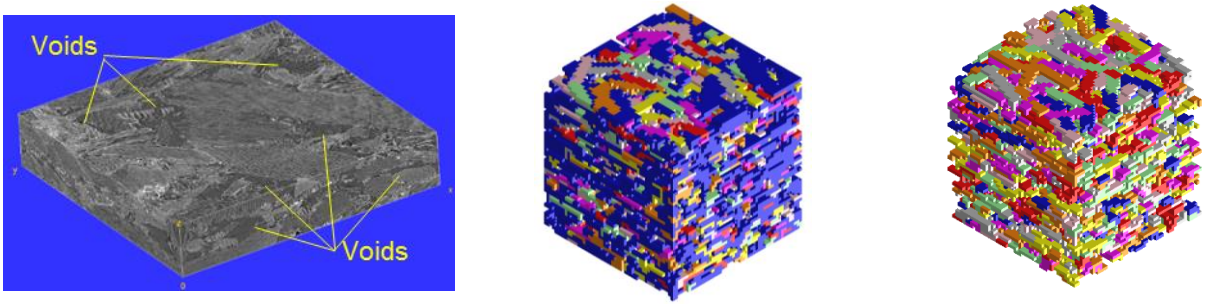

a b c

Figure 187: RVE – 3D reconstructed volume particleboard comparison. a) Micro-CT volume; b) Core's RVE with UF-Adhesive; c) Core's RVE without UF-Adhesive.

It is worth mentioning that Digimat generates the core's RVE with the UF-adhesive considering it as pure matrix component that incorporates the fibres as a short fibre composite where the reinforcement fibres are completely immersed in a polymeric matrix. The core's RVE obtained by considering the adhesive is not similar to the real volume as it is possible to see in Figure 187b (model with UF adhesive) compared to Figure 187a (volume reconstructed by micro-CT). In the real particlewood sample, the adhesive mainly covers the surface of the wood particles, while in the Digimat RVE appears as a uniformly distributed phase. Figure 187c shows the core's RVE built using

only two phases (wood and voids), which appears to be more similar to the real core in terms of void distributions and absence of visible glue, although this resulted in a much lower stiffness.

Using the elements and the instruments described during this last Chapter, it was possible to build a first micromechanical model of the core of the particleboard. In particular, using Micro-CT images it was possible to detect size and orientations of the fibres dispersed in the material's volume, to analyse the particleboard constituents, measure geometric properties and volume fraction of the constituents. These input data were used to build the 3D RVE of the particleboard, necessary for the identification of the elastic constants by homogenization.

Two Digimat models were built, one that considering the presence of Urea Formaldehyde adhesive and another without it. The model with UF better matched the experimental results, at least with respect to the longitudinal modulus. The value of the out of plane shear modulus is comprised between the value obtained by Iosipescu testing and that identified indirectly by three point bending tests.

Comparison between the particles size acquired with the Micro-CT images and the backlit table highlighted large differences. As discussed, this is due to the fact that the Particleboard specimens, used to perform the Micro-CT analysis, are too small. In fact, some of the wood particles, were cut for the extraction of the micro-CT samples. Results indicate that out of plane orientation of wood particles plays an important role. Therefore, in a future work, it might be useful to perform again the Micro-CT acquisition on larger particleboard specimens to identify correctly the wood particles sizes and their orientations. In any case, the micro-modelling tools used in this chapter seem promising.

4.6 Conclusion and Further developments.

In this PhD work, particleboard panels of 8, 18 and 38mm of thickness made of recycled wood were studied focusing in particular on 18mm. The study developed in this thesis in particular on the panel's core was conducted as a preliminary analysis of the existing panels, aiming at the development of experimental and numerical analysis tools useful for the design of modified panels, designed in the perspective of reducing panel's weight and improving its bending performances. The particleboard panel was analysed and characterised at different levels: macro and micro.

The first chapter was dedicated to the characterization of the present particleboard's constituents and the determination of the density profile though the thickness. To accomplish these first goals, Micro-CT reconstruction of the material and analysis was performed in both qualitative and quantitative manners. The results have shown the particle' dispositions, their microstructure, adhesive distribution and voids. Moreover, vertical density profile was determined by proper grey level calibration using reference materials of known density. Comparing the vertical density of the 18mm particleboard determined by Micro-CT analysis with those evaluated by standard x Ray analysis using an industrial equipment (DPX-300) showed a 10% shift. This mismatch can be ascribed to different factors: environmental conditions not constant across Micro-CT acquisition and standard X Ray analysis, micro CT sample's dimensions not representative of the particleboard and probably phase contrast effect. This latter cause, is still unresolved and therefore the material's density used in the following characterisation was the industrial one determined by quality control equipment DPX-300. Nevertheless, micro CT provided other useful data that were used in the micro-modelling task.

Once known the morphological aspects of the particleboard and its density profile, as reported in Chapter 3, a macro level experimental characterization was conducted performing Three Point Bending Test with variable span and modelling the material as a sandwich structure to determine longitudinal and shear elastic moduli by the proper optimisation algorithm. The best results were obtained considering the particleboard's stiffness profile along the thickness as bi-linear in the skin and constant in the core. The shear elastic constants were validated by shear Iosipescu and Three Point Bending tests coupled with Digital Image Correlation to properly determine the shear strain of the samples. The 18mm particleboard gave the best results matching the elastic constant determined by these experimental methods while for the 38mm larger differences between the values of the elastic constants obtained by different identification methods were observed. Possible causes of this shift could be the proximity of the regions where shear strains were extracted to the loading nose or the supports of the machine and probably out-of-plane displacement disturbing the measurements by the DIC method. However, by these results, it was possible to derive statistical relationships expressing

the panel's elastic longitudinal modulus as a function of the density, valid for particleboard made of recycled wood. These results could be useful to predict the elastic modulus of a panel with modified density in the perspective of weight reduction.

Lastly, in Chapter 4 the 18mm particleboard was modelled at the micro level, creating its microstructure by RVE generation using Digimat-FE module. To perform this last task, geometrical particle's data, their orientations distribution and constituents' volume fractions (wood-adhesive-voids) were determined by Micro-CT on samples extracted from panels and backlit images analysis of raw, unprocessed fibres. Another crucial aspect is the assignment of the correct mechanical properties to the wood fibres, that was performed assuming a transverse isotropic model with properties corresponding to those of the solid wood species most frequently employed in the furniture industry. Before RVE's generation, the dimensions of the representative volume and the performances of different RVE generation algorithms were evaluated to best represent the morphological aspect of the particleboard. The best response was obtained using the stacking algorithm provided in Digimat-FE to build a 30x30x30mm RVE. Two modelling strategies were assessed: with and without modelling the contribution of UF adhesive. Comparing the elastic constants results determined after RVE's homogenization with those obtained at the macro level, a good agreement was found with a RVE built with a matrix phase representing the UF adhesive, although the real adhesive distribution around wood particles was not modelled.

As further developments on the microstructure generation and macro-level approaches, the results of this work suggests performing other Micro-CTs with particleboard's samples of dimensions equal to or larger than 30x30x10mm, improving the mechanical characterization of the 38 mm panels by designing a more appropriate test rig and extending the analysis to 8mm panels.

Based on the results presented in this thesis, the knowledge of the mechanical behaviour of particleboard made of recycled wood was improved and it would be possible to use these results to understand better the effects of possible modifications (aiming at lightweight solutions) of the composition of the panel's core on the mechanical behaviour of this material.

References

1. Measurement of the surface roughness of wood based materials used in furniture manufacture. Zhong, Z. W., Hiziroglu, Salim and Chan, C. T.M. 2013, ELSEVIER Measurement, pp. 1482-1487.
2. Flynn, J. and Holder, C. A. A Guide to Useful Wood of the World. Madison Wisconsin USA : International Wood Collectors Society, Forest Product Society, 2001.
3. Eco-innovation of a wooden chilhood furniture set: An example of environmental solutions in the wood sector. Gonzàlez-Garcìa, Sara, et al. 426 (p.318-326), Santiago de Compostela, Spain : ELSEVIER , 2012, Vol. Science of the Total Environment.
4. Handbook, Wood. Wood as an Engineering Material. Madison, Wisconsin, USA : Forest Products Society, 1999.
5. Federation, European Panel. Products & Producers. European Panel Federation. [Online] SRG Group web development. http://www.europanels.org/products--producers/products.
6. Kues, Ursula. Wood Production, Wood Technologies, and Biotechnological Impacts. Gottingen, Germany : Universitatsverlag Gottingen, Umwelt Stiftung, 2007. ISBN: 978-3-940344-11-3.
7. Properties of medium density fiberboards made from renewable biomass. Philip Ye, X., et al. 98 PP. 1077- 1084, USA : Elsevier Science Direct, 2007.
8. Life cycle inventory of Medium Density FIberboard. Rivela, Beatriz, Moreira, M. Teresa e Feijoo, Gumersindo. 12 PP. 143-150, Spain : LCA Wood and Other Renewable Resources, 2007, Vol. 3. DOI: http://dx.doi.org/10.1065/lca2006.12.290.
9. Modeling and Simulation of the hot-pressing process in the production of medium density fiberboard (MDF). Carvalho, Luisa M.H. e Costa, Carlos A.V. 170:1 PP.1-21, Portugal : Chemical Engineering Communications, 1998. DOI: 10.1080/00986449808912732.
10. Callegari, Guido e Zanuttini, Roberto. Boislab, il legno per un'architettura sostenibile. Torino : Alinea Editrice, 2013.
11. MyBricoShop MDF. MyBricoShop MDF. [Online] http://www.mybricoshop.com/panneli-in-legno-2/pannello-mdf-detail.
12. EPF. Dry Process Fiberboard. EPF. [Online] http://www.mdf-info.eu/generalit/fabbricazione-dellmdf.
13. —. OSB Today's most versatile wood-based panel. EPF. [Online] http://www.osb-info.org/index.php?lang=uk.
14. MyBricoShop. MyBricoShop OSB. MyBricoShop OSB. [Online]. http://www.mybricoshop.com/panneli-in-legno-2/pannelli-osb-detail.
15. EPF. OSB Tecnical information sheet. EPF. [Online] http://www.osb-info.org/technical.html.
16. board, NFB Natural Fibre. About NFB. Natural Fibre board. [Online] SRG group. http://www.naturalfiberboard.eu/about-nfb.
17. B.V., Rowood. ROWOOD Impteurs van hout en plaatmaterialen. Rowood. [Online] http://www.rowood.net/nl-nl/producten/hardboard.aspx.
18. B.V., ECOBOARD INTERNATIONAL. Eco Board Softboard. ECO BOARDS. [Online] ECOBOARDS. http://ecoboardinternational.com/ecoboard-softboard/.
19. Board, Natural Fibre. NFB Hardboard. Natural Fibre Board. [Online] SRG Group. http://www.naturalfiberboard.eu/nfb-hardboard.
20. NFB Softboard. NFB Natural Fibre Board. [Online] http://www.naturalfiberboard.eu/nfb-softboard.

21. EWPAA. Library, Plywood Manufacture. EWPAA Engineered wood products association of australasia. [Online] 2015. https://www.ed.ewp.asn.au/Public_Access/Library/document.aspx?articleid=19&from=Search.
22. Plywood Manufacture. Australia : EWPAA, 2012.
23. PLYWOOD, YORKSHIRE. Plywood. YORKSHIRE PLYWOOD. [Online] Linfoots. http://www.yorkshireplywood.co.uk/brazilian-hardwood-plywood.cfm.
24. The down to earth woodworker. Wood News Online. [Online] Highland Hardware, Inc, 2013. http://www.woodnewsonline.com/DTEW/1306jun/downtoearthwoodworker4.html.
25. Plywood, Austral. Austral Plywood - Technical characteristics. Austral Plywood. [Online] Austral Plywood, 2016. http://www.australply.com.au/index.php/technical/characteristics.
26. SRL, Saviola Holding. Gruppo Mauro Saviola. Gruppo Mauro Saviola. [Online] Saviola Holding. http://www.grupposaviola.com/pannello-nobilitato/.
27. Hybrid Chipboard panels based on sugarcane bagasse, urea formaldehyde and melamine formaldehyde. Monterio de Barros Filho, Roberto, et al. PP. 369-373, Brazil : Elsevier, Industrial Crops and Products, 2011, Vol. 33.
28. Suitability of kiwi (Actinidia sinesis Planch.) prunings for particleboard manufacturing. Nemli, Gokay, et al. PP. 39-46, Turkey : Elsevier, Industrial crops and products, 2003, Vol. 17.
29. Suitability of date palm (Phoenix Dactyferia) banches for particleboard production. Nemli, G, Kalaycioglu, H. e Alp, T. PP. 411-412, Turkey : Holz als Roh und Werkstoff, 2001, Vol. 59.
30. Evaluation of the physical, mechanical properties and formaldheyde emission of particleboard manufactured from waste stone pine (Pinus Pinea L.) cones. Buyuksari, Umit, et al. PP. 255-259, Turkey : Elsevier, Bioresource technology, 2009, Vol. 101.
31. UNI. EN 312 Particleboards Specifications. European Standard : UNI, 2010.
32. unificazione, UNI - Ente nazionale italiano di. UNI EN 310 Determinazione del modulo di elasticità a flessione e della resistenza a flessione. Milano : UNI - Ente nazionale italiano di unificazione , 1994.
33. UNI. EN319 Particleboards and fiberboards - Determination fo tensile strength perpendicular to the plane of the board. s.l. : EN, 1994.
34. Davoli, Piermaria, et al. Comportamento meccanico dei materiali. Milano : McGraw-Hill, 2005. ISBN 88-386-6150-2.
35. Influence of board density, mat construction, and chip type on performance of particleboard made from eastern redcedar. Zhiyong, Cai, et al. 12, Japan : Forest product Journal, December 2004, Vol. 54.
36. Effect of mat moisture content and press closing speed on the formation of density profile and properties of particleboard. Ee Ding, Wong, et al. Japan : Journal Wood Science, 1998, Vol. 44.
37. Choiche of an analytical scheme in correlating strain energy release rate, crack length and opening of the face of an adhesively bonded, thick composite DCB specimen. Bernasconi , Andrea e Azhar, Jamil. Aalborg : O.T.Thomsen, Bent F. Sorensen; Christian Berggreen, 2013.
38. Energy release rate of symmetric adhesive joints. Krenk, S. s.l. : Engineering Fracture Mechanics, 1992, Vol. 43 pp. 549-559.
39. Determination of in-plane shear properties by three-point flexure test of +-45° anti-symmetric laminates. Vargas, Gustavo e Mujika, Faustino. San Sebastian, Spain : Polymer Testing, 2010, Vol. 30 pp. 204-215.
40. Daniel, I. M. e Ishai, O. Engineering Mechanics of Composite Materials. New York : Oxford University, 1994.
41. Whitney, J. M. Structural Analysis of Laminated Anisotropic Plates. Lancaster : Technomic, 1987.

42. On the determinationof out-of-plane elastic properties of honeycomb sandwich panels. Mujika, Faustino, Pujana, J. e Olave, M. Spain : Polymer Testing, 2011, Vol. 30 pp. 222-228.
43. On the Displacement Field for Unidirectional Off-Axis Composites in 3 Point Flexure - Part II: Numerical and Experimental Results. Mujika, Faustino, De Benito, A, e Mondragon, I. 13, Spain : Journal of Composite Materials, 2003, Vol. 37.
44. Multiscale Methods for Composites: A Review. Kanoute, P., et al. Spain : Arch Comput Methods Eng, 2009, Vol. 16.
45. A multiscale mean-field homogenization method for fiber-reinforced composites with gradient-enhanced damage models. Wu, L., et al. PP 164-169, Belgium : Comput. Methods Appl. Mech. Engrg., 2012.
46. Engineering Damage Mechanics: Ductile, Creep, Fatigue and Brittle Faliures. Lemaitre, J. e Desmorat, R. Berlin : Springer-Verlag, 2005. ISBN 3540215034.
47. Transoframtion Field Analysis of inelastic composites materials. Dvorak, G. J. 2132 - PP. 311-327, s.l. : Procedings: Math. Phys. Sci. , 1992, Vol. 437.
48. A new mean field micromechanical approach to capture grain size effect. Pipard, J. M., et al. PP. 604-610, France : Computational Material Science, 2009, Vol. 45.
49. The Mori-Tanaka method applied to textile composite materials. Gommers, B., Verpoest, I. e Van Houtte, P. 6 PP. 2223-2235, Belgium : Elsevier Science Ltd., 1998, Vol. 46.
50. An extended Mori-Tanaka model for the elastic moduli porous materials of finite size. Gong, S., Li, Z. e Zhao, Y. Y. PP. 6820-6830, China : Acta Materialia, 2011, Vol. 59.
51. Acta Metall. Mori, T. e Tanaka, K. PP. 571, 1973, Vol. 21.
52. Pseudo-grain discretization and full Mori Tanaka formulation for random heterogeneous media: Predictive abilities for stresses in individual inclusions and the matrix. Jain, Atul, et al. PP. 86-93, Belgium : Composites science and technology, 2013, Vol. 87.
53. Investigations on micro-mechanical and thermal characteristics of glass fiber reinforced epoxy based binary composite structure using finite element method. Patniak, Amar, et al. PP. 142-151, India : Computational Material Science, 2012, Vol. 62.
54. Ronald, F. e Gibbson. Principles of Composite Materials Mechanics. s.l. : Mc-GrawHill. ISBN: 0-07-113335-6.
55. Journal of Applied Polymer Science. He, T e Porter, R. S. PP. 1945-1953, 1988, Vol. 35.
56. —.Ibarra, L., Macias, M. e Palma, E. PP. 831-842, 1995, Vol. 57.
57. Numerical simulation of the effects of volume fraction, aspect ratio and fibre length distribution on the elastic and thermoelastic properties of short fiber composites. Hine, Peter J., Lusti, Hans Rudolf e Gusev, Andrei A. PP.: 1445-1453, UK; Swiss : Composites science and technology, 2002, Vol. 62.
58. Numerical Homogenization for composite materials analysis. Comparison with other micro mechanical formulations. Otero, F., et al. PP. 405-416, Spain : Composite Structure, 2015, Vol. 122.
59. A numerical procedure simulating rc structures reinforced with frp using the serial/parallel mixing theory. Martinez, X., et al. PP. 18-1604, s.l. : Computational Struct, 2008, Vol. 18.
60. Stock, Stuart R. MicroComputed Tomography Methodology and applications. USA : CRC Press Taylor & Francis Group, 2009. ISBN: 13:978-1-4200-5876-5.
61. A High-Fidelity and Micro-Anatomically Accurate 3D Finite Element Model for Simulations of Functional Mitral Valve. Lee, Chung-Hao, et al. PP. 416-424, USA : Springer-Verlag Berlin Heidelberg, 2013.
62. Characterizing Three-Dimensional Textile Ceramic Composites Using Syncrothron X-Ray Micro-Computed Tomography. Bale, Hrishikesh, et al. 95 PP. 392-402, USA : The American Ceramic Society, 2012, Vol. 1.

63. Internal damage investigation of the impacted glass/galss + aramid fiber reinforced composites by micro-computerized tomography. Sinan, Fidan, Sinmazcelik, Tamer e Avcu, Egemen. PP. 1-7, Turkey : Elsevier NDT International, 2012, Vol. 51. DOI 0963-8695.
64. Tables of X-Ray Mass Attenuation Coefficients and Mass-Energy Absorption Coefficients. Hubbel, J. H. e Seltzer, S. M. Gaithesburg, MD : National Institute of Standard and Technology, 2016, Vol. http://physics.nist.gov/xaamdi.
65. Agency, International Atomic Energy. https://www-nds.iaea.org/publications/. https://www-nds.iaea.org/publications/. [Online] https://www-nds.iaea.org/publications/.
66. Nowotny, Robert. XMuDat ver 1.0.1. Austria : s.n., 1998.
67. Lightsources, Elettra and FERMI. Elettra Sincrotrone Trieste. Elettra Sincrotrone Trieste. [Online] https://www.elettra.trieste.it/it/index.html.
68. Synchrotron Radiation Micro-Tomography: a Non-Invasive Tool for the Characterization of Archaeological Wood. Dreossi, D., et al. PP. 1-39, Italy : Wood Science for Conservation of Cultural Heritage, 2010, Vol. 1.
69. Three-Dimensional Non-Destructive Analysis of Wood Samples Using Synchrotron Radiation Microtomography. Zanini, F., et al. Italy : Conference proceedings: Giornata del gruppo interdivisionale di chimica dei beni culturali (PISA - IT), 2002.
70. Assessment of Digital Image Correlation measurement errors: methodology and results. Bornert, M., et al. 3 PP. 353-370, France : Experimental Mechanics, 2009, Vol. 49.
71. A comparative study of random patterns for digital image correlation. Stoilov, G., Kavardzhhikov, V. e Pashkouleva, D. 2 PP. 55-66, Bulgaria : Journal of Theoretical and Applied Mechanics, 2012, Vol. 42.
72. Adaptation of Open Source 2D DIC Software Ncorr for Solid Mechanics Applications. Harilal, R. e Ramij, M. India : 9th International Symposium on Advanced Science and Technology in Experimental Mechanics, 2014.
73. A methodology for high resolution digital image correlationin high temperature experiments. Blaber, J., Adair, B. S. e Antoniou, A. Georgia : Review of scientific instruments, 2015, Vol. 86.
74. Solutions, Correlated. Correlated Solutions. Correlated Solutions. [Online] 2016. http://correlatedsolutions.com/vic-2d/.
75. Dynamics, Dantec. Dantec Dynamics. Dantec Dynamics Q-400. [Online] 2016. http://www.dantecdynamics.com/q-400-dic.
76. V1.2, N-Corr. N-Corr V1.2. N-Corr V1.2. [Online] 2016. http://www.ncorr.com/index.php.
77. MathWorks. MathWorks. MathWorks. [Online] 2016. http://it.mathworks.com/products/matlab/.
78. Deformation Measurements by Digital Image Correlation: Implementation of a Second-Order Displacement Gradient. Lu, H. e Cary, P. D. 4 PP. 393-400, USA : Experimental Mechanics, 2000, Vol. 40.
79. Submicron deformation field measurement: Part 1. Developping a digital scanning tunneling microscope. Vendroux, G. e Knauss, W. G. PP. 18-38, s.l. : Experimental Mechanics, 1998, Vol. 38.
80. Applied numerical analysis . Gerald, C. F. e Wheatley, P. O. s.l. : Addison-Wesley Readings MA, 1994.
81. Nextdayscience. Nextdayscience - Parafilm. Nextdayscience. [Online] Nextdayscience. http://www.nextdayscience.com/lab-ware/parafilm.htm.
82. Enhanched and flexible software tools at SYRMEP. Brun, F. Szeged : Elettra Sincrotrone Trieste, 2016.
83. Fiji. Fiji. Fiji. [Online] 2016. http://fiji.sc/.
84. Detection and distribution analysis of organosolicon compounds in wood by meand of SEM-EDX and Micro-CT. De Vetter, L., et al.

85. Visualization and numerical analysis of adhesive distribution in particleboard using X-Ray micro-computed tomography. Evans, Philip, et al. PP.754-762, Canada, Australia : International Journal of Adhesion and Adhesive, 2010, Vol. 30.
86. UNI- Ente nazionale italiano di unificazione . UNI EN 322 Determinazione dell'umidità. Milano : UNI, 1994.
87. Wetting and film formation of wheat gluten dispersions applied to wood structures as particle board adhesives. Khosravi, S., et al. PP. 476-482, Sweden : European Polymer Journal, 2015, Vol. 67.
88. Medical CAT-Scanning: X-Ray Absorption coefficients, CT number and their relation to wood density. Lindgren, L. O. PP.341-349, Sweden : Wood Science and Technology, 1991, Vol. 25.
89. Wood Density Determination by X- and Gamma-Ray Tomography. Macedo, A., et al. PP. 535-540, Brazil : Holzforschung, 2002, Vol. 56.
90. Non-destructive wood density distribution measurements using computed tomography. Lindgren, O. PP. 295-299, Sweden : Holz als Roh- und Werkstoff, 1992, Vol. 50.
91. Synchrotron X-Ray microtomography imaging and analysis of wood degraded by Physisporinus vitreus and Xylaria longipes. Gilani, Marjan Sedighi, et al. PP. 149-157, Belgium, Switzerland : Journal of Structural biology, 2014, Vol. 187.
92. Measurement of linear attenuation coefficients of breast tissues by synchrotron radiation computed tomography. Chen, R. C., et al. PP. 4993-5005, UK : Physics in Medicine and Biology, 2010, Vol. 55.
93. GROUP, IMAL PAL. IMAL DPX 300. IMALPAL. [Online] 2016. http://www.imalpal.com/it/scheda.php?pr=111.
94. Scintillation detectors for xrays. Nikl, Martin. PP. 37-54, Czech Republic : Measurement Science and Technilogy, 2006, Vol. 17.
95. unificazione, UNI - Ente nazionale italiano di. UNI EN 322 Determinazione della massa volumica. Milano, Italy : UNI - Ente nazionale italiano di unificazione, 1994.
96. International, ASTM. D7250/D7250M - 06 Standard pratice for Determining Sandwich Beam Flexural and Shear Stiffness. United States : ASTM International, 2012.
97. MTS. MTS. MTS. [Online] 2004. http://www.mts.com/en/index.htm.
98. International, ASTM. ASTM D5379/D5379M-12 Standard test method for Shear Properties of Composite Materials by the V-Notched Beam Method. United States : ASTM Inrternational.
99. Babler, Justin e Antoniou, Antonia. Ncorr - Instruction Manual V1.2.1. United States : Georgia Institute of Technology, 2015.
100. Montgomery, Runger Hubele. Statistica per l'ingegneria. Milano : EGEA S.P.A, 2007. ISBN 978-88-238-2037-1.
101. Measurement of the shear modulus of wood by static bending test. Yoshihara, Hiroshi, et al. PP.15-20, Japan : Journal Wood Science, 1997, Vol. 44.
102. Cellular solids - Structures and Properties. Gibson, L. G. e Ashby, M. F. Oxford : Pergamon Press, 1988.
103. Zenkert, D. The Handbook of Sandwich Construction. s.l. : EMAS Publishing, 1997.
104. Davoli, Piermaria, et al. Costruzione di Macchine 1. Milano : McGraw-Hill, 2007. ISBN-88-386-6380-7.
105. Bernasconi, Andrea, et al. Fondamenti di Costruzione di Macchine. Milano : McGraw-Hill, 2006. ISBN-88-386-6344-0.
106. Carini, Andrea e Villa , Tiziano. Multiscale Models for the mechanical behaviour of particleboard. Milano, Italia : Politecnico di Milano, Tesi di laurea in ingegneria meccanica, 2016.
107. Xstream. DIGIMAT User's Manual (Release 2016.0). Belgium : Xstream MSC software company, 2016.

108. Micromechanical simulations of biaxial yield, hardening and plastic flow in short glass fiber reinforced polyamide. Selmi, A., Doghri, I. e Adam, L. PP. 696-706, Tunis : International Journal of Mechanical Sciences , 2011, Vol. 53.
109. Multiscale homogenization model for thermoelastic behavior of epoxy-based composites with polydispersed SiC nanoparticles. Seongmin, Chang, et al. PP. 342-353, South Korea and Seul : Composite Structure , 2015, Vol. 128.
110. Allevi, Alessio e Rossin, Davide. La progettazione eco-compatibile con le poliammidi rinforzate in fibra di vetro riciclate. Tesi di Laurea in Ingegneria Meccanica Politecnico di Milano. Milano : Politecnico di Milano (Davoli - Bernasconi), 2003-2004.
111. Scientific, Horiba. A guidebook to particle size analysis. Irvine USA : Horiba Instruments, INC. (www.horiba.com/us/particle), 2016.
112. The use of tensor to describe and predict fiber orientation in short fiber composites. Advani, S. G. e Tucker, C. L. PP 751-784, s.l. : Journal of rheology, 1987, Vol. 31.
113. Active contours without edges . Chan, T. F. e Vese, L. A. 2 PP. 266-277, s.l. : IEEE Transactions on image processing, 2001, Vol. 10.
114. Geodesic active contours. Kassel, V., Kimmel, R. e Sapiro, G. 1 PP.61-79, s.l. : International Journal of computer vision, 1997, Vol. 22.
115. On-line tool wear monitoring using geometric descriptiors from digital images. Castejon, M., et al. PP. 1847-1853, Spain and Colombia : International journal of Machine tools and Manufacture design research and application, 2007, Vol. 47.
116. Real-Time Scene Text Localization and Recognition. Neumann, Lukas e Matas , Jiri. PP 3538-3545, Czech Republic : s.n., 2012. 978-1-4673-1228-8/12.
117. UTCT. Texas Geoscience. QUANT 3D. [Online] Texas Geoscience. http://www.ctlab.geo.utexas.edu/software/quant3d/.
118. Phase contrast micro-tomography and morphological analysis of a short carbon fibre reinforced polyamide. Cosmi, Francesca, Bernasconi, Andrea e Sodini, Nicola. PP. 23-30, Italy : Composites Science and Technology, 2011, Vol. 71.
119. Combined effect of notches and fibre orientation on fatigue behaviour of short fibre reinforced polyamide. Bernasconi, Andrea, Cosmi, Francesca e Zappa, Emanuele. PP. 435-445, Italy : Strain, Blackwell Publishing, 2010, Vol. 46.
120. Quant3D, UTCT -. Quant3D User's Guide. s.l. : UTCT, 2008.
121. Characterization of internal void structure of strand-based wood composites using X-Ray tomography and digital tools. Zhang, Bing, et al. United States and China : Proceedings pf McMat 2005, 2005.
122. A threshold selection method from Gray-Level Histograms. Otsu, Nobuyuki. PP 62-66, Tokyo; Japan : IEEE Transactions On System, Man, and Cybernetics , 1979, Vol. 9.
123. Rowell, Roger M. Handbook of wood chemistry and wood composites. USA : CRC Press, 2013. ISBN 978-1-4398-5380-1.
124. Measurement of standard and off-axis elastic moduli and poisson's ratio of spruce and yew wood in the transverse plane. Garab , Jozsef, et al. PP. 451-464, Hungary; Switzerland : Wood Science and Technology, 2010, Vol. 44.
125. Three-dimensional elastic behaviour of common yew and Norway spruce. Keunecke, Daniel, Hering, Stefan e Niemz, Peter. PP.: 633-647, Switzerland : Wood Science and Technology, 2008, Vol. 42.
126. Mechanics of wood and wood composites. Bodig, J. e Jayne, B. A. New York : Van Nostrand, 1982.
127. Properties of wood-plastic composites made of milled particleboard and polypropylene. Gozdecki, Cezary, et al. PP.:87-95, Poland : Europena Journal of wood product, 2015, Vol. 73.

128. Unificazione, European Standard - Ente Nazionale Italiano di. Structural timber - Strength classes. Milano : Ente Nazionale Italiano di Unificazione, 2009. UNI EN 338:2009.
129. Green, David W., Winandy, Jerrold E. e Kretschmann, David E. Mechanical Properties of Wood. [aut. libro] Forest products laboratory. Wood Handbook - Wood as an engineering material. Madison W. I - U.S. : Department of Agricolture, Forest Service, 1999.
130. Martienssen, Werner e Warlimont, Hans. Springer Handbook of Condensed Matter and Materials Data. Germany : Springer, 2004. ISBN 3-540-44376-2.
131. Matbase. Matbase; materials thermosetr. [Online] https://www.matbase.com/material-categories/natural-and-synthetic-polymers/thermosets/material-properties-of-urea-formaldehyde-uf.html#thermal-properties.
132. Hrdness evaluation of cured urea-formaldehyde resins with different formaldehyde/urea ratios using nanoindentation method. Park, Byung-Dae, et al. Republic of Korea; USA; China : European Polymer Journal, 2013, Vol. http://dx.doi.org/10.1016/j.eurpolymj.2013.06.013.
133. Determining the representative volume element size for three-dimensional microstructural material characterization. Part 1: Predictive models. Harris, William M. e Chiu, Wilson K. S. PP. 552-561, USA : Journal of power sources, 2015, Vol. 282.
134. Microstructural randomness versus representative volume element in thermomechanics. Ostoja-Starzewski, M. PP.:25-35, Canada : Journal of applied mechanics, 2002, Vol. 69.